

ISLAND EFFECTS ON RAINFALL FOR THE HAWAIIAN ISLANDS WITH
MOUNTAINTOPS BELOW THE TRADE WIND INVERSION

A DISSERTATION SUBMITTED TO THE GRADUATE DIVISION OF THE UNIVERSITY
OF HAWAI'I AT MĀNOA IN PARTIAL FULFILLMENT OF THE REQUIREMENTS FOR

THE DEGREE OF

DOCTOR OF PHILOSOPHY

IN

ATMOSPHERIC SCIENCES

May 2020

By

Feng Hsiao

Dissertation Committee:

Yi-Leng Chen, Chairperson

Michael Bell

Fei-Fei Jin

Bin Wang

Kwok Fai Cheung

Acknowledgments

First and foremost, I must express my deep appreciation for my advisor, Prof. Yi-Leng Chen. Prof. Chen has always been supportive of both academically and personally. I am continuously amazed by the range and diversity of his knowledge (from religion to earth sciences). I am deeply inspired by his enthusiasm for knowledge and grateful for the financial support he gave me throughout the years. Without his support, pursuing a Ph.D. degree would have been nearly impossible.

I also must address my appreciation for the rest of my committee: Profs. Michael Bell, Kwok Fai Cheung, Fei-Fei Jin, and Bin Wang. They have continuously provided me with constructive feedback and warm encouragement, which are essential to this dissertation. Each time we met, they gave me numerous interesting ideas. I must particularly emphasize the tremendous help I received from Prof. Jin. In my final months, constructive feedback and warm encouragements from him help me complete the journey.

I would like to thank Dr. Ning Li and Melissa Iwamoto at PacIOOS during the project cooperation. The graduate assistantship from them granted to me not only expanded my research experience but also substantially reduced my financial burden. Further, the friends in the ATOMS department play a very important role in my professional development. Aside from providing immeasurable camaraderie, they have stimulated me through meaningful discussions on issues and questions I have faced during the coursework and my research. I would just like to especially thank Hiep Van Nguyen, Chuan-Chi Tu, Chih-Ying Chen, David Hitzl, Chuan-Kai Wang, Lei Zhang, Yu Du, Boyi Lu, and Po-Cheng Chen.

Last but not least, I am grateful that I have an extremely supportive family. In particular, I would like to thank my parents for their unconditional support.

Abstract

The goal of this research is to investigate the island-scale rainfall, weather, and climate over various local communities in Hawai‘i, especially for islands (O‘ahu and Kaua‘i) with mountain heights below the typical trade wind inversion.

High-resolution modeling and satellite observations during July–August 2013 are used to the physical processes responsible for wake circulation and clouds over O‘ahu in the lee-side wake zone under trade wind conditions. In the morning, orographic clouds are more significant on the windward side of the Ko‘olau Range when trades are stronger, and are advected downstream by trade winds aloft. During the daytime, warmer air over the island interior is advected off the western leeward coast by downslope winds under strong trades. In contrast, upslope/sea-breeze flow occurs along the leeward coast under weak trades with orographic clouds on the western leeward slopes after sunrise under weak trades. These clouds are advected westward by the combined trade wind and the easterly return flow aloft, resulting in more significant cloudiness in the wake zone with larger horizontal extent in the early afternoon when trades are weaker.

Short-lived afternoon heavy rainfall events may form over Central O‘ahu during seasonal transition periods (June and October) under favorable large-scale settings. These include a deep moist layer with relatively high total precipitable water (TPW, > 40 mm), a blocking pattern in mid-latitudes with a northeast–southwest moist tongue from low latitudes ahead of an upper-level trough, the absence of a trade wind inversion, and variable ($< 3 \text{ m s}^{-1}$) low-level winds. Our high-resolution (1.5 km) model results show that daytime land surface heating deepens the mixed layer over Central O‘ahu while the top of the mixed layer reaches the lifted condensation level. Meanwhile, the development of onshore/sea-breeze flows, driven by land–sea thermal contrast, brings in moist maritime air over the island interior. Finally, convergence of the onshore flows

over Central O‘ahu provides the localized lifting required for the release of instability. Based on synoptic and observational analyses, nowcasting with a lead time of 2–3 hours ahead of this type of event is possible. In the absence of orographic effects after removing model topography, the destabilizing effects of daytime heating, horizontal advection of moist maritime air inland by the onshore/sea-breeze flows, convergence over Central O‘ahu, and the subsequent development of the heavy showers over land are still simulated. However, when surface fluxes are turned off in the NF run, convective cells are not simulated in the area. These results indicate that daytime heating is crucial for the development of this type of heavy rainfall event under favorable large-scale settings.

During typical summer trade wind conditions, orographic precipitation occurs frequently over the mountainous Hawaiian Islands. The mountaintop of Kaua‘i, one of the wettest spots on earth, has the highest rainfall amount during the summer months among the Hawaiian Islands. Based on model sensitivity test, our results show that the orographically induced moisture flux convergence and orographic lifting at the slope surface are the two most dominant terms for the rainfall production. In addition, rainfall production also related to TPW in the environment. Under undisturbed summer trade-wind weather, the moisture flux convergence is related to orographic and local effects, including: flow deceleration on the windward side due to orographic blocking, interactions between the incoming flow and offshore flow due to nocturnal and/or evaporative cooling, and convergence between the incoming winds and opposing sea breezes in the leeward side. Furthermore, moisture flux convergence is enhanced by latent heat release. The vertical lifting by winds on the slope surface could be attributed to mechanical lifting and modified by daytime upslope and nighttime downslope winds. For previous theoretical studies on orographic precipitation based on Froude number and orographic rainfall index, the orographically induced

moisture convergence and convective feedbacks as well as diurnal variations in land surface heating are largely ignored.

The El Niño-Southern Oscillation (ENSO) is a prominent mode of climate variability at the inter-annual time scale. During the negative phase of ENSO (El Niño), Hawai‘i frequently experiences droughts in winter, which continue into the following spring. Less is known about the impact of El Niño on local spatial patterns of rainfall, temperature, moisture and winds. Recent studies have shown that there are two different flavors of El Niño [east Pacific type/Cold Tongue (CT) and central Pacific type/warm pool (WP)]. With large spatial variations of local climate, better understanding of the impact of El Niño favors on different island communities is investigated with regional and island-scale simulations. During El Niño winters, especially under CT events, synoptic subsidence is greater with lower TPW over Hawai‘i than long-term seasonal mean due to a merged inter-tropical convergence zone and South Pacific convergence zone and eastward shift of the Walker Circulation. During El Niño springs, the enhanced tropical convergence weakens with less significant impacts on subsidence over the Hawai‘i than during winters. The results from 6-km simulations during 1979–2017 shows drier conditions during the CT events than during the WP events, and the dry conditions are more significant in winter. During El Niño winters, the Hawaiian region has positive temperature anomalies at the 700 hPa level and are more significant (1.0 K) during the CT winters than during the WP winters (0.5 K).

Five CT, six WP, and six neutral events during winter and spring are simulated with an island-scale model over O‘ahu and Hawai‘i. The simulated rainfall patterns are comparable to the Rainfall Atlas of Hawai‘i, however, the high-resolution model overestimates the rainfall amount. During both types of El Niño events, the nighttime cooling accentuated by less atmospheric water vapor affects the simulated surface temperatures over the regions below the trade wind inversion.

For island regions above the trade wind inversion, surface warming is accentuated by increased subsidence associated with the Hadley circulation. For Hawai‘i Island, drought conditions are expected during the CT winters over the mountaintops of Mauna Kea and Mauna Loa and in the leeward side of the Kohala Mountains due to decreased trade wind and low TPW. During the CT springs, persistently weak trade wind speed and low TPW result in maximum rainfall deficiencies over the windward slopes and mountaintops below the trade wind inversion. However, the dry conditions over the windward slopes are less significant during the CT springs than during the CT winters. The only region with greater daily rainfall during the CT springs is off the Kona coast, before sunrise, resulting from the convergence of katabatic flows with the westerly winds offshore. The rainfall distributions during the WP events are quite similar to those during the CT events, however, the dry conditions are less significant due to higher TPW in the environment.

For islands with mountaintops below the trade-wind inversion, during the CT winters, increased synoptic subsidence and low TPW are crucial in resulting in drier or even drought conditions over the mountaintops, e.g. the Ko‘olau Mountains on O‘ahu. Daily rainfall over the Ko‘olau Mountains and windward coast are lower during the CT winters than the neutral winters. During the CT springs, the dry conditions are still simulated over mountainous regions. For WP events, mountainous regions with drier than neutral conditions are less significant. During the WP springs, more rainfall is only simulated over the southwestern coasts in the afternoon hours than during the neutral springs due to enhanced thermally driven circulations over the leeward coasts due to warmer surface daytime temperature over land than during the neutral springs.

Table of Contents

Acknowledgments.....	ii
Abstact	iii
Table of Contents	vii
List of Tables.....	xi
List of Figures	xiii
Chapter 1 Introduction.....	1
1.1 Background	1
1.2 Literature Review	2
1.3 Scientific Objective.....	10
Chapter 1 Figures.....	13
Chapter 2 Data and Model Description	17
2.1 NCEP Climate Forecast System (CFS) data	17
2.2 Model Description.....	17
Chapter 2 Figures.....	20
Chapter 3 Effects of Trade Wind Strength on Airflow and Weather over O‘ahu	22
3.1 Introduction	22
3.2 Methodology	26
3.2.1 Strong and Weak Trade Categories	26
3.2.2 Study Area and Model Verifications	27

3.3	Effects of Trade Wind Strength on Cloud Patterns, Airflow and Thermodynamic Fields	30
3.3.1	Satellite Observations of Cloud Patterns	31
	i) Strong trades.....	31
	ii) Weak trades.....	31
3.3.2	Numerical Simulations	33
	i) 0500HST	33
	ii) 1400HST	35
3.4	Summary	37
Chapter 3	Tables.....	39
Chapter 3	Figures.....	43
Chapter 4	Heavy Rainfall Events over Central O‘ahu under Weak Wind Conditions during Seasonal Transitions.....	68
4.1	Introduction	68
4.2	Data and Methodology	71
4.3	A Composite Study	73
4.3.1	Synoptic Conditions.....	73
4.3.2	Observational Analysis.....	74
4.3.3	Numerical Simulations	75
4.4	A Case Study of the Central O‘ahu Storm	76

4.4.1	Synoptic Conditions.....	76
4.4.2	Surface Observations.....	77
4.4.3	Storm Evolution.....	77
4.5	Numerical Simulations of the 8 June 2003 Case.....	78
4.5.1	The Evolution of the Mixed Layer	78
4.5.2	The Evolution of Simulated Surface Winds and Vertical Motion.....	79
4.5.3	The Evolution of Simulated Radar Reflectivities	82
4.5.4	Simulated Rainfall in Comparison with Observations	82
4.5.5	Model Sensitivity Tests	82
4.6	Summary	84
Chapter 4	Tables.....	86
Chapter 4	Figures.....	88
Chapter 5	The Factors Affecting Orographic Precipitation over Kaua‘i.....	112
5.1	Introduction.....	112
5.2	Method	114
5.3	Model Results.....	116
5.3.1	Simulated Mean State	116
5.3.2	Simulated Total Rainfall of CTRL	117
5.3.3	Sensitivity to Terrain Heights, Steepness of Mountain, and Geolocations .	118
5.4	Summary	122

Chapter 5	Tables	123
Chapter 5	Figures.....	127
Chapter 6	The Influences of Different El Niño Flavors on Island-scale Rainfall and Weather for the Hawaiian Islands with Mountaintops below and above the Trade Wind Inversion	141
6.1	Introduction	141
6.2	Study Area and Methodology	144
6.2.1	Model Description and Initialization	144
6.2.2	The Definitions of CT and WP El Niño Events	145
6.3	Results.....	146
6.3.1	Key Features between CT and WP El Niño Events	146
6.3.2	Synoptic Analysis	146
6.3.3	El Niño Impacts on Rainfall over the Hawaiian Region	152
6.3.4	El Niño Impacts on Rainfall over the Islands with Mountaintops below and above the Trade Wind Inversion.....	159
6.4	Summary	164
Chapter 6	Tables	167
Chapter 6	Figures.....	168
Chapter 7	Discussion and Summary.....	223
Reference	243	

List of Tables

Table 3.1 A list of the nine weak trade wind day and the nine strong trade wind days. The wind data at the upstream point of O‘ahu (21.5°N, 157.5°W) are daily averages of CFSv2 analysis.....	39
Table 3.2 The temporal resolution and geolocation of the 24 weather stations.	40
Table 3.3 Error statistics of surface temperature and surface relative humidity for model points corresponding to the 18 weather stations during the 36 trade wind days from July–August 2013.....	41
Table 3.4 Error statistics of surface wind for model points corresponding to the 17 weather stations during the 36 trade wind days from July–August 2013.....	42
Table 4.1. A list of the 13 heavy rainfall events, including the date, accumulated rainfall maximum during 0900–1700 HST, and the disaster records in the NCEI storm event database.....	86
Table 4.2 Error statistics for the weather stations reporting during 0900–1100 HST for the 13 heavy rainfall days. The error statistics are computed every hour.	87
Table 5.1 The temporal resolution and geolocation of the nine weather stations during the 38 trade wind days in July–August 2013. The italicized stations represent the stations with observation time ending at 34–35 min.....	123
Table 5.2 Error statistics for the weather stations on the trade wind days.....	124
Table 5.3 The geolocation and elevations of the 13 rain gauge stations during the 38 trade wind days in July–August 2013.....	125
Table 5.4 Error statistics for the 13 rain gauge stations during the trade wind days.	125

Table 6.1 Classification of El Niño events from 1950–2017 based on Ren and Jin (2011) indices.

..... 167

List of Figures

Fig. 1.1 Averaged 10-m wind for the period of 11 July through 24 August 1990: (a) HaRP observations at 0200 HST; (b) HaRP observations at 1400 HST; (c) MM5 24-h forecast valid at 0200 HST; and (d) MM5 12-h forecast valid at 1400 HST. One pennant, full barb, and half barb represent 5, 1, and 0.5 m s⁻¹, respectively (Yang et al., 2005)..... 13

Fig. 1.2 (a) The mean simulated horizontal distribution of surface winds (black) and observed surface winds (red) at 13 stations during July – August 2005 at 1400 HST; one pennant 5 m s⁻¹, full barb 1 m s⁻¹, half barb 0.5 m s⁻¹. (b) Same as (a) but for 0500 HST (Nguyen et al., 2010). 14

Fig. 1.3 Three-hour rainfall accumulation during July - August 2005: observed (left) and simulated (right) rainfall (mm) (Nguyen et al. 2010). 15

Fig. 1.4 Total rainfall accumulation (mm) for 9 Aug 2005 for the (a) control case and the (b) no mountain case. (Nguyen et al., 2010). 16

Fig. 2.1 (a) New land-cover/use data for O‘ahu with 1.5-km grids adapted from the Coastal Change Analysis Program (C-CAP) High-Resolution Land Cover. (b) New vegetation fraction (%) adapted from the C-CAP High-Resolution Land Cover..... 21

Fig. 3.1 The island of O‘ahu. Elevation contours are in 200-m intervals. A brown × represents the surface weather stations during July–August 2013. A solid line indicates the position for the cross-section analysis. 43

Fig. 3.2 The mean TPW (mm) from CFS during July–August (a) of 1979–2015 and (b) 2013. (c) Scatter plot of the composite mean of total precipitable water during July–August and the mean total precipitable water during July–August 2013. 44

Fig. 3.3 The mean wind at 1000 hPa from CFS during July–August (a) for 1979–2015 and (b) 2013. (c) The wind difference between (a) and (b).	45
Fig. 3.4 Three nesting domains employed in the simulations with grid sizes of 13.5 km, 4.5 km, and 1.5 km, respectively. The black star represents the upstream point for O‘ahu used in this study (21.5°N, 157.5°W).....	46
Fig. 3.5 Histogram of (a) wind direction and (b) wind speed from CFSv2 at the upstream point during July – August 2013.....	47
Fig. 3.6 Composite analysis of simulated surface wind (black barb, $m s^{-1}$) and observed surface wind (purple barb, $m s^{-1}$) for the 36 trade wind days at (a) 0500 HST, and (b) 1400 HST. One pennant is $5 m s^{-1}$, a full barb is $1 m s^{-1}$, a half barb is $0.5 m s^{-1}$, and a circle denotes calm wind.....	48
Fig. 3.7 Observed (dash line) and simulated (solid line) diurnal variations of surface temperature ($^{\circ}C$) at various stations for July–August 2013.....	49
Fig. 3.8 Same as Fig. 3.7, but of surface relative humidity (%).	50
Fig. 3.9 Same as Fig. 3.7, but of surface zonal wind ($m s^{-1}$).	51
Fig. 3.10 Same as Fig. 3.7, but of surface meridional wind ($m s^{-1}$).....	52
Fig. 3.11 Effective albedo (%) derived from the GOES-15 visible channel over O‘ahu for strong trades at (a) 0830, (b) 1130, (c) 1430, and (d) 1730 HST during July–August 2013.....	53
Fig. 3.12 Same as Fig. 3.11, but for weak trades.	54
Fig. 3.13 The difference of effective albedo (%) over Oahu between strong trades and weak trades (strong – weak) at (a) 0830, (b) 1130, (c) 1430, and (d) 1730 HST during July–August 2013.....	55
Fig. 3.14 Same as Fig. 3.6, but at 0500 HST for (a) strong trades and (b) weak trades.	56

Fig. 3.15	The vertical cross-section along the northeast–southwest line in Fig. 3.1 of simulated potential temperature (K, contour) and simulated vertical motion (m s^{-1} , color shading) at 0500 HST for (a) strong trades and (b) weak trades.	57
Fig. 3.16	Same as Fig. 3.15, but shading is mixing ratio (g kg^{-1}) and contours are equivalent potential temperature (K).	58
Fig. 3.17	The vertical cross-section along the northeast–southwest line in Fig. 3.1 of simulated cloud water content (g kg^{-1} , color shading) and simulated zonal and vertical wind (arrow, u : m s^{-1} , w : cm s^{-1}) at 0500 HST for (a) strong trades and (b) weak trades.	59
Fig. 3.18	Vertically integrated cloud water content (mm, shading) at 0500 HST for (a) strong trades and (b) weak trades.	60
Fig. 3.19	Same as Fig. 3.6, but at 1400 HST.	61
Fig. 3.20	Same as Fig. 3.15, but at 1400 HST.	62
Fig. 3.21	Same as Fig. 3.16, but at 1400 HST.	63
Fig. 3.22	Same as Fig. 3.17, but at 1400 HST.	64
Fig. 3.23	Same as Fig. 3.18, but at 1400 HST.	65
Fig. 3.24	A schematic diagram of the cloud formation at 1400 HST over O‘ahu under (a) strong trade wind and (b) weak trade wind conditions. Color shading represents horizontal wind speed (m s^{-1}), black arrows represent the mean streamline above the mountaintops, and blue arrows represent surface wind.	66
Fig. 3.25	Same as Fig. 3.13, but for Kaua‘i and Ni‘ihau.	67
Fig. 4.1	(a) A map of the Hawaiian Islands with the three nesting domains employed in the simulations with grid sizes of 13.5 km, 4.5 km, and 1.5 km, respectively. The blue dot represents the location of the Moloka‘i radar station. (b) The island of O‘ahu with elevation	

contours every 200-m. The Xs represent the MesoWest surface weather stations. For the 2003 case study, seven stations (red Xs) are used. For the composite study during 2000–2015, 16 stations (red and brown Xs) are used. The blue dots represent the Hydronet rain gauge locations. The solid lines indicate the locations of the cross-sectional analysis. The gray star and black star represent an upstream point (21.5°N, 157.5°W) and a point over Central O‘ahu (21.5°N, 158.05°W), respectively. 89

Fig. 4.2 (a) The NCEP CFSR (CFSv2) geopotential height (gpm, contours) and wind barbs (pennant: 50 m s⁻¹; full barb: 10 m s⁻¹; half barb: 5 m s⁻¹; open circle: calm) at 300 hPa at 1400 HST for the 13-day composite. The red cross represents the location of O‘ahu and the dashed line represents a trough. (b) The NCEP CFSR total precipitable water (mm, color shades), surface wind barbs (pennant: 5 m s⁻¹; full barb: 1 m s⁻¹; half barb: 0.5 m s⁻¹; open circle: calm), and mean sea-level pressure (hPa, black contours) at 1400 HST for the 13-day composite. The black cross represents the location of O‘ahu (c) Composite Skew *T*–log *P* diagram from the NCEP CFSR (CFSv2) at 21.5°N, 157.5°W at 1400 HST for the 13 days. Pennants, full barbs, half barbs, and open circles represent 5 m s⁻¹, 1 m s⁻¹, 0.5 m s⁻¹ and calm, respectively. 90

Fig. 4.3 Mean observed radar echoes (dBZ, color shades) and mean observed surface wind (black wind barb, pennant: 5 m s⁻¹; full barb: 1 m s⁻¹; half barb: 0.5 m s⁻¹; open circle: calm) from the 13 cases at (a) 0900, (b) 1000, (c) 1100, (d) 1200, (e) 1300, (f) 1400, (g) 1500, (h) 1600, and (i) 1700 HST. The black box indicates the region for the area-average. 92

Fig. 4.4 Scatter plot of area-average observed radar echoes and area-average simulated radar echoes. The dotted line is a line of best fit. 93

Fig. 4.5 Time series of area-averaged (Fig. 4.3f) observed (solid lines) and simulated (red dash lines) radar reflectivitie during 0900–1700 HST for seasonal transitions (a) the 5 cases in June and (b) the 8 cases in October. 94

Fig. 4.6 Mean simulated radar reflectivity (dBZ, color shades), mean simulated surface wind (m s^{-1} , black wind barbs), and mean observed surface wind (m s^{-1} , red wind barbs) from the 13 case composite at (a) 0900, (b) 1000, (c) 1100, (d) 1200, (e) 1300, (f) 1400, (g) 1500, (h) 1600, and (i) 1700 HST. Pennants, full barbs, half barbs, and open circles represent 5 m s^{-1} , 1 m s^{-1} , 0.5 m s^{-1} and calm, respectively. 95

Fig. 4.7 Same as Fig. 4.2, but at 1400 HST 8 June 2003. 96

Fig. 4.8 Radar reflectivity (dBZ, color shades) from the Moloka‘i radar site and observed surface wind (red wind barbs, pennant: 5 m s^{-1} ; full barb: 1 m s^{-1} ; half barb: 0.5 m s^{-1} ; open circle: calm) at (a) 0700, (b) 0800, (c) 0900, (d) 1000, (e) 1100, (f) 1200, (g) 1300, (h) 1400, and (i) 1500 HST 8 June. 97

Fig. 4.9 IR brightness temperature (K, color shades) at (a) 0700, (b) 0800, (c) 0900, (d) 1000, (e) 1100, (f) 1200, (g) 1300, (h) 1400, and (i) 1500 HST 8 June. 98

Fig. 4.10 Skew T – $\log p$ diagram from WRF simulations at Central O‘ahu (21.5°N , 158.05°W) at (a) 0700 HST and (b) 1100 HST 8 June. Pennants, full barbs, half barbs, and open circles represent 5 m s^{-1} , 1 m s^{-1} , 0.5 m s^{-1} and calm, respectively. The red dashed line represents the temperature profile of a rising air parcel. 99

Fig. 4.11 Vertical profiles at Central O‘ahu (21.5°N , 158.05°W) of (a) potential temperature (K), (b) equivalent potential temperature (K), (c) mixing ratio (g kg^{-1}), and (d) relative humidity (%) from 0700–1100 HST 8 June. (e) Time series of LCL (solid) and CAPE

(dash) at Central O‘ahu (21.5°N, 158.05°W) during 0700–1100 HST 8 June. CAPE is calculated from the level of free convection to the equilibrium level.	100
Fig. 4.12 Simulated vertical motion at 900 hPa (m s^{-1} , color shades), simulated surface vertical motion due to orographic lifting ($wsfc$) (m s^{-1} , black contours), simulated surface wind (black wind barbs, pennant: 5 m s^{-1} ; full barb: 1 m s^{-1} ; half barb: 0.5 m s^{-1} ; open circle: calm), and model terrain height (gray contours, 100-m intervals) at (a) 0700, (b) 0900, (c) 1000, and (d) 1100 HST 8 June.	102
Fig. 4.13 Vertical cross-section along the northwest–southeast line in Fig. 1b showing equivalent potential temperature (K, color shades), horizontal wind speed along the cross section (blue contour with 2-m s^{-1} intervals), vertical motion (black contours with 0.1-m s^{-1} intervals during 0700–1000 HST; with 0.5-m s^{-1} intervals during 1100–1500 HST) at (a) 0700, (b) 0800, (c) 0900, (d) 1000, (e) 1100, (f) 1200, (g) 1300, (h) 1400, and (i) 1500 HST 8 June. The 0 point of the x-axis represents the southernmost point of the northwest–southeast line in Fig. 4.1b.	103
Fig. 4.14 Simulated radar reflectivity (dBZ, color shades) and model terrain height (gray contours, 100-m intervals) at (a) 0700, (b) 0800, (c) 0900, (d) 1000, (e) 1100, (f) 1200, (g) 1300, (h) 1400, and (i) 1500 HST 8 June. Black wind barbs represent simulated surface wind (pennant: 5 m s^{-1} ; full barb: 1 m s^{-1} ; half barb: 0.5 m s^{-1} ; open circle: calm).	104
Fig. 4.15 (a) Accumulation of simulated rainfall (mm, color shades) and accumulation of rain gauge observation (mm, black triangle with label) from 1100–1600 HST 8 June. (b) Radar QPE (mm, color shades) from the Moloka‘i radar site on 8 June. Rain gauges with no rainfall accumulation (0.0 mm) are not shown.	105
Fig. 4.16 Same as Fig. 4.13, but for the no orographic run.	106

Fig. 4.17 Same as Fig. 4.12, but for the no orographic run.	107
Fig. 4.18 Same as Fig. 4.14, but for the no surface flux run.....	108
Fig. 4.19 Mean simulated radar reflectivity (dBZ, color shades), mean simulated surface wind (m s^{-1} , black wind barbs), and mean observed surface wind (m s^{-1} , red wind barbs) from the 13 NoOrog runs at (a) 0900, (b) 1000, (c) 1100, (d) 1200, (e) 1300, (f) 1400, (g) 1500, (h) 1600, and (i) 1700 HST. Pennants, full barbs, half barbs, and open circles represent 5 m s^{-1} , 1 m s^{-1} , 0.5 m s^{-1} and calm, respectively.....	109
Fig. 4.20 Same as Fig. 4.19, but for NoFlux runs.....	110
Fig. 4.21 A schematic diagram showing the island-induced airflow for the development of the short-lived afternoon heavy rainfall events over Central O‘ahu under weak wind conditions ($< 3 \text{ m s}^{-1}$) and favorable large-scale settings. The red circle shows the area with low-level convergence.	111
Fig. 5.1 (a) A map of the Hawaiian Islands. The 4 nested domains employed in the simulations with grid sizes of 27 km, 9 km, 3 km, and 1 km, respectively. (b) The island of Kaua‘i. Elevation contours are in 100-m intervals. A red x represents a surface weather station. A blue dot represents a rain gauge.....	127
Fig. 5.2 The model terrain height (m) for (a) CTRL; (b) CTRL_Oahu; (c) RTH; (d) SZ and (e) RP.....	129
Fig. 5.3 The simulated mean surface wind (m s^{-1} , black wind barb), observed surface wind (m s^{-1} , red wind barb) and model terrain height (grey contour with interval of 100 m) (a) during the trade wind conditions at (b) 1400 HST and (c) 0500 HST. (d) The accumulated rainfall (mm, color shading) during the 38 trade wind days in July–August 2013.	130

Fig. 5.4 The time series of daily rainfall accumulation (mm) at the 13 rain gauges during the trade wind days.	135
Fig. 5.5 The simulated accumulated rainfall (mm) during the 38 trade wind days for (a) CTRL, (b) CTRL_Oahu, (c) RTH, (c) SZ, and (d) RP.	136
Fig. 5.6 The simulated ORI ($\text{kg m}^{-1} \text{s}^{-1}$) during the trade wind days for (a) CTRL, (b) CTRL_Oahu, (c) RTH, (c) SZ, and (d) RP. The black asterisks indicate the ORI maximum.	137
Fig. 5.7 The simulated storage term (mm day^{-1} , color shading) during the trade wind days for (a) CTRL, (b) CTRL_Oahu, (c) RTH, (c) SZ, and (d) RP.	138
Fig. 5.8 The vertically integrated moisture flux convergence (mm day^{-1} , color shading) during the trade wind days for (a) CTRL, (b) CTRL_Oahu, (c) RTH, (c) SZ, and (d) RP.....	139
Fig. 5.9 The vertical moisture transport due to orographic lifting (mm day^{-1} , color shading) during the trade wind days for (a) CTRL, (b) CTRL_Oahu, (c) RTH, (c) SZ, and (d) RP.	140
Fig. 6.1 (a) Domains of regional simulation (grid size: 18, 6 km), (b) domains of island-scale simulations for Hawai'i (grid size: 27, 9, 3 km), and (c) domains of island-scale simulations for O'ahu (grid size: 13.5, 4.5, 1.5 km).	168
Fig. 6.2 Time series of (a) N_{ct} and (b) N_{wp} indices. Black lines indicate one standard deviation of N_{ct} and N_{wp} indices.	169
Fig. 6.3 The seasonal composite of divergence (s^{-1} , color shading) and wind speed (m s^{-1} , contour) at 200 hPa for (a) CT winters, (b) CT springs, (c) WP winters, (d) WP springs, (e) all 38 winters, and (f) all 38 springs. The black thick line indicates the location of vertical cross-sections.	170

Fig. 6.4 The seasonal anomalies of divergence (color shading: s^{-1}) at 200 hPa for (a) CT winters, (b) CT springs, (c) WP winters, and (d) WP springs.....	172
Fig. 6.5 Same as Fig. 6.3, but divergence is calculated using the ageostrophic wind at 200 hPa.	173
Fig. 6.6 Same as Fig. 6.4, but divergence is calculated using the ageostrophic wind at 200 hPa.	174
Fig. 6.7 The composite of vertical velocity ($Pa\ s^{-1}$, color shading) at 500 hPa and wind speed ($m\ s^{-1}$, contour) at 200 hPa for (a) CT winters, (b) CT springs, (c) WP winters, (d) WP springs, (e) all 38 winters, and (f) all 38 springs.....	175
Fig. 6.8 The seasonal anomalies of vertical velocity ($Pa\ s^{-1}$, color shading) at 500 hPa for (a) CT winter, (b) CT spring, (c) WP winter, and (d) WP spring.	177
Fig. 6.9 The seasonal composite of a north-south vertical cross-section along 160 °W for (a) CT winters, (b) CT springs, (c) WP winters, (d) WP springs, (e) all 38 winters, and (f) all 38 springs. Color shading is pressure vertical motion ($Pa\ s^{-1}$); vectors are meridional wind ($V: m\ s^{-1}$) and negative vertical velocity ($-\omega: 0.01\ Pa\ s^{-1}$).....	178
Fig. 6.10 The seasonal anomalies of a north-south vertical cross-section along 160 °W for (a) CT winters, (b) CT springs, (c) WP winters, (d) WP springs, (e) all 38 winters, and (f) all 38 springs. Color shading is pressure vertical motion ($Pa\ s^{-1}$).....	180
Fig. 6.11 The seasonal composite of a north-south vertical cross-section along 160 °W for (a) CT winters, (b) CT springs, (c) WP winters, (d) WP springs, (e) all 38 winters, and (f) all 38 springs. Color shading is equivalent potential temperature (K); Contours are zonal wind ($U: m\ s^{-1}$).	181
Fig. 6.12 Same as Fig. 6.11, but contours are meridional wind ($V: m\ s^{-1}$).....	182

Fig. 6.13	The seasonal composite of wind (m s^{-1}) at 1000 hPa for (a) CT winters, (b) CT springs, (c) WP winters, (d) WP springs, (e) all 38 winters, and (d) all 38 springs. The reference arrow represents 10 m s^{-1} .	183
Fig. 6.14	The seasonal anomalies of wind (m s^{-1}) at 1000 hPa (a) CT winters, (b) CT springs, (c) WP winters, (d) WP springs, (e) all 38 winters, and (d) all 38 springs. The reference arrow represents 10 m s^{-1} .	185
Fig. 6.15	Same as Fig. 6.13, but for geopotential height (m, contour) at 1000 hPa.	186
Fig. 6.16	Same as Fig. 6.14, but for geopotential height (m, contour) at 1000 hPa.	187
Fig. 6.17	Same as Fig. 6.13, but for temperature (K, color shading) at 1000 hPa.	188
Fig. 6.18	Same as Fig. 6.14, but for temperature (K, color shading) at 1000 hPa.	189
Fig. 6.19	Same as Fig. 6.13, but for total precipitable water (mm, color shading).	190
Fig. 6.20	Same as Fig. 6.14, but for total precipitable water (mm, color shading).	191
Fig. 6.21	The regressions of GPCP rainfall data onto (a) N_{ct} and (b) N_{wp} indices.	192
Fig. 6.22	The seasonal composite of simulated surface wind (m s^{-1} , color shading) for (a) CT winters, (b) CT springs, (c) WP winters, (d) WP springs, (e) all 38 winters, and (f) all 38 springs.	193
Fig. 6.23	The seasonal anomalies of simulated surface wind (m s^{-1} , color shading) for (a) CT winter, (b) CT spring, (c) WP winter, and (d) WP spring.	194
Fig. 6.24	Same as Fig. 6.22, but for simulated total precipitable water (mm, color shading).	195
Fig. 6.25	Same as Fig. 6.23, but for simulated total precipitable water (mm, color shading).	196
Fig. 6.26	The composite anomalies of simulated water vapor mixing ratio (g kg^{-1} , color shading) for the CT winters at (a) 900 hPa, (c) 800 hPa, and (e) 700 hPa. (b), (d), and (f) are same as (a), (c), and (e), but for WP winters.	197

Fig. 6.27	Same as Fig. 6.26, but for spring.....	198
Fig. 6.28	Same as Fig. 6.23, but for simulated surface temperature (K, color shading).	199
Fig. 6.29	Same as Fig. 6.26, but for simulated temperature (K, color shading).....	200
Fig. 6.30	Same as Fig. 6.27, but for simulated temperature (K, color shading).....	201
Fig. 6.31	The composite seasonal rainfall accumulation from the Rainfall Atlas of Hawai‘i (mm, color shading) for (a) 4 CT winters, (b) 4 CT springs, (c) 5 WP winters, (d) 5 WP springs, (e) all 33 winters, and (d) all 33 springs during 1979–2012.	202
Fig. 6.32	The anomalies of seasonal rainfall accumulation from the Rainfall Atlas of Hawai‘i (mm, color shading) for (a) 4 CT winters, (b) 4 CT springs, (c) 5 WP winters, and (d) 5 WP springs during 1979–2012.....	203
Fig. 6.33	Same as Fig. 6.31, but for simulated seasonal rainfall accumulation (mm, color shading).....	204
Fig. 6.34	Same as Fig. 6.32, but for seasonal simulated rainfall accumulation (mm, color shading).....	205
Fig. 6.35	The seasonal composite of simulated daily rainfall (mm, color shading) for (a) CT winters, (b) CT springs, (c) WP winters, (d) WP springs, (e) all 38 winters, and (d) all 38 springs.	206
Fig. 6.36	The seasonal anomalies of simulated daily rainfall (mm, color shading) for (a) CT winters, (b) CT springs, (c) WP winters, and (d) WP springs.	207
Fig. 6.37	The simulated daily rainfall (mm, color shading) over Hawai‘i Island during (a) the CT winters, (c) the WP winters, and (e) the neutral winters. The seasonal rainfall from the Rainfall Atlas of Hawai‘i during (b) the CT winters, (d) the WP winters, and (f) the neutral winters. Black solid contours represent simulated daily rainfall over 17 mm (interval 1 mm).	

Black dashed line represents 0.5 mm simulated daily rainfall contour. Black asterisk represents the location of daily rainfall maximum.	208
Fig. 6.38 The simulated daily rainfall over O‘ahu Island during (a) the CT winters, (c) the WP winters, and (e) the neutral winters. The seasonal rainfall from the Rainfall Atlas of Hawai‘i during (b) the CT winters, (d) the WP winters, and (f) the neutral winters. Black solid contours represent simulated daily rainfall over 16 mm (interval 1 mm). Black dashed line represents 0.5 mm simulated daily rainfall contour. Black asterisk represents the location of daily rainfall maximum.	210
Fig. 6.39 Same as Fig. 6.37, but for springs.	212
Fig. 6.40 Same as Fig. 7.38, but for springs.	213
Fig. 6.41 The seasonal anomalies of simulated surface wind ($m s^{-1}$, color shading) over Hawai‘i Island during (a) CT winters and (b) WP winters. (c) Same as (a), but over O‘ahu Island. (d) Same as (c), but over O‘ahu Island. Black contours represent model elevation in 500 m intervals.	214
Fig. 6.42 The seasonal anomalies of simulated TPW (mm, color shading) over Hawai‘i Island during (a) CT winters and (b) WP winters. (c) Same as (a), but over O‘ahu Island. (d) Same as (c), but over O‘ahu Island. Black contours represent model elevation in 500 m intervals.	215
Fig. 6.43 The accumulated daily rainfall (mm, color shading) over Hawai‘i Island during (a) CT winters, and (b) WP winters. (c) Same as (a), but over O‘ahu Island. (d) Same as (b), but over O‘ahu Island. Grey contours represent model elevation in 500 m intervals. Black asterisk represents the location of daily rainfall deficiency maximum.	216

Fig. 6.44	The seasonal anomalies of simulated surface temperature (K, color shading) over Hawai‘i Island during (a) CT winters and (b) WP winters. (c) Same as (a), but over O‘ahu Island. (d) Same as (c), but over O‘ahu Island. Black contours represent model elevation in 500 m intervals.....	217
Fig. 6.45	At 0500 HST, the seasonal anomalies of simulated surface temperature (K, color shading) over Hawai‘i Island during (a) CT winters and (b) WP winters. At 0500 HST, the seasonal anomalies of simulated surface wind (m s^{-1} , wind barb) and rainfall anomalies (mm day^{-1} , color shading) over Hawai‘i Island during (c) CT winters and (d) WP winters.....	218
Fig. 6.46	Same as Fig. 6.41, but during springs.....	219
Fig. 6.47	Same as Fig. 7.42, but during springs.....	220
Fig. 6.48	Same as Fig.6.43, but during springs.....	221
Fig. 6.49	Same as Fig. 6.44, but during springs.....	222

Chapter 1 Introduction

1.1 Background

The trade-wind belt in the subtropics has a rainfall minimum in the global rainfall distribution due to large-scale subsidence associated with the descending branch of the Hadley cell. The Hawaiian Island chain lies within the trade-wind belt, with a quasi-permanent subtropical high located northeast of the islands. During the summer, the subtropical high is not only quasi-stationary but strongest, with a center located near 35°N , 155°W producing persistent trade winds with a maximum occurrence of $\sim 93\%$ in August (Schroeder 1993). Conversely, during the winter months the subtropical high is the weakest and shifts southeastward with a mean January position near 30°N , 130°W , and a subtropical ridge axis extends southwestward to near 25°N . During the Hawaiian cool season (November – April), the trade-wind frequency for Hawai‘i decreases to less than 50% due to equatorward excursions of synoptic-scale extra-tropical systems (Schroeder 1993; Garza et al. 2012), which can produce heavy rains, strong winds, and high surf (Kodama and Barnes 1997). Among these are cold fronts, Kona storms (or subtropical cyclones), and upper-level troughs during the winter season and tropical storms during the summer (Blumenstock and Price 1967; Worthley 1967; Wang et al. 1998). Most areas of Hawai‘i exhibit higher rainfall during the cool season than the summer months, except the western lee side of the island of Hawai‘i where trade winds are absent behind the high mountains (Giambelluca et al. 1986, 2013; Huang and Chen 2018). Although the aforementioned synoptic-scale systems are major producers of Hawaiian rainfall, the trade winds are still an important source even in the cool season (Lyons 1982).

The local weather and climate over the Hawaiian Islands are some of the most spatially diverse on Earth due to large variation among mountain heights (500 m–4 km), sizes (12 km–140 km in diameter) and shapes. With steep terrain and abundant moisture, orographic clouds and local showers are frequent over the Hawaiian Islands. Furthermore, rainfall, temperature, humidity, wind, and incident solar radiation exhibit pronounced spatial variability related to terrain and local winds (Giambelluca et al. 1986, 2013). Due to the interactions between the trade winds, trade-wind inversion, steep terrain, and land–sea thermal contrast, the Hawaiian Island chain is a unique natural laboratory for the investigation of the effects of topography and local circulations on regional and island-scale airflow, rainfall, weather, and climate.

Past research involving the island-scale rainfall, weather and climate under summer trade-wind conditions has been done for the island of Hawai‘i, the largest island in the Hawaiian chain with mountaintops (> 3.5 km) that are well above the trade-wind inversion (~ 1.9 km) (Winning et al. 2017). Some of these studies have focused on localized heavy rainfall and high wind events, strong coastal winds and orographically induced airflows (Kodama and Barnes 1997; Hitzl et al. 2014; and others). However, only a few studies have focused on rainfall, airflow, weather, and climate for the islands with tops below the trade-wind inversion. The purpose of this dissertation is to investigate the island-scale weather and climate over various local communities in Hawai‘i, particularly those with local mountain heights below the typical trade wind inversion height.

1.2 Literature Review

The pressure and wind patterns that occur under a steady trade-wind flow over the Hawaiian Islands have received considerable attention in the past (Smith 1982, 1989; Smolarkiewicz and Rotunno 1990; Schär and Durran 1977; and others). Perturbations induced by airflow past the Hawaiian Islands produce a variety of phenomena, such as hydraulic jumps

(Lavoie 1974; Smith and Grubišić 1993), wake vortices (Nickerson and Dias 1981; Smolarkiewicz and Rotunno 1990; Smith and Grubišić 1993; Schär and Durran 1977; Yang and Chen 2003; Yang et al. 2005; Carlis et al. 2010), trapped mountain lee waves (Burroughs and Larson 1979; Li and Chen 2017), strong downslope winds on the lee-side slopes of mountains or ridges with tops below the trade-wind inversion (Zhang et al. 2005b), and strong channel winds in the channel exit (Hitzl et al. 2014).

Leopold (1949) described the trade-wind inversion as a "lid" forcing trade-wind flow to move around the islands with mountains extending well above the trade-wind inversion. For 3D flow over isolated topography, Schär and Smith (1993) showed the dependence of airflow on the ratio of mountain height to fluid depth ($M = h/H$), where H is the depth of the lower fluid (in the case of the Hawaiian Islands, the trade-wind inversion height [Chen and Feng 1995; Feng and Chen 2001; Chen and Feng 2001]). For a stably stratified airflow past a bell-shaped axisymmetric mountain, without considering diabatic heating, surface friction or the diurnal heating cycle, the Froude number ($Fr = U/Nh$, where U is the upstream wind speed, N is the Brunt-Väisälä frequency, and h is the height of the barrier) is the control parameter for the flow regime (Smolarkiewicz et al. 1988; Rasmussen et al., 1989; and others). For typical summer trade-wind conditions over the island of Hawai'i, the Froude number is between 0.2 and 0.5 and the low-level flow is predicted to be deflected around the island.

In addition to dynamic forcing related to orographic effects on the island-scale airflow, thermodynamic fields and rainfall distributions over the Hawaiian Islands are significantly modulated by the diurnal heating cycle and feedback effects of convection (Leopold 1949; Lavoie 1967; Takahashi 1977; Garrett 1980; Schroeder et al. 1977; Chen and Nash 1994; Reisner and Smolarkiewicz 1994; Carbone et al. 1995; Chen and Wang 1994; Wang and Chen 1995, 1998;

Austin et al. 1996; Feng and Chen 1998; Li and Chen 1999; Frye and Chen 2001; Zhang et al. 2005a,c; Esteban and Chen 2008; and others). The island-scale diurnal wind variations with daytime sea-breeze-upslope wind and nocturnal land-breeze-downslope wind develop in weak wind regions as a result of orographic effects and are more pronounced when the prevailing wind is light. For instance, Schroeder (1981) documented a sea breeze circulation that forms over the northwestern shore of the island of Hawai'i. Because this region is largely sheltered from the trades by Mauna Kea (summit elevation 4.1 km), the sea breeze forms regularly.

Banta (1990) found that mountain flows, which are driven by the large-scale winds interacting with the topography and the diurnal heating cycle, play a significant role in determining where convective cells will initiate and how precipitation will be distributed spatially. Giambelluca et al. (1986, 2013) compiled a rainfall atlas for the major Hawaiian Islands showing that a persistent orographic lifting of moisture-laden northeast trade winds contributes to a rainfall maximum over the windward regions. For mountains with tops above the trade-wind inversion, maximum mean rainfall is found on the windward mountain slopes below the trade-wind inversion. Areas with less rainfall are found over leeward lowlands and atop the highest mountains. However, for mountains with tops below the inversion, the rainfall maximum occurs near the summits. Nullet and McGranaghan (1988) utilized the same database developed by Giambelluca et al. (1986) and compared the rainfall difference between the open ocean and the Hawaiian Islands. Their results indicate that the shape of islands is important to rainfall enhancement by orographic effects. Yang and Chen (2008) showed that in addition to the terrain/mountain height and shape, island size is a critical factor affecting rainfall production and distribution for the island of Hawai'i. This is because island size affects the steepness of the terrain slopes (and hence orographic lifting) and in turn the advection timescale for an air parcel to reach the mountain tops. For islands such as

O‘ahu and Kaua‘i, which are relatively small in size (<50 km) and have mountain tops below the trade-wind inversion, the advection timescale for air parcels to reach the mountain tops is shorter than (or comparable to) the typical time scale for the development of trade-wind showers (~20 minutes) (Takahashi 1988). This factor allows the maximum rainfall to occur on the mountain tops. For larger islands, which have a longer advection time scale, trade-wind showers occur before reaching the mountain tops.

For typical trade-wind conditions, the lifting condensation level (LCL) over O‘ahu is about 400 m at night and 800 m in the early afternoon (Nguyen et al. 2010). Compared with the ridge tops of the Ko‘olau Mountains on O‘ahu (500 m to 960 m), the LCL is slightly lower than the mountain tops. The advection time for the air parcel to reach the ridgetops after reaching the LCL is apparently too short (5–10 min) for the initiation of precipitation through the collision-coalescence process (~20 min). Therefore, the existence of trade-wind cumuli upstream is needed for the occurrence of orographic precipitation over O‘ahu under undisturbed summertime trade wind weather (Hartley and Chen 2010).

For the above reasons, to properly simulate the island flow regime and orographic effects on rainfall and micro-scale climate, it is imperative that the 3-D terrain height, shape, and size of each island, as well as the coastlines, are properly depicted in numerical models.

Land surface processes are another important factor in the accurate prediction of rainfall and local weather in regional mesoscale models. Chen and Dudhia (2001a, b) have addressed issues related to the implementation of an advanced land surface–hydrology model in the MM5 model. Their results suggest that the model provides not only reasonable diurnal variations of surface heat fluxes but also reasonable seasonal evolutions of soil moisture. To improve the description of land surface properties over the Hawaiian Islands, Zhang et al. (2005a) compiled

the vegetation types and vegetation fraction from the USGS 1:100,000-scale Land Use Land Cover Level II Data for Hawai'i (USGS 1986) and the soil types from soil surveys in Hawai'i (Foote et al. 1972; Sato et al. 1973) for the entire state with a resolution of 30", or roughly 1 km. In addition to better land surface data, the 24-h forecast of the high-resolution soil parameters (soil temperature and soil moisture) from the model runs of the previous day were used to provide the updated values. With adequate depiction of the terrain and coastlines, and proper treatment of lower boundary conditions over the islands coupled with an advanced Noah Land Surface Model (LSM), high-resolution models can simulate the local and diurnal effects over the Hawaiian Islands with reasonable accuracy (Yang et al. 2005; Carlis et al. 2010; Nguyen et al. 2010).

Yang et al. (2005) used the vegetation types, vegetation fraction, and soil types from the soil surveys compiled by Zhang et al. (2005a) and performed a 36-h simulation starting from 1200 UTC using the MM5/LSM model for each day of the Hawaiian Rainband Project (HaRP). The model run, initialized by the NCEP/NCAR reanalysis, is begun one month before HaRP in order to generate the initial soil moistures and temperatures. The simulated data between hours 12 and 36 of each day are used as the simulated diurnal cycle for the next day, with updated surface parameters from the 24-h simulation of the previous day. The evolution of the composite simulated island-scale rainfall and airflow features during HaRP, including the flow deceleration and splitting of the incoming trade-wind flow and the evolution of the diurnal sea breeze/land breeze circulation cells on the windward side, the thermally driven diurnal winds, and the wake circulations on the lee side, compare favorably with observations from 50 NCAR PAM stations (Fig. 1.1), Hilo soundings and aircraft flight-level data. Their sensitivity tests show that with more accurate surface conditions in the model coupled with the LSM, the simulated thermal forcing over land is improved. For instance, the Hilo soundings used in the global analysis are greatly affected

by the massive volcanic mountains, with much weaker wind speeds than those found over the open ocean.

Carlis et al. (2010) show that the previously observed closed circulation over the Central Valley of Maui, or the Maui Vortex, represents the northern cyclonic vortex of the dual counter-rotating vortices in the lee of Haleakalā (3,055 m MSL) and extends up to the base of the trade-wind inversion with a westerly reversed flow ($>2 \text{ m s}^{-1}$). The Maui Vortex has a relatively narrow East-West extent in the lowest levels, especially at night, due to the strong deflected northerly winds from the windward foothills of the West Maui Mountains. The results of Carlis et al. (2010) are in contrast to the traditional view (Leopold 1949; Ueyoshi et al. 1996) that the Maui Vortex forms as the low-level easterly trade-wind flow is blocked by the West Maui Mountains and channeled through the Central Valley between the West Maui Mountains and Haleakalā volcano and enhanced by the daytime westerly anabatic winds on the lee-side slopes of Haleakalā. They show that because the Maui Vortex and the westerly return flow in low levels are mainly over land, they are strongly modulated by the diurnal heating cycle. With relatively calm winds, clear skies, dry soils, and semi-arid ground cover, the morning transition in the lee of Haleakalā is completed within two hours after sunrise. In contrast, the evening transition on the lee-side slopes due to nocturnal cooling is a slow process. The onset of the easterly katabatic winds starts on the lee-side slopes and progresses slowly downward over the Central Valley until around midnight. Over the West Maui Mountains (1,764 m MSL), with their height below the trade-wind inversion, dual counter-rotating vortices are present below the 1-km level in the wake and are more significant at night, with a strong downslope flow on the lee-side slopes followed by a hydraulic jump. In the afternoon, downslope winds are weak, with combined westerly onshore/sea-breeze flow along the

lee-side coast. Orographic blocking is also evident over eastern Moloka‘i (1,512 m MSL) with strong downslope winds, especially at night.

Hitzl et al. (2014) extend the understanding of orographic effects from islands to ocean channels. It is well known that the winds downstream of islands are usually weaker for tens to several hundreds of kilometers in the wake zone due to the blocking effect of the mountains and surface drag over the terrain. In contrast, the wind speeds within the ocean channels between islands in Hawai‘i are stronger than the upstream values. Hitzl et al. (2014) used the WRF/LSM to diagnose the overall airflow and meteorological conditions over the Hawaiian Island chain and surrounding coastal waters during the summer months. The simulated winds are validated with the observed hourly winds at 11 buoy sites, including within and downstream of the ‘Alenuihāhā Channel, and compared with the overall flow pattern from the QuikSCAT ocean surface winds and historical aircraft and ship observations in the coastal waters. Their high-resolution (2-km grid sizes) simulations show that the wind acceleration in the channel exit and the adjacent coastal waters is driven by the orographically induced along-gap pressure gradients resulting from adiabatic warming/cooling due to local vertical motions. Their sensitivity tests of the WRF/LSM indicate that the strongest winds occur immediately downstream of the ‘Alenuihāhā Channel due to perturbation pressure differences in the entrance and exit region of the channel.

Nguyen et al. (2010) used MM5/LSM to simulate airflow and weather over O‘ahu during July–August 2005 under summer trade-wind conditions. With a 1.5-km resolution, the island effects on airflow and rainfall are simulated reasonably well for the first time (Fig. 2). In addition, model sensitivity tests are performed to diagnose the role of thermal forcing versus orographic blocking on the development of the westerly reversed flow in the wake zone off the western lee-side coast during the daytime. Their results suggest that the development of daytime westerly

onshore/reversed flow in the wake is related to land surface heating over the leeward western coast superimposed by latent heat release of orographic precipitation over the Ko‘olau Mountains. From the results of their ‘no mountain’ case, it is apparent that persistent orographic lifting is crucial for the development of trade wind showers over O‘ahu (Fig. 4).

Li and Chen (2017) used the WRF/LSM successfully to simulate two trapped mountain lee waves downstream of O‘ahu during the onset, development, and dissipation of these two events. Their results suggest that the favorable conditions for the occurrence of traverse trapped lee waves are 1) $Fr > 1$; 2) insufficient convective available potential energy (CAPE) for the air parcel to become positively buoyant after being lifted to the top of the stable trade wind inversion layer; and 3) increasing cross-barrier wind speed with respect to height through the stable inversion layer, satisfying Scorer's criteria between the inversion layer and the layer aloft (Scorer 1949; 1952). At the inversion base, the Scorer parameter $L2$ has a maximum, and wave amplitudes there are the greatest. Based on their sensitivity tests, the moisture content near and beneath the inversion base is important as latent heat release decreases stability, resulting in longer wavelengths and larger wave amplitudes than with no latent heat release.

In addition, high-resolution models also have been used as a diagnostic tool to study the physical processes involved in the development of significant weather events over the Hawaiian Islands, including localized heavy rainfall (e.g., Zhang et al. 2005c; Tu and Chen 2011) and orographically enhanced high-wind (Zhang et al. 2005b) events during the winter months. The El Niño-Southern Oscillation (ENSO) is a prominent mode of climate variability at the interannual time scale. It is well known that the main impact of El Niño in Hawai‘i is on water resources during the cool season (Chu 1995). Recent studies have made it increasingly clear that there are two different flavors of El Niño (Kug et al. 2009; Yeh et al. 2009; Kao and Yu 2009; Ren and Jin

2011) that influence the global climate in different ways: one with an anomalous warming center in the eastern Pacific (EP) or cold tongue region (CT) and the other in the central Pacific (CP) or warm pool region (WP). Note that most of the central equatorial Pacific warming El Niño events occurred in and after 1992 and are not included in Chu's (1995) study. Furthermore, less is known about the impacts of these two flavors of El Niño on local spatial patterns of rainfall, temperature, moisture, and winds. With large spatial variations of local climate, a better understanding of the impact of El Niño on various island communities is highly desirable in regard to water resources, agriculture and terrestrial ecosystems.

1.3 Scientific Objective

In this dissertation, I will study the island-scale weather and climate over various local communities in Hawai'i, especially those with mountain heights below the typical trade wind inversion height. The research will focus on the following areas: 1) wake zone dynamics under trade wind conditions over O'ahu; 2) short-lived afternoon heavy rainfall events over Central O'ahu during seasonal transitions (June and October) ; 3) orographic precipitation over Kaua'i; and 4) island-scale response to El Niño events (O'ahu vs. Hawai'i).

1. Wake zone dynamics under trade wind conditions over O'ahu

Yang et al. (2008a) proposed a combination of mechanical lee side convergence of island-deflected airflows and warm air moving downstream (warm advection) to explain the cloud formation in the wake zone of Kaua'i in the afternoon hours. As the island interior heats up, the trades advect warm air from the island to the wake zone, decreasing the local air pressure. The low-level convergence is enhanced, which results in cloud trails in the wake zone. In this study, the thermal advection mechanism of O'ahu wake clouds under trade wind conditions will be reexamined using global analysis, surface data, satellite data and simulated island-scale

airflow and weather using the high-resolution WRF/LSM. The key question: Is the westerly reversed flow in the afternoon related to thermal forcing (land–sea thermal contrast) or lee side convergence due to warm advection or orographic blocking.

2. Heavy rainfall events over Central O‘ahu under variable wind conditions during seasonal transitions (June and October) between 2000 and 2015

Short-lived heavy rainfall events may form over Central O‘ahu during the daytime during seasonal transitions under favorable large-scale conditions including the presence of an upper-level trough with a moist tongue and high total precipitable water (TPW). For this research, my focus will be on the initiation of convective storms over the Central O‘ahu Plain under weak wind conditions. The large-scale conditions and the island effects including the impacts of daytime land surface heating on the mixed layer, instability, island-scale airflow, and local forcing will be studied through the analysis of high-resolution model simulations and model sensitivity tests.

3. Factors affecting orographic precipitation over Kaua‘i

The mountaintops of O‘ahu and Kaua‘i are 1,220 m and 1,598 m, respectively. Moreover, the mountaintop of Kaua‘i is well known as one of the wettest spots on earth. In this study, simulated surface wind and rainfall from high-resolution models will be validated with surface weather stations and rain gauge data during the summer and winter months. Model sensitivity tests will be used to investigate rainfall difference between O‘ahu and Kaua‘i. The key question: Is the island of Kaua‘i ideal for generating the maximum orographic precipitation during the summer months due to its mountain height, island size, and/or geo-location?

4. Island-scale rainfall response to El Niño events (O‘ahu vs. Hawai‘i)

Two different flavors of ENSO [east Pacific type/Cold Tongue (CT) and central Pacific type/warm pool (WP)] have been reported in recent years. The CT and WP events are defined by the Niño-CT index and Niño-WP index, which were proposed by Ren and Jin (2011). The focus in this study is on the influences of different El Niño flavors on island-scale airflow, rainfall distribution, and local weather for the island of O‘ahu, which has mountains and ridges with tops below the trade wind inversion, and for the island of Hawai‘i, which has high mountains extending well above the trade wind inversion. Global analysis, 6-km simulated fields for the regional domain covering the entire state of Hawai‘i, and high-resolution island-scale data for both types of events during 1979 - 2016 will be analyzed.

Chapter 1 Figures

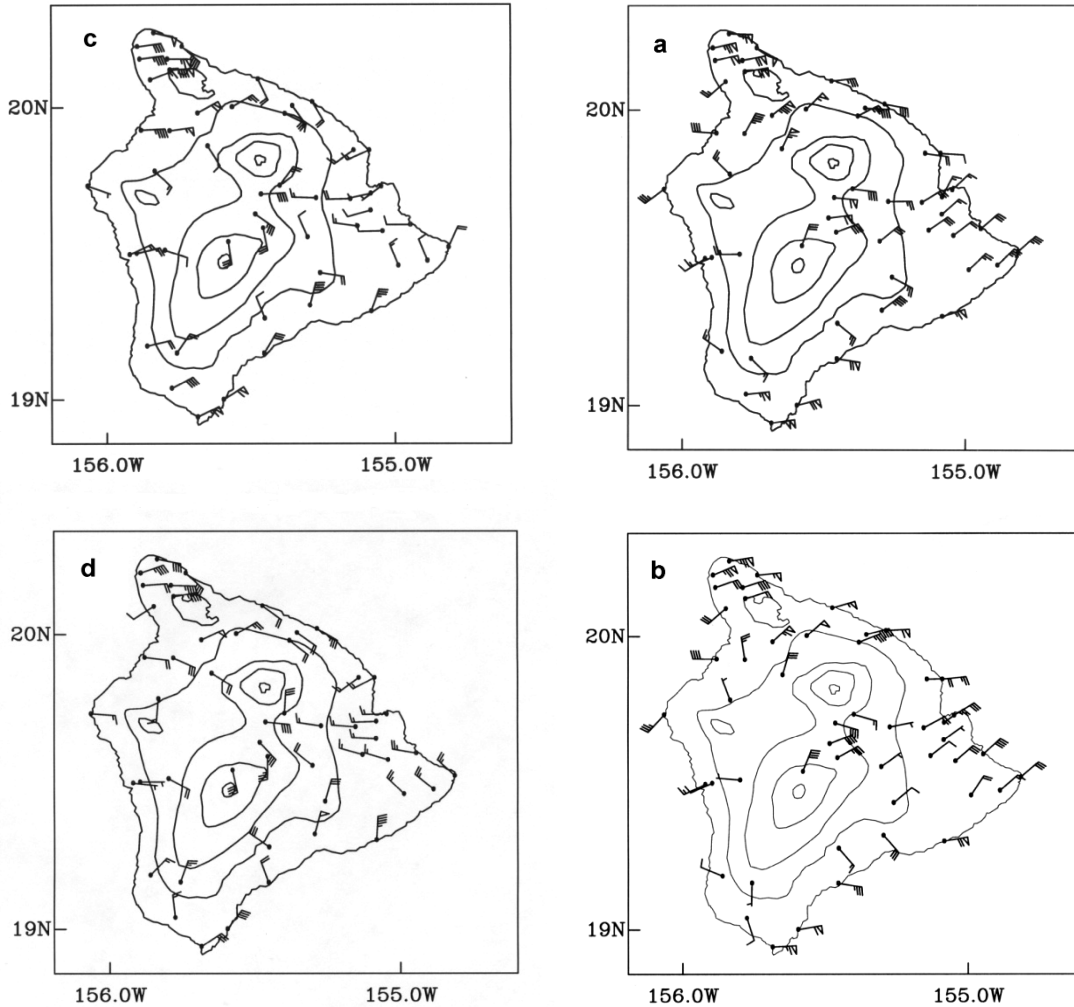


Fig. 1.1 Averaged 10-m wind for the period of 11 July through 24 August 1990: (a) HaRP observations at 0200 HST; (b) HaRP observations at 1400 HST; (c) MM5 24-h forecast valid at 0200 HST; and (d) MM5 12-h forecast valid at 1400 HST. One pennant, full barb, and half barb represent 5, 1, and 0.5 m s⁻¹, respectively (Yang et al., 2005).

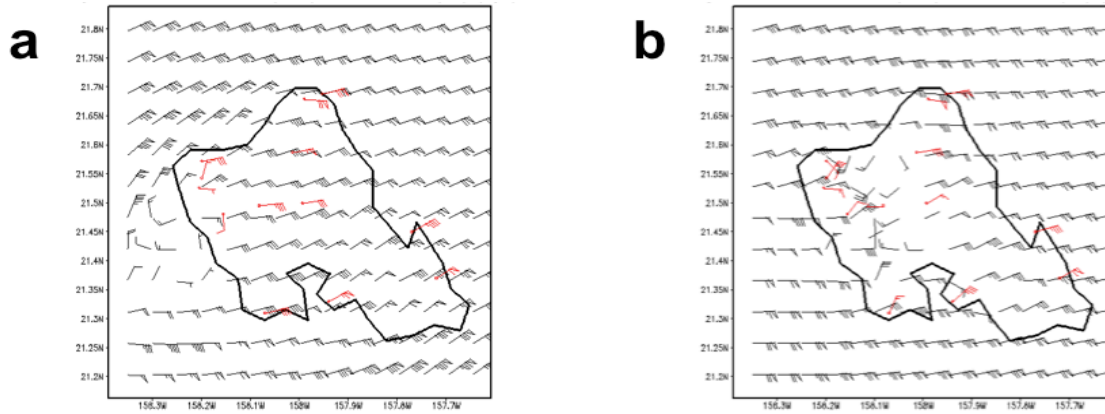


Fig. 1.2 (a) The mean simulated horizontal distribution of surface winds (black) and observed surface winds (red) at 13 stations during July – August 2005 at 1400 HST; one pennant 5 m s^{-1} , full barb 1 m s^{-1} , half barb 0.5 m s^{-1} . (b) Same as (a) but for 0500 HST (Nguyen et al., 2010).

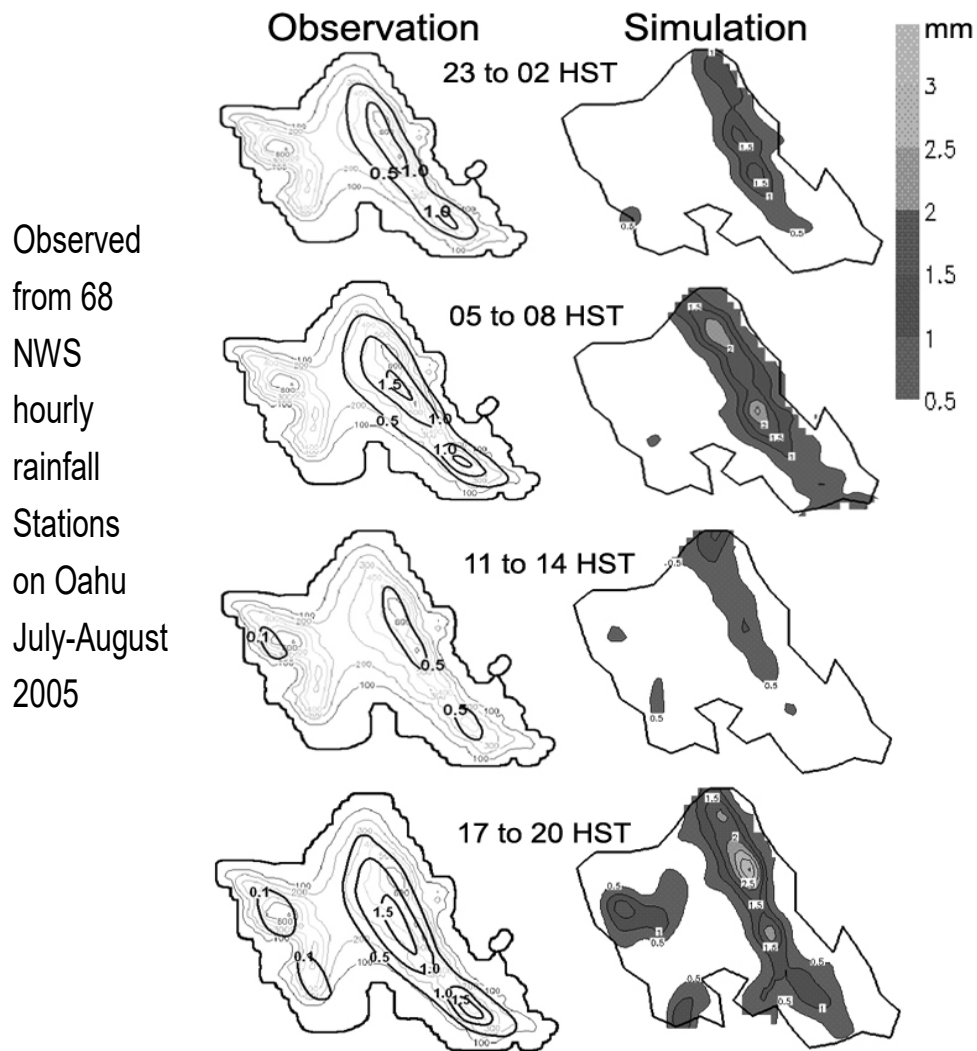


Fig. 1.3 Three-hour rainfall accumulation during July - August 2005: observed (left) and simulated (right) rainfall (mm) (Nguyen et al. 2010).

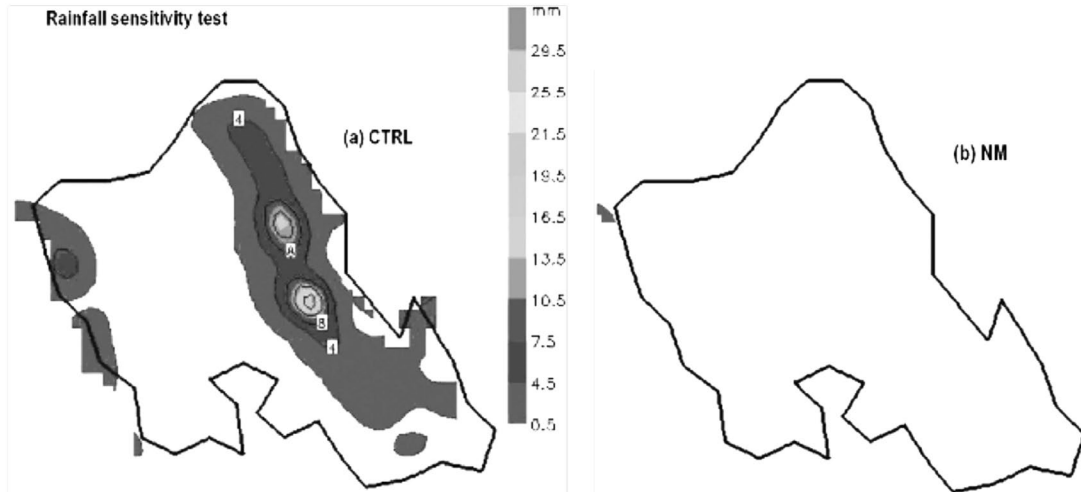


Fig. 1.4 Total rainfall accumulation (mm) for 9 Aug 2005 for the (a) control case and the (b) no mountain case. (Nguyen et al., 2010).

Chapter 2 Data and Model Description

2.1 NCEP Climate Forecast System (CFS) data

The National Centers for Environmental Prediction (NCEP) launched a fully coupled ocean-land-atmosphere dynamical Climate Forecast System (CFS) in August 2004. In March 2011, CFS was upgraded to version 2 (CFSv2, Saha et al. 2014) with improvements in forecast model states (atmospheric and ocean models), fully coupled among atmosphere-ocean-sea ice-land, and the initial states provided by the latest data assimilation systems. The operational CFSv2 ensures a continuity of the climate record and provides a valuable, up-to-date dataset for studying many aspects of predictability on the seasonal and sub-seasonal timescales. To create initial conditions for CFSv2 historical forecasts and to provide estimates and diagnoses of the climate state over a 30-year period (1981–2010), a coupled atmospheric-ocean-sea ice-land reanalysis (Climate Forecast System Reanalysis, CFSR) for 1979–2010 was made (Saha et al. 2010) with the same dynamical cores that were used to create the CFSv2. The 6-hourly NCEP CFSR (CFSv2) $0.5^\circ \times 0.5^\circ$ gridded data are used to analyze the synoptic weather conditions and upstream trade wind conditions before and after 2011, respectively.

2.2 Model Description

The WRF-ARW model (Skamarock and Klemp 2008) Version 3.6.1 initialized at 0000 UTC (1400 Hawaiian Standard Time: HST = UTC–10 hours) each day using the NCEP CFSR (CFSv2) data is used as a research tool to study the four topics enumerated in Chapter 1. Two-way nested domains are employed with 38 vertical levels from the surface to the 100-hPa level with smaller increments (11 levels) at the lower levels and in the trade wind inversion layer than above (Chen and Feng 2001).

The physics options include: Betts-Miller-Janic (BMJ) cumulus parameterization scheme (Janjic' 1994, 2000), although it is not used in the domains with grid size < 9 km, and the Yonsei University (YSU) planetary boundary layer scheme (Hong et al. 2006) and Single-Moment 6-Class Microphysics scheme (WSM6, Hong and Lim 2006), which uses five prognostic hydrometeor categories (including ice, hail, graupel, rain, and cloud water). The cloud droplet number condensation is reduced from the default value of 100 cm^{-3} to 50 cm^{-3} because of the typically clean maritime conditions found in Hawai'i (Hudson 1993). The Rapid Radiative Transfer Model (RRTM, Mlawer et al. 1997) longwave radiation scheme, Dudhia shortwave radiation scheme (Dudhia 1989) and a revised surface layer scheme (Jiménez et al. 2012) are also used.

Similar to Nguyen et al. (2010), the Noah land surface model (Chen and Dudhia 2001) is employed using the vegetation cover and soil properties compiled by Zhang et al. (2005a,b) from the USGS Land Use Land Cover Level II Data (USGS 1986) and soil surveys for the state of Hawai'i (Foote et al. 1972; Sato et al. 1973). Considering the recent housing development of the Second City (Kapolei) (Fig. 2.1), the U.S. Geological Survey (USGS) land use data compiled by Zhang et al. (2005a,b) are replaced by the recently updated land cover from the Coastal Change Analysis Program (C-CAP, NOAA 2019) (Fig. 2.1). In the WRF model, the initial soil moisture is derived from the global model without considering the precipitation in the past. O'ahu is represented by only a single grid box in the CFSR, which is why the initial soil moisture is completely uniform across the island. Following Zhang et al. (2005a,b) and Yang et al. (2005), the 24-hour simulations of the high-resolution soil moisture and soil temperature from the model run of the previous day are used to provide the updated soil conditions for the next run. After running the simulations prior to the events that we interested in for one month, we then started the actual case simulations. The first 12-h of model output are considered as the model spin-up period

because the initial conditions interpolated from the CFS analyses to the high-resolution model domain contain very low-resolution information on orographic and other local effects on airflow, cloud, and precipitation. The 24-hour model simulation (13th to the 36th hour) is used as the simulated diurnal cycle (0300 HST to 0200 HST the next day) for each day.

Chapter 2 Figures

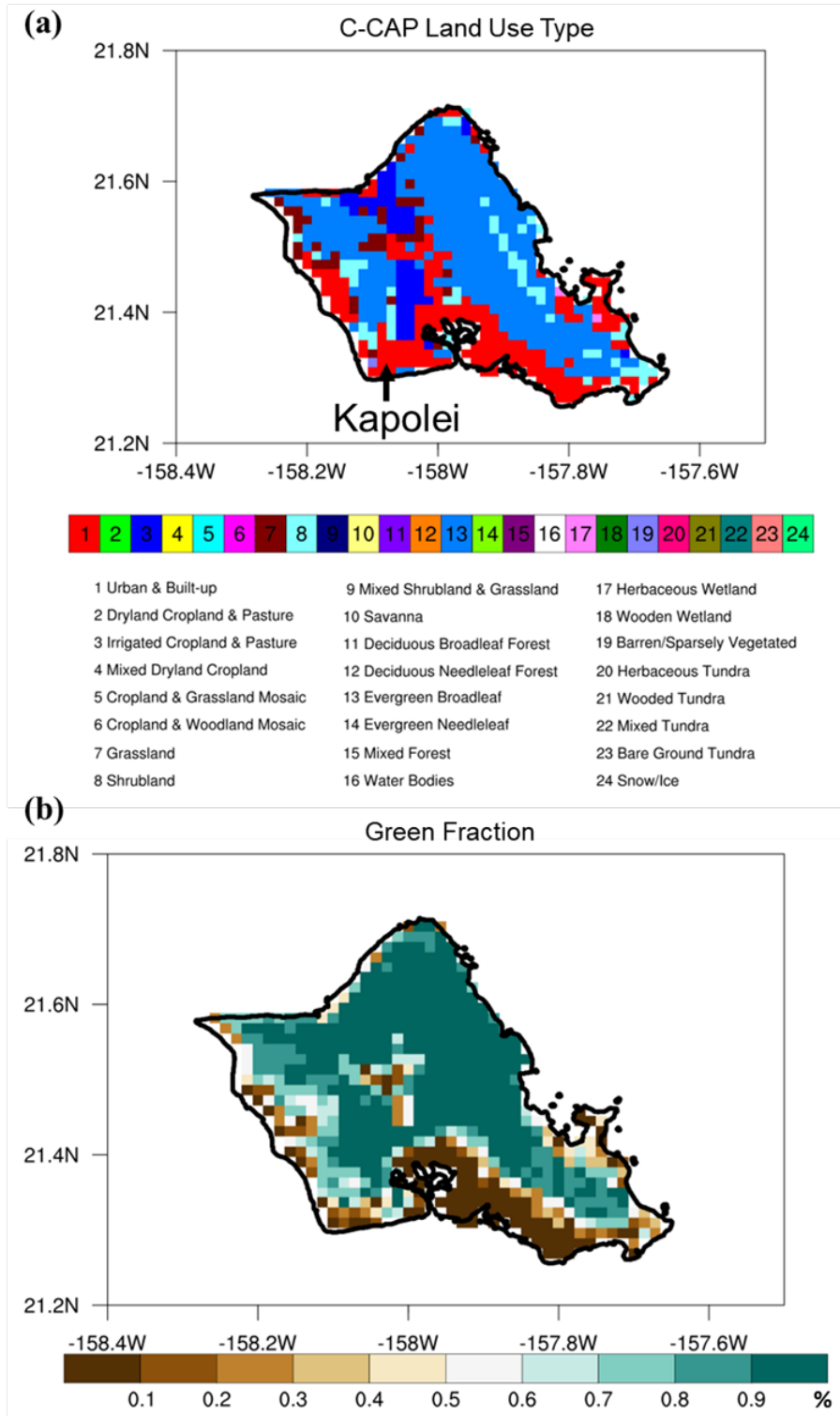


Fig. 2.1 (a) New land-cover/use data for O‘ahu with 1.5-km grids adapted from the Coastal Change Analysis Program (C-CAP) High-Resolution Land Cover. (b) New vegetation fraction (%) adapted from the C-CAP High-Resolution Land Cover.

Chapter 3 Effects of Trade Wind Strength on Airflow and Weather over O‘ahu

3.1 Introduction

Mountains perturb incident airflow by mechanically lifting or deflecting it and by generating differential surface heating that drives thermal circulations. Many theoretical (e.g., Drazin 1961; Lilly and Klemp 1979; Smith 1982; 1985), experimental (e.g., Brighton 1978; Hunt and Snyder 1980), and numerical (e.g., Smolarkiewicz and Rotunno 1989; Schär and Durran 1997; Epifanio and Rotunno 2005) studies on stratified flow over mountains have been conducted. However, most of the previous studies on airflow past three-dimensional (3D) mountains are based on idealized studies (e.g., Smolarkiewicz et al. 1988; Smolarkiewicz and Rotunno 1989; Schär and Smith 1993; Schär and Durran 1997; Epifanio and Rotunno 2005).

The dynamics of mechanically forced flows over an isolated mountain may be explained with the Froude number ($Fr = U/Nh$, where U is the upstream wind speed, N is the stability and h is the mountain height). For $Fr \gg 1$, the surface airflow can move up and over the mountain (Smolarkiewicz et al. 1988). The transition from blocked to unblocked flow generally occurs when U/N is equal to or slightly greater than h . For hydrostatic flow over a bell-shaped mountain, Miles and Huppert (1969) found the transition to occur more precisely at $h = 0.85 U/N$. For $Fr \ll 1$, the approaching low-level flow decelerates and is deflected around the island obstacle.

In addition to dynamic forcing, the island-scale airflow and weather are affected by the diurnal heating cycle (e.g., Chen and Nash 1994; Chen and Wang 1994; Chen and Li 1995; Yeh and Chen 1998; Wang and Chen 1998; Feng and Chen 2001; Yang and Chen 2003; Yang et al. 2005; Kerns

et al. 2010) and rain evaporative cooling (e.g., Carbone et al. 1998; Li and Chen 1999; Frye and Chen 2001; Tu et al. 2017). Reisner and Smolarkiewicz (1994) studied low Fr (< 1) flow past a 3D obstacle with uniform heating at the surface and showed that with sufficient heating, the transition from blocked to unblocked flow could possibly occur. Diabatic heating has also been found to affect this flow transition (Miglietta and Buzzi 2001; Colle 2004). The diabatic effects associated with latent heat release due to cloud and precipitation formation strengthen orographic lifting while reducing perturbation surface pressure on the windward side, resulting in weaker orographic blocking (Chen and Feng 2001).

Leopold (1949) showed that for mountains with tops well above the trade wind inversion in Hawai'i (~1.9 km, Winning et al. 2017), the inversion serves as a lid forcing the low-level flow to be deflected by the terrain (Schär and Smith 1993). For the island of Hawai'i, with peaks well above the trade wind inversion, the island-scale airflow and weather are affected by the trade wind inversion height in addition to Fr (Chen and Feng 1995; 2001). For islands with mountain heights above the trade wind inversion (Haleakalā on Maui, and Mauna Loa and Mauna Kea on Hawai'i), a westerly reversed flow between the counter-rotating vortices in the lee-side wake zone occurs and is stronger and deeper with higher moisture content when trades are stronger (Yang and Chen 2003; Yang et al. 2005; Yang et al. 2008a; Carlis et al. 2010). For the Island of Hawai'i, with a deeper and moister westerly reversed flow off the central leeward coast (or the Kona coast) when trades are stronger, both the nocturnal rainfall along the Kona coast and afternoon rainfall maximum on the Kona lower slopes are larger (Yang et al. 2008a). The nocturnal rainfall along the Kona coast is caused by the convergence between the westerly reversed flow and nighttime offshore flow, whereas the afternoon rainfall on the lower Kona slopes is caused by the development of upslope flow in response to solar heating (Chen and Nash 1994; Yang et al. 2008a).

The island of O‘ahu (Fig. 3.1), with a horizontal area of 1,545 km², is dominated by two separate volcanic mountain ranges oriented in a northwest–southeast direction: the Wai‘anae mountain range along the western lee-side coast and the Ko‘olau mountain range along the northeastern windward coast, with a broad "valley" (the Central O‘ahu Plain) between them. The highest peak, Mount Ka‘ala (1227 m), on O‘ahu is over the Wai‘anae mountain range along the western lee-side coast (Fig. 3.1). For the Ko‘olau mountain range (highest peak ~946 m) along the northeastern windward coast of O‘ahu, with h of ~1000 m, a mountain half width (L) of 10 km, $U \sim 8\text{--}10 \text{ m s}^{-1}$, $N \sim 10^{-2} \text{ s}^{-1}$, and a Coriolis parameter (f) of $\sim 10^{-4} \text{ s}^{-1}$, Fr is ~ 1 . With $Fr \sim 1$, flow splitting is less likely to occur on the windward side under normal east-north-easterly trade wind flow as compared to the island of Hawai‘i. For normal trade wind conditions ($U \sim 8 \text{ m s}^{-1}$), Nguyen et al. (2010) showed that U/N averaged over the 300–600 m layer is about 1500 m. With $Fr > 1$, the flow regime passing the Ko‘olau Mountains during the daytime is characterized as a “flow over” regime, with mountain waves above the peaks.

Yang et al. (2008b) used cruise measurements and satellite data to examine the wake circulation over Kaua‘i and O‘ahu. Their results show that the afternoon westerly onshore/sea breeze flows over the western coasts of Kaua‘i and O‘ahu are present and that the vertical extent of the westerly flow is ~ 400 m above sea level. Similar results are shown in Lane et al. (2006), who studied island-induced circulations and turbulence over Kaua‘i using WRF-ARW.

Elongated cloud trails are another feature found in these leeside wake zones. This feature has been observed in island wakes in various parts of the world, including: Anegada, British Virgin Islands (Malkus 1963), Nantucket, Massachusetts (Malkus and Bunker 1952), the Pacific island of Guadalupe (Dorman 1994), Nauru (Nordeen et al. 2001), Hawai‘i (Yang et al. 2008b,c), Lesser Antilles (Kirshbaum and Fairman 2015), and Bermuda (Johnston et al. 2018). In satellite images

and surface observations, leeside cloud trails are evident over both flat and mountainous islands, especially during the afternoon hours (Nordeen et al. 2001; McFarlane et al. 2005; Matthews et al. 2007; Kirshbaum and Fairman 2015; Johnston et al. 2018).

Yang et al. (2008b,c) studied cloudiness off the leeside coasts of Kaua‘i and Ni‘ihau using satellite data and numerical simulations. They stated that afternoon cloud frequency in August was enhanced past each of these two islands. For Kaua‘i and Ni‘ihau, the highest peaks are 1569 m and 390 m, respectively. With mountaintops below the trade wind inversion, Yang et al. (2008b,c) attributed the afternoon cloud trails to a combination of mechanical leeside convergence of island-deflected airflows and warm air advection from the island to the wake zone. They suggest that the warm advection during the daytime causes an increase in the air temperature and enhanced low-level wind convergence in the wake zone. At night, cold advection by land breezes suppresses cloud formation in the wake. In contrast to the thermal advection mechanism proposed by Yang et al. (2008b,c), there are studies showing the importance of temperature gradients in controlling the strength of thermally driven circulations (e.g., Crook, 2001; Nguyen et al., 2010; Jury and Chiao, 2013; Kirshbaum and Fairman, 2015).

Despite its relatively small size ($\sim 1545 \text{ km}^2$), a pronounced diurnal cycle over O‘ahu is evident under summer trade wind conditions (Leopold 1948; Nguyen et al. 2010; Hartley and Chen 2010). Hartley and Chen (2010) found that in summer, orographic precipitation over the Ko‘olau mountain range is greater during strong trade wind days ($> 8 \text{ mm day}^{-1}$) than weak trade wind days ($\sim 4 \text{ mm day}^{-1}$) without much rainfall over the Wai‘anae mountain range ($0\text{--}2 \text{ mm day}^{-1}$). Most stations over the Ko‘olau mountain range have an early morning/nocturnal rainfall maximum (Hartley and Chen 2010; Nguyen et al. 2010). When trade wind speeds are low, afternoon sea breezes occur at all southern and Wai‘anae stations (Leopold 1948). Precipitation on the western

leeside coast is infrequent with a slight peak in the hourly rainfall frequency (5–10%) in the early afternoon due to the development of the afternoon sea breezes (Hartley and Chen 2010).

In model sensitivity tests (Nguyen et al. 2010), the daytime westerly onshore flow along the western leeside coast of O‘ahu is thermally driven and is related to land surface heating superimposed by latent heat release from persistent orographic precipitation over the Ko‘olau mountains. When the westerly onshore flow occurs during the daytime, it brings cool, moist, maritime air inland. In this chapter, the island-scale (1.5 km) simulations of the WRF-ARW/LSM with full-physics are used to examine the circulations and mechanisms for the airflows and development of cloudiness in the leeside wake zone of O‘ahu. To investigate the impacts of thermal advection and diurnal heating cycle on airflow and cloudiness over O‘ahu, especially off the leeside coast, the effects of trade wind strength (strong trade wind versus weak trade wind) on the cloudiness, island induced flow and thermodynamic fields on the leeside of the island are investigated.

3.2 Methodology

3.2.1 Strong and Weak Trade Categories

The pattern of TPW during July–August 2013 is similar to the long-term July–August mean during 1979–2015 with a 0.97 cross-correlation (Fig. 3.2). The trade wind speed during July–August 2013 is relatively weaker ($\sim 1 \text{ m s}^{-1}$) than the two-month composite during 1979–2015 (Fig. 3.3). In this study, July–August 2013 is used as a reference for typical summer conditions. The daily mean wind data at an upstream point of O‘ahu (21.5°N , 157.5°W , Fig. 3.4) from CFSv2 analysis (every 6 hours) are used to determine the upstream prevailing wind conditions for each day. The histograms for daily mean wind direction and daily mean wind speed during July–August

2013 show that the prevailing wind direction is mainly from 60 to 90 degrees with wind speed from 6 to 9 m s⁻¹ (Fig. 3.5). Days with wind directions between 60 to 90 degrees with wind speed > 3 m s⁻¹ without the presence of synoptic disturbances over the Central Pacific (tropical storms, upper-level lows/troughs, and wind shear lines associated with mid-latitude storms) (Hartley and Chen 2010) during the two-month period are classified as trade wind days (36 days total). The nine days (~25% of the total trade wind days) with the strongest trade wind speed are classified as strong trade wind days with trade-wind speed varied from 9.5 to 12.2 m s⁻¹. The nine days with the weakest trade wind speed are classified as weak trade wind days with trade-wind speed varied from 4.2 to 7.1 m s⁻¹. The mean wind speeds for strong and weak trade categories are 10.3 m s⁻¹ and 6.2 m s⁻¹, respectively. Dates of the strong and weak trade wind are listed in Table 3.1. The mean *Fr* for the strong and weak trade categories are 1.0 and 0.6, respectively. Thus, under weak trades, it is unlikely for the incoming trade winds to flow over the island.

3.2.2 Study Area and Model Verifications

The domain setup for O‘ahu includes three nested domains with horizontal grid sizes of 13.5, 4.5, and 1.5 km and horizontal dimensions of 65 × 62, 64 × 58, and 79 × 64. The 1.5-km domain covers the entire island of O‘ahu (Fig. 3.4). The mountaintops of the Ko‘olau Range and the Wai‘anae Range are 740 m and 887 m in the innermost domain, respectively.

Model verification was conducted for the 36 days in the July–August 2013 period. Observational surface wind speed, surface wind direction, air temperature, and dew point were acquired from the MesoWest cooperative network (Horel et al. 2002) following quality control using MesoWest data quality ratings (Splitt and Horel 1998), with further subjective checks for spatial and temporal consistency during manual analysis. MesoWest observations typically represent averages over the entire reporting interval, which can vary from 5 minutes to an hour

(Horel et al. 2002). Observations within 20 minutes of the verification times were used for the validation. The station network, temporal resolution, and geolocation of the 24 stations are listed in Table 3.2. Quantitative verifications between model output and observations are made for surface wind, surface temperature, and relative humidity (RH), including statistical errors.

To evaluate the model performance quantitatively, the simulated surface variables are interpolated to 24 surface stations (Table 3.2) every hour during the 36 trade wind cases because the station locations do not match perfectly with the model grids. Therefore, a 4-point interpolation is used to calculate the simulated variables horizontally at the station locations. The weighted 4-point average interpolation can be expressed as:

$$F_h = \frac{\sum_{i=1}^4 d_i f_i}{\sum_{i=1}^4 d_i} \quad (3.1)$$

Where

F_h is the horizontal interpolation value at the station;

f_i , $i = 1$ to 4, are grid point values at the 4-nearest grid points; and

d_i , $i = 1$ to 4 are distances from the station to the grid point.

For interpolation of the surface air temperature in the coastal areas, only the nearest points over land were used to avoid including ocean points since surface air temperature is significantly affected by land/sea heating efficiency.

Then, the simulated temperature is adjusted with an environmental lapse rate of -6.5 K km^{-1} to account for the height difference between the model terrain and the surface station elevation:

$$F_s = F_h + \gamma(Z_m - Z_s) \quad (3.2)$$

where

F_h is the temperature value from equation (1);

γ is the lapse rate - 6.5 K km⁻¹; and

Z_m and Z_s are model terrain height and station elevation, respectively.

Error statistics for model output are calculated for surface temperature, relative humidity (RH), and surface wind (Tables 3.3 and 3.4). In addition to model bias, the observational uncertainties may also exist. The error statistics are comparable to those presented by Nguyen et al. (2010) using the Fifth-Generation Penn State/NCAR Mesoscale Model (MM5) model. The composite simulated surface winds at 0500 HST and 1400 HST during the 36 trade wind days are consistent with observations (Fig. 3.6).

The simulated diurnal variations are consistent with observations. For stations on the windward side, the diurnal ranges in the surface air temperature and RH are smaller than stations in the island interior and lee-side coasts with higher nighttime minimum air temperature and RH but with cooler and moister air in the afternoon (Figs. 3.7 and 3.8). Stations along the leeward coasts and central valley, especially those areas with urban land use, have the largest diurnal range in the surface air temperature and moisture (Figs. 3.7 and 3.8). Similarly, winds along the windward coast well exposed to the incoming trades have smaller diurnal variations as compared to other stations (Figs. 3.6, 3.9, and 3.10). Stations along the south shore and leeward coasts have the largest diurnal variations in response to the diurnal heating cycle. Over the Central Oahu Plain, winds are affected by the mountain/valley wind circulations from both mountain ranges. Along the western lee-side coast, winds are weaker and during the daytime, weak westerly reversed flow/sea breezes are apparent (Figs. 3.6, 3.9, and 3.10).

At KTAH and KFWH, the model underestimates surface temperature with a negative 1–1.5 bias in surface temperature. The model systematically overestimates RH for the 11 of all 13 stations. Relatively larger positive bias (>5%) are found over the windward side (KFWH and

PHNG) and the southern coast (PHJR, PHNL, and WWFH). Three stations on the western coast (KKRH, HFO05, and D3665) have relatively large root-mean-square errors in zonal wind speed than other stations (Table 3.4). The zonal wind errors at these stations mainly occur during the daytime as the model has difficulty in simulating westerly onshore flow (Fig. 3.9), even simulated surface temperatures are comparable to observations (Fig. 3.7). In this case, the model errors may be partly due to the fact that the 1.5-km grid size cannot accurately depict the steepness of the Wai‘anae mountain range. Distances among AN161, AN162, and OOUH are less than 1.5 km, but diurnal variations of surface wind at these stations (Figs. 3.9 and 3.10) are slightly different from each other, indicating the observational uncertainties may also exist. PHNL is the only station with large positive bias ($>1 \text{ m s}^{-1}$) in zonal and meridional winds. The observed wind speed at PHNL is stronger than other stations over the southern coast (AN161, AN162, OOUH, HOFH) (Figs. 3.9 and 3.10).

3.3 Effects of Trade Wind Strength on Cloud Patterns, Airflow and Thermodynamic Fields

In this section, satellite observations and model simulations are used to investigate how trade wind speed affects the wake circulations and clouds off the leeward coast of O‘ahu. Geostationary Operational Environmental Satellite-15 (GOES-15) visible images are first converted to effective albedo to delineate the distributions of clouds during different times of the day under strong and weak trade wind conditions for comparison. Then, the numerical simulations are used to study the influences of trade wind strength on circulations, thermal fields, and cloud distributions over the island and off the leeward coast during different times of day.

3.3.1 Satellite Observations of Cloud Patterns

i) Strong trades

There are large temporal variations in the effective albedo over and downstream of O‘ahu during the daytime (Fig. 3.11). In the early morning, the effective cloud albedo over the island increases after sunrise. The highest values ($> 25\%$) occur over the Ko‘olau mountain range around noon under direct sunlight (Fig. 3.11b), and extend to the island interior with a smaller secondary maximum ($\sim 20\%$) over the peaks of the Wai‘anae mountain range. The maximum effective albedo occurs around noontime over the Ko‘olau mountain range and persists until early afternoon (Fig. 3.11c) because of the development of orographic clouds caused by orographic lifting by a combination of strong trade wind and anabatic flow. During the same period, the high effective albedo values over the Wai‘anae mountain range (20%) are less than the Ko‘olau mountain range as some of the moisture associated with the incoming flow is removed by orographic precipitation over the Ko‘olau mountain range (Nguyen et al. 2010).

The effective albedo associated with clouds downstream of the island is low in the early morning but continues to increase until the early afternoon. The clouds off the leeward coast mainly occur around noontime and in the early afternoon (1130–1430 HST) and are most significant in the early afternoon. The effective albedo off the leeward coast decreases after the early afternoon and is low again at 1730 HST (Fig. 3.11d).

ii) Weak trades

The temporal and spatial variations of effective albedo during the daytime are similar to strong trades for weak trades (Fig. 3.12). However, under weak trades, the effective cloud albedo off the leeward coast is smaller at 0830 HST than for strong trades with minimum values $< 2.5\%$

(Fig. 3.12a). With less significant orographic lifting, the values of effective albedo along the Ko‘olau mountain range in the morning hours (Figs. 3.12a,b) are lower than for strong trades (Figs. 3.11a,b).

At 1130 HST, the albedo is $> 25\%$ over the two mountain ranges and off the leeward coast is slightly less for weak trades (Fig. 3.13b) with a shorter horizontal extent (Fig. 3.12b) compared to strong trades. This result suggests that in the morning hours the advection of clouds from the Wai‘anae mountain range toward the leeward coastal area is less significant under weaker trades. The effective albedo over central O‘ahu is also less when trades are weaker (Fig. 3.13b). It appears that drifting remnants of orographic clouds from the Ko‘olau mountain range downstream are less prevalent when trades are weaker.

For both strong and weak trades, clouds begin to build along the Wai‘anae mountain range and over the leeward side of O‘ahu in the late morning and extend more than 50 km off the leeward coast in the early afternoon (Figs. 3.11c and 3.12c). At 1430 HST, with less moisture removal by orographic precipitation over the Ko‘olau mountain range under weak trades and the development of upslope flows on both sides of the Wai‘anae mountain range (Hartley and Chen, 2010), the values of effective cloud albedo over the Wai‘anae mountain range are larger (Fig. 3.12c) than for strong trades (Fig. 3.11c). The effective albedo in the wake zone and over the Wai‘anae mountain range is larger and extends farther downstream when trades are weaker (Figs. 3.11c, 3.12c, and 3.13c). The cloudiness off the leeward coast for both trade wind conditions decreases in the late afternoon (Figs. 3.11d and 3.12d). However, the drifting clouds off the leeward coast and in the wake zone are more significant when trades are weaker (Fig. 3.13d).

3.3.2 Numerical Simulations

To better interpret the satellite observations and improve the understanding of cloud formation over O‘ahu, numerical simulations are conducted. In this section, the diurnal cycle of island-scale airflow and weather under strong and weak trade wind conditions is examined to understand the physical reasons for the variations in afternoon cloud formation off the leeward coast. Because the mountain and leeward cloud patterns are different between the morning and afternoon we will first compare the model results in the early morning between strong and weak trades followed by a comparison for the afternoon.

i) 0500HST

Figure 3.14 shows the simulated surface winds at 0500 HST for strong and weak trade conditions. The incoming northeasterly trade wind decelerates as it approaches the Ko‘olau mountain range. At night, air at low levels over the island becomes cool and stable due to surface radiative cooling. The stability of the nighttime low-level air prohibits vertical mixing of trade wind momentum (Leopold, 1948). Therefore, the surface wind speed over central O‘ahu is weak ($< 2 \text{ m s}^{-1}$) for both trade wind conditions (Fig. 3.14). At 0500 HST, westerly katabatic flows are present on the eastern slopes of the Wai‘anae mountain range. Downslope/offshore flows are also present on the western leeward coast for both strong and weak trades. With nighttime cooling, the simulated and observed offshore flows over the northern and southern coasts are more prominent for weak trades than for strong trades in agreement with observations (Fig. 3.14). The weak wind region over the western slopes of the Wai‘anae mountain range is simulated and extends westward during the nighttime. With orographic blocking due to surface cool and stable air, simulated surface airflow patterns share similarities between both strong and weak trade wind conditions, e.g., flow deceleration on the windward side, calm wind over the island interior and wake zone,

strong winds along the two mountain ranges, and katabatic winds on the eastern slopes of the Wai‘anae mountain range (Fig. 3.14). The greatest difference in surface airflows between the two regimes is overall weaker surface wind speed over the island when trades are weaker, especially over the island interior and in the wake zone. Furthermore, offshore flows over the northern and the southern coasts are more evident when trades are weaker (Fig. 3.14b). When trade wind is weak, the environmental pressure gradient is small, leading to dominant local forcing. Surface radiative cooling over the island, prohibiting vertical mixing of trade wind momentum, is more significant when trades are weak. This more significant surface cooling results in cool and dense air over island interior that drives the stronger offshore flows under weak trades.

The vertical cross-sections of simulated potential temperature and vertical motion along the northeast–southwest line in Fig. 3.1 at 0500 HST (Fig. 3.15) show upslope flow over the eastern slope of the Ko‘olau mountain range, downslope flow over the western slope of the Ko‘olau mountain range, and low-level easterly winds for both trade wind conditions. When trades are stronger, stronger downslope winds are simulated above the leeward slopes of the Wai‘anae mountain range, followed by a more significant mountain wave pattern as compared to weak trade conditions (Fig. 3.15a). The adiabatic descent of the stronger downslope winds results in warm and dry air over the leeward slopes of the Wai‘anae mountain range (Figs. 3.15a and 3.16a).

The cloud water content at 0500 HST (Fig. 3.17) shows cloud formation over the Ko‘olau mountain range due to orographic lifting under both trade wind conditions. When trades are stronger, more vertically integrated cloud water content is simulated over the Ko‘olau mountain range, central O‘ahu, and the eastern slopes of the Wai‘anae mountain range (Fig. 3.17a), resulting from strong impinging trades being lifted by the mountains. Furthermore, westward drifting of the cloud water content from the Ko‘olau mountain range toward the island interior by the trade

winds aloft is more significant when trades are stronger (Figs. 3.17a and 3.18a), consistent with the satellite observations presented in Section 3.3.1 (Figs. 3.11 and 3.12).

ii) 1400HST

At 1400 HST, flow deceleration along the windward side is less significant than at night with combined upslope/trade wind flow on the eastern slopes of the Ko‘olau mountain range (Fig. 3.19). The tip jets ($> 10 \text{ m s}^{-1}$) around the corners of the island are stronger and closer to the coast at 1400 HST than 0500 HST. Under weak trades, onshore flow is simulated at two surface stations along the western coast (HFO05 and D3665) (Fig. 3.19b) consistent with observations. In contrast, the westerly onshore flow along the western coast is not simulated for strong trades (Fig. 3.19a). HFO05 and D3665 (Fig. 3.1 and 3.19b) show weak mean westerly winds ($1\text{--}1.5 \text{ m s}^{-1}$) in the afternoon under strong trade wind conditions (Fig. 3.19a). The discrepancy may result from the modeled mountaintop of the Wai‘anae range being lower than its actual height.

Under strong trades, upslope and downslope easterly winds are simulated over the windward and leeside slopes of both the Ko‘olau and Wai‘anae mountain ranges at 1400 HST with mountain waves downstream (Fig. 3.20a). Over central O‘ahu, the potential temperature is homogeneous due to vertical mixing initiated by solar heating. Clouds are simulated over the Ko‘olau mountain range due to combined trade-upslope flow on the windward side (Fig. 3.22a). With removal of some moisture by orographic precipitation over the Ko‘olau mountain range, it is relatively dry over the Wai‘anae mountain range and off the leeside coast (Fig. 3.21a).

Under weak trade wind conditions (Fig. 3.20b), the downslope flow over the western slope of the Wai‘anae mountain range is absent. In addition to the eastern windward slopes, ascending motions are simulated over the western leeside coast (Fig. 3.20b) and the western slopes of the Wai‘anae mountain range due to orographic lifting of the westerly onshore flow/sea breezes (Fig.

3.20b). The moist westerly onshore/sea-breeze flow from the ocean is lifted by the Wai‘anae mountain range with the combined trade wind and the easterly return flow aloft (Fig. 3.21b). Clouds are simulated over the western slopes of the Wai‘anae mountain range (Fig. 3.22b), which are advected westward by the combined trade wind/return flow aloft (Figs. 3.22b, and 3.23b). These results are consistent with satellite observations (Figs. 3.11, and 3.12).

The results of the numerical simulations and satellite data are used to produce a schematic diagram of the O‘ahu cloud formations in the afternoon (Fig. 3.24) under different trade wind conditions. With increasing solar heating, orographic clouds start to build up on the Wai‘anae mountain range and are more significant when trades are weaker (Fig. 3.24b). Furthermore, under weaker trades, leeside sea breezes/onshore flow develops with upslope flow and orographic clouds on the western slopes of the Wai‘anae mountain range. These clouds are advected westward by the combined trade wind aloft and the easterly return flow associated with low-level sea breezes/upslope flow. As a result, leeside cloudiness is more significant with larger horizontal extent in the early afternoon when trades are weaker.

With mountain heights below the trade wind inversion, the diurnal evolution of cloudiness over the islands of Kaua‘i and Ni‘ihau and their respective leeside wake zones (Fig. 3.25) are similar to O‘ahu (Fig. 3.13). With a higher mountain peak over Kaua‘i (1569 m) than the Ko‘olau mountain range over O‘ahu (946 m), the orographic clouds on the windward side of Kaua‘i are more significant as compared to O‘ahu (Fig. 3.25). However, similar to O‘ahu, cloudiness over the western leeside and in the wake zone of Kaua‘i is more extensive with a larger horizontal extent in the early afternoon due to thermally induced circulations when trades are weaker.

3.4 Summary

Orographic lifting and thermally driven circulations due to solar heating are important for cloud formation over O‘ahu. After sunrise, orographic clouds on the windward side of the Ko‘olau mountain range are caused by the orographic lifting of the combined decelerated trade wind/onshore flow. These clouds are more significant on the windward side of the Ko‘olau Range when trades are stronger, and drift westward downstream by the trade wind flow aloft.

With continued solar heating after sunrise, orographic cloudiness increases over the Wai‘anae mountain range, and along the western leeside coast, especially under weak trade wind conditions. Under weak trades, the land–sea thermal contrast is critical for lee side circulations and cloud formation over the Wai‘anae mountain range and wake zone in the afternoon. Under weak trade conditions, the westerly upslope/sea-breeze flow develops over the western leeside coast during the afternoon hours due to the land–sea thermal contrast. The westerly onshore/upslope flow in the wake zone brings in maritime air along the western coast and up the western slope of the Wai‘anae mountain range. Clouds then form over the leeside slopes of the Wai‘anae mountain range and are advected westward by the combined trade wind/easterly return flow above the mountaintops. Clouds off the leeside coast are most prevalent with the largest horizontal extent in the afternoon hours, especially under weak trade wind conditions.

With stronger trade wind speed, the airflow goes over the Ko‘olau and Wai‘anae mountain ranges with significant upslope and downslope winds. The wake zone is drier and warmer than under weak trades due to adiabatic sinking on the leeside of the Wai‘anae mountain range and warm advection by the easterly winds. The land–sea thermal contrast that drives the westerly onshore/sea-breeze flow over the wake zone is absent under strong trades. Without the moist onshore/westerly winds off the leeside coast, the clouds forming over the mountaintops of the

Wai‘anae mountain range during the daytime are due to orographic lifting of the easterly trade flow aloft.

Chapter 3 Tables

Table 3.1 A list of the nine weak trade wind day and the nine strong trade wind days. The wind data at the upstream point of O‘ahu (21.5°N, 157.5°W) are daily averages of CFSv2 analysis.

	Date	Wind speed	Wind direction
Weak trade	23 Jul 2013	4.2	75.0
	20 Aug 2013	4.9	76.7
	30 Aug 2013	5.6	62.9
	4 Jul 2013	6.3	72.3
	23 Aug 2013	6.6	88.0
	26 Jul 2013	6.8	73.4
	25 Jul 2013	6.9	77.7
	8 Aug 2013	7.0	77.0
	7 Aug 2013	7.1	75.4
Strong trade	16 Aug 2013	9.5	76.6
	15 Aug 2013	9.6	83.7
	26 Aug 2013	9.7	76.3
	27 Aug 2013	9.7	82.4
	11 Aug 2013	9.8	81.1
	18 Aug 2013	10.3	79.5
	17 Aug 2013	10.8	75.4
	12 Jul 2013	11.0	78.2
	10 Jul 2013	12.2	83.5

Table 3.2 The temporal resolution and geolocation of the 24 weather stations.

STNID	NETWORK	Temporal Resolution	Lon	Lat	Elevation (m)
AN161	AIRNOW	Hourly	-157.86	21.31	15.9
AN162	AIRNOW	Hourly	-157.87	21.30	3.1
AN774	AIRNOW	Hourly	-157.97	21.39	14.9
AS839	APRSWXNET/CWOP	5 mins	-157.71	21.30	131.1
D3665	APRSWXNET/CWOP	15 mins	-158.15	21.39	14.9
D5064	APRSWXNET/CWOP	15 mins	-158.18	21.58	0.9
E2357	APRSWXNET/CWOP	10 mins	-157.75	21.41	27.1
HFO04	HNLWFO	Hourly	-157.99	21.70	4.6
HFO05	HNLWFO	Hourly	-158.20	21.45	1.5
HFO06	HNLWFO	Hourly	-158.02	21.48	264.3
HOFH	RAWS	Hourly	-158.02	21.36	1.5
KFWH	RAWS	Hourly	-157.95	21.69	1.5
KKRH	RAWS	Hourly	-158.26	21.57	288.7
KTAH	RAWS	Hourly	-157.99	21.68	181.7
MOKH	NOS-NWLON	Hourly	-157.79	21.43	4.9
OOUH	NOS-NWLON	6 mins	-157.87	21.31	0.0
PHHI	NWS	Hourly	-158.03	21.48	255.1
PHJR	NWS	Hourly	-158.07	21.31	10.1
PHNG	NWS	Hourly	-157.77	21.45	4.9
PHNL	NWS	Hourly	-157.94	21.33	3.1
SCBH	RAWS	Hourly	-158.08	21.50	298.7
SCEH	RAWS	Hourly	-157.99	21.50	381.0
SCSH	RAWS	Hourly	-158.11	21.48	453.9
WWFH	RAWS	Hourly	-157.98	21.39	1.5

Table 3.3 Error statistics of surface temperature and surface relative humidity for model points corresponding to the 18 weather stations during the 36 trade wind days from July–August 2013.

Station ID.	T(°C)			RH (%)		
	BIAS	MAE	RMSE	BIAS	MAE	RMSE
AS839	-0.7	0.9	1.2	0.4	4.1	5.2
D3665	-0.1	1.0	1.3	1.6	8.6	10.2
D5064	0.7	1.3	1.6	N/A	N/A	N/A
E2357	N/A	N/A	N/A	3.4	6.0	7.6
HOFH	-0.7	1.3	1.6	3.6	9.7	11.2
KFWH	-1.0	1.1	1.3	6.5	7.2	8.4
KKRH	-0.7	1.1	1.3	4.5	8.0	9.8
KTAH	-1.5	1.7	1.9	-1.7	5.6	7.3
MOKH	-0.9	1.1	1.3	N/A	N/A	N/A
OOUH	-0.2	1.1	1.3	N/A	N/A	N/A
PHHI	-0.1	1.0	1.3	4.4	7.9	9.7
PHJR	0.1	0.8	1.0	5.4	7.6	9.0
PHNG	-0.4	1.2	1.5	5.3	7.1	9.1
PHNL	-0.2	0.7	0.9	7.5	8.8	10.2
SCBH	-0.7	1.3	1.6	N/A	N/A	N/A
SCEH	N/A	N/A	N/A	-0.7	7.0	9.4
SCSH	-0.5	1.2	1.6	N/A	N/A	N/A
WWFH	-0.2	1.1	1.4	5.4	7.7	9.3

Table 3.4 Error statistics of surface wind for model points corresponding to the 17 weather stations during the 36 trade wind days from July–August 2013.

Station ID.	U(m s ⁻¹)			V(m s ⁻¹)		
	BIAS	MAE	RMSE	BIAS	MAE	RMSE
AN161	-1.6	1.8	2.1	-0.6	1.0	1.3
AN162	-0.9	1.3	1.5	0.5	0.8	1.1
AN774	0.3	1.3	1.6	0.6	0.8	1.1
D3665	-0.8	2.4	3.1	-0.1	1.5	1.9
HFO04	-0.8	1.0	1.3	1.3	1.4	1.6
HFO05	-0.4	1.9	2.7	-0.1	0.8	1.2
HFO06	0.9	1.4	1.8	1.0	1.3	1.6
HOFH	0.0	1.1	1.5	-0.3	0.8	1.1
KFWH	0.4	1.0	1.3	0.6	1.1	1.4
KKRH	0.6	2.0	2.5	1.4	1.9	2.4
KTAH	-0.2	0.9	1.3	-0.3	0.8	1.0
OOUH	-1.0	1.3	1.6	-0.1	0.9	1.2
PHJR	-0.8	1.1	1.4	-0.8	1.1	1.4
PHNG	0.2	0.8	1.1	0.0	0.8	1.0
PHNL	1.3	1.7	2.2	1.6	1.8	2.2
SCBH	-0.5	1.1	1.4	0.4	1.2	1.5
WWFH	0.6	1.2	1.6	0.6	1.0	1.2

Chapter 3 Figures

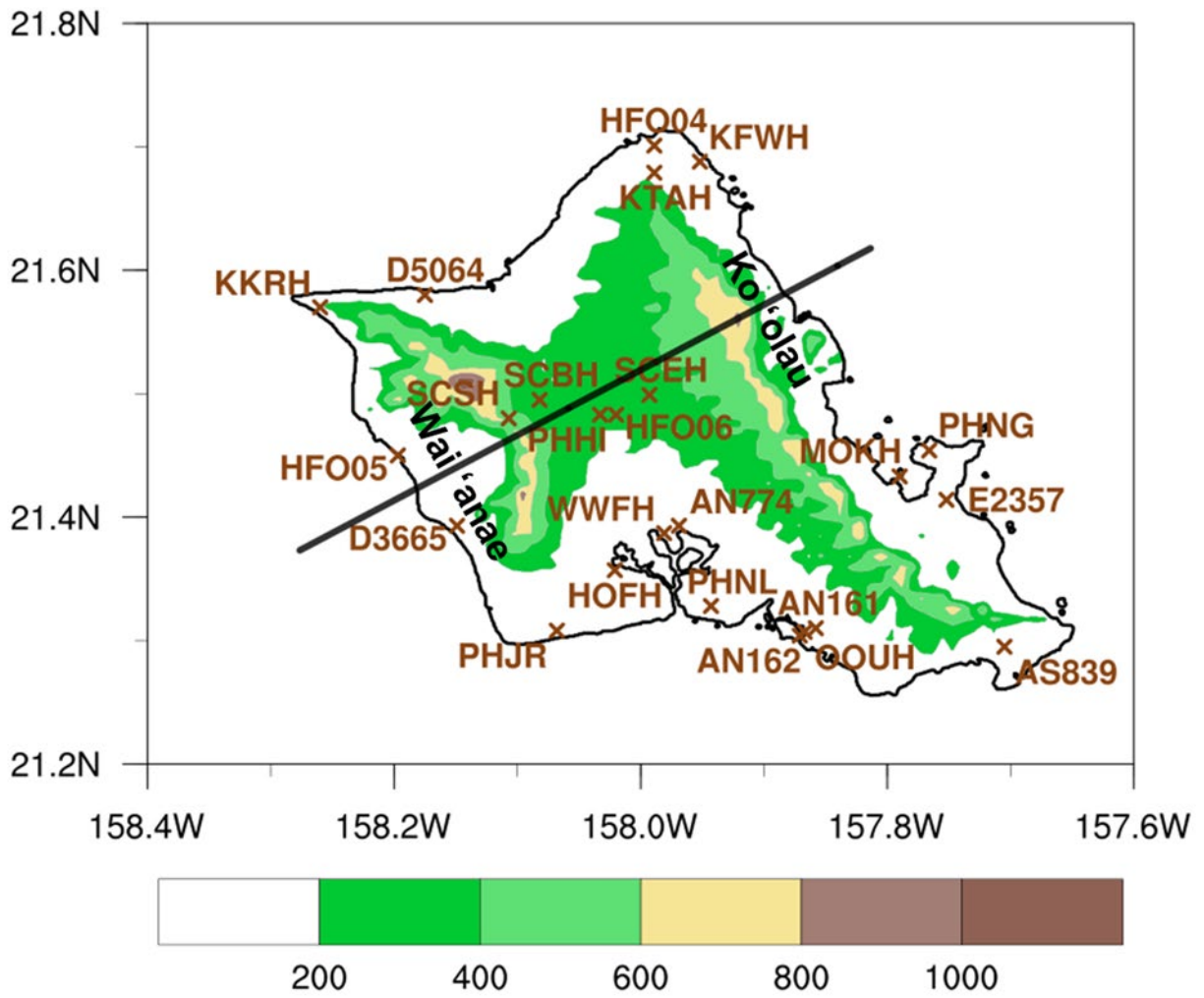


Fig. 3.1 The island of O‘ahu. Elevation contours are in 200-m intervals. A brown × represents the surface weather stations during July–August 2013. A solid line indicates the position for the cross-section analysis.

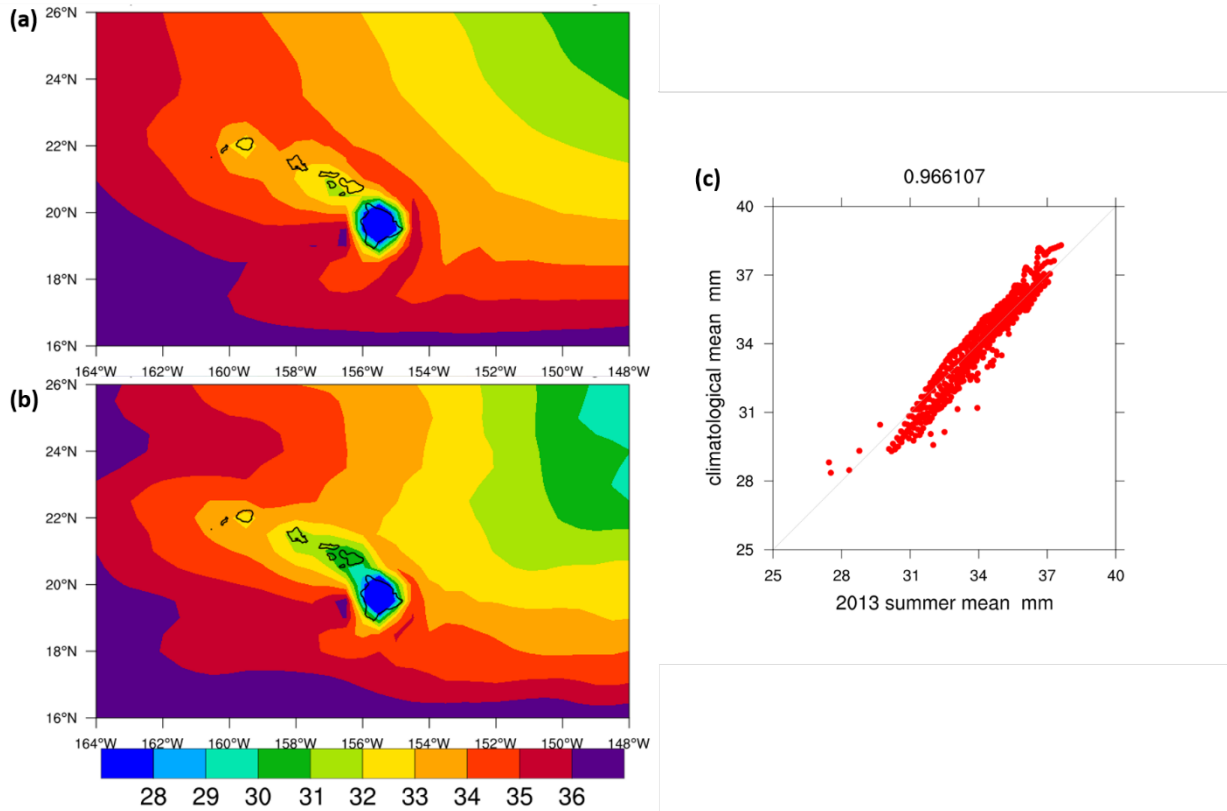


Fig. 3.2 The mean TPW (mm) from CFS during July–August (a) of 1979–2015 and (b) 2013.

(c) Scatter plot of the composite mean of total precipitable water during July–August and the mean total precipitable water during July–August 2013.

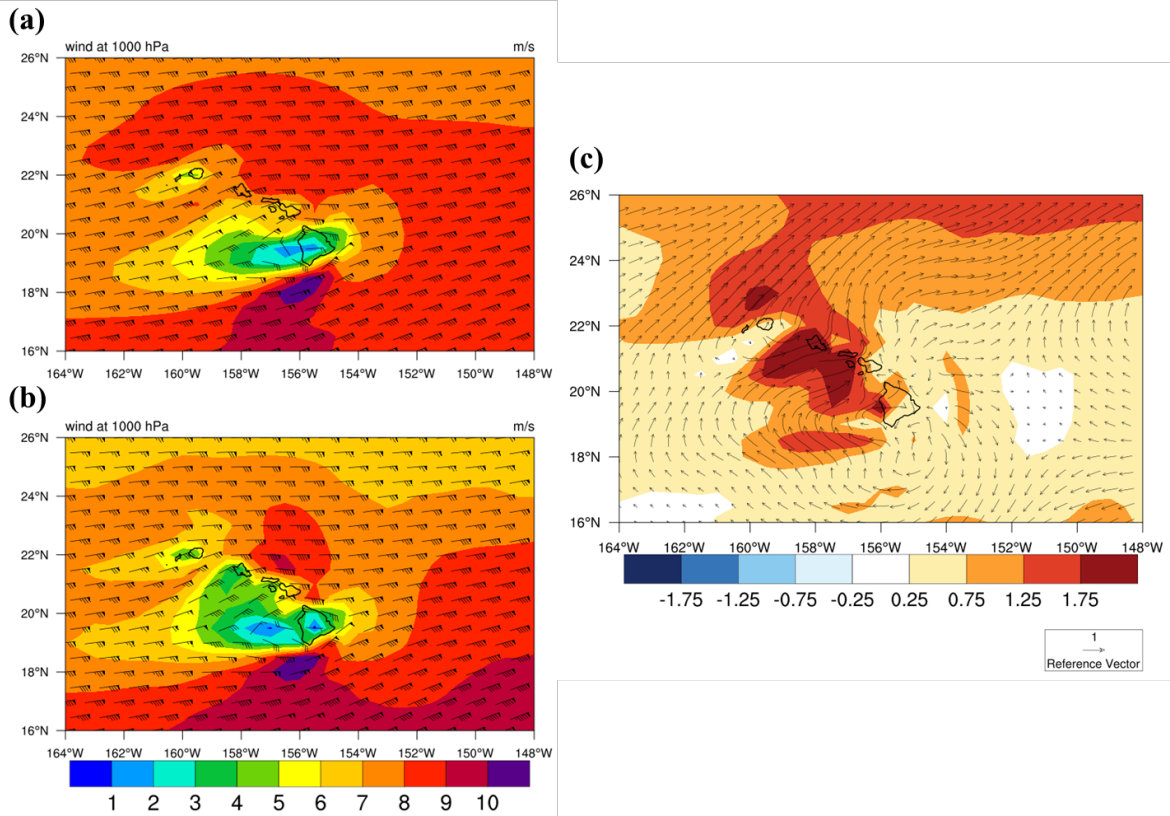


Fig. 3.3 The mean wind at 1000 hPa from CFS during July–August (a) for 1979–2015 and (b) 2013. (c) The wind difference between (a) and (b).

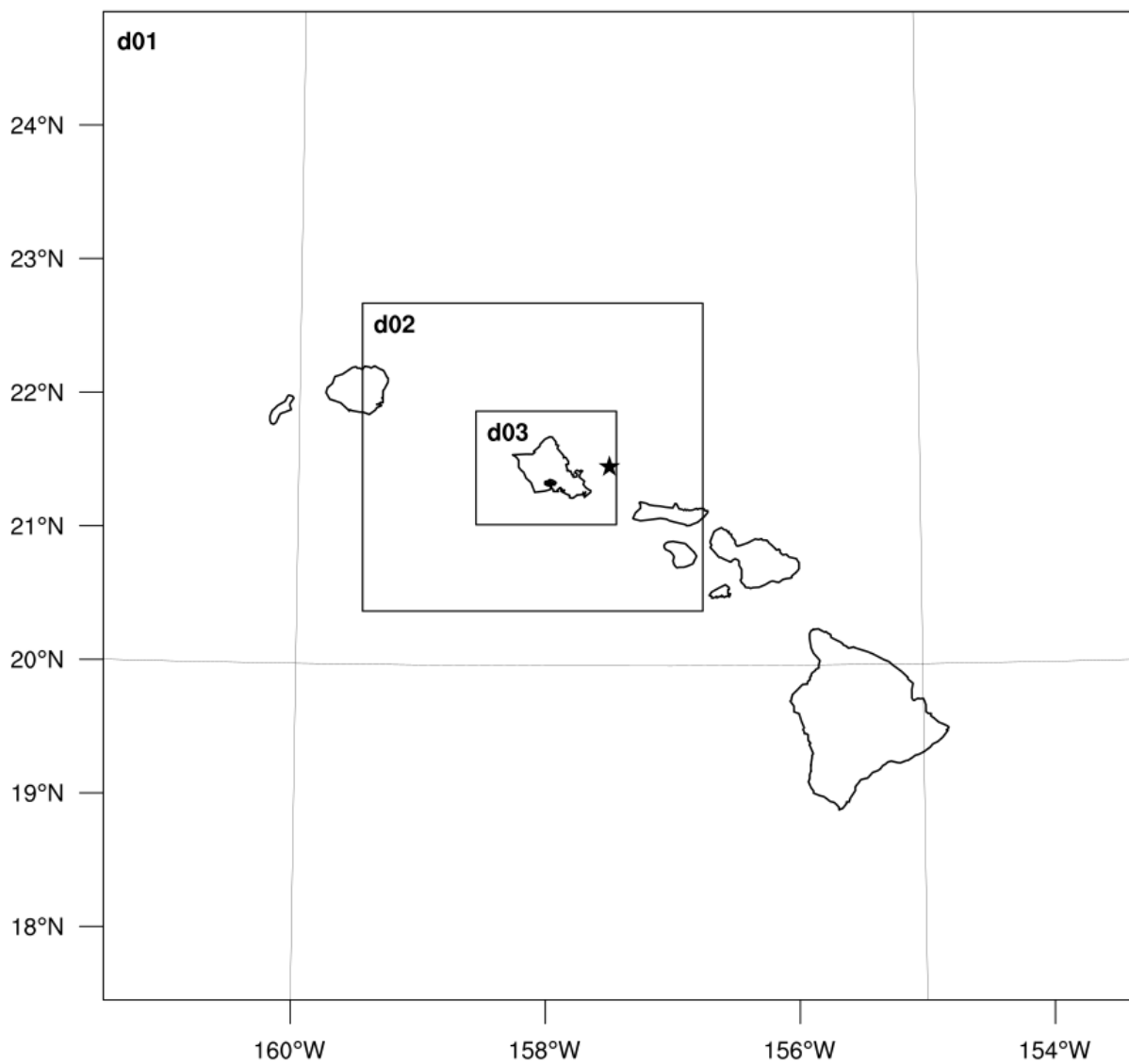


Fig. 3.4 Three nesting domains employed in the simulations with grid sizes of 13.5 km, 4.5 km, and 1.5 km, respectively. The black star represents the upstream point for O'ahu used in this study (21.5°N, 157.5°W).

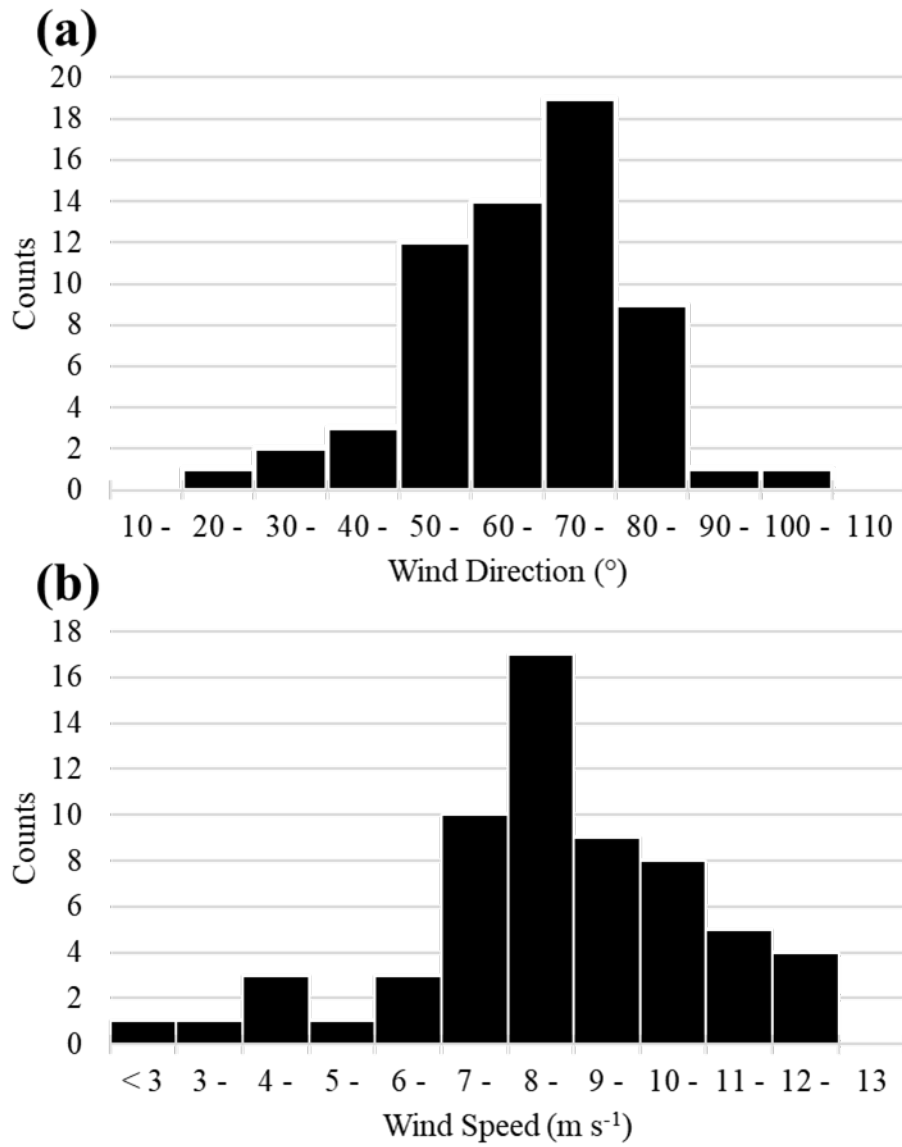


Fig. 3.5 Histogram of (a) wind direction and (b) wind speed from CFSv2 at the upstream point during July – August 2013.

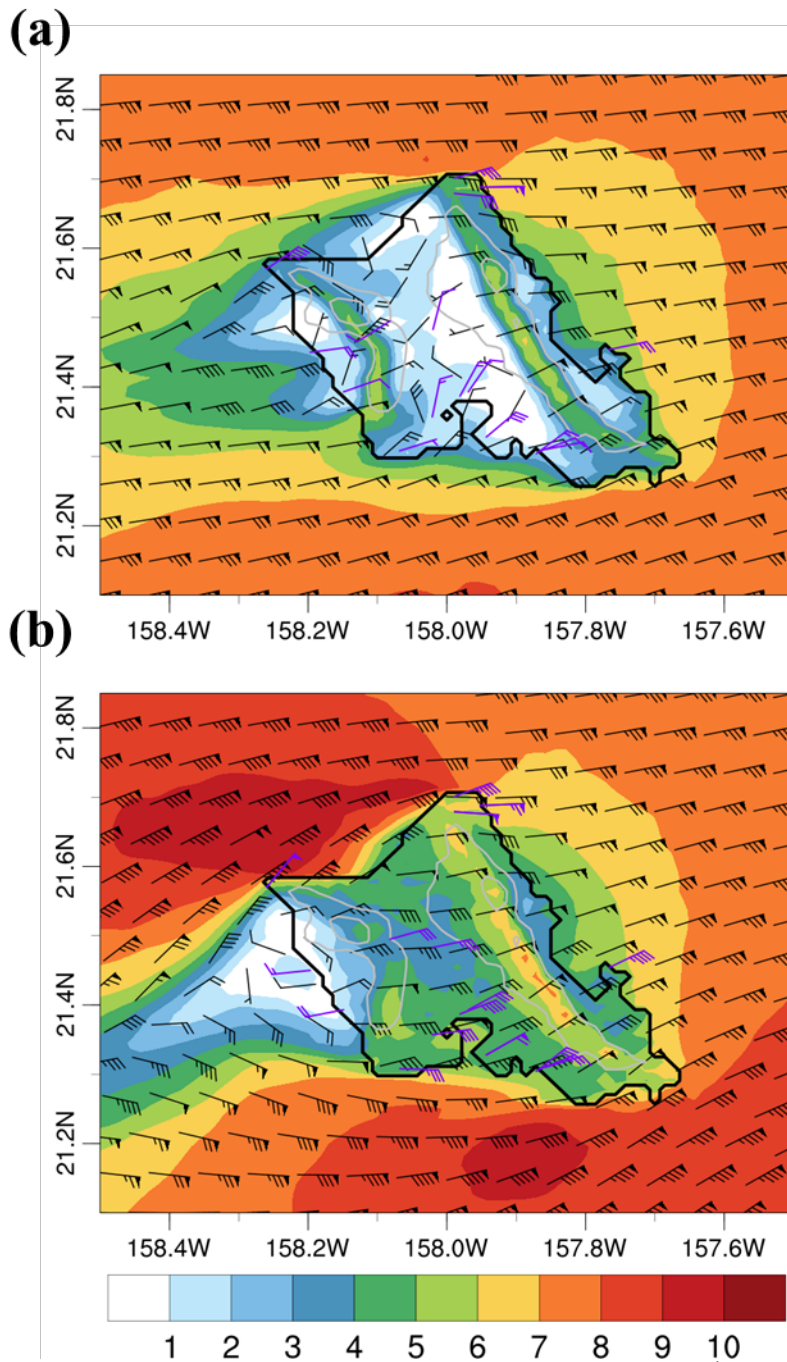


Fig. 3.6 Composite analysis of simulated surface wind (black barb, m s^{-1}) and observed surface wind (purple barb, m s^{-1}) for the 36 trade wind days at (a) 0500 HST, and (b) 1400 HST. One pennant is 5 m s^{-1} , a full barb is 1 m s^{-1} , a half barb is 0.5 m s^{-1} , and a circle denotes calm wind.

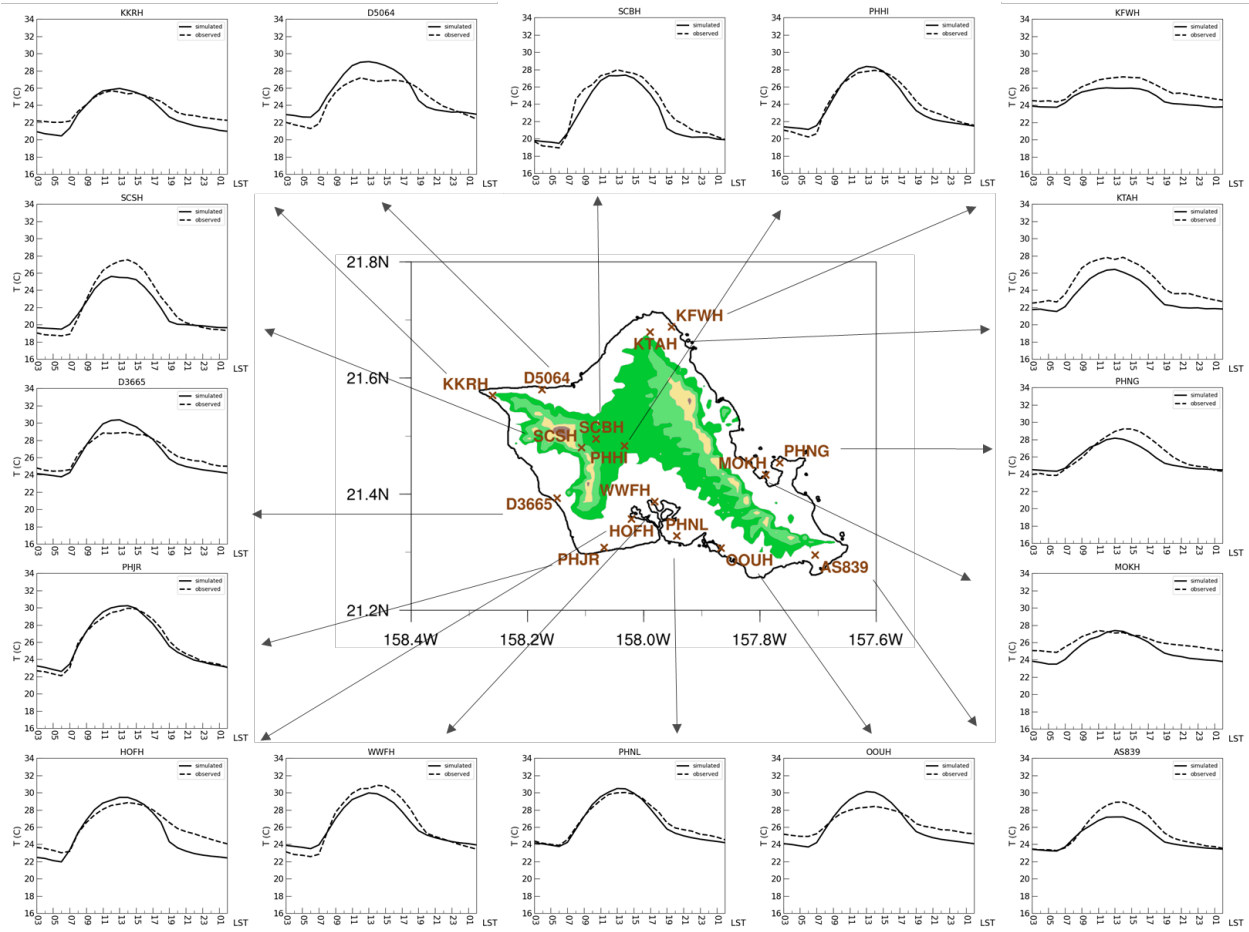


Fig. 3.7 Observed (dash line) and simulated (solid line) diurnal variations of surface temperature (°C) at various stations for July–August 2013.

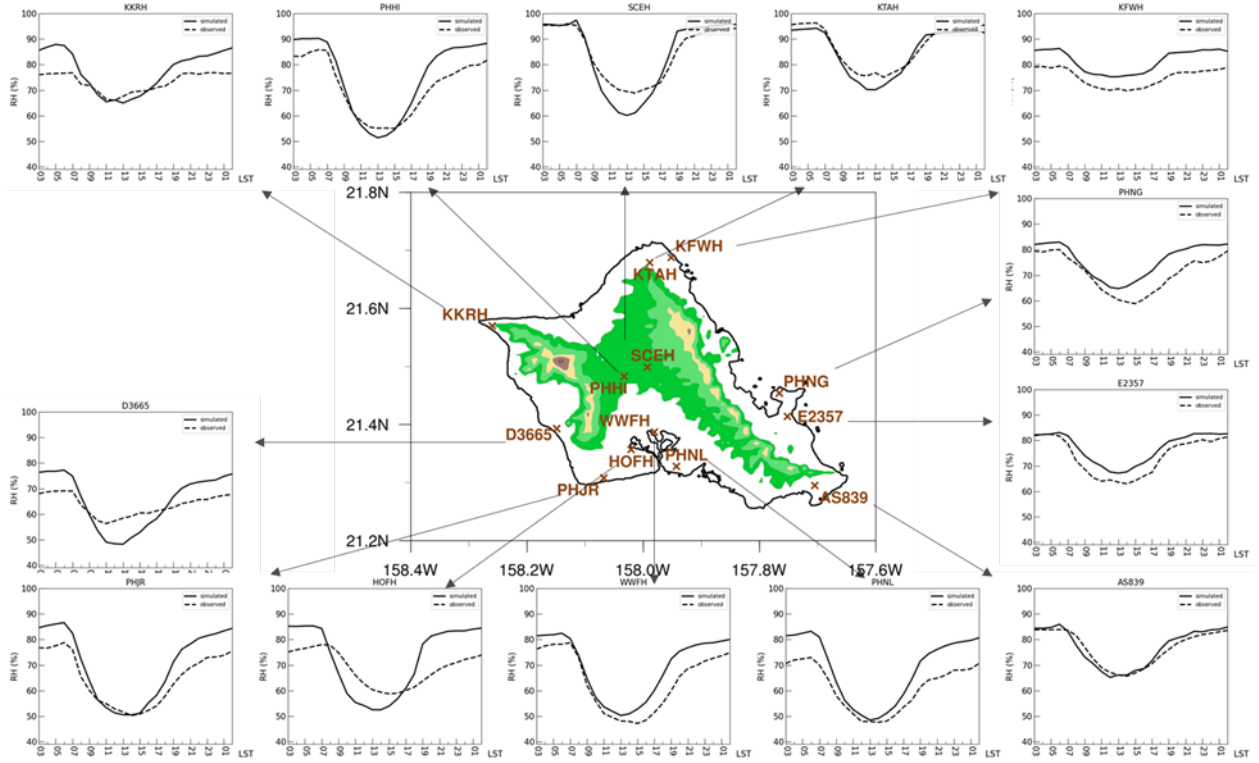


Fig. 3.8 Same as Fig. 3.7, but of surface relative humidity (%).

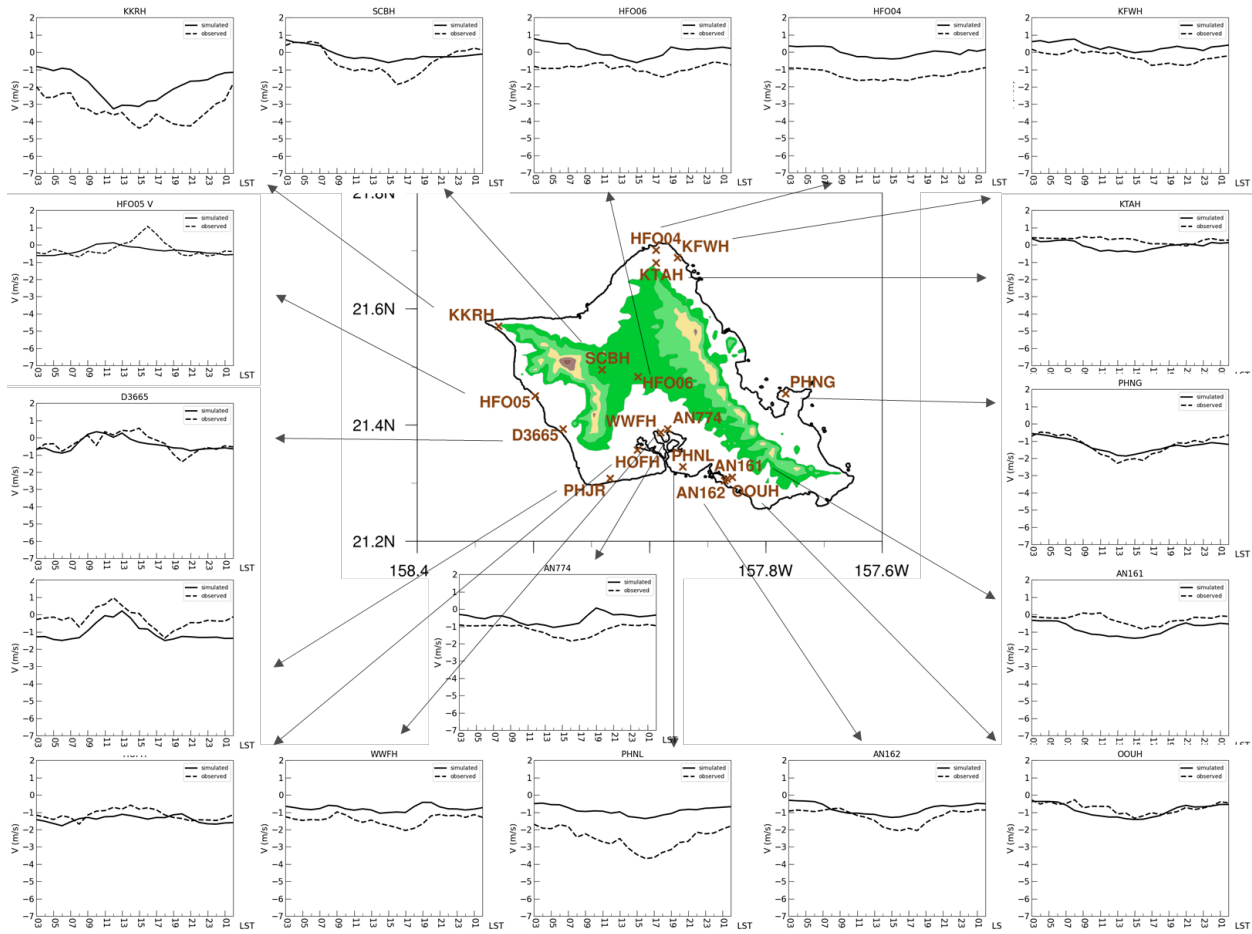


Fig. 3.10 Same as Fig. 3.7, but of surface meridional wind (m s^{-1}).

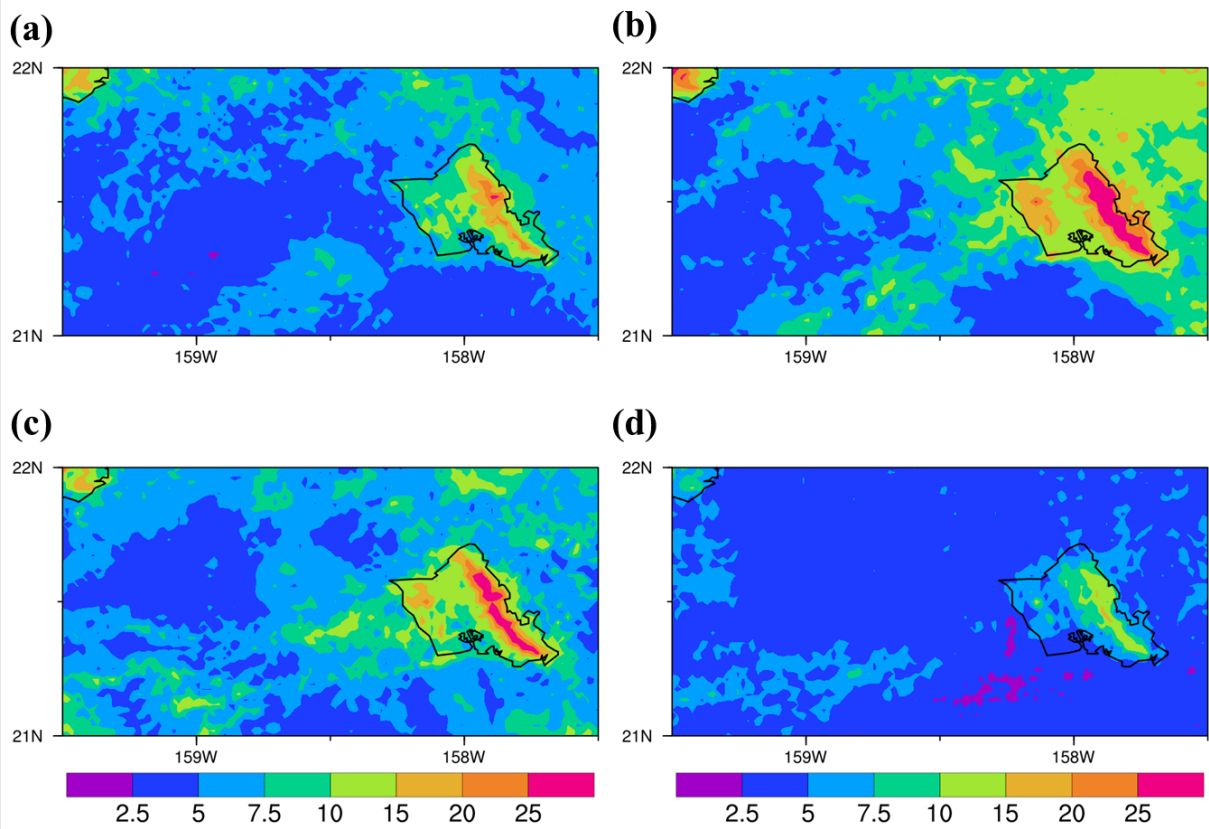


Fig. 3.11 Effective albedo (%) derived from the GOES-15 visible channel over O‘ahu for strong trades at (a) 0830, (b) 1130, (c) 1430, and (d) 1730 HST during July–August 2013.

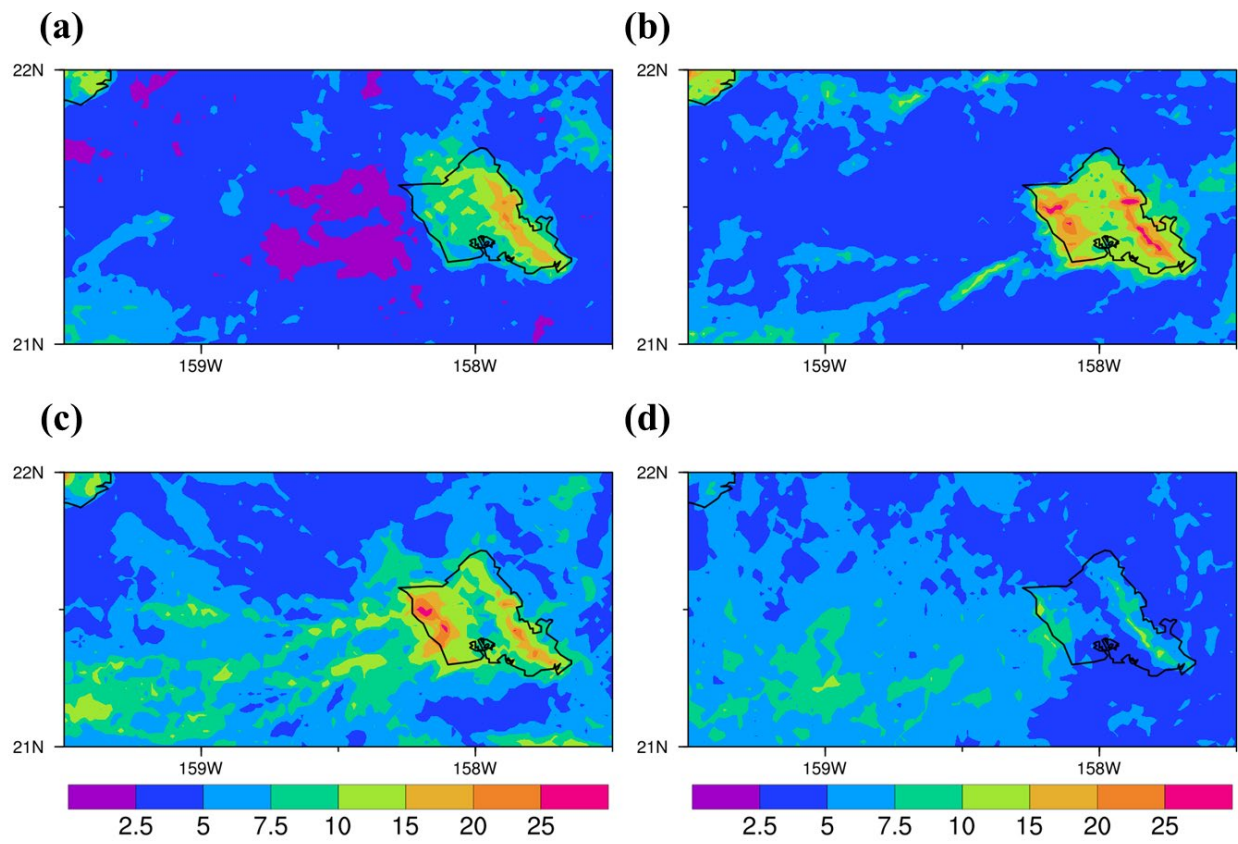


Fig. 3.12 Same as Fig. 3.11, but for weak trades.

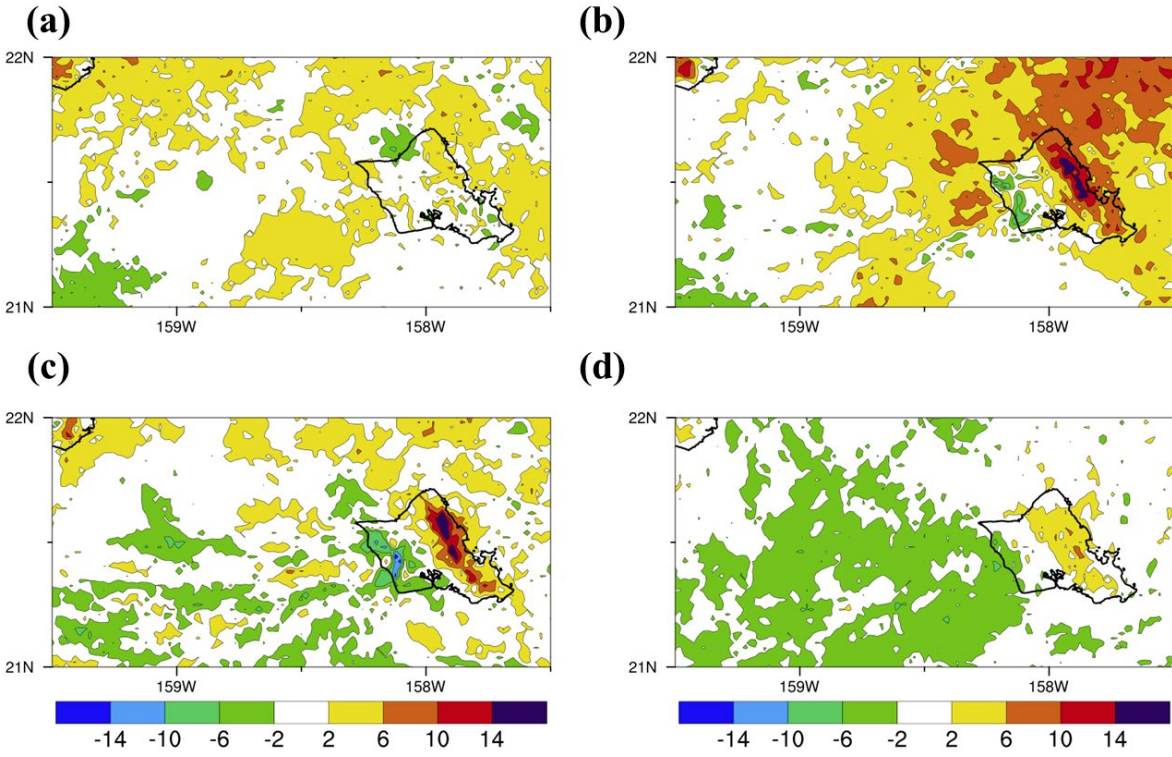


Fig. 3.13 The difference of effective albedo (%) over Oahu between strong trades and weak trades (strong – weak) at (a) 0830, (b) 1130, (c) 1430, and (d) 1730 HST during July–August 2013.

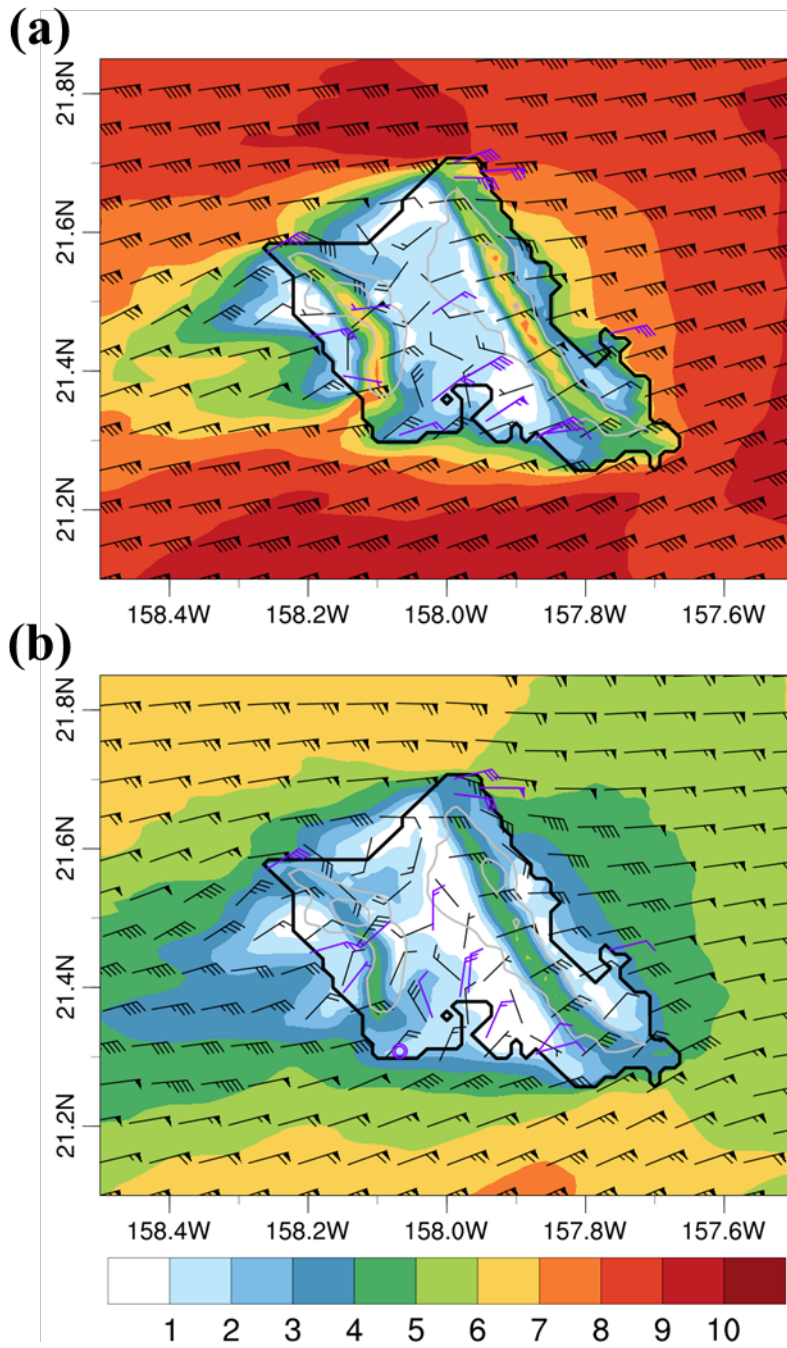


Fig. 3.14 Same as Fig. 3.6, but at 0500 HST for (a) strong trades and (b) weak trades.

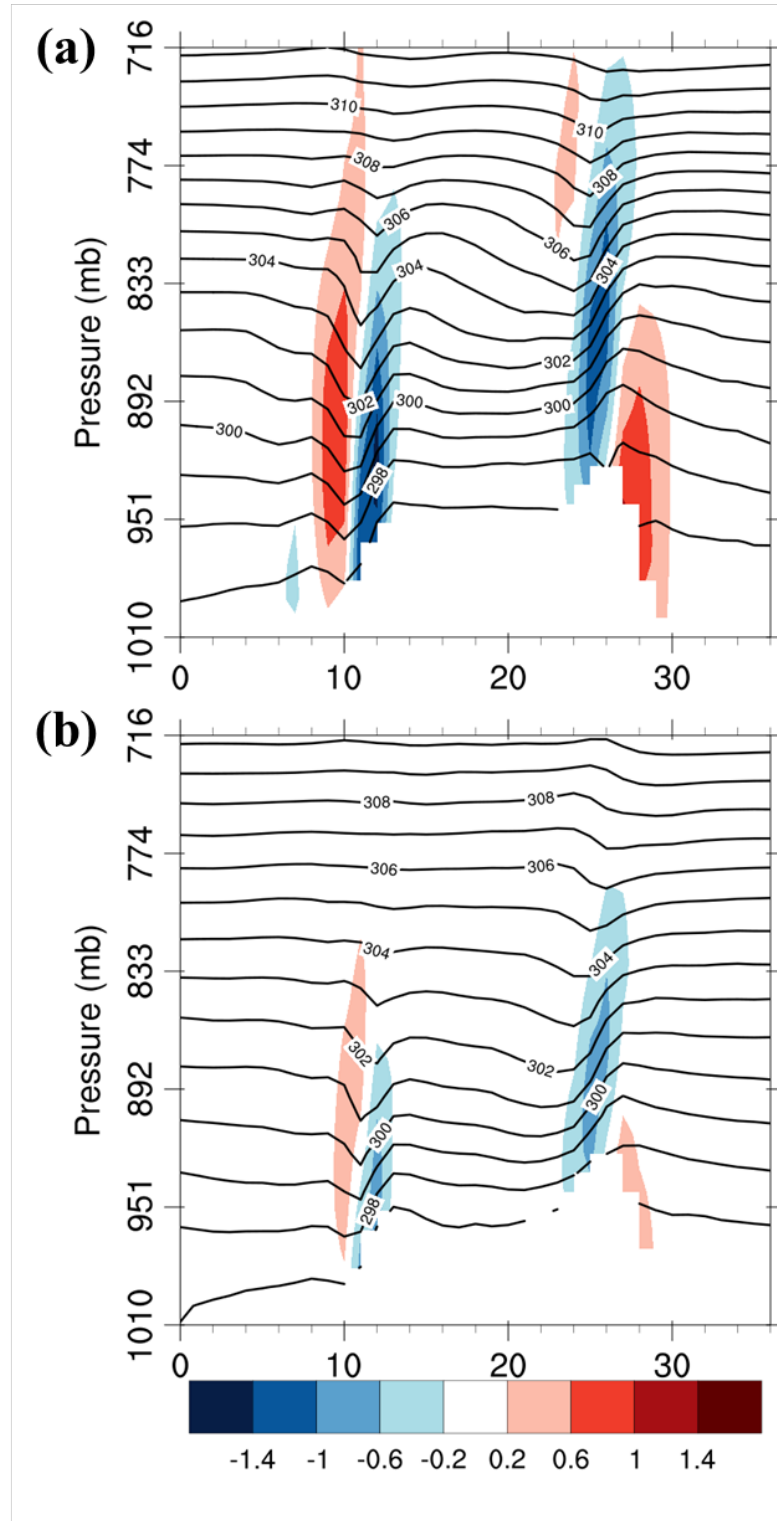


Fig. 3.15 The vertical cross-section along the northeast–southwest line in Fig. 3.1 of simulated potential temperature (K, contour) and simulated vertical motion (m s^{-1} , color shading) at 0500 HST for (a) strong trades and (b) weak trades.

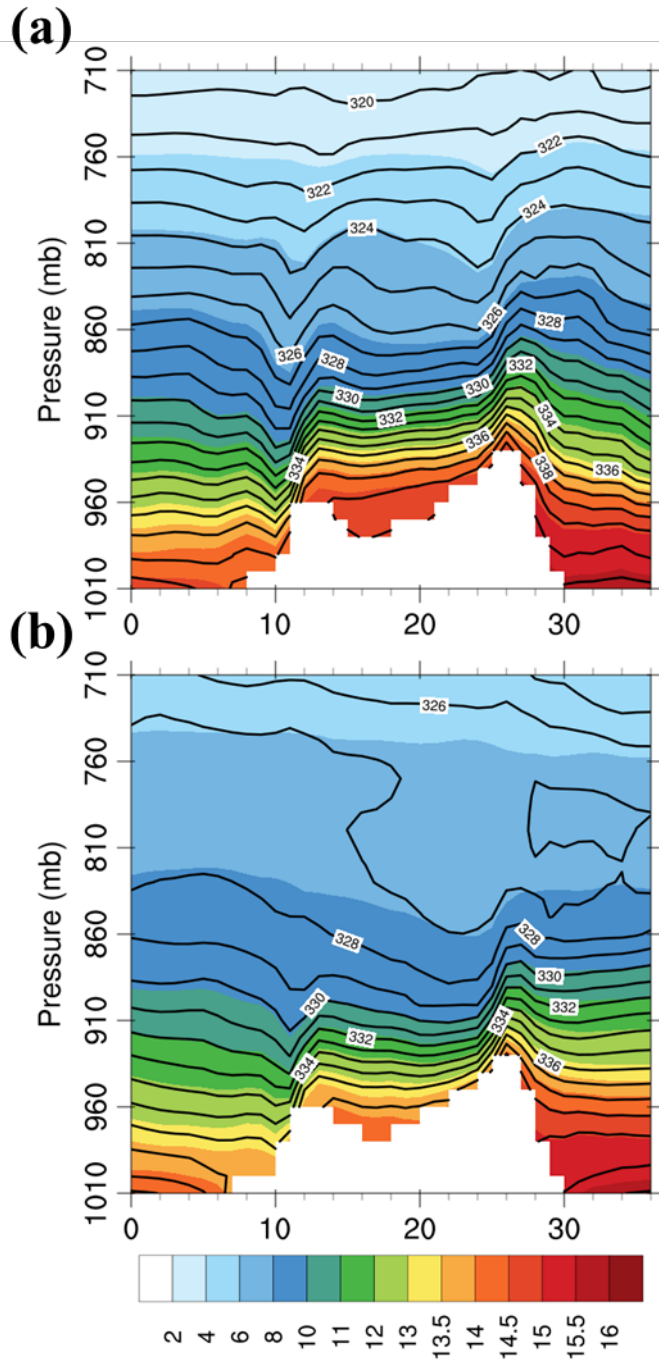


Fig. 3.16 Same as Fig. 3.15, but shading is mixing ratio (g kg^{-1}) and contours are equivalent potential temperature (K).

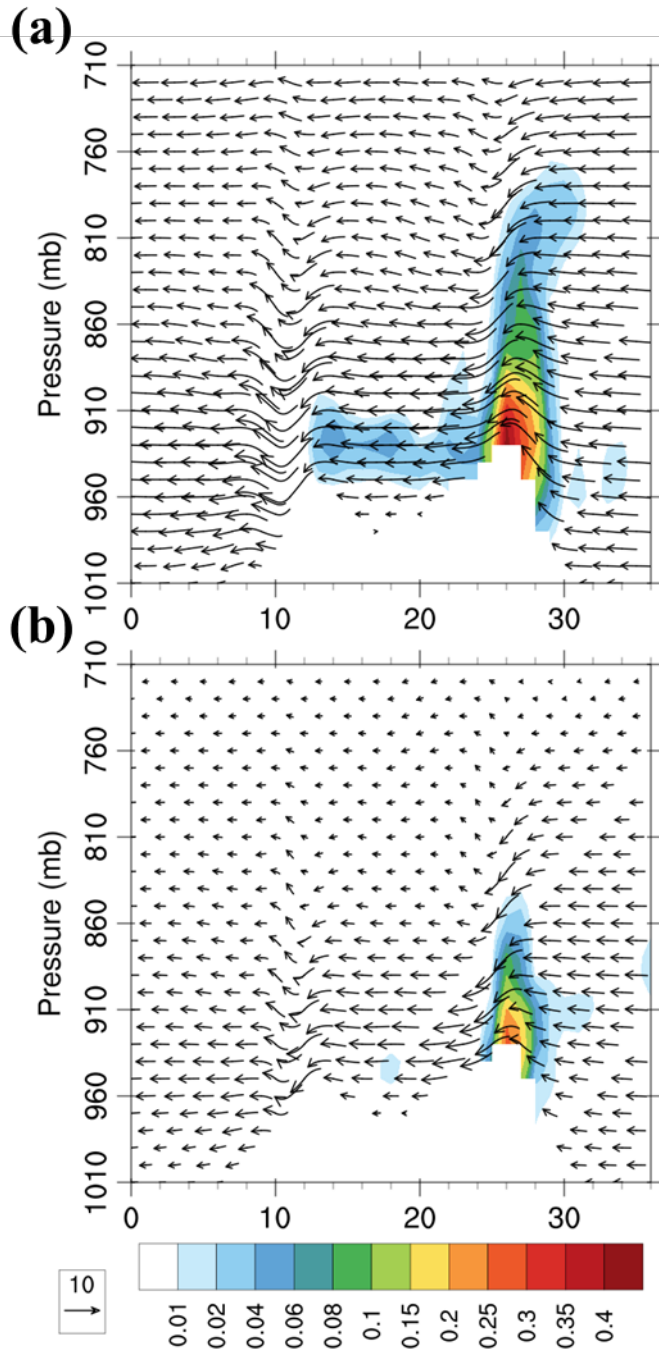


Fig. 3.17 The vertical cross-section along the northeast–southwest line in Fig. 3.1 of simulated cloud water content (g kg^{-1} , color shading) and simulated zonal and vertical wind (arrow, u : m s^{-1} , w : cm s^{-1}) at 0500 HST for (a) strong trades and (b) weak trades.

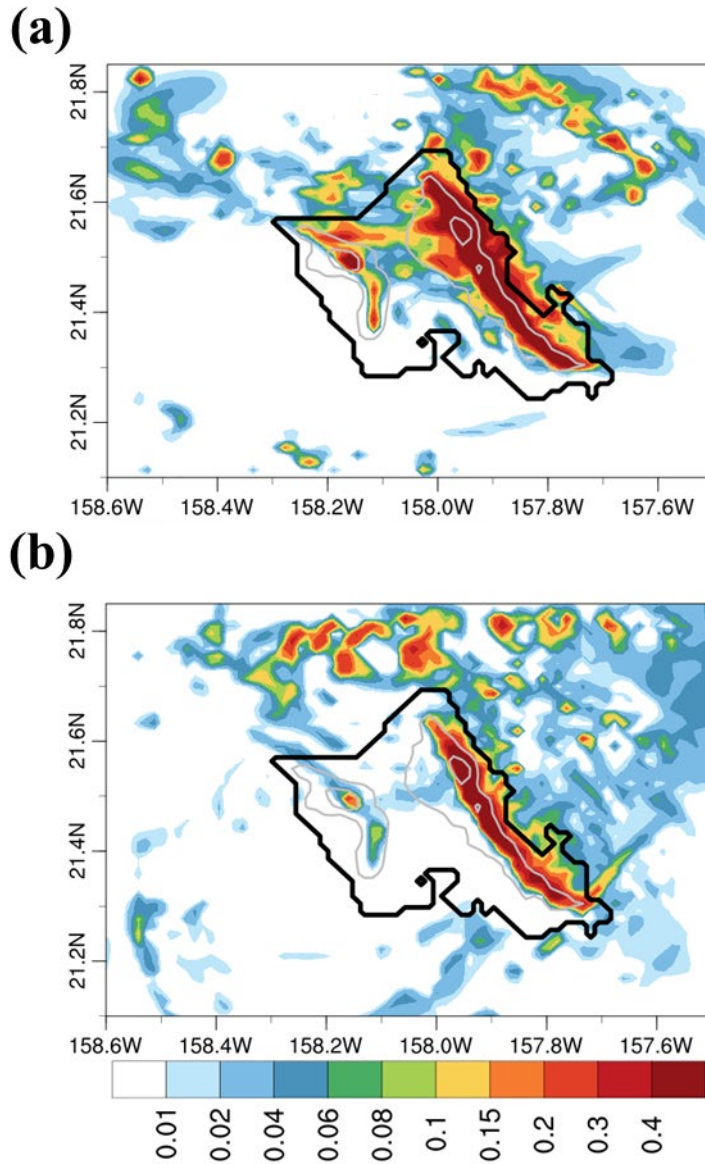


Fig. 3.18 Vertically integrated cloud water content (mm, shading) at 0500 HST for (a) strong trades and (b) weak trades.

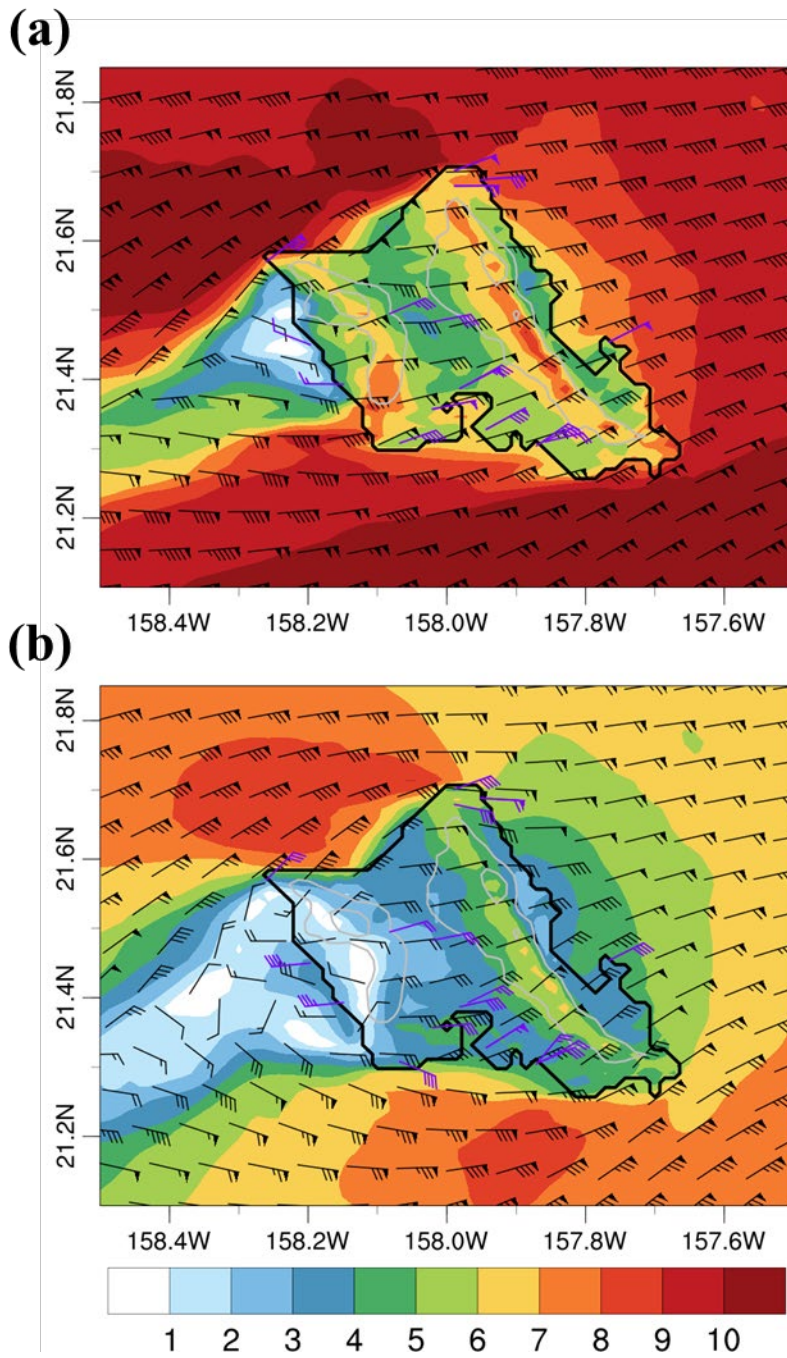


Fig. 3.19 Same as Fig. 3.6, but at 1400 HST.

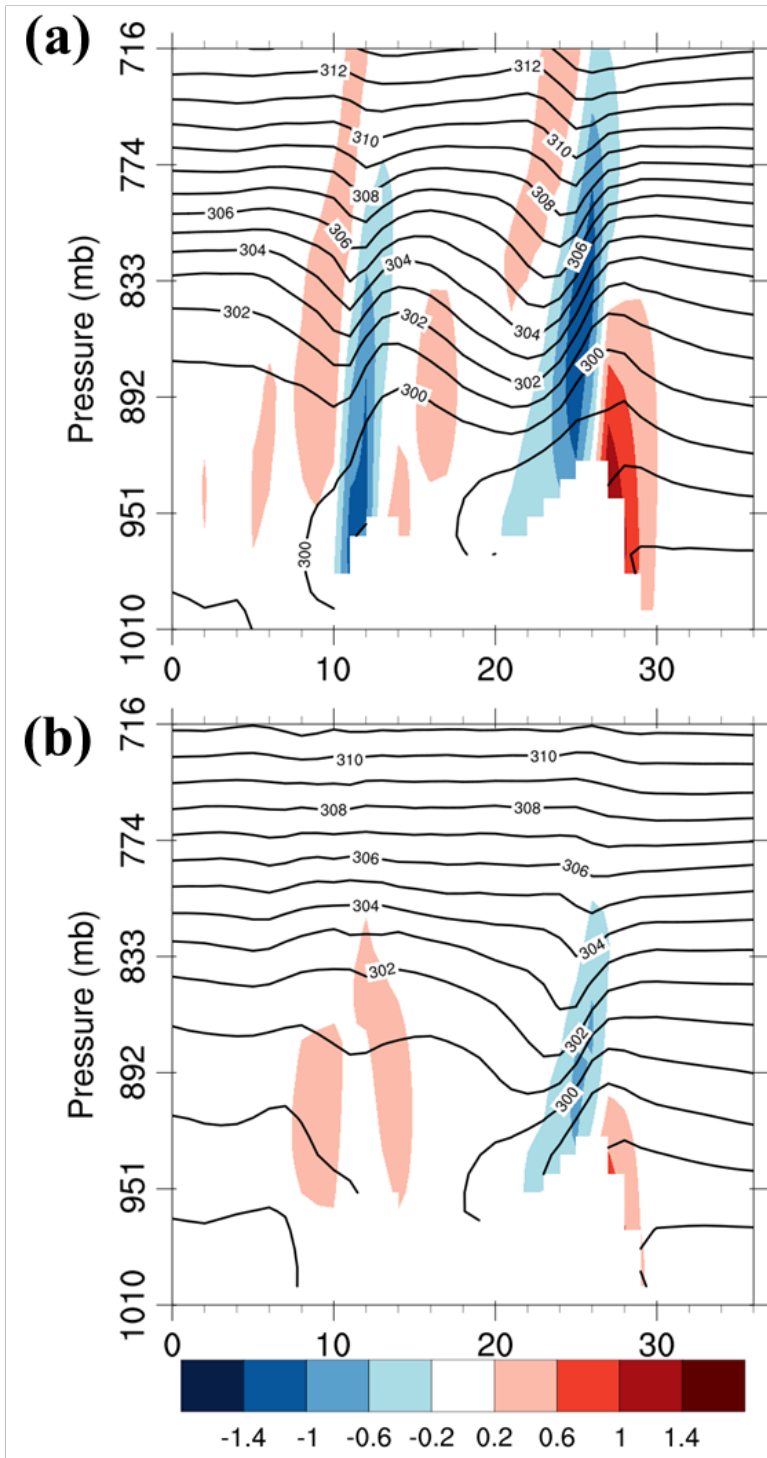


Fig. 3.20 Same as Fig. 3.15, but at 1400 HST.

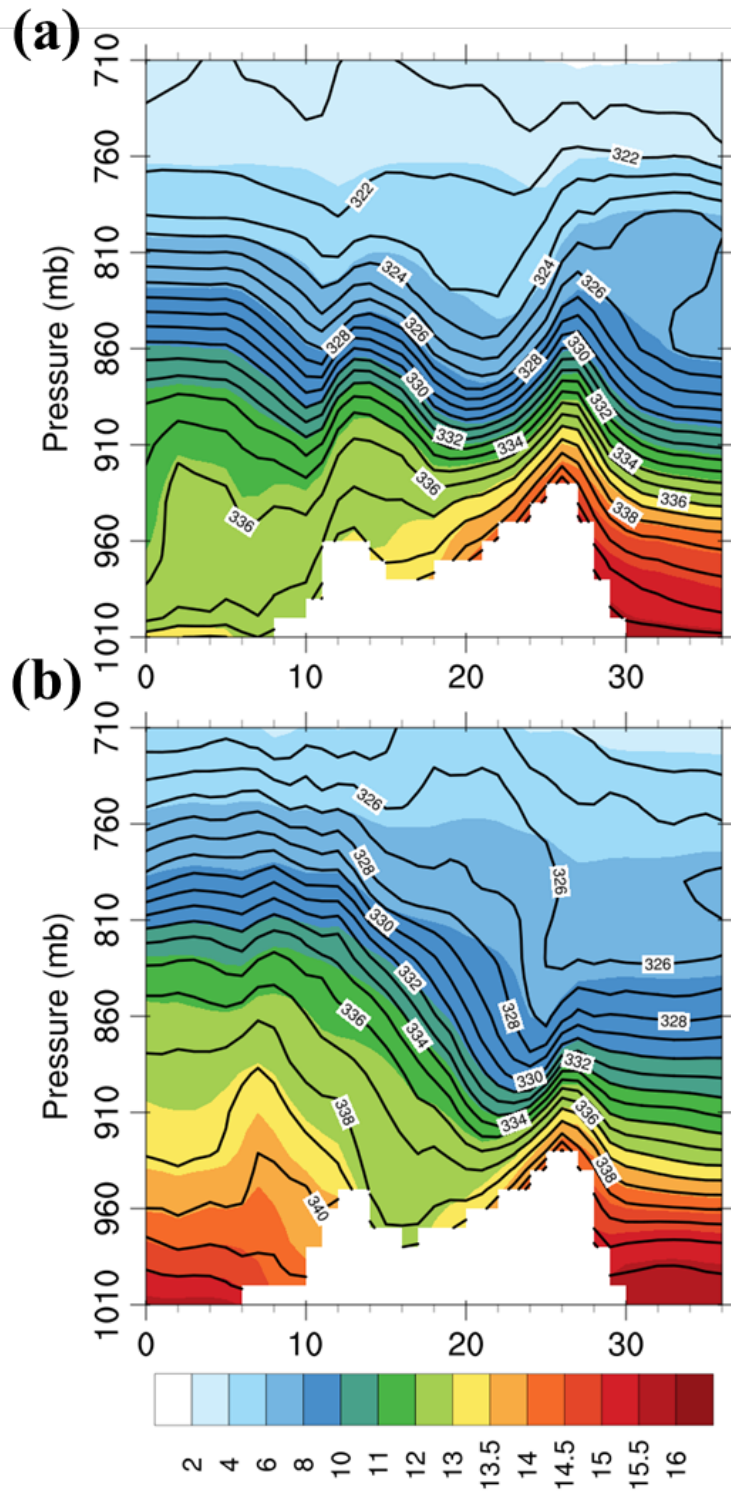


Fig. 3.21 Same as Fig. 3.16, but at 1400 HST.

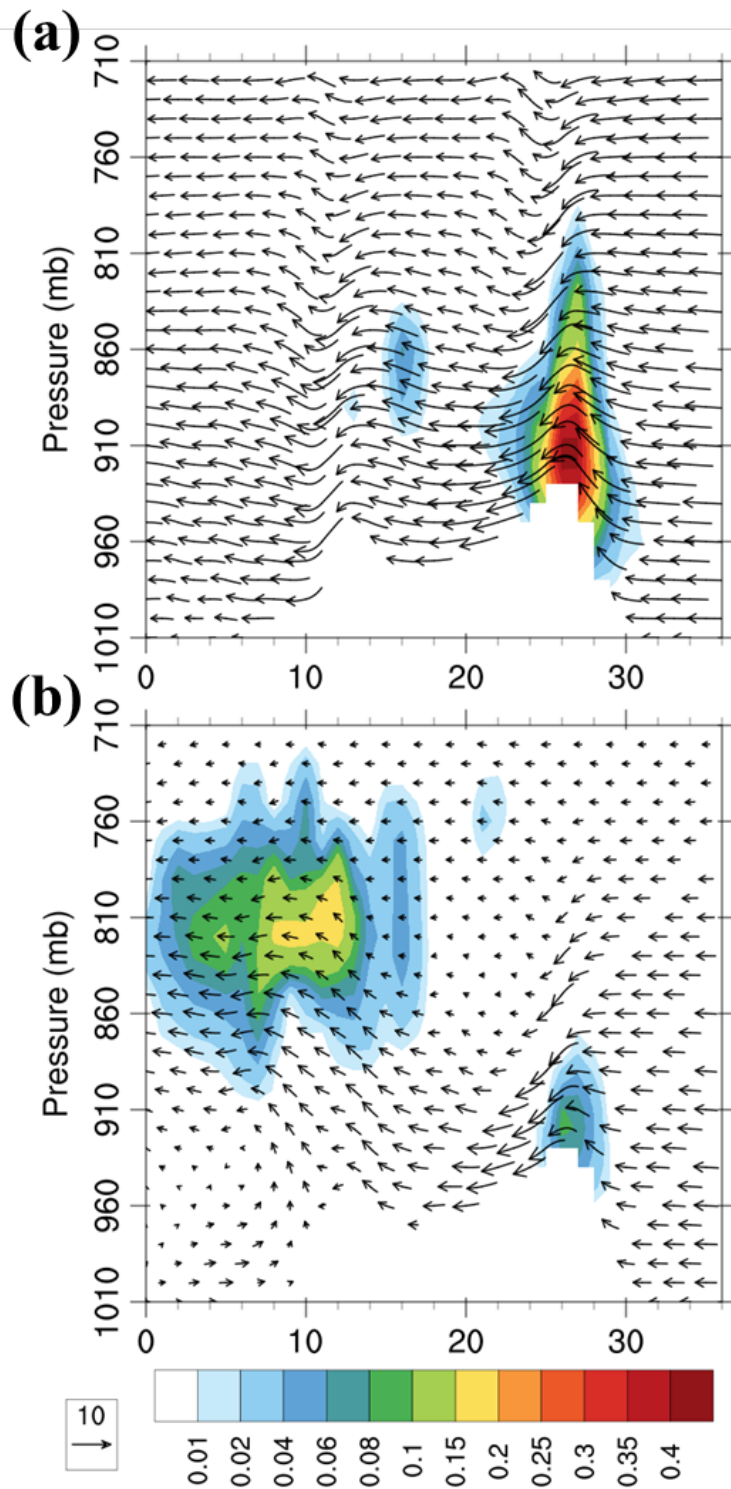


Fig. 3.22 Same as Fig. 3.17, but at 1400 HST.

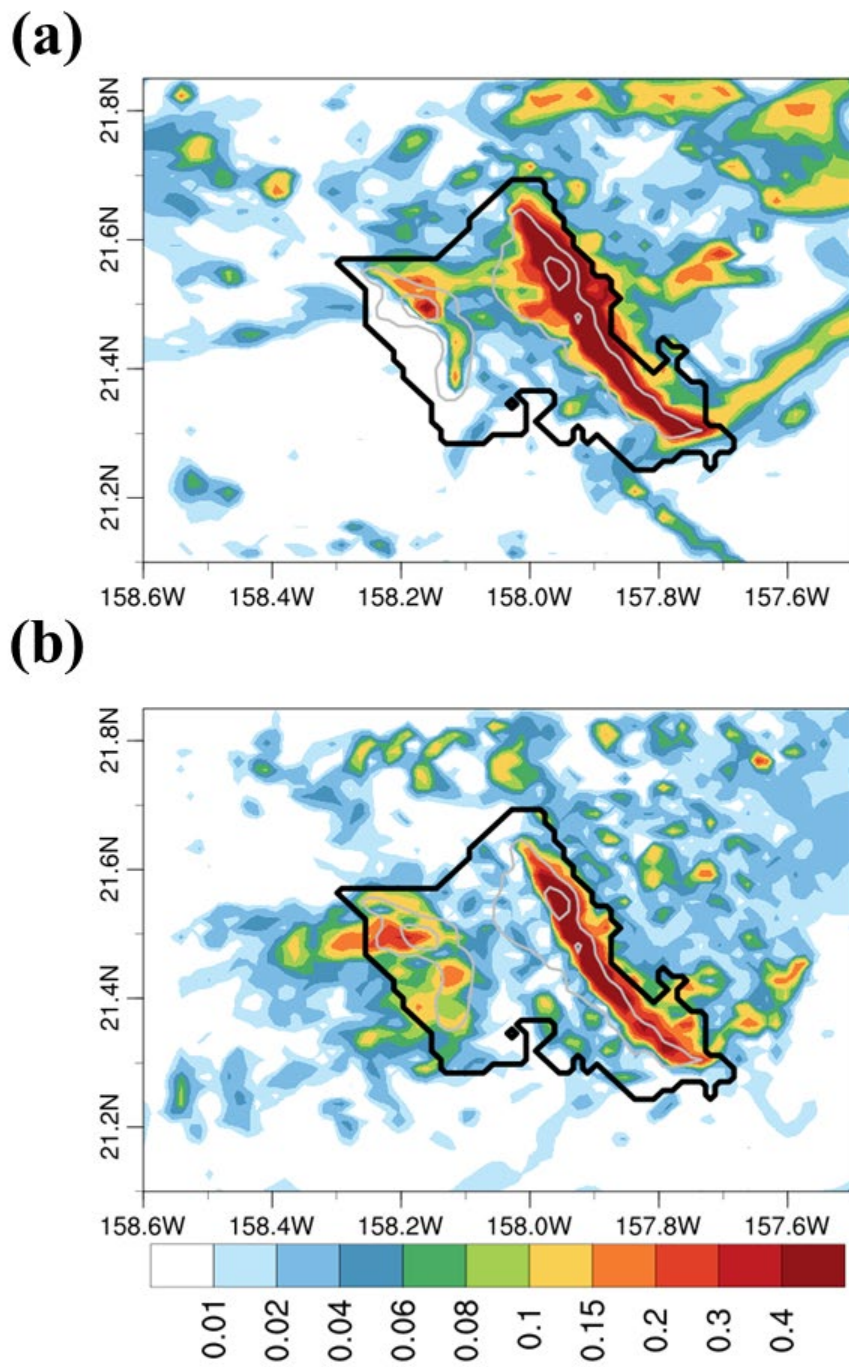


Fig. 3.23 Same as Fig. 3.18, but at 1400 HST.

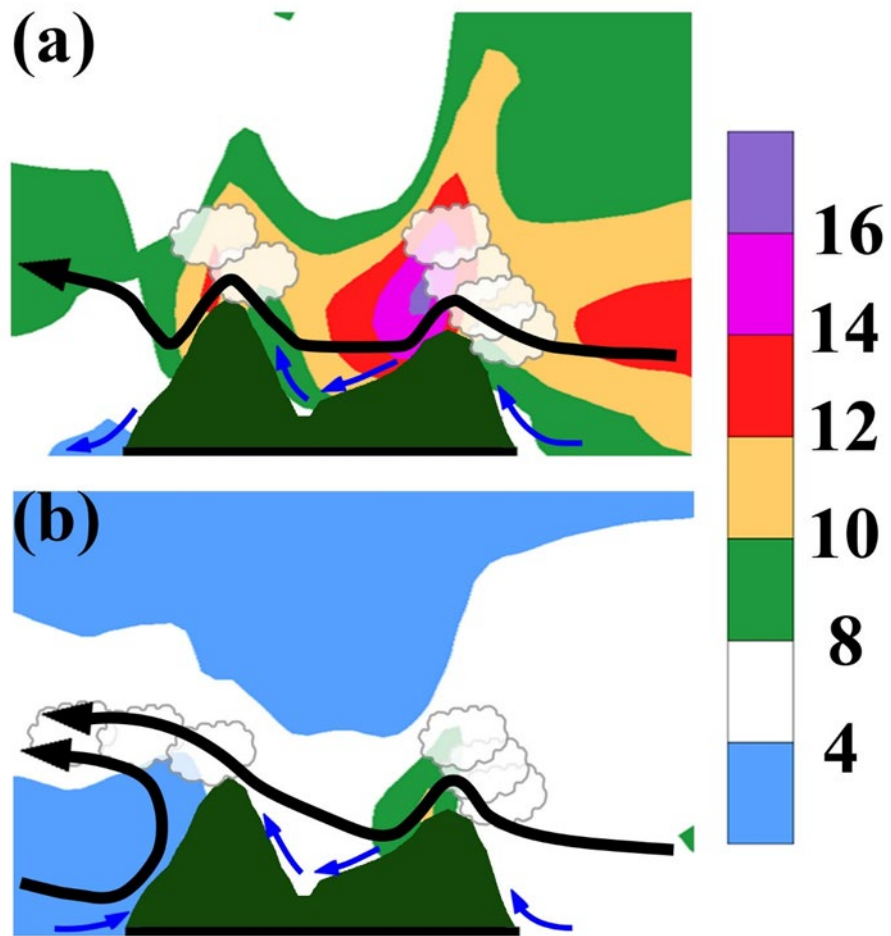


Fig. 3.24 A schematic diagram of the cloud formation at 1400 HST over O'ahu under (a) strong trade wind and (b) weak trade wind conditions. Color shading represents horizontal wind speed (m s^{-1}), black arrows represent the mean streamline above the mountaintops, and blue arrows represent surface wind.

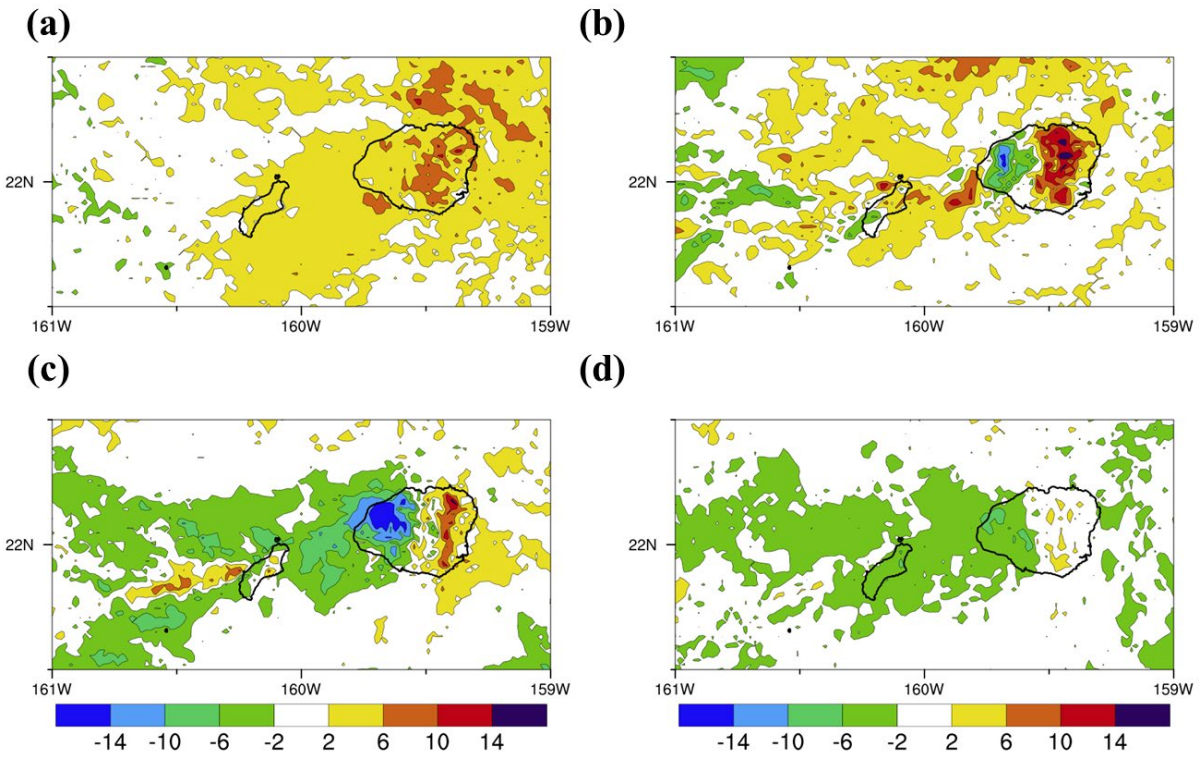


Fig. 3.25 Same as Fig. 3.13, but for Kaua'i and Ni'ihau.

Chapter 4 Heavy Rainfall Events over Central O‘ahu under Weak Wind Conditions during Seasonal Transitions

4.1 Introduction

The island of O‘ahu has a small land surface area (1536 km²) with a horizontal dimension about 40 km. The terrain of the island is dominated by two narrow, nearly parallel mountain ranges, the Ko‘olau Mountain Range and the Waianae Mountain Range, with peaks of 944 and 1227 m, respectively and relatively flat terrain over Central O‘ahu. Both mountain ridges are oriented in the northwest-to-southeast direction with tops well below the typical base of the trade wind inversion over the open ocean (~1.9 km) (Bingaman 2005; Winning et al. 2017). Throughout the year, the northeast trade winds (7–10 m s⁻¹) have a maximum chance of occurrence (93%) during August (Schroeder 1993). During the cool season (November- April), the surface winds upstream of Hawaii shift to a more easterly direction with slightly slower wind speed and is frequently interrupted by synoptic disturbances, including cold fronts, upper-level troughs, and Kona storms (subtropical cyclones) (Blumenstock and Price 1967).

Heavy rainfall events are major meteorological disasters that occur around the globe. Heavy rainfall events in diverse locations share essential similarities: copious moisture and destabilization effects due to lifting (e.g., Ogura et al. 1985; Wang et al. 1985; Kodama and Barnes 1997; Lin et al. 2001; Chiao et al. 2004; Medina et al. 2005). One of the greatest problems facing weather forecasters in the Hawaiian Islands is the prediction of heavy rains and attendant flash floods (Schroeder 1977). Except heavy rainfall caused by tropical storms, these events typically occurred

during the winter storm season (Haraguchi 1977; Dracup et al. 1991; Cram and Tatum 1979) associated with synoptic disturbances (Blumenstock and Price 1967; Wang et al. 1998). These events are localized in nature related to terrain and local winds (e.g., Schroeder 1977; Kodama and Barnes; Zhang et al. 2005; Tu et al. 2011).

Occasionally, during the transition seasons between the cool and warm seasons (June and October), short-lived localized heavy rainfall events may form over Central O‘ahu in the afternoon hours under the variable wind ($< 3 \text{ m s}^{-1}$) conditions defined by Hartley and Chen (2010), using reanalysis data at an upstream point to classify these wind conditions. Despite their short duration (~ 3 hours), these events may cause small stream and drainage ditch flooding and landslides, which can disrupt traffic and result in property damage (NCEI 2017). In contrast to heavy orographic precipitation events during the winter storm season (e.g., Schroeder 1977; Tu and Chen 2011), these events occur over the semi-arid Central O‘ahu where the terrain is relatively flat. With a horizontal island dimension of ~ 40 km, these localized events are poorly predicted by operational global models with a 0.25° grid size. According to the archived forecast issued by the National Weather Service (NWS) Honolulu office, afternoon showers over the island interior were only predicted on 5 of 13 days (case selection in Section 4.2). A better description and understanding of the physical processes leading up to the initiation of this type of event is needed in order to aid short-range weather forecasting.

Over isolated mountainous tropical and subtropical islands, heavy local showers are frequent due to terrain and local circulations. Rainfall modulated by terrain and locally driven diurnal winds over subtropical islands has been studied in various locations around the world, including over islands in the Maritime Continent (Qian 2008), Puerto Rico (Jury and Chiao 2013), Taiwan (e.g., Yeh and Chen 1998; Kerns et al. 2010, Ruppert et al. 2013), Tiwi Islands (Carbone et al. 2000),

Dominica (Smith et al. 2012; Wang and Kirshbaum 2015) and others. Carbone et al. (2000) showed that all mesoscale convective systems over the Tiwi Islands are initiated by a confluence of island-scale sea breeze fronts or convergence among sea breezes and convective cool pools. Jury and Chiao (2013) simulated lee-side thermally driven circulations and afternoon thunderstorms under trade wind conditions. They showed that the occurrences of afternoon convection over the western slopes of Puerto Rico are driven by thermal forcing by the land surface. Their model results suggest that a dry bias in the initial soil moisture may result in stronger sea-breeze convergence and stronger orographic lifting by the western leeside slopes. Wang and Kirshbaum (2015) simulate thermally forced convection due to elevated heat sources over Dominica (mountaintops ~ 1.5 km) during a weak wind day ($< 2 \text{ m s}^{-1}$). Their sensitivity tests confirm that thermal forcing drives the convection over the island interior due to the development of onshore/upslope flows. The lifting is caused by a combination of orographic lifting by the upslope flow and convergence in the island interior (their Fig. 9).

Under summer trade-wind weather, there are considerable variations in airflow, thermodynamic variables, and rainfall throughout the diurnal cycle despite O'ahu's relatively small size (Hartley and Chen 2010; Nguyen et al. 2010). Rainfall occurrences in the vicinity of the Ko'olau Mountain Range have a nocturnal maximum, which is attributed to a combination of nocturnal cloud-top radiative cooling and orographic blocking when the land surface is the coldest (Nguyen et al. 2010; Hartley and Chen 2010). During the daytime hours, sea breezes develop along leeside of the Wai'anae coast, especially under weak trades (Hartley and Chen 2010). Over Central O'ahu between the Ko'olau Mountains and the Wai'anae Mountains, winds are calm with low hourly rainfall frequency ($< 5\%$) in the afternoon hours and very little rainfall ($< 1 \text{ mm day}^{-1}$).

The main goals of this research are to identify related favorable and common large-scale settings, and island-scale features and circulations for Central O‘ahu’s heavy rainfall events that occurred during the seasonal transitions (June and October). This paper is organized as follows. The data and method are given in Section 4.2. Section 4.3 presents the common favorable synoptic environment for this type of event by reviewing the large-scale settings for each event in our composite analyses. The model results are validated using surface (Table 4.2) and radar observations. The simulated evolution of these events is compared with the composite surface and radar observations. A case study is presented in Section 4.4 which provides additional insights on the physical processes involved in the development of this type of event, including the favorable large-scale settings, local conditions, and storm evolution. In Section 4.5, model simulations with sensitivity tests allow us to study the physical processes involved in the initiation and maintenance of this event in sufficient detail including the mixed layer growth over Central O‘ahu after sunrise and before the onset of convection, the level of saturation that is first simulated, the effects of daytime land surface heating and orographic effects on the formation of this event. The results and findings from this study are summarized in Section 4.6.

4.2 Data and Methodology

The CFSR data at an upstream point (21.5°N, 157.5°W, black star in Fig. 4.1b) of O‘ahu, which is unaffected by orography or by convection over the island, is selected to assess the environmental conditions and instability. The GOES infrared (IR) images are used to identify the initiation of the convective events. The archived Doppler radar observations from the Moloka‘i station (Fig. 4.1a, blue dot) from the National Centers for Environmental Information (NCEI) depict the horizontal distribution of the column-maximum reflectivity from the volume scan within the range of the radar every 5–7 minutes. There are 26 NWS Honolulu Forecast Office (HFO)

Hydronet stations with rain gauge data over O‘ahu from 2000–2015 (Fig. 4.1b, blue dots) (<http://www.prh.noaa.gov/hnl/hydro/hydronet/hydronet-data.php>). The Hydronet rain gauge network reports measurements at 15-min intervals with a resolution of 0.254 mm (0.01 in.). The hourly radar quantitative precipitation estimates (QPE) from NCEI are also available. Observations of surface wind speed, surface wind direction, air temperature, and dewpoint are from the MesoWest cooperative network (Horel et al. 2002) and are quality controlled using the MesoWest data quality ratings (Splitt and Horel 1998), with further subjective checks for spatial and temporal consistency during manual analysis. MesoWest observations typically represent averages over the reporting interval, which can vary from 5 minutes to an hour. The stations with observations within 15 minutes of and nearest to the verification times are used for model validation (Fig. 4.1b, crosses).

From 2000 to 2015, a total of 33 daytime (from 1000 to 1600 HST) heavy rainfall events were reported over O‘ahu in the storm events database (NCEI 2017) during the warm season (May–October). The definition of heavy rainfall follows the NWS criteria from the Storm Data preparation directive (NWS 2016): “unusually large amount of rain that led to damage”. The GOES IR images and radar reflectivities from the Moloka‘i radar are reviewed to select days in which heavy rain formed over Central O‘ahu. Hurricanes and days with fronts are removed from our samples. Days with wind speeds greater than 3 m s^{-1} at our upstream point (21.5°N , 157.5°W ; gray star in Fig. 4.1b) from the CFSR (CFSv2) 1000-hPa level data at 1200 UTC are also excluded. Only 13 days between June and October satisfy our criteria (Table 4.1). These events occurred mainly during the transitions between warm and cool seasons. There is no clear correlation between the occurrence of local heavy rainfall and large-scale climate variability (e.g., El Niño–Southern Oscillation).

This chapter presents 3 experiments denoted as CTRL, NoOrog, and NoFlux to study the physical processes involved in the occurrence of afternoon heavy rainfall events. The CTRL run uses the full model physics, high-resolution model terrain, updated soil temperature, soil moisture, and surface temperature from previous simulations. The NoOrog run has the same updated lower boundary conditions over the island as the CTRL run but reduces island topography to sea level to test the effects of orographic blocking and lifting. The NoFlux run is similar to the CTRL run, but the surface heat and moisture fluxes are turned off to test the effects of thermal forcing by the land surface

4.3 A Composite Study

In this section we examine the general characteristics of our 13 heavy rain events using composites. We also assess the overall accuracy of our numerical simulations through a quantitative comparison with both surface station data and radar reflectivities.

4.3.1 Synoptic Conditions

To better understand the favorable conditions for these rare events, a synoptic analysis of a 13-day composite is presented. The pre-cursors of this type of event are an upper-level shortwave trough coming down from the northwest with a blocking high over the mid-Pacific in mid-latitudes, a weak surface wind shear line, a moisture tongue with TPW > 40 mm over the Hawaiian region, and weak low-level winds.

At the 300-hPa level, the composite synoptic geopotential height exhibits an omega blocking pattern. A shortwave trough was located over the Hawaiian Islands (Fig. 4.2a). At the surface, a shear line and the associated axis of high TPW (> 40 mm) were located over the Hawaiian Islands (Fig. 4.2b). The composite Skew T -log p plot for all 13 days at the designated

upstream point (Fig. 4.2c) shows that the pre-storm environmental conditions are characterized by a) a conditionally unstable atmosphere (below 500 hPa) with the equilibrium layer (EL) at 250 hPa, b) absence of a trade wind inversion, c) a deep moist layer with relatively high (> 40 mm) TPW, and CAPE ~ 382 J kg $^{-1}$ (Fig. 4.2c). CAPE is calculated based on temperature and mixing ratio of an air parcel originated from the 1000-hPa level. The mean winds at low levels are weak southeasterlies (< 3 m s $^{-1}$) (Fig. 4.2c).

4.3.2 Observational Analysis

From the 13-day composite analysis, weak onshore flows (~ 1 m s $^{-1}$) are observed over O‘ahu’s coasts at 0900 HST (Fig. 4.3a). At this time, the stations over Central O‘ahu exhibit weak winds. At 1000 HST, the onshore flows over the southern coast increase to 3–4 m s $^{-1}$ (Fig. 4.3b). Prior to the onset of the convection (~ 2 –3 hours) over Central O‘ahu, the onshore flows from the northwestern and the southeastern coasts converge over Central O‘ahu (Figs. 4.3c–d). At 1600 HST, weakened onshore flows over the northern and southern coasts (~ 1.5 m s $^{-1}$, Fig. 4.3i) are still observed.

Error statistics for hourly 2-m air temperature, 2-m dewpoint, and 10-m winds for these events from 0900–1100 for the 13 days are given in Table 4.1. Both model bias and observational uncertainties exist. The magnitudes of both the MAE (1.5°C) and the RMSE (1.8°C) for all stations are comparable to Nguyen et al. (2010) using the MM5 model. The error statistics of dewpoint at 15 stations (dewpoint measurements at MKGH are only 11 in total) show that the model systematically underestimates dewpoint (bias from -0.1 to -2.9°C) with RMSE values ranging from 0.8 to 3.3°C. Station MKGH has the largest errors in temperature and dewpoint. A possible reason for this is the unusually high daytime surface temperatures which occurred during

4 June–8 June 2003. The highest recorded temperature was $\sim 36^{\circ}\text{C}$ at 1400 HST 8 June, which is unrealistic.

For surface winds, the largest RMSE occurred at stations located over the island corners (KFWH, PHJR, and KKRH), where the tip jet effect is most significant. Other stations show that the RMSE of surface wind speed varies from 0.8 to 2.3 m s^{-1} . Wind errors at the stations over Central O‘ahu and the southern coast are relatively small ($\text{RMSE} < 1.8\text{ m s}^{-1}$). Overall, the simulated surface winds are in reasonable agreement with observations.

High-resolution models rarely simulate convection exactly at the right place, and heavy rainfall may occur at the region without any rainfall observations; for example, 12 October and 14 October 2013, there were no rainfall observations over Central O‘ahu. Thus, to verify the timing and the location of simulated convection, area averages of the composited observed radar reflectivities and the composited simulated radar reflectivities are calculated within the box. Fig. 4.4 shows the scatter plot of area-averaged observed radar reflectivities and area-averaged simulated radar reflectivities at various times of the day. Overall, the model slightly overestimates reflectivities during 1000–1100 HST and 1600–1700 HST (Fig. 4.4). The time series plots of observed and simulated area-averaged radar reflectivities attest that most of these events are reasonably well simulated (Fig. 4.5).

4.3.3 Numerical Simulations

Based on the observational analysis of the 13 days, island-scale sea breezes/onshore flows are observed prior to the onset of convection over Central O‘ahu. Fig. 4.6 shows that the prevailing wind is weak southeasterly. At 1000 HST, onshore flows $\sim 2\text{--}3\text{ m s}^{-1}$ are simulated over O‘ahu’s coasts (Fig. 4.6b). At 1100 HST, the speed of the onshore flows over the northern and southern coasts increases to $4\text{--}5\text{ m s}^{-1}$ (Fig. 4.6c). Radar echoes of $\sim 30\text{ dBZ}$ are simulated over the two

mountain ranges and Central O‘ahu (Fig. 4.6c). During 1200–1300 HST, the widespread radar echoes are simulated over the island interior (Figs. 4.6d–e). At 1400 HST, radar echoes > 40 dBZ are simulated over Central O‘ahu (Fig. 4.6f). These persist for around 2 hours and dissipate around 1700 HST (Figs. 4.6g–i).

Both observations and simulations show that these heavy rainfall cases start with light showers over the Ko‘olau and the Wai‘anae Mountains with onshore flows from the eastern and western coasts at 1000 HST. Subsequently, the onshore flows from the northwestern and southeastern coasts converge over Central O‘ahu, initiating the Central O‘ahu storm with a northeast–southwest elongated feature at 1100 HST. The simulated radar echoes at the initial stage are consistent with the observed patterns, except the simulated reflectivities are slightly overestimated. Observations show that these short-lived heavy rainfall events end by 1600 HST. However, the model simulated heavy rainfall persists about one hour longer (~ 1700 HST) than observations. Furthermore, the area of simulated maximum radar reflectivities at 1400 HST over Central O‘ahu is slightly smaller than in observations.

4.4 A Case Study of the Central O‘ahu Storm

4.4.1 Synoptic Conditions

At the 300-hPa level, the synoptic patterns on 2 June 2003 exhibit an unusual Rex blocking pattern (Rex 1950), which evolves into an omega-blocking pattern on 6 June (not shown). On 8 June, the upper-level trough (T) associated with the blocking pattern is in the vicinity of the Hawaiian Islands (Fig. 4.7a). Furthermore, the northerly flow behind the upper-level trough (T) advects cold air to the State (Fig. 4.7a). At 0200 HST, the horizontal distribution of TPW has a

northeast–southwest maximum axis (> 43 mm) ahead of the trough northwest of O‘ahu, reaching O‘ahu around 1400 HST (Fig. 4.7b).

The Skew T – $\log p$ diagram at a point upstream of O‘ahu (21.5°N , 157.5°W , black star in Fig. 4.1b) from CFSR at 1400 HST 8 June indicates weak southeasterly winds (~ 3 m s $^{-1}$) at low levels and an absence of the typical trade wind inversion (Fig. 4.7c). Winds are east/northeasterlies (~ 5 m s $^{-1}$) between the 900-hPa and 700-hPa levels, becoming northwesterlies/northerlies (~ 15 m s $^{-1}$) above the 700-hPa level. The temperature profile is close to pseudo-adiabatic above the 500-hPa level with a positive (907 J kg $^{-1}$) CAPE. The equilibrium layer (EL) is at 200 hPa. The storm environment is consistent with common features found in the composite analyses.

4.4.2 Surface Observations

At 0700 HST, offshore flows were observed at stations near O‘ahu’s coast (Fig. 4.8a). Over the island interior, mountain winds were evident on the eastern slopes of the Wai‘anae Mountains and the western slopes of the Ko‘olau Mountains (Fig. 4.8a). At SCBH, which is in the eastern foothills of the Wai‘anae Mountains, the southwesterly katabatic flow becomes northerly anabatic flow after 0900 HST as a result of daytime land surface heating (Fig. 4.8c). At PHNL, the offshore flow at 0800 HST is replaced by sea breeze after 0900 HST (Fig. 4.8c). At O‘ahu’s coastal stations, the offshore flows before 0700 HST (Fig. 4.8a) shift to onshore flows well before 1100 HST (Fig. 4.8e).

4.4.3 Storm Evolution

At 1100 HST, weak, isolated radar echoes were detected on the northwestern leeward slopes of the Ko‘olau Mountains (Fig. 4.8e). At 1200 HST, an arc-shaped radar echo was observed over Central O‘ahu (Fig. 4.8f). Radar echoes also developed over the northwestern foothills of the

Ko‘olau Mountains (Fig. 4.8f). At 1300 HST, radar echoes covered most of Central O‘ahu (Fig. 4.8g) and moved southwestward (Figs. 4.8h–i). At 1500 HST, the strongest radar echoes were off the Wai‘anae coast (Fig. 4.8i).

Based on GOES IR imagery, a low-level cloud area associated with the weak shear line, with cloud-top brightness temperatures < 280 K, passed O‘ahu from the northwest to the southeast between 1000–1300 HST (Figs. 4.9d–g). At 1200 HST, convective clouds with cloud-top brightness temperatures of ~ 274 K were observed over Central O‘ahu (Fig. 4.9f). These clouds developed into deep convection with brightness temperatures of ~ 256 K at 1300 HST (Fig. 4.9g) and radar echo tops of 7 km (not shown). At 1400 HST, cold clouds with cloud-top temperatures < 220 K covered most of Central O‘ahu (Fig. 4.9h). The deepest echoes ~ 10 km occurred over the Wai‘anae Mountains when the storm moved southwestward (not shown). During the later stages, the cold cirrus clouds moved southeastward (Fig. 4.9i) with the upper-level northwesterly winds (Fig. 4.7c).

4.5 Numerical Simulations of the 8 June 2003 Case

4.5.1 The Evolution of the Mixed Layer

The simulated Skew T – $\log p$ chart over Central O‘ahu (Fig. 4.1b, black star) at 0700 HST on 8 June indicates weak low-level southeasterly winds (< 2 m s^{-1}) with no CAPE (Fig. 9a). At 1100 HST, the environment is saturated between 860 hPa and 800 hPa with CAPE ~ 555 J kg^{-1} . The unusually high value of TPW ~ 40 mm is higher than the climatological value in June (31–32 mm). Weak northerly winds (< 2 m s^{-1}) are present below 860 hPa (Fig. 4.10b), becoming east-northeasterly between 840 hPa and 700 hPa, turning to north-northwesterlies above the 700-hPa

level. The vertical wind profile and the evolution of radar echoes suggest that precipitation is advected by the east-northeasterly flows above 840 hPa to the southwestern coast (Fig. 4.8i).

The evolution of the mixed layer after sunrise is depicted by the simulated vertical profiles of thermodynamic variables over Central O‘ahu. At 0700 HST, the nocturnal stable layer is eliminated (Figs. 4.11a–b) after sunrise. From 0900–1100 HST, low-level potential temperature (θ) continues to increase with the deepening of the mixed layer (Fig. 4.11a). At 1100 HST, the mixed layer top is ~ 1.5 km above sea level with homogenous θ below (~ 300 K) (Fig. 4.11a). From 0700 to 0800 HST, the mixing ratio in the lowest layer (< 0.7 km) increases (Fig. 4.11c) as the katabatic winds are replaced by northwesterly onshore flow (Fig. 4.8a). From 0800–1100 HST, the onshore flow brings in maritime air with higher mixing ratio as the mixed layer deepens (Fig. 4.11c). Convective inhibition (CIN) is zero after sunrise and CAPE over Central O‘ahu reached a maximum (566 J kg^{-1}) at 1000 HST. In the meantime, the LCL is raised to the 869-hPa level after the development and deepening of the mixed layer (Fig. 4.11e). Saturation between 1.4–2 km is simulated at 1100 HST (Fig. 4.11d), which is above both the LCL and LFC ~ 876 hPa (Fig. 4.11e)

In summary, the vertical profiles of the simulated thermodynamic variables over Central O‘ahu show that after sunrise, the mixed layer deepens with increasing temperature and moisture due to surface heat and moisture fluxes. Then, the land–sea thermal contrast drives sea breeze/onshore flows, which bring in maritime air over Central O‘ahu (Figs. 4.8a–c). In the meantime, the LCL (~ 876 hPa) (Fig. 4.11e) is just below the top of the mixed layer (~ 850 hPa) (Fig. 4.10b) with saturation between the LCL and 2-km in height (Fig. 4.11d). Saturation occurring above the mixed layer top is caused by rising motion over Central O‘ahu.

4.5.2 The Evolution of Simulated Surface Winds and Vertical Motion

The vertical motion at the surface due to orographic lifting is defined as

$$w_{sfc} = \vec{v} \cdot \nabla h \quad (4.1)$$

where \vec{v} is the simulated surface horizontal wind (m s^{-1}) and h is the model terrain height (m). In this section, the horizontal distributions of the vertical motion at the surface due to orographic lifting are compared with the horizontal distributions of vertical motion at the 900-hPa level which is above the ridgetop.

At 0600 HST, winds along O‘ahu’s coasts have an offshore component with mountain winds over the lee side of the Ko‘olau Mountains and the western slopes of the Wai‘anae Mountains (Fig. 4.12a). Three hours after sunrise, the simulation shows onshore flows along all coasts with valley winds over Central O‘ahu, consistent with observations (red barbs) (Fig. 4.12b). At 1000 HST, northwesterly sea breezes from the north shore and southeasterly sea breezes from the southern coast converge over Central O‘ahu with vertical motion $\sim 1 \text{ m s}^{-1}$ at the 900-hPa level (Fig. 4.12c). At 1100 HST, the vertical motion over Central O‘ahu exceeds 1 m s^{-1} (Fig. 4.12d). The first radar echo over Central O‘ahu was observed at 1200 HST. The time lag between surface convergence and the first echo is about 2–3 hours.

From 0900–1000 HST, rising motion at the 900-hPa level is simulated over the western slopes of the Ko‘olau Mountains, where the combined easterly/upslope flow moves over the ridgetop and converges with the westerly upslope winds from Central O‘ahu (Figs. 4.12b–c). Over the Wai‘anae Mountains, rising motion is simulated near the ridgetop where the onshore/upslope flow from the western coast converges with the valley winds from the eastern slopes (Figs. 4.12b–c). At the slope surface, rising motion (w_{sfc}) occurs mainly over the eastern slopes of the Ko‘olau Mountains and the western slopes of the Wai‘anae Mountains due to orographic lifting of the

onshore/upslope flows. At the 900-hPa level, vertical motion associated with upslope flows is insignificant (Fig. 4.12b–c) and is inadequate to lift the air parcel to above the LFC (~ 876 hPa) (Fig. 4.7c).

For the case studied over Dominica by Wang and Kirshbaum (2015), the storm occurs on the slope where the upslope flow from the western slope moves over the ridgetop and converges with the upslope flow from the other side of the mountain. For our case, the strongest vertical motion occurs over Central O‘ahu with a flat terrain without orographic lifting. Note that the onshore/sea-breeze flows from the northwestern and the southeastern shores are about $4\text{--}6\text{ m s}^{-1}$ (Fig. 4.8), which is much stronger than the upslope flows from both sides of the mountains ($1\text{--}3\text{ m s}^{-1}$) for both the Ko‘olau Mountains and the Wai‘anae Mountains. The relatively strong onshore flows coming from coasts and penetrating the semi-arid flat terrain is linked to the development of deepening of the mixed layer (~ 1.5 km) over Central O‘ahu (Fig. 4.11). As a result, the most intense convective showers are initiated over the convergence over Central O‘ahu (Figs. 4.8 and 4.9).

Figure 4.13 shows a northwest–southeast vertical cross-section (see Fig. 4.1b) of equivalent potential temperature (θ_e) and winds. At 0700 HST, weak offshore flows with relatively low θ_e are simulated along the northern coast (Fig. 4.13a). At 0900 HST, northerly onshore flows from the northern coast and southerly onshore flows from the southern coast are developing (Fig. 4.13c). The sea breezes from the northern and the southern coasts reach Central O‘ahu at 1000 HST (Fig. 4.13d). The air coming from the south shore has slightly higher θ_e as compared to the air coming from the north shore (Figs. 4.13a–d). At 1100 HST, the sea breezes with high θ_e (338–340 K) converge below the 1-km level over Central O‘ahu with divergence above (1–2.5 km) (Fig. 4.13e). The rising motion transports low-level air with high θ_e above the 1-km level (Fig. 4.13e). The

convergence of the moist onshore flows over Central O‘ahu provides the lifting mechanism for the release of instability.

4.5.3 The Evolution of Simulated Radar Reflectivities

Before noon, the horizontal distributions of observed and simulated radar reflectivities reveal scattered echoes along the two mountain ranges. More scattered showers are simulated along the western slope of the Ko‘olau Mountain Range than are observed during this period (Figs. 4.14c–e). At noon, the observed and simulated radar reflectivities both show arc-shaped echoes over Central O‘ahu with maximum reflectivities of > 40 dBZ (Figs. 4.14f and 4.8f). At 1400 HST, the simulated radar echoes drift southwestward (Fig. 4.14h) due to the northeasterlies between 870–700 hPa with simulated heavy rainfall over the southwestern coast. By 1500 HST, the convection has moved southwestward to the open ocean, and only scattered showers are simulated over the western slopes of the Ko‘olau Mountain Range (Fig. 4.14i). At 1500 HST, strong convection > 40 dBZ no longer exists over Central O‘ahu as the storm dissipates (Fig. 4.8i).

4.5.4 Simulated Rainfall in Comparison with Observations

From 1100–1600 HST 8 June, a large amount of precipitation was recorded by the Hydronet stations in Central O‘ahu, with rain rates of ~ 48 mm h^{-1} . Most of the rainfall was observed during 1400–1600 HST, with a maximum rainfall accumulation of ~ 58 mm (Fig. 4.15a). The simulated precipitation over Central O‘ahu is less (~ 30 mm), compared to the rain gauge measurements and radar estimation (Figs. 4.15a–b). The observed local rainfall maximum over the Wai‘anae Mountains (~ 50 mm) is simulated.

4.5.5 Model Sensitivity Tests

Fig. 4.16 shows the evolution of simulated radar echoes from the NoOrog runs on 8 June. Without orographic effects, the prevailing southeasterly winds are simulated over the island interior with slightly lower speeds than over the open ocean due to surface friction (Figs. 4.16a–b). Thermally driven sea breezes start developing at 1000 HST. Scattered radar echoes are simulated over Central and Western O‘ahu at 1100 HST (Fig. 4.16e). The vertical motion at the 900-hPa level shows that low-level lifting is mainly caused by low-level convergence of the thermally driven sea breeze circulations (Figs. 4.17c–d). At 1300 HST, an arc-shaped radar echo is simulated over Central O‘ahu in response to low-level lifting (Fig. 4.16g). With mid-level easterlies, the simulated convection moves westward, similar to the movement of observed radar echoes (Figs. 4.16g–i; Figs. 4.8g–i). The results of the NoOrog runs show that, as in the CTRL run, the timing of convection development is close to observation, but the location of convective initiation is slightly westward as the onshore flow from the east, in the absence of orographic blocking by the Ko‘olau Mountains, is stronger. The results of the NoOrog runs indicate that orographic effects may not be essential for the development of this type of heavy rainfall event. In contrast, Nguyen et al. (2010) showed that without terrain, trade-wind showers fail to develop over both the Ko‘olau Mountains and the Wai‘anae Mountains. Their results attest to the importance of orographic lifting on the production of summer trade-wind rainfall over O‘ahu. Nevertheless, not all strong trade wind days will produce more trade-wind rainfall than weak trade wind days. Hartley and Chen (2010) showed that most of the orographic showers on the windward side of O‘ahu are from pre-existing trade-wind cumuli or showers that drift inland and are enhanced by terrain.

For the NoFlux run, the island-scale airflow is affected by orographic blocking. Simulated winds over windward slopes and Central O‘ahu are weak and variable during 0700–1000 HST

(Figs. 4.18a–d). Sea breezes/onshore flows are absent in the NoFlux run. Vertical motion is not simulated at 900 hPa (not shown). The NoFlux run does not produce convective cells over O‘ahu (Fig. 4.18). Without surface fluxes, the lifting mechanism by the onshore/sea breeze convergence over Central O‘ahu fails to develop. These results attest that onshore flows driven by land–sea thermal contrast are crucial for the increase in instability and the generation of low-level convergence, leading to the initiation of convection over Central O‘ahu. The same sensitivity tests (NoOrog and NoFlux) have been performed for all 13 days with similar results (Fig. 4.19 and 4.20).

4.6 Summary

The Central O‘ahu storm is initiated by thermal forcing from the land surface. There are three types of lifting associated with this type of event (Fig. 4.12d): 1) lifting by the upslope flow on the eastern slope of the Ko‘olau Mountains and on the western slope of the Wai‘anae Mountains; 2) convergence on the western slope of the Ko‘olau Mountains and on the eastern slope of the Wai‘ane Mountains; 3) convergence over Central O‘ahu. For orographic lifting of the upslope flow (Type 1), the advection time scale for the maritime air to reach the ridgetop from the coast is too short (10 minutes or less) to produce orographic showers (Hartley and Chen 2010). In fact, at 1100 HST, the vertical motion due to orographic lifting above the ridgetop by these upslope flows is insignificant. For the convergence zone where the upslope flow ($1\text{--}2\text{ m s}^{-1}$) from the coast moves over the ridgetop and converges with the upslope flow ($\sim 1\text{ m s}^{-1}$) from the island interior, scattered showers are generated near the ridgetops (Fig. 4.12d). This type of thermally driven convection is similar to the case reported by Wang and Kirshbaum (2015). Nevertheless, the most intense storm occurs over Central O‘ahu where the sea breezes ($3\text{--}5\text{ m s}^{-1}$) from the northwestern coast converge with the sea breezes ($4\text{--}6\text{ m s}^{-1}$) coming from the SE shore. The mixed layer on

the slope surface is rather shallow (< 400 m above the slope surface) (not shown) as the daytime heating on the tropical rainforest is reduced by the cold advection associated with the upslope flow (Wekker and Kossmann 2015). In contrast, air within the semi-arid Central O‘ahu is bounded by two narrow mountain ranges with continuous heating after sunrise. For the 8 June 2003 case, the mixed layer grows to 1.5 km above sea level, which is above both the LCL and LFC (~ 1.4 km), with saturation from 1.4 km to above 2 km at 1100 HST. With persistent convergence over Central O‘ahu, the deep convection finally develops after 1200 HST (Fig. 4.21).

A diurnal heating cycle is present throughout the year, especially during the summer months. However, the Central O‘ahu storms occur mainly during the seasonal transitions (June and October) and are rather uncommon (13 days from 2000 to 2015). The work by Hartley and Chen (2010) shows no convection over Central O‘ahu during the summer months under weak and variable winds. Thus, sea-breeze convergence alone is inadequate to initiate Central O‘ahu storms. Favorable large-scale conditions are needed, which are most likely to be met during the seasonal transitions, including a deep moist layer, a blocking pattern in the mid-latitudes with a northeast–southwest moist tongue with relatively high TPW (> 40 mm) ahead of an upper-level trough, the absence of a trade wind inversion, and weak low-level winds.

The Central O‘ahu storm is difficult to forecast using operational global models because of the relatively coarse model resolution. In this chapter, the value of island-scale high-resolution models is demonstrated in predicting this type of event. However, if the large-scale environment is poorly predicted by the global models, it is unlikely that high-resolution models will correctly forecast the island-scale response. Yet, based on the synoptic pre-cursors delineated in this paper and using observations in the early morning, it may be possible to nowcast occurrences of the Central O‘ahu storm in the early afternoon.

Chapter 4 Tables

Table 4.1. A list of the 13 heavy rainfall events, including the date, accumulated rainfall maximum during 0900–1700 HST, and the disaster records in the NCEI storm event database.

Date	NCEI information	max obs. acc. rainfall 09-17 HST (mm)
2003-06-04	Small stream and drainage ditch flooding	18.54
2003-06-05	Small stream and drainage ditch flooding	15.98
2003-06-06	Small stream and drainage ditch flooding	15.23
2003-06-07	Small stream and drainage ditch flooding	29.21
2003-06-08	A mudslide that closed Highway for several hours	57.91
2004-10-12	Small stream and drainage ditch flooding	14.22
2006-10-08	Small stream and drainage ditch flooding, and ponding of roadways	16.25
2006-10-10	Small stream and drainage ditch flooding, and ponding of roadways	20.57
2013-10-12	Small hail reported in central Oahu	8.37
2013-10-13	Small hail reported in central Oahu	57.66
2013-10-14	Small hail reported in central Oahu	2.29
2013-10-27	Ponding on roadways, small stream and drainage ditch flooding, and minor debris flows	49.53
2014-10-07	Ponding on roadways, and small stream and drainage ditch flooding	14.73

Table 4.2 Error statistics for the weather stations reporting during 0900–1100 HST for the 13

heavy rainfall days. The error statistics are computed every hour.

Station ID.	NETWORK	U(m s ⁻¹)			V(m s ⁻¹)		
		BIAS	MAE	RMSE	BIAS	MAE	RMSE
HOFH	RAWS	0.7	1.0	1.3	0.6	1.4	1.8
KFWH	RAWS	-0.2	1.5	2.0	0.0	1.0	1.3
KKRH	RAWS	-0.1	0.6	0.8	1.9	2.0	3.0
KTAH	RAWS	0.4	1.5	1.9	-0.4	1.1	1.3
KWLH	RAWS	0.0	0.6	0.8	0.0	1.0	1.2
MKGGH	RAWS	1.1	1.3	1.9	0.5	1.2	1.6
MKRH	RAWS	-0.4	1.2	1.4	0.2	1.8	2.3
ORFH	RAWS	0.3	0.8	1.0	1.2	1.3	1.7
PHHI	NWS	0.5	1.0	1.2	0.4	1.2	1.6
PHJR	NWS	0.9	1.3	2.0	-0.8	1.2	1.3
PHNG	NWS	0.2	0.7	0.9	0.4	1.1	1.2
PHNL	NWS	0.5	1.0	1.3	-0.8	1.4	1.7
SCBH	RAWS	0.4	1.1	1.3	0.2	1.2	1.7
SCEH	RAWS	-0.7	0.9	1.2	0.6	1.0	1.4
WNVH	RAWS	0.5	1.4	1.6	-0.5	1.0	1.2
WWFH	RAWS	0.0	0.8	1.0	0.4	1.2	1.4
ALL		0.3	1.0	1.4	0.3	1.3	1.6

Station ID.	NETWORK	T(°C)			Td (°C)		
		BIAS	MAE	RMSE	BIAS	MAE	RMSE
HOFH	RAWS	0.5	0.7	0.7	1.6	2.3	2.7
KFWH	RAWS	-0.9	1.1	1.2	-0.1	1.0	1.3
KKRH	RAWS	-0.1	0.6	0.8	-0.3	0.6	0.8
KTAH	RAWS	-2.1	2.1	2.3	-2.0	2.1	2.5
KWLH	RAWS	-1.2	1.4	1.7	-0.8	1.3	1.4
MKGGH	RAWS	-3.0	3.0	3.5	-2.9	2.9	3.3
MKRH	RAWS	-1.8	2.0	2.1	-0.9	1.3	1.5
ORFH	RAWS	2.2	2.3	2.6	-0.8	1.7	2.4
PHHI	NWS	0.3	1.2	1.4	-1.2	1.8	2.1
PHJR	NWS	0.9	1.1	1.4	-0.6	0.9	1.1
PHNG	NWS	0.7	1.1	1.5	-0.9	1.1	1.3
PHNL	NWS	1.4	1.4	1.6	-1.0	1.2	1.3
SCBH	RAWS	-1.5	1.7	2.1	-1.3	1.9	2.5
SCEH	RAWS	-2.1	2.1	2.6	-2.0	2.2	2.8
WNVH	RAWS	-2.4	2.5	2.8	-0.1	1.3	1.7
WWFH	RAWS	-0.5	0.7	0.9	-0.1	0.9	1.0
ALL		-0.6	1.5	1.8	-0.9	1.5	1.9

Chapter 4 Figures

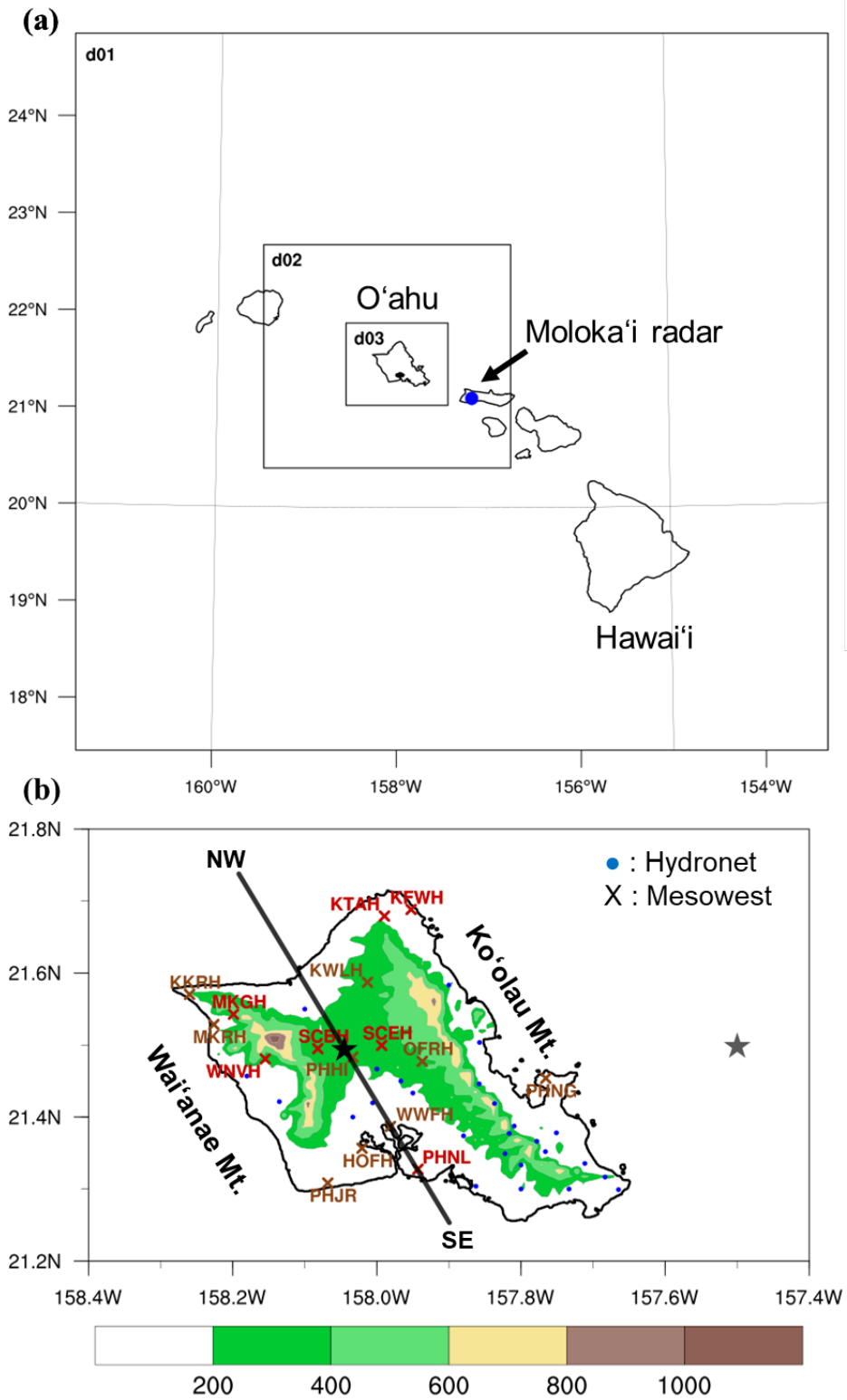


Fig. 0.1 (a) A map of the Hawaiian Islands with the three nesting domains employed in the simulations with grid sizes of 13.5 km, 4.5 km, and 1.5 km, respectively. The blue dot represents the location of the Moloka'i radar station. (b) The island of O'ahu with elevation contours every 200-m. The Xs represent the MesoWest surface weather stations. For the 2003 case study, seven stations (red Xs) are used. For the composite study during 2000–2015, 16 stations (red and brown Xs) are used. The blue dots represent the Hydronet rain gauge locations. The solid lines indicate the locations of the cross-sectional analysis. The gray star and black star represent an upstream point (21.5°N, 157.5°W) and a point over Central O'ahu (21.5°N, 158.05°W), respectively.

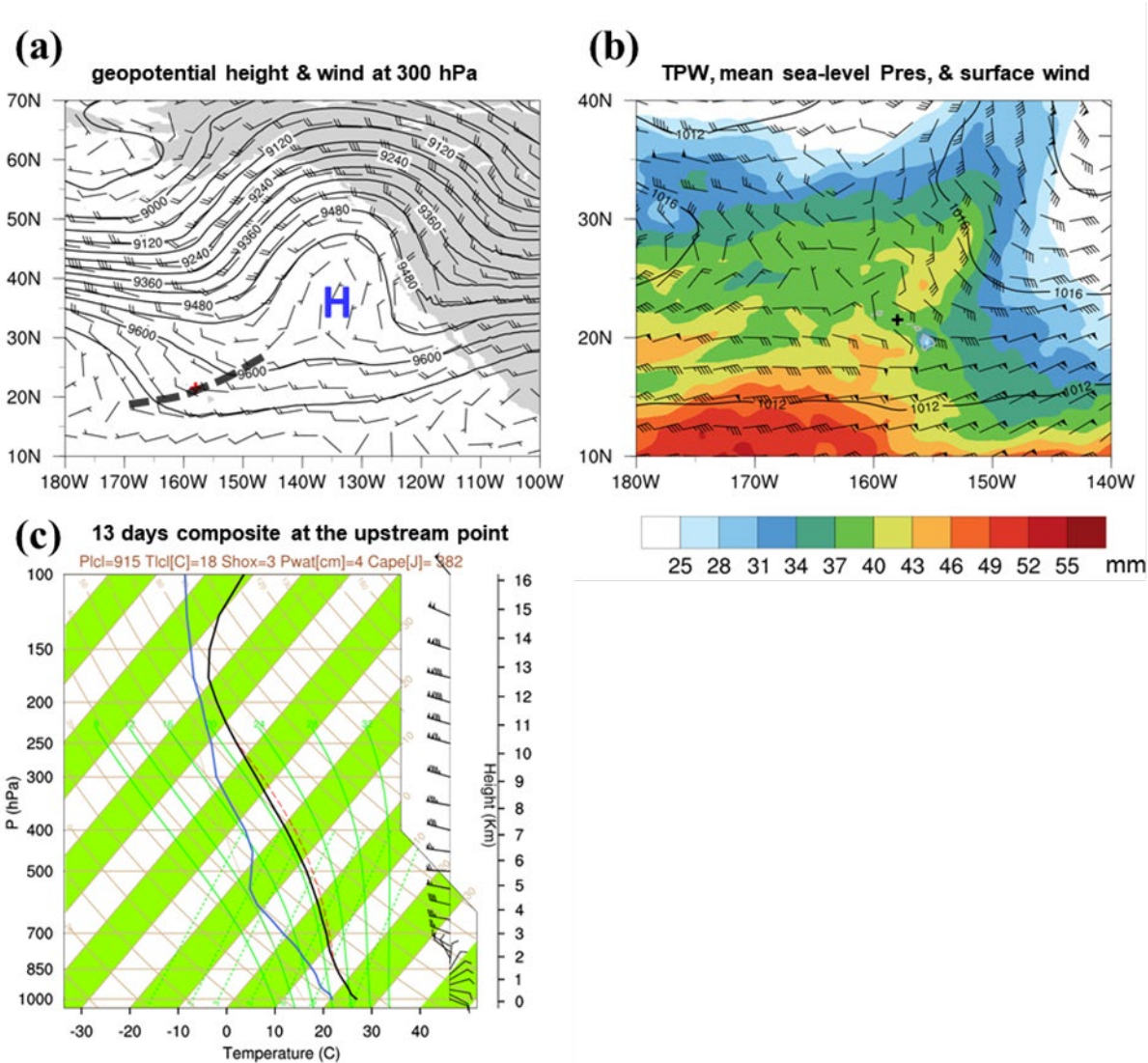


Fig. 0.2 (a) The NCEP CFSR (CFSv2) geopotential height (gpm, contours) and wind barbs (pennant: 50 m s^{-1} ; full barb: 10 m s^{-1} ; half barb: 5 m s^{-1} ; open circle: calm) at 300 hPa at 1400 HST for the 13-day composite. The red cross represents the location of O'ahu and the dashed line represents a trough. (b) The NCEP CFSR total precipitable water (mm, color shades), surface wind barbs (pennant: 5 m s^{-1} ; full barb: 1 m s^{-1} ; half barb: 0.5 m s^{-1} ; open circle: calm), and mean sea-level pressure (hPa, black contours) at 1400 HST for the 13-day composite. The black cross represents the location of O'ahu (c) Composite Skew T -log P diagram from the NCEP CFSR (CFSv2) at 21.5°N , 157.5°W at 1400 HST for

the 13 days. Pennants, full barbs, half barbs, and open circles represent 5 m s^{-1} , 1 m s^{-1} , 0.5 m s^{-1} and calm, respectively.

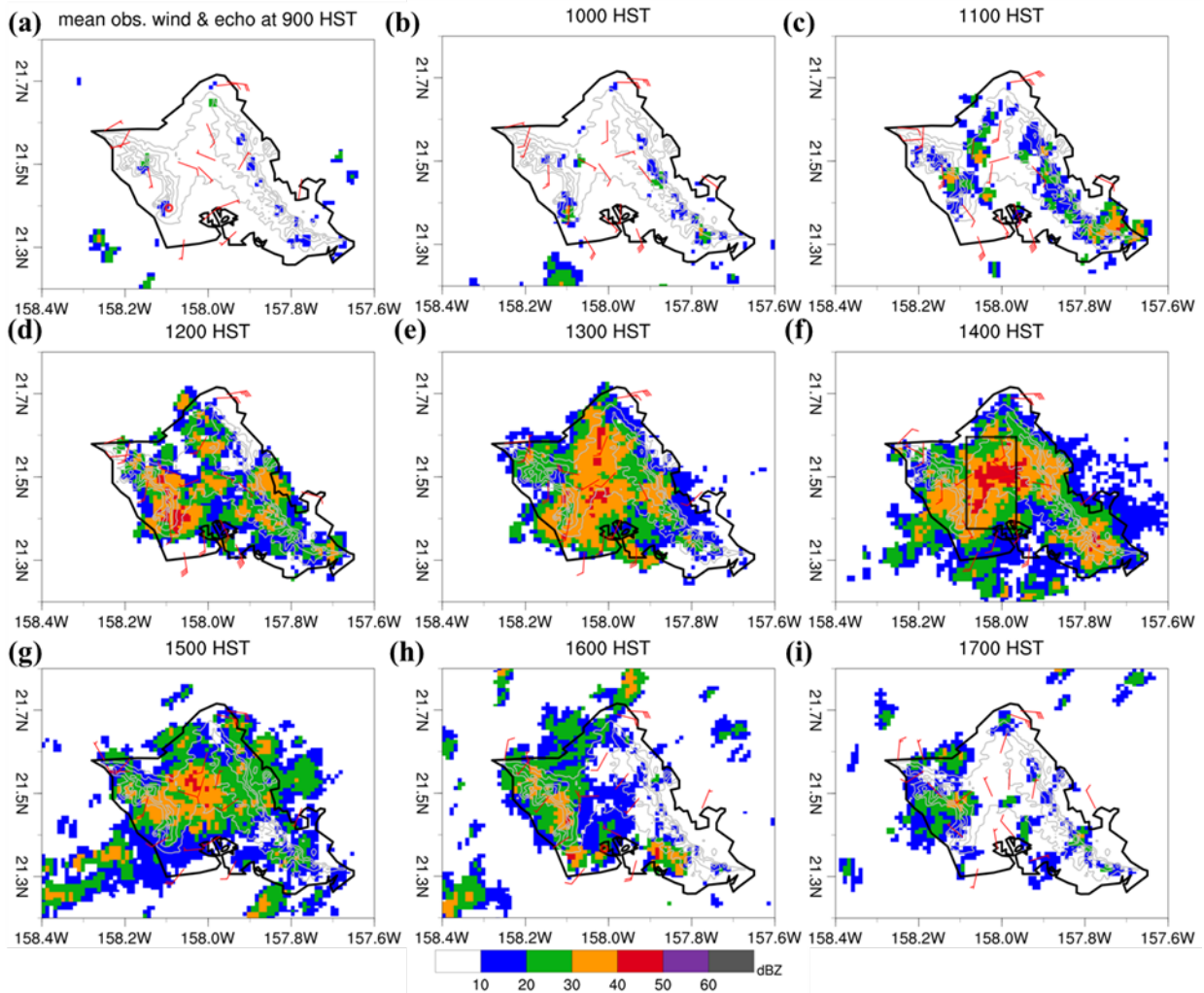


Fig. 0.3 Mean observed radar echoes (dBZ, color shades) and mean observed surface wind (black wind barb, pennant: 5 m s^{-1} ; full barb: 1 m s^{-1} ; half barb: 0.5 m s^{-1} ; open circle: calm) from the 13 cases at (a) 0900, (b) 1000, (c) 1100, (d) 1200, (e) 1300, (f) 1400, (g) 1500, (h) 1600, and (i) 1700 HST. The black box indicates the region for the area-average.

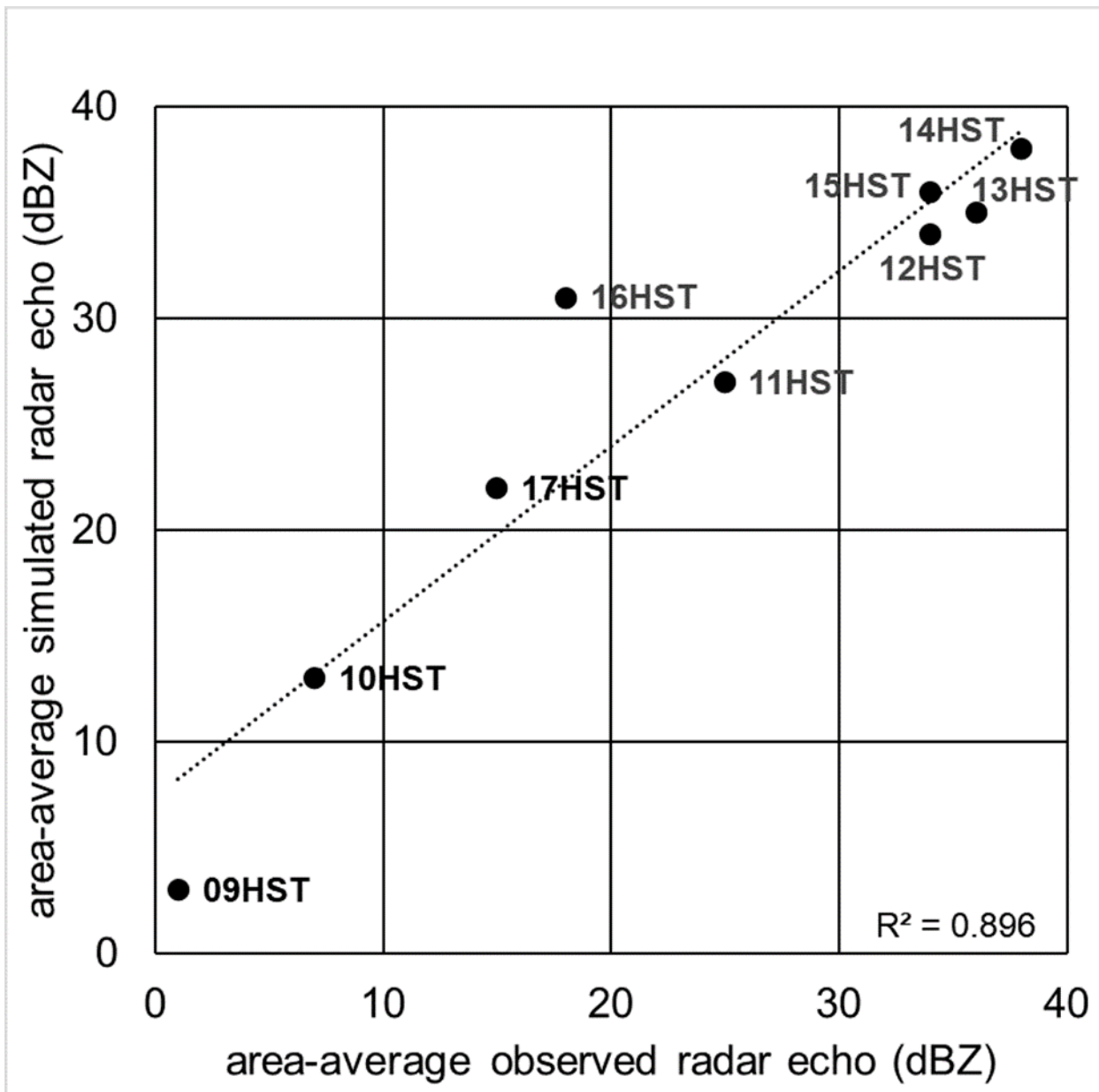


Fig. 0.4 Scatter plot of area-average observed radar echoes and area-average simulated radar echoes. The dotted line is a line of best fit.

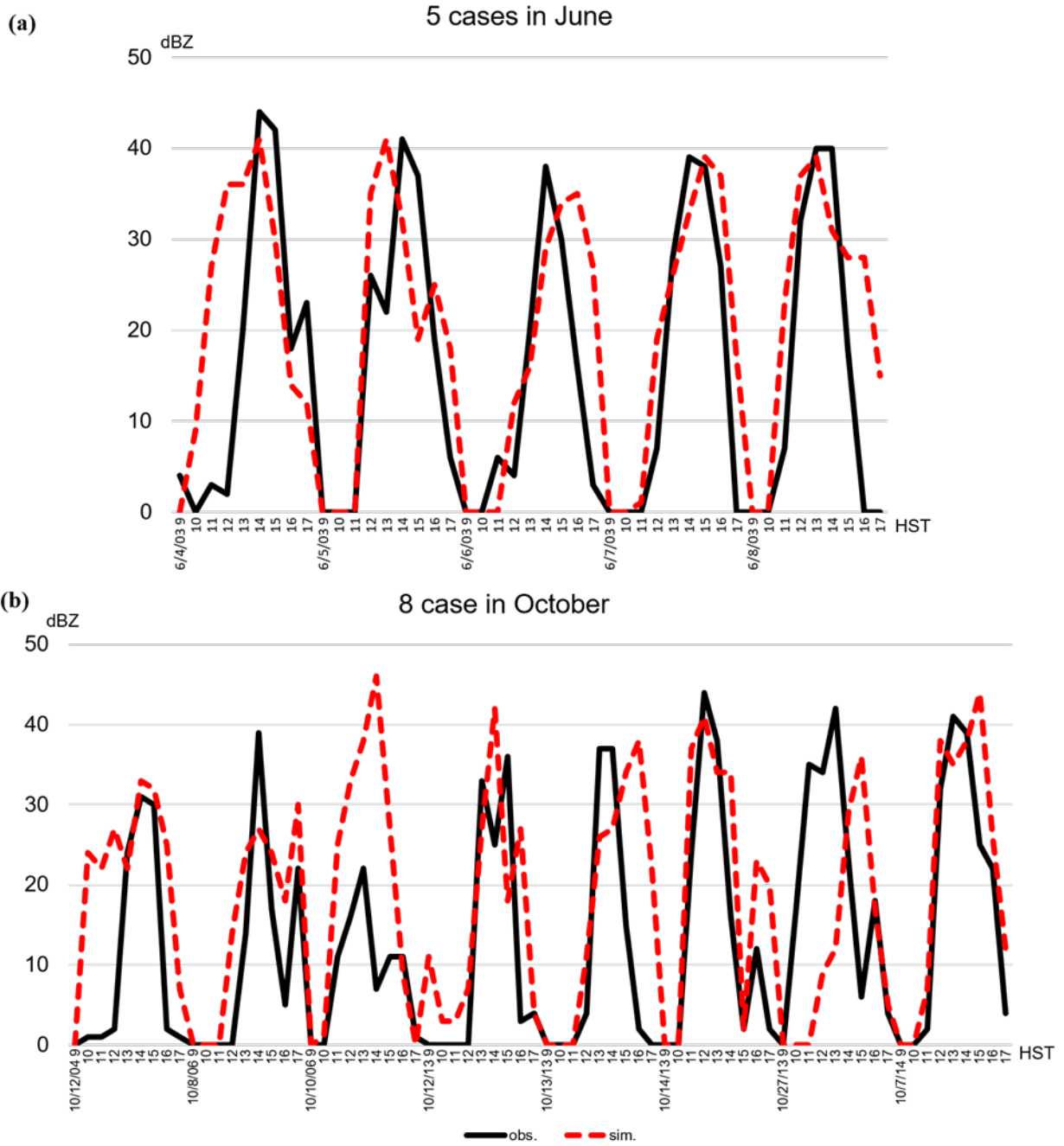


Fig. 0.5 Time series of area-averaged (Fig. 4.3f) observed (solid lines) and simulated (red dash lines) radar reflectivity during 0900–1700 HST for seasonal transitions (a) the 5 cases in June and (b) the 8 cases in October.

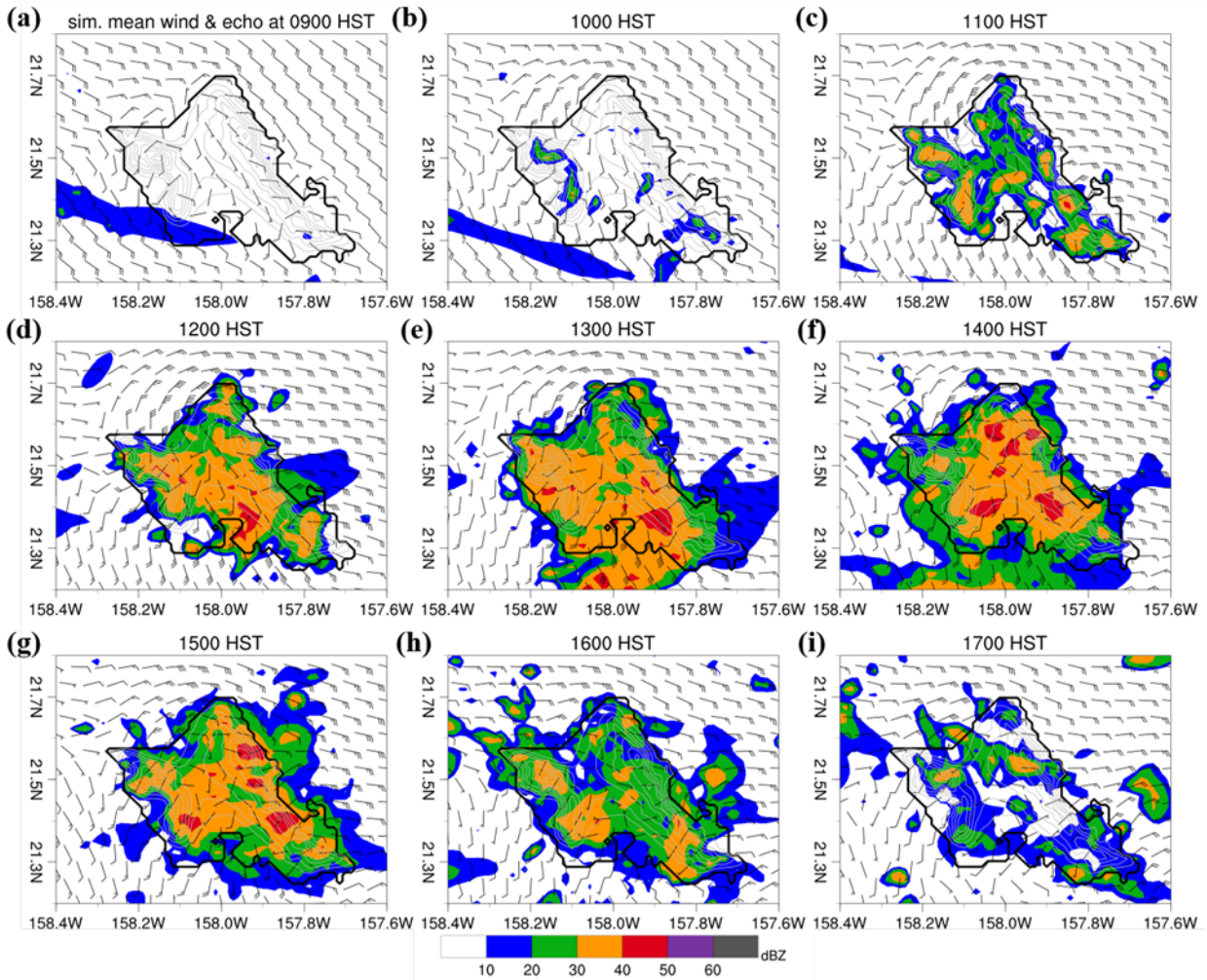


Fig. 0.6 Mean simulated radar reflectivity (dBZ, color shades), mean simulated surface wind (m s^{-1} , black wind barbs), and mean observed surface wind (m s^{-1} , red wind barbs) from the 13 case composite at (a) 0900, (b) 1000, (c) 1100, (d) 1200, (e) 1300, (f) 1400, (g) 1500, (h) 1600, and (i) 1700 HST. Pennants, full barbs, half barbs, and open circles represent 5 m s^{-1} , 1 m s^{-1} , 0.5 m s^{-1} and calm, respectively.

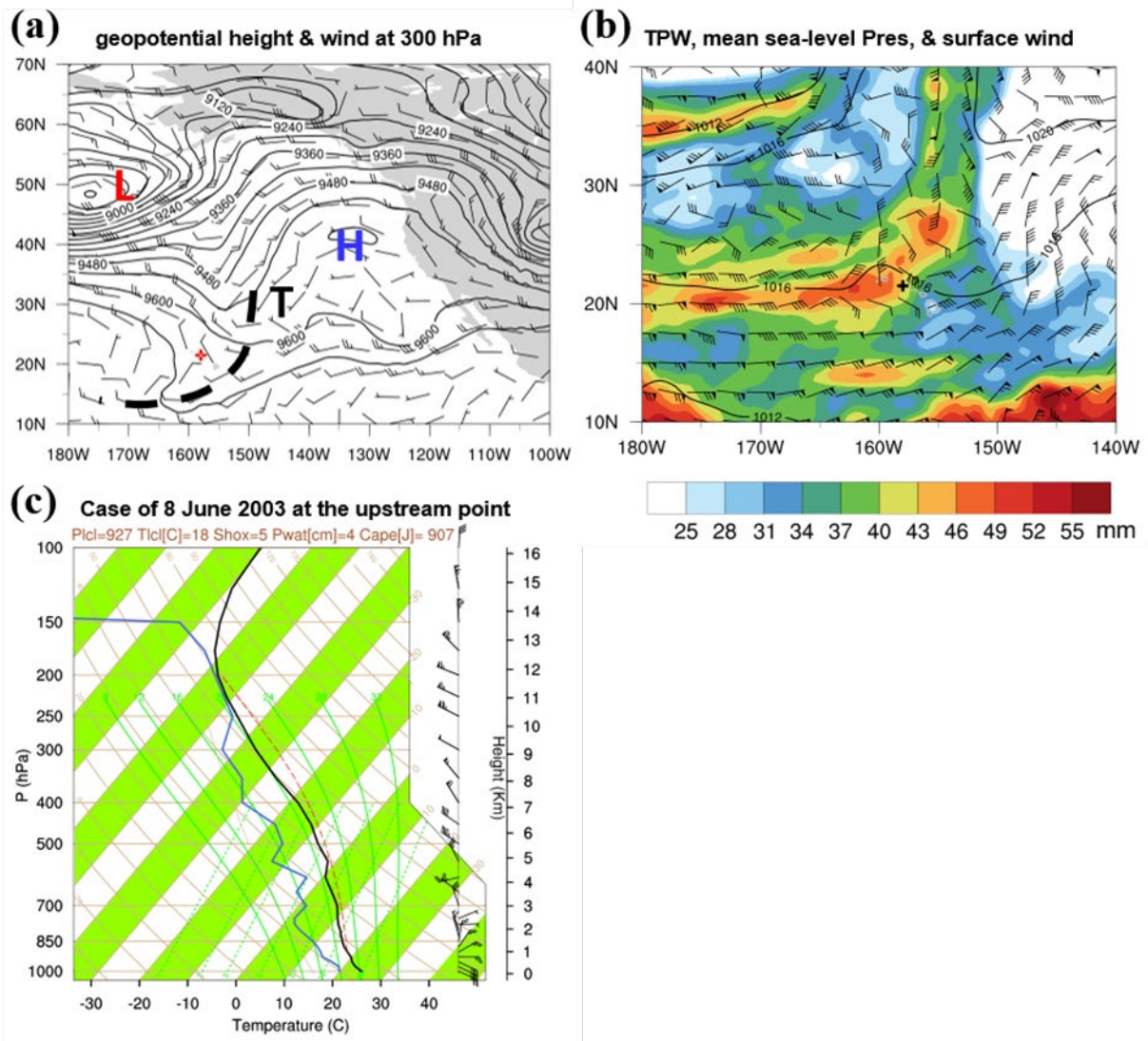


Fig. 0.7 Same as Fig. 4.2, but at 1400 HST 8 June 2003.

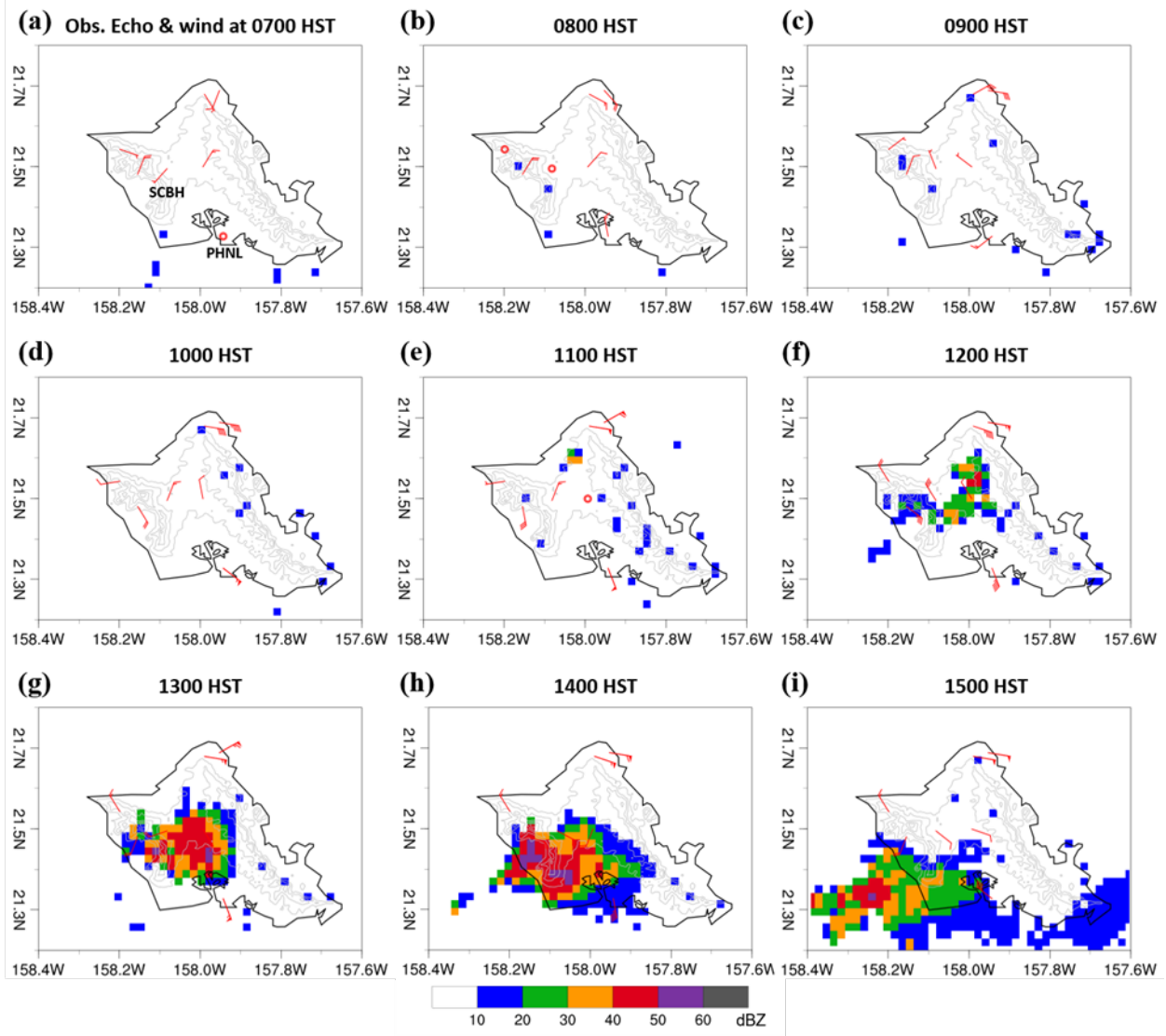


Fig. 0.8 Radar reflectivity (dBZ, color shades) from the Molokai radar site and observed surface wind (red wind barbs, pennant: 5 m s^{-1} ; full barb: 1 m s^{-1} ; half barb: 0.5 m s^{-1} ; open circle: calm) at (a) 0700, (b) 0800, (c) 0900, (d) 1000, (e) 1100, (f) 1200, (g) 1300, (h) 1400, and (i) 1500 HST 8 June.

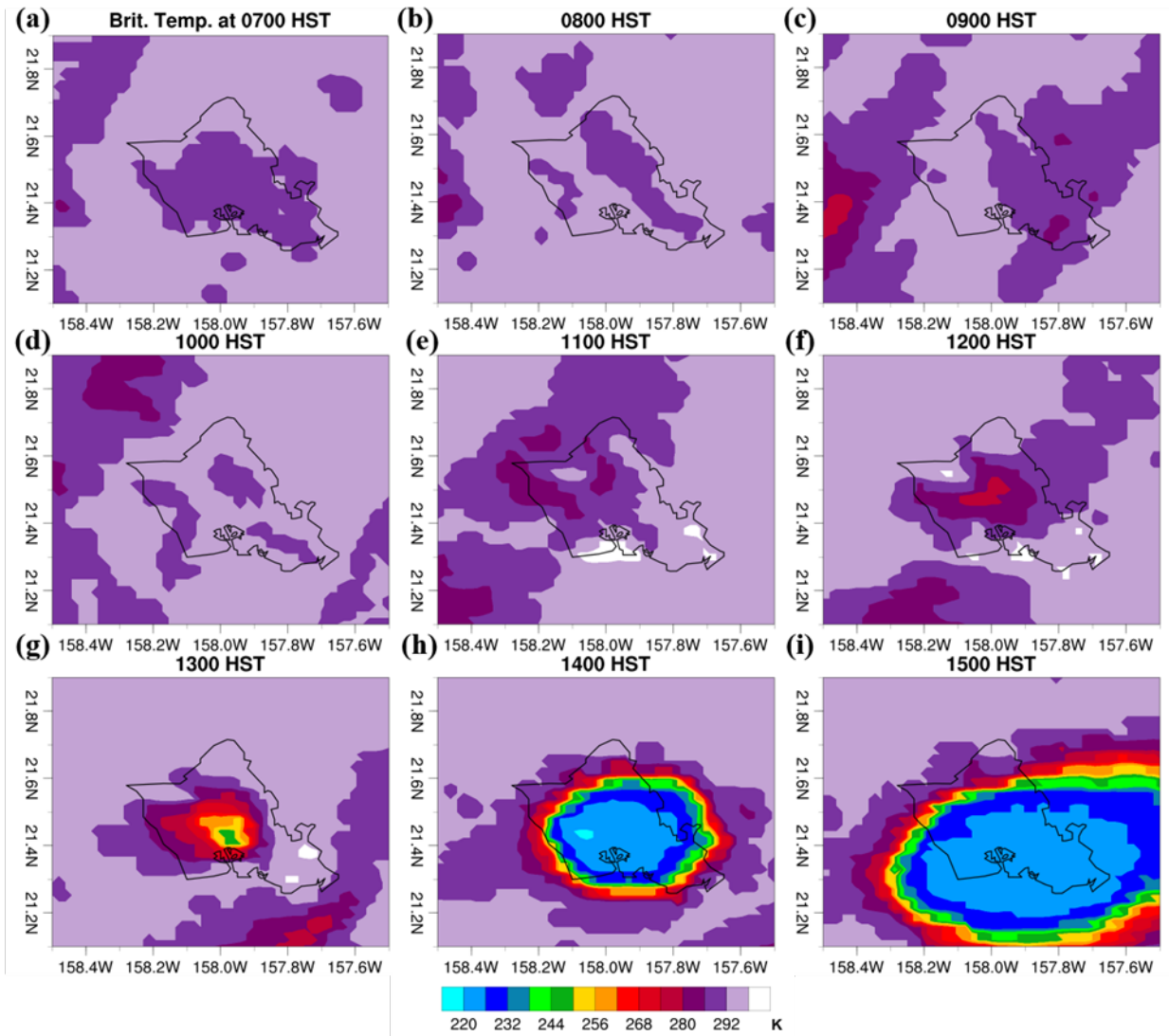


Fig. 0.9 IR brightness temperature (K, color shades) at (a) 0700, (b) 0800, (c) 0900, (d) 1000, (e) 1100, (f) 1200, (g) 1300, (h) 1400, and (i) 1500 HST 8 June.

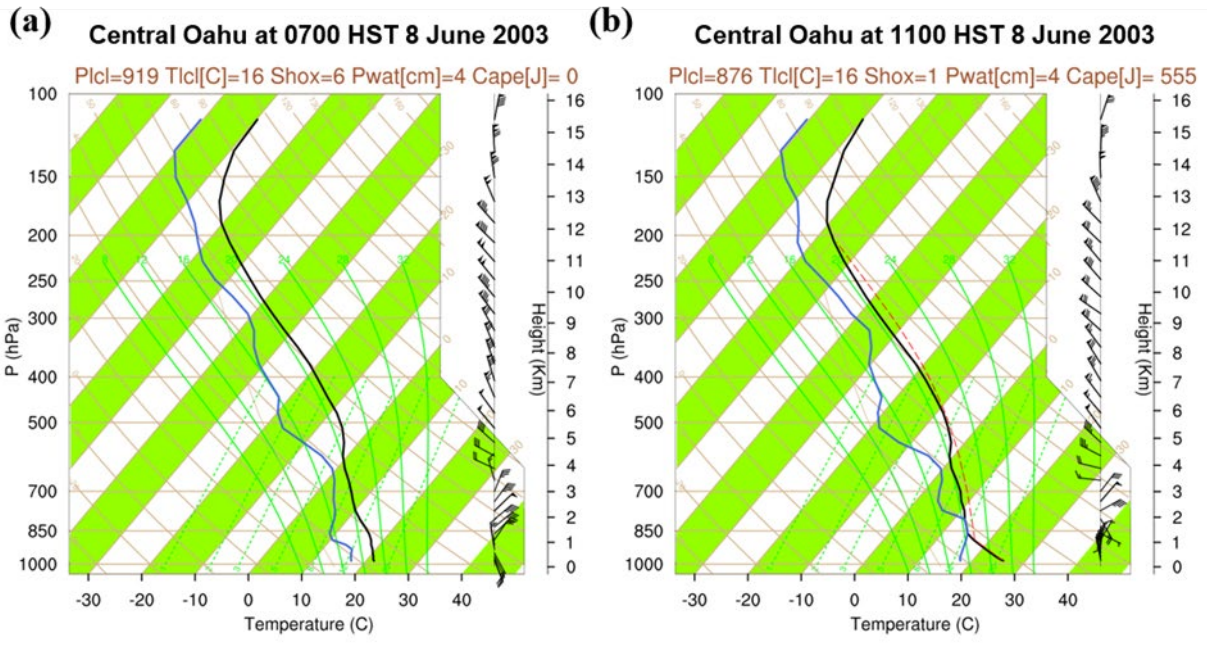


Fig. 0.10 Skew T - $\log p$ diagram from WRF simulations at Central O'ahu (21.5°N , 158.05°W) at (a) 0700 HST and (b) 1100 HST 8 June. Pennants, full barbs, half barbs, and open circles represent 5 m s^{-1} , 1 m s^{-1} , 0.5 m s^{-1} and calm, respectively. The red dashed line represents the temperature profile of a rising air parcel.

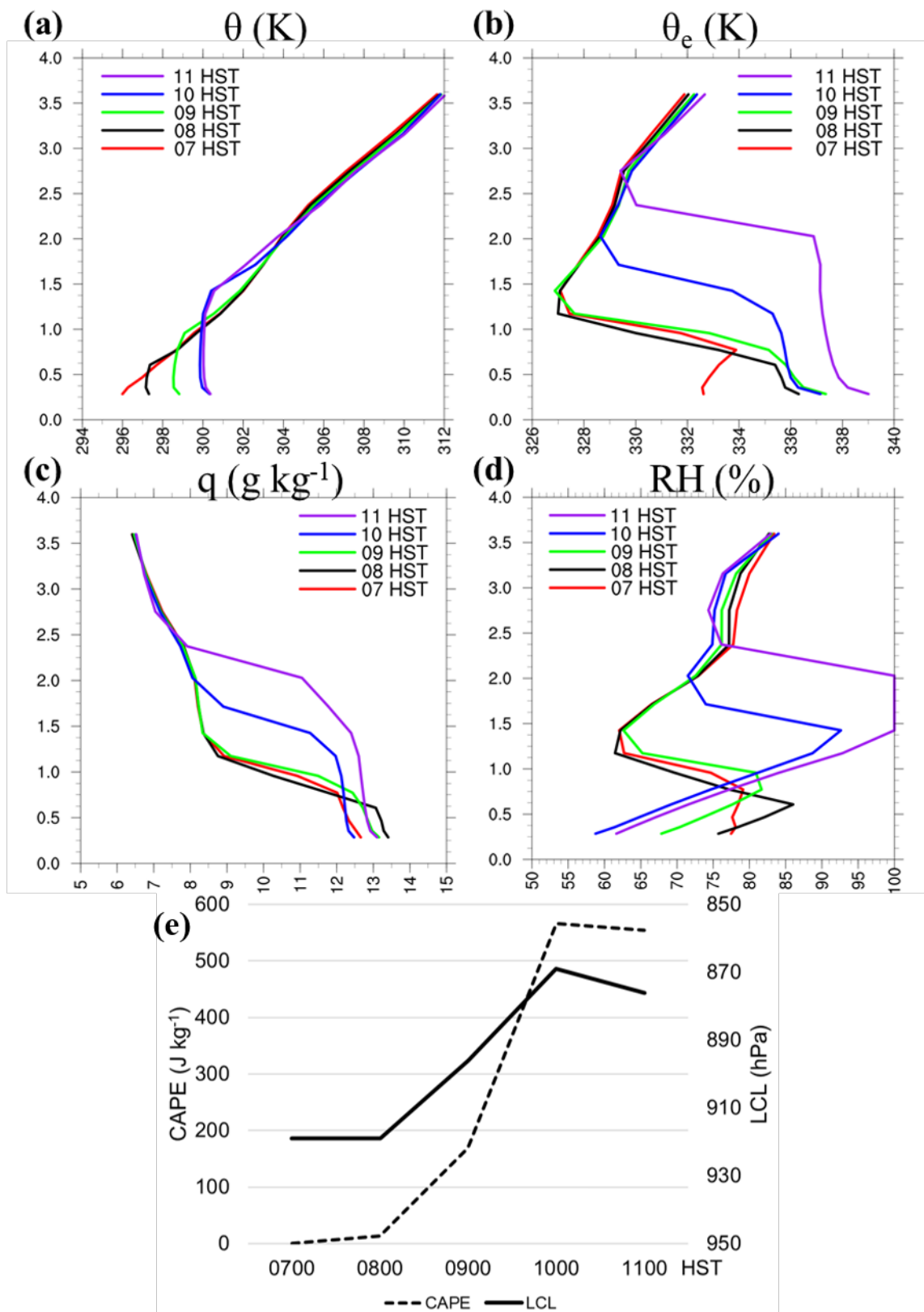


Fig. 0.11 Vertical profiles at Central O'ahu (21.5°N, 158.05°W) of (a) potential temperature

(K), (b) equivalent potential temperature (K), (c) mixing ratio (g kg^{-1}), and (d) relative humidity (%) from 0700–1100 HST 8 June. (e) Time series of LCL (solid) and CAPE (dash) at Central O‘ahu (21.5°N , 158.05°W) during 0700–1100 HST 8 June. CAPE is calculated from the level of free convection to the equilibrium level.

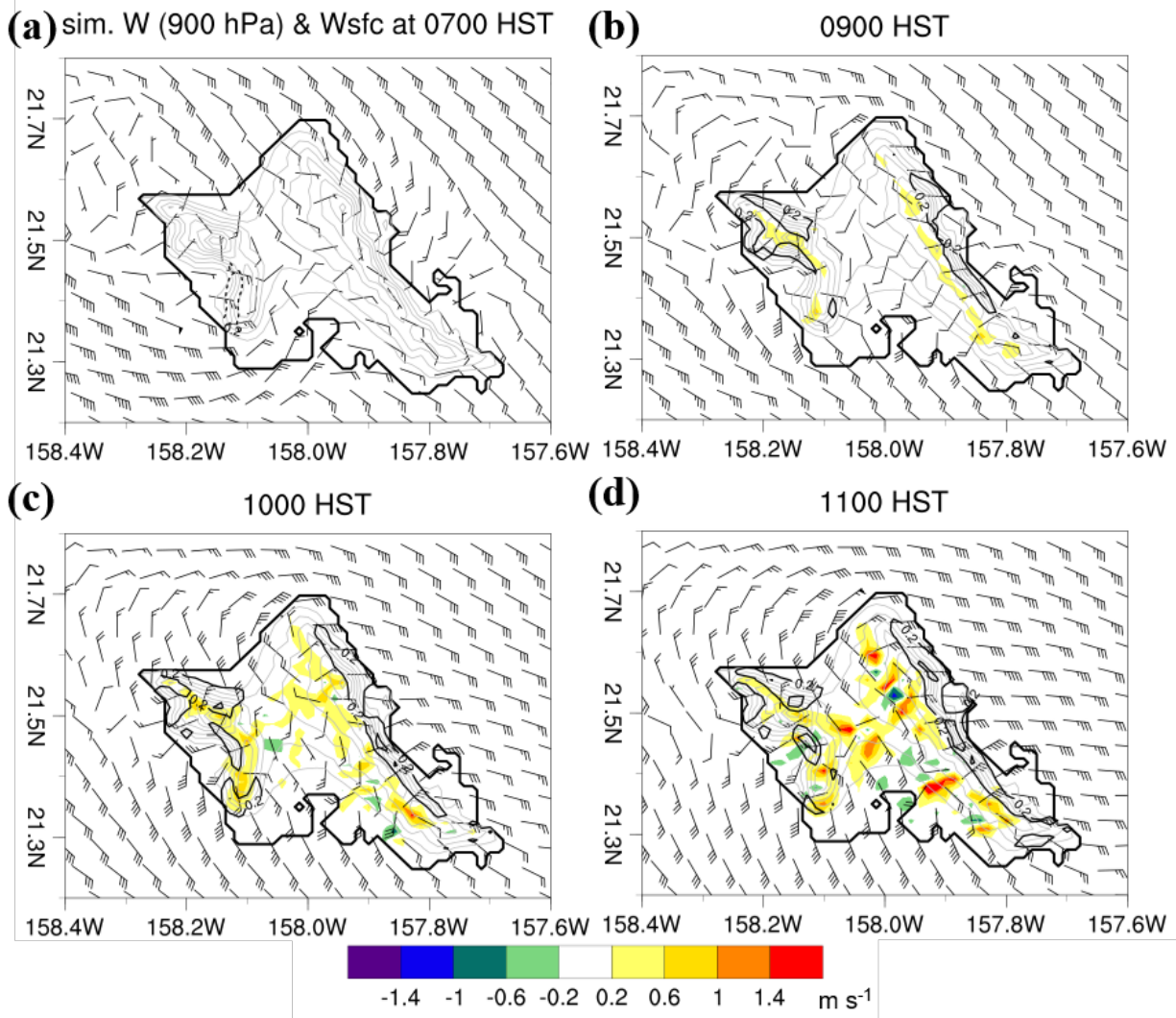


Fig. 0.12 Simulated vertical motion at 900 hPa (m s^{-1} , color shades), simulated surface vertical motion due to orographic lifting (w_{sfc}) (m s^{-1} , black contours), simulated surface wind (black wind barbs, pennant: 5 m s^{-1} ; full barb: 1 m s^{-1} ; half barb: 0.5 m s^{-1} ; open circle: calm), and model terrain height (gray contours, 100-m intervals) at (a) 0700, (b) 0900, (c) 1000, and (d) 1100 HST 8 June.

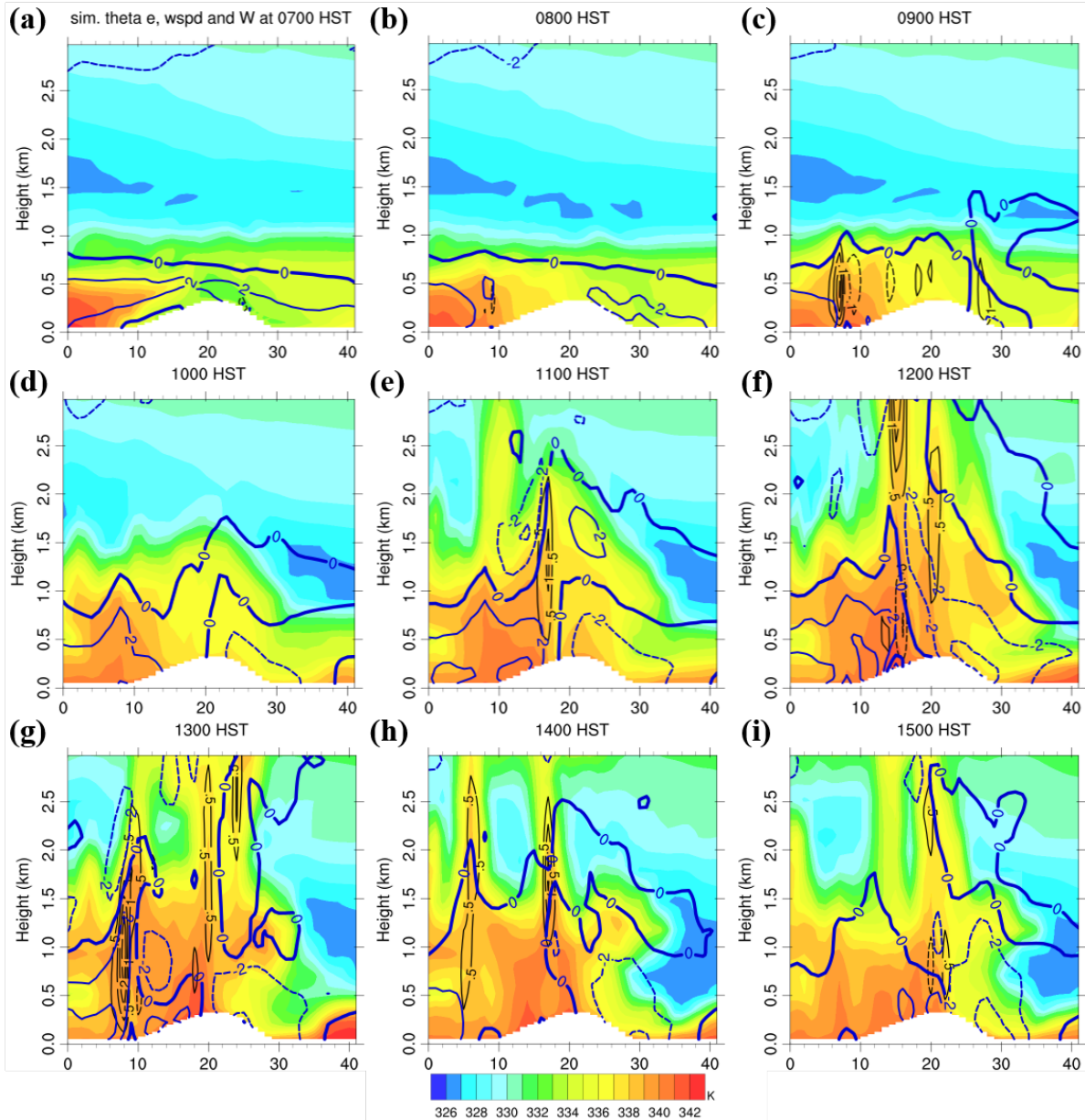


Fig. 0.13 Vertical cross-section along the northwest–southeast line in Fig. 1b showing equivalent potential temperature (K, color shades), horizontal wind speed along the cross section (blue contour with 2-m s^{-1} intervals), vertical motion (black contours with 0.1-m s^{-1} intervals during 0700–1000 HST; with 0.5-m s^{-1} intervals during 1100–1500 HST) at (a) 0700, (b) 0800, (c) 0900, (d) 1000, (e) 1100, (f) 1200, (g) 1300, (h) 1400, and (i) 1500 HST 8 June. The 0 point of the x-axis represents the southernmost point of the northwest–southeast line in Fig. 4.1b.

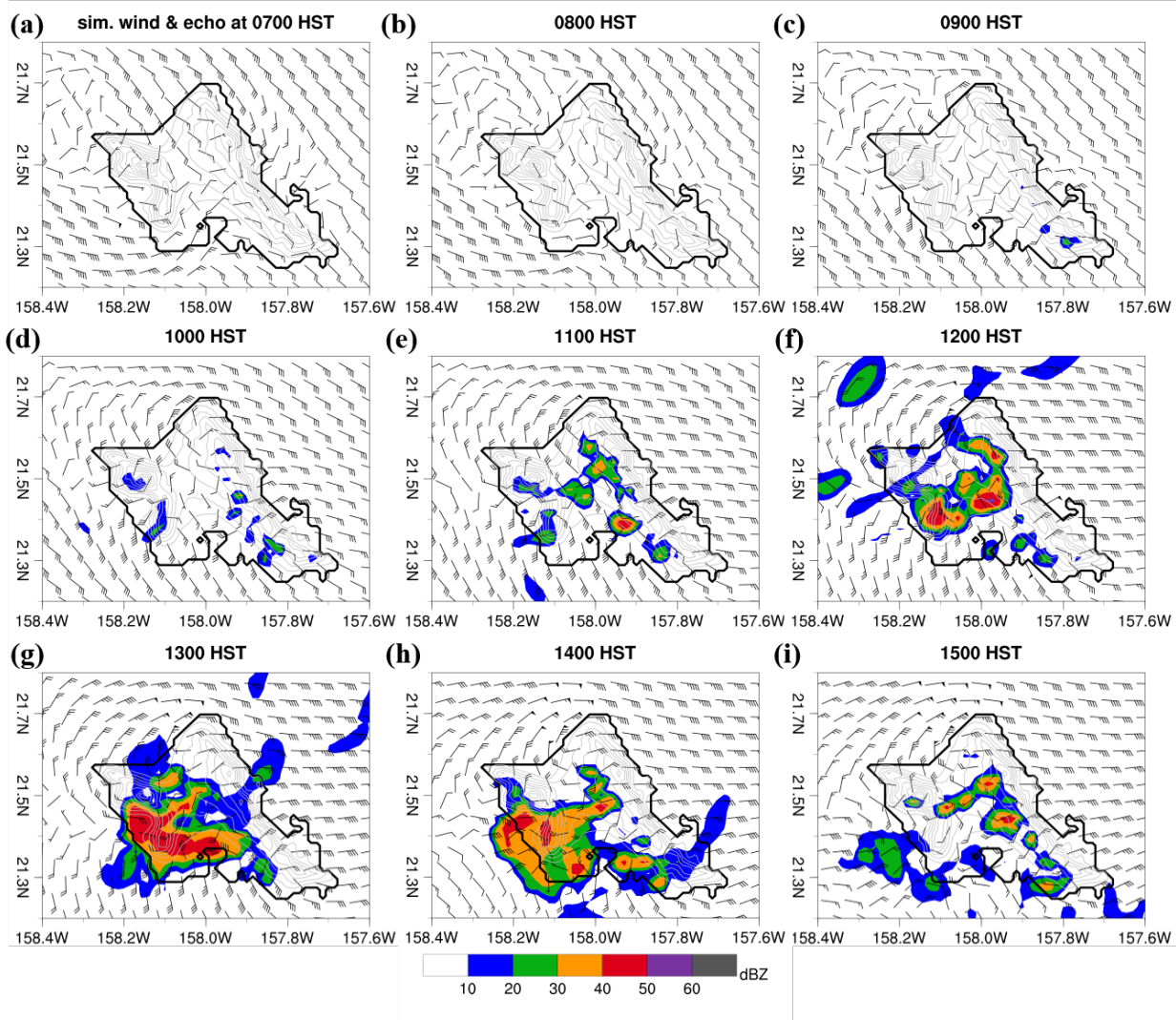


Fig. 0.14 Simulated radar reflectivity (dBZ, color shades) and model terrain height (gray contours, 100-m intervals) at (a) 0700, (b) 0800, (c) 0900, (d) 1000, (e) 1100, (f) 1200, (g) 1300, (h) 1400, and (i) 1500 HST 8 June. Black wind barbs represent simulated surface wind (pennant: 5 m s^{-1} ; full barb: 1 m s^{-1} ; half barb: 0.5 m s^{-1} ; open circle: calm).

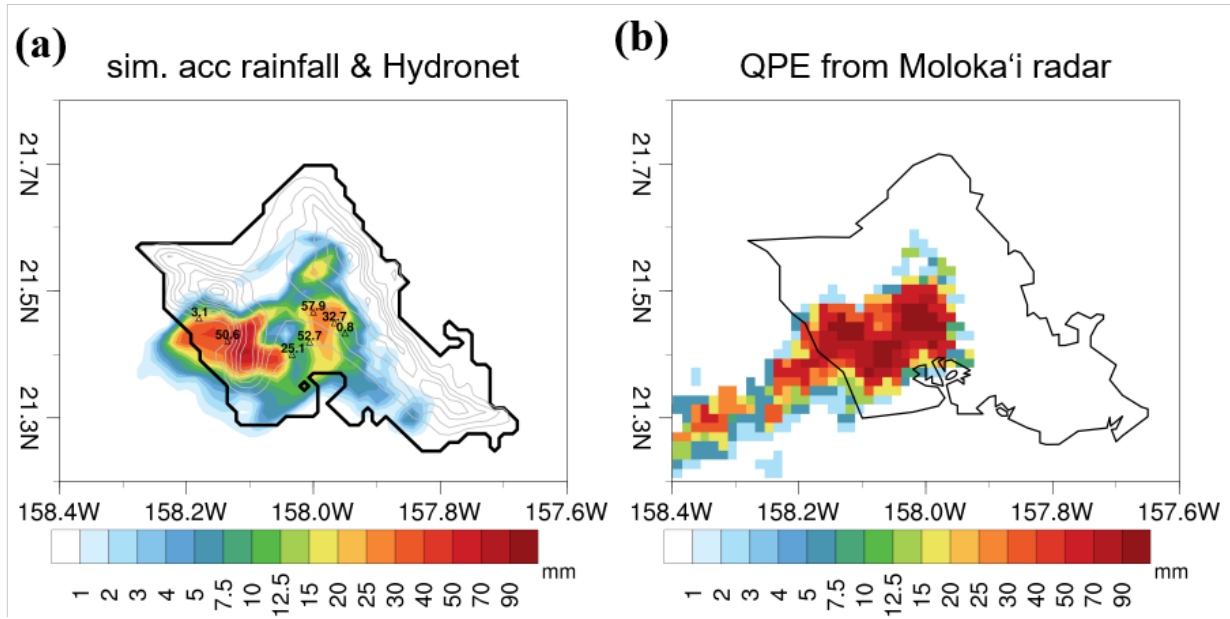


Fig. 0.15 (a) Accumulation of simulated rainfall (mm, color shades) and accumulation of rain gauge observation (mm, black triangle with label) from 1100–1600 HST 8 June. (b) Radar QPE (mm, color shades) from the Moloka‘i radar site on 8 June. Rain gauges with no rainfall accumulation (0.0 mm) are not shown.

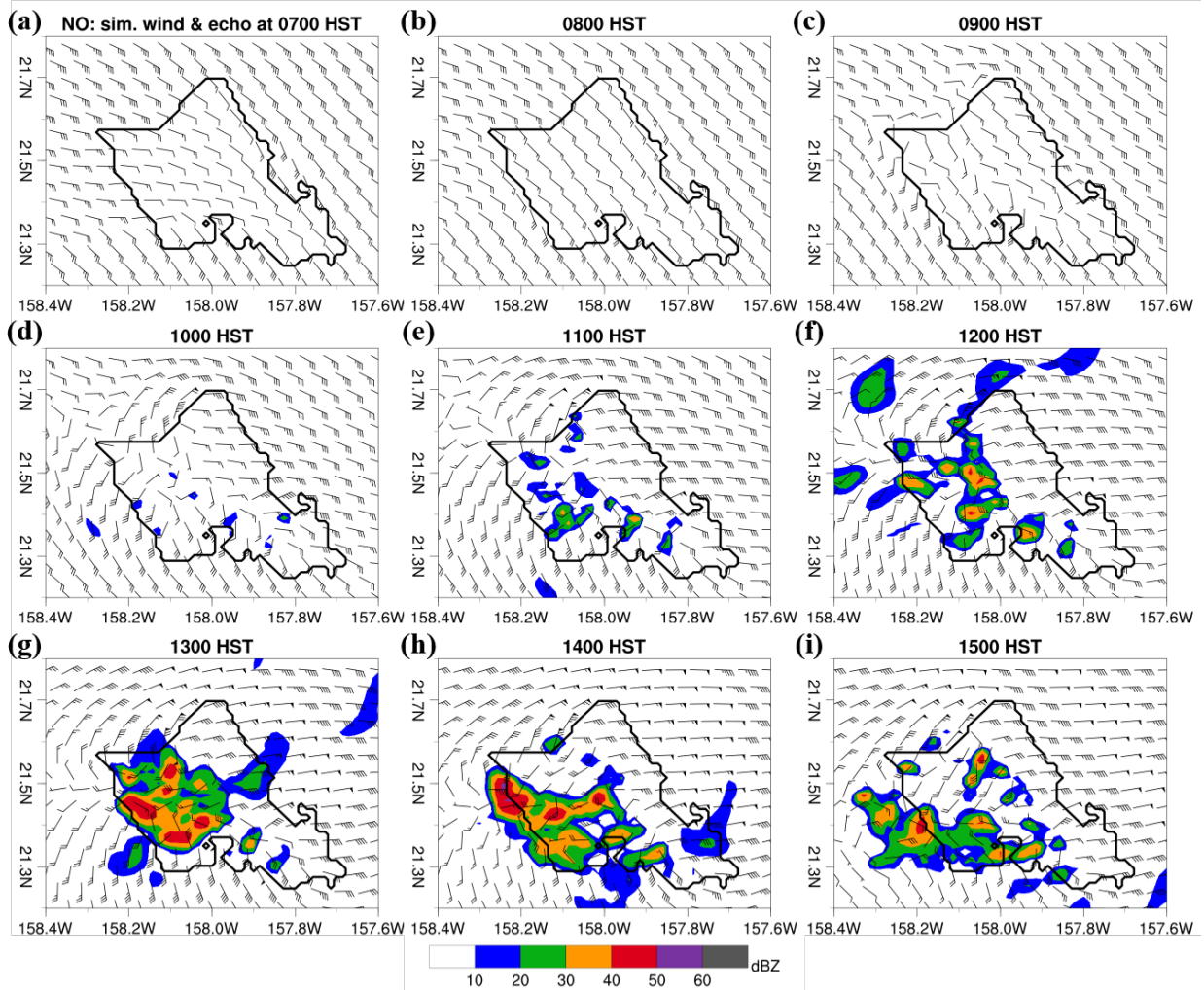


Fig. 0.16 Same as Fig. 4.13, but for the no orographic run.

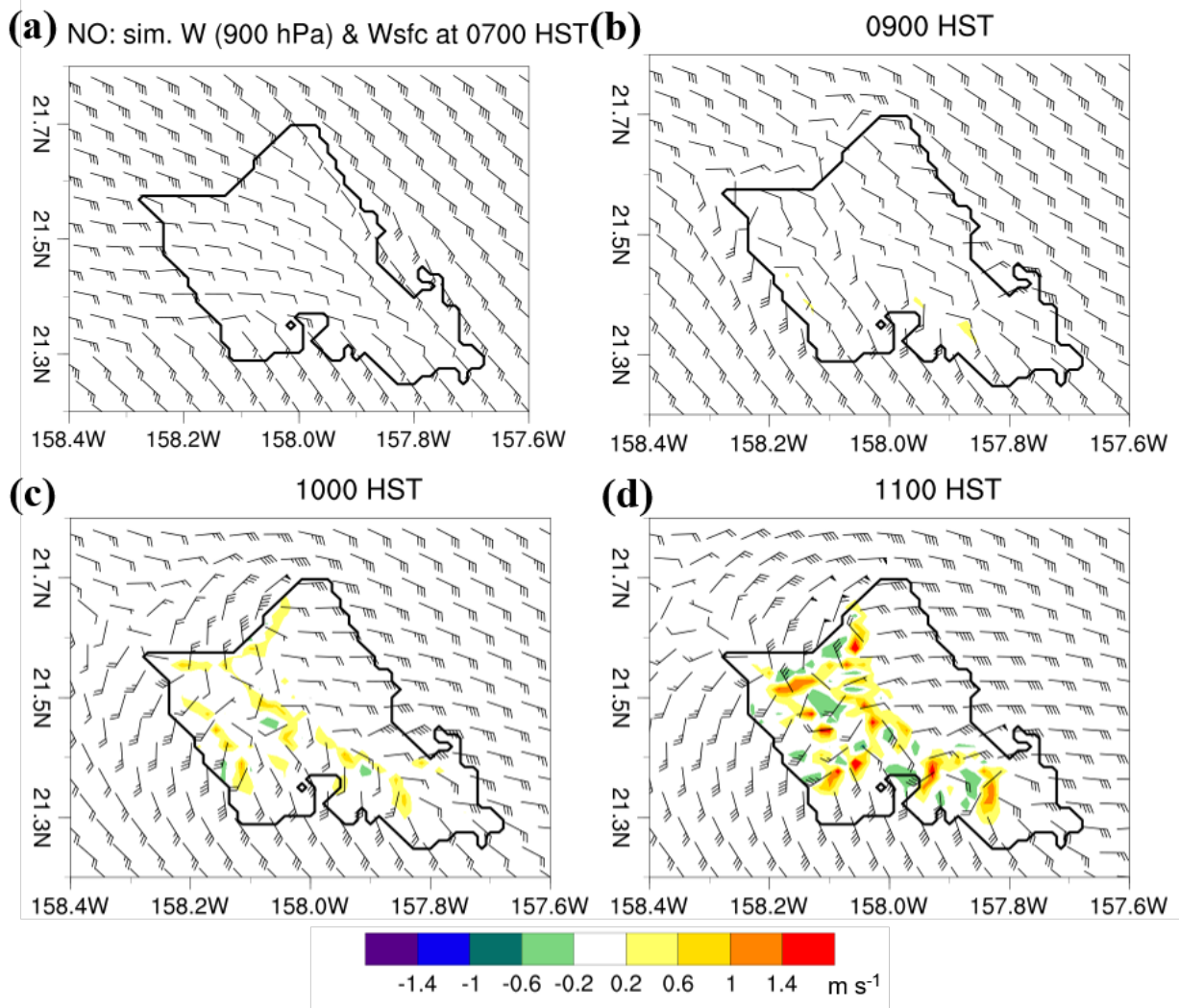


Fig. 0.17 Same as Fig. 4.12, but for the no orographic run.

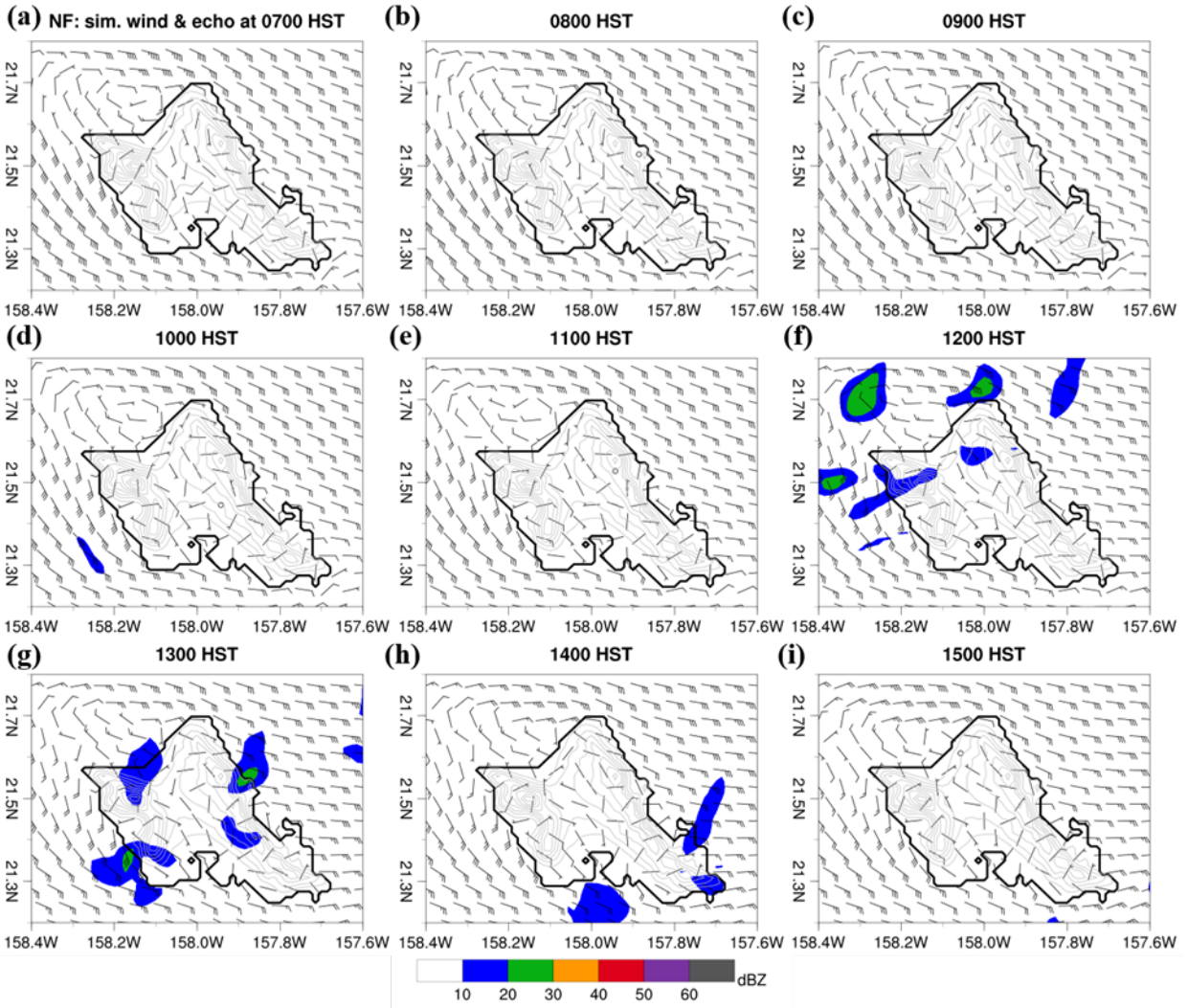


Fig. 0.18 Same as Fig. 4.14, but for the no surface flux run.

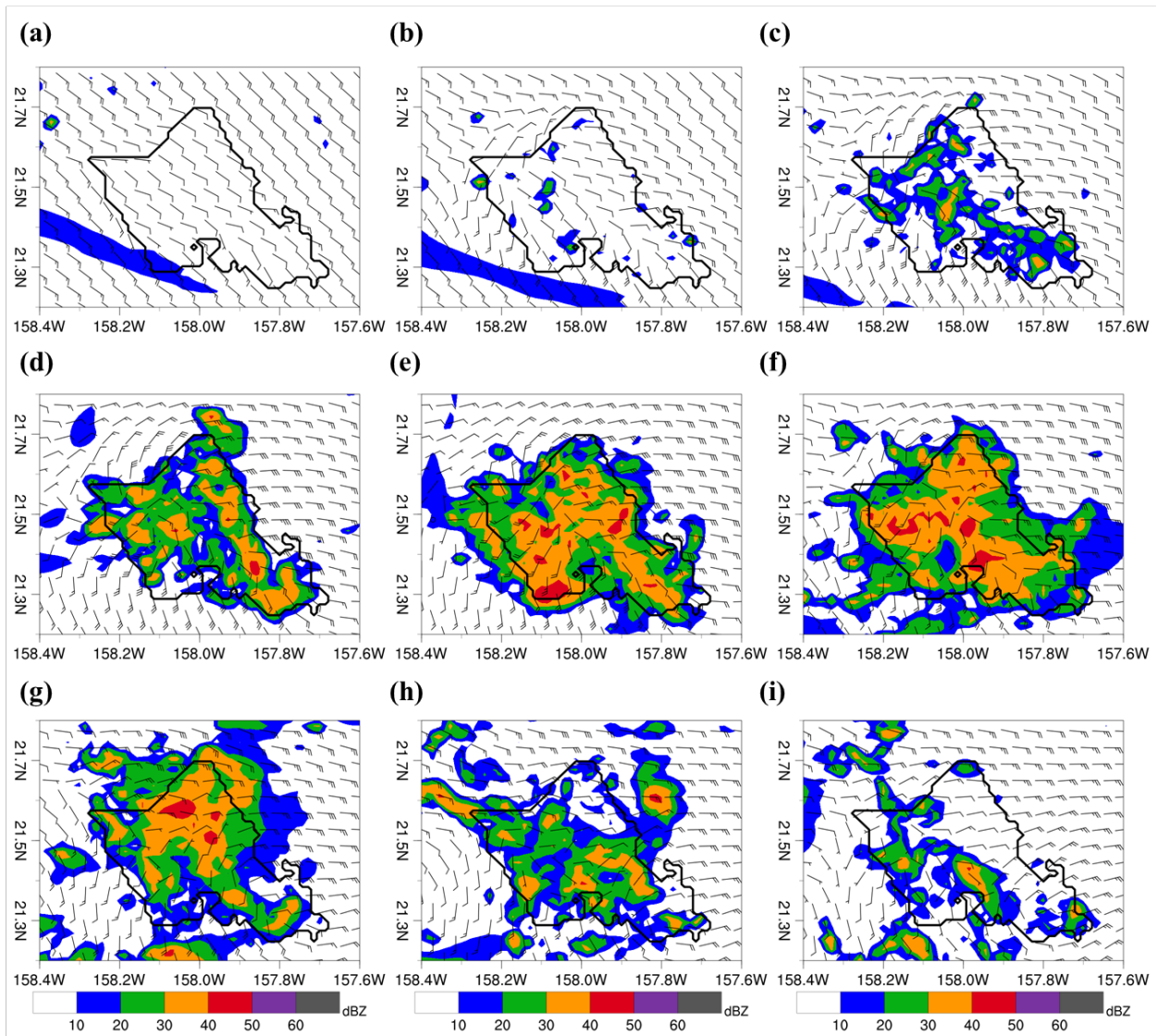


Fig. 0.19 Mean simulated radar reflectivity (dBZ, color shades), mean simulated surface wind (m s^{-1} , black wind barbs), and mean observed surface wind (m s^{-1} , red wind barbs) from the 13 NoOrog runs at (a) 0900, (b) 1000, (c) 1100, (d) 1200, (e) 1300, (f) 1400, (g) 1500, (h) 1600, and (i) 1700 HST. Pennants, full barbs, half barbs, and open circles represent 5 m s^{-1} , 1 m s^{-1} , 0.5 m s^{-1} and calm, respectively.

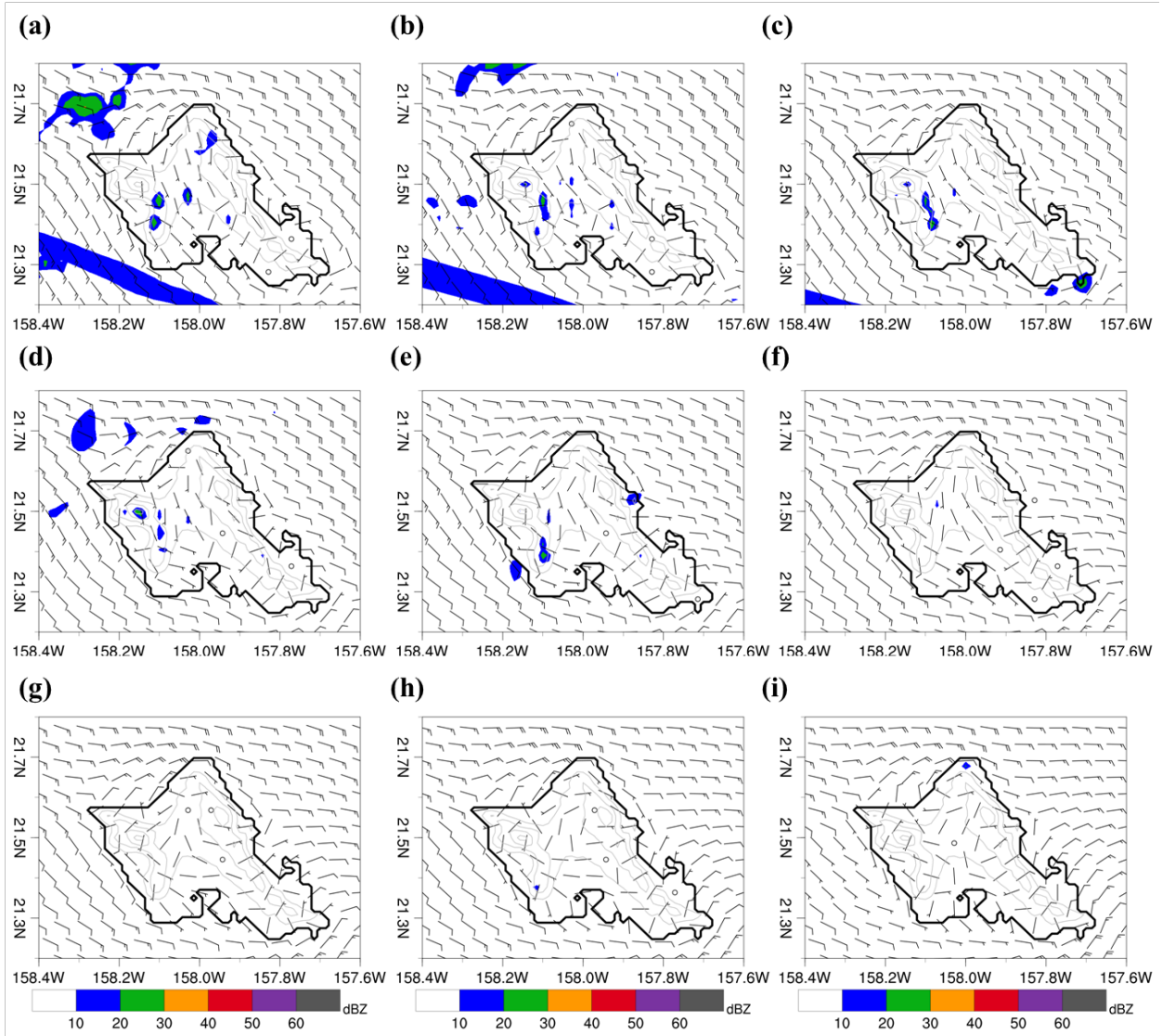


Fig. 0.20 Same as Fig. 4.19, but for NoFlux runs.

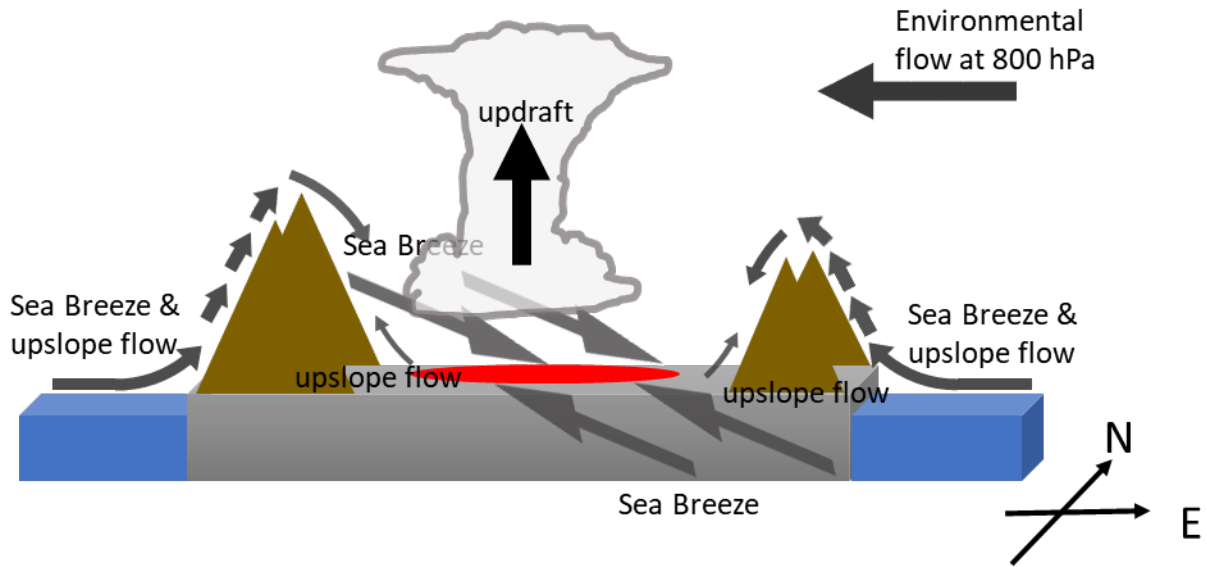


Fig. 0.21 A schematic diagram showing the island-induced airflow for the development of the short-lived afternoon heavy rainfall events over Central O‘ahu under weak wind conditions ($< 3 \text{ m s}^{-1}$) and favorable large-scale settings. The red circle shows the area with low-level convergence.

Chapter 5 The Factors Affecting Orographic Precipitation over Kaua‘i

5.1 Introduction

In the trade wind region, a subsidence inversion generally limits cloud tops to a maximum height of 2 km, resulting in most precipitation under trade wind conditions being from warm clouds. Though limited in the warm rain process, considerable rainfall and rainfall gradients have been observed over the mountainous islands under trade wind conditions. Atmospheric moisture in the tropical ocean regions is abundant and the geometry, orientation, and small-scale topographic features dictate where maximum precipitation will occur (Kleeman 1989; Barros and Lettenmaier 1993; Lenters and Cook 1995; Seluchi and Marengo 2000; Vera et al. 2002; Garreaud et al. 2003; Egger et al. 2005; Bhushan and Barros 2007; and others).

Over the Hawaiian Islands, trade winds and the inversion prevail 93% of the time during the summer months (Schroder 1993). Rainfall analyses in the Hawaiian Islands have shown the dependence of the rainfall maximum location on mountain heights (Giambelluca et al. 1986; 2013). For the mountaintops above the trade wind inversion (~ 1.9 km), the rainfall maximum lies on the windward slope. By contrast, for mountains with tops below the trade wind inversion, such as Kaua‘i and O‘ahu, the rainfall maximum occurs over the mountaintops.

Smith (1989) pointed out that “Kaua‘i is about as high as it can be without flow splitting and therefore receives enormous rainfall” on its mountaintop. Mt. Wai‘ale‘ale on Kaua‘i has a height of about 1,598 m and an Froude number (Fr) of about 0.6 under typical trade wind conditions. Ramage and Schroeder (1999) showed that at the summit of Mt. Wai‘ale‘ale significant rain results

from moderate or fresh trade winds being lifted along the eastern escarpment, but only when a band or area of cumulus extends upwind of the mountain. Cloud lines associated with shear lines, synoptic disturbance associated with upper-level troughs, or even dying tropical cyclones to the south account for much of the rain, though short-lived mesoscale cloud systems are also critical. The importance of pre-existing cumulus cloud upstream has also been confirmed by Hartley and Chen (2010) who studied the relationship among the orographic lifting, rainfall frequency and rainfall amount over O‘ahu.

In Hawai‘i, island size is another factor that can affect the island-scale circulations, weather, and climate. Terrain size is considered as a factor influencing surface friction (Grubišić et al. 1995) and surface thermal forcing (Reisner and Smolarkiewicz 1994), which may affect the island-scale circulations. Based on a linear theory of moist stable orographic precipitation, Smith and Barstad (2004) suggested that the location of the maximum rainfall shifts from the windward slope to the hilltop as mountain width in line with the flow decreases. For narrow mountains and high wind speeds, spillover is possible. Yang and Chen (2008c) studied the effects of terrain and sizes on rainfall for the island of Hawai‘i using a mesoscale model. Their results indicate that the island size affects orographic lifting, surface forcing, and the advection timescale for an air parcel to reach the mountaintop. For the island of Kaua‘i, the advection time scale between the air parcel reaching the LFC and the summit is comparable to the typical timescale for the development of trade-wind showers (~ 20 min) (Takahashi, 1988), resulting in maximum orographic precipitation to occur at the mountaintops.

A previous observational study over the island of Hawai‘i (Carbone et al. 1998) showed a strong positive linear relationship between the rainfall over the windward side and Fr . For example, the rainfall maximum increases to 10 times the oceanic average with elevated Fr (> 0.3). For Fr

below typical trade wind conditions (< 0.3), the maximum rainfall is only five times greater than over the open ocean. Fr is regarded as a non-dimensional parameter describing the strength of island blocking. From these observations, Carbone et al. suggest that the rainfall production on the windward side of the Big Island is statistically related to the strength of orographic blocking as defined by Fr and modeled by Smolarkiewicz et al. (1988). The overall motivation for this work is to improve our understanding of mechanisms responsible for the occurrence of a rainfall maximum over Kaua‘i among the Hawaiian Islands, with emphasis on the interaction among orographic effects, terrain height, and island size.

5.2 Method

According to long-term July–August mean of TPW and wind in Chapter 3 (Fig. 3.2 and 3.3), July–August 2013 is used as a reference for typical summer conditions. First, simulations with the updated land use, soil type, and terrain height are conducted as control simulations (referred to as CTRL). The initial soil temperature and soil moisture for the WRF/LSM were generated from model simulations during June 2013 to obtain the updated mesoscale surface properties which are not well-described in the CFS data. The domain setup is a 4-way nesting with horizontal grid sizes of 27, 9, 3, and 1 km and horizontal dimensions of 100×80 , 109×97 , 112×73 and 112×100 (Fig. 5.1), respectively. The top of Mt. Wai‘ale‘ale is 1425 m in the innermost domain. The elevation smoothing inherent to the 1-km grid decreases the actual mountaintop (1598 m) by 179 m. In addition to the CTRL run, the following model sensitivity tests are conducted: 1) reducing the mountain height to a similar height as the Ko‘olau Mountains on O‘ahu (792 m) while the island size remains the same (referred to as RTH). The Fr of RTH is greater (~ 0.6) than that of CTRL (~ 0.35); 2) shrinking the island in the E-W direction to half that of CTRL without changing the mountain height (referred to as SZ). In the SZ run, the Fr is the

same as in the CTRL run, but the terrain is steeper in the E-W direction; and 3) transplanting Kaua'i to the geolocation of O'ahu (referred to as RP) to assess the hypothesis that the northernmost island receives more rainfall due to frontal systems from the northwest. Rainfall for O'ahu is also simulated during the same period to compare with the RP runs (referred to as CTRL_Oahu). The initialization and simulation procedure for the WRF/LSM for RTH, SZ, and RP are the same as for CTRL. The land surface properties (vegetation cover, soil type, and land use type) of RTH are identical to CTRL. The island in the SZ run is centered at the mountaintop (1,425 m) of CTRL in the E-W direction. Therefore, the mountaintop height in the SZ run is the same as in CTRL. To shrink the island size in the E-W direction, the odd-numbered grids, starting from the coordinate origin (mountaintop location) and moving in the east and west directions, are removed. For the RP run, the island of Kaua'i is replaced by the island of O'ahu with the updated land surface properties from the same dataset. The terrain of RTH, SZ, and RP are shown in Fig. 5.2.

Although trade wind conditions are persistent during the summer months, extreme weather events (e.g. tropical cyclones) may contaminate the dataset used in this chapter, which focuses on orographic rainfall under typical trade wind conditions. Therefore, the 1000-hPa CFS wind direction at an upstream (159.5°E , 22°N) at 0000 UTC is used to determine the trade wind conditions. Winds between 60–90 degrees at this location are considered as trade wind days. This criterion indicates 43 days during July–August 2013 as trade wind days. However, as shown in Chapter 4, a synoptic upper-level trough may accentuate rainfall under weak trade wind conditions. The CFS 500-hPa weather map is used to remove days in which the Hawaiian Islands are beneath an upper-level trough. In this case, the total trade wind days without synoptic disturbances are 38 days. There are nine hourly weather stations with datasets compiled by MesoWest during the 38

trade winds days (Fig. 5.2 and Table 5.1). Five of these stations are from the RAWS network and the others are from NWS network (Table 5.1). Due to the limited amount of stations during this period, four of the RAWS stations, which report observations at 35 min point of each hour, are also included. The observed surface wind speed, surface wind direction, air temperature, and dewpoint from these stations are used to validate the model simulations during the 38 trade wind days. Eight hydronet stations and 5 USGS stations were reporting rain gauge data over Kaua'i during July–August 2013 (Fig. 5.1b, blue dots). Both the hydronet and USGS rain gauge networks report their measurements at 15 min intervals with a resolution of 0.254 mm (0.01 in.). The location and elevation of the rain gauges are listed in Table 5.3

5.3 Model Results

5.3.1 Simulated Mean State

Based on the mean observed and simulated wind during the trade wind days of July – August 2013 (Fig. 5.4a), the flow decelerates and deflects as it approaches Kaua'i island because of orographic blocking and surface friction. Strong winds ($> 8 \text{ m s}^{-1}$) are simulated over the northwestern and southwestern corners of Kaua'i, resulting from tip effects around the corners of the island (Ramage and Oshiro 1977; Nguyen et al. 2010). On the windward side of Mt. Wai'ale'ale, the wind speed is at a minimum over the windward slopes ($< 2 \text{ m s}^{-1}$ versus $6\text{--}7 \text{ m s}^{-1}$ over the open ocean; Fig. 5.4a). Another weak wind region ($< 2 \text{ m s}^{-1}$) is simulated over the western coast and the western slopes of Mt. Wai'ale'ale. The simulated weak wind region extends from the western slope of Mt. Wai'ale'ale to the leeside ocean.

Error statistics for the 9 MesoWest stations are listed in Table 5.2. Generally, the simulated winds are comparable with surface observations with small bias ($< 1 \text{ m s}^{-1}$) and RMSE ($< 3 \text{ m s}^{-1}$)

¹). However, the errors related to surface air temperature and dewpoint are largest over high elevations and the western coasts. The model underestimation of surface temperature at several of the RAWS stations (MNRH, PLRH, POPH, and WHGH) may result from the time difference between the time of the observations and the time of the model output. A comparison of the mean observed and simulated winds at the 9 MesoWest stations showed that the model is capable of simulating the effects of the terrain on wind speed island wide. However, the mean wind directions related to weak wind regions (mean wind speed $< 1 \text{ m s}^{-1}$) are relatively inconsistent. For instance, the simulated wind direction over the western coast is northeasterly instead of the observed northwesterly.

Island-scale airflows are sensitive to the diurnal cycle (Fig 5.4b and 5.4c). At 1400 HST, the wind speed over the windward coast is $4\text{--}5 \text{ m s}^{-1}$, resulting from the combination of prevailing trade and onshore flow (Fig 5.4b). On the leeward side, westerly onshore flow is observed and simulated over the western coast. The tip-jets are more significant when the wind speed is $>9 \text{ m s}^{-1}$. At 0500 HST, the decrease in wind speed from the open-ocean ($6\text{--}7 \text{ m s}^{-1}$) to the windward coast ($2\text{--}3 \text{ m s}^{-1}$) is significant, in agreement with observations (Fig 5.4c). With cooler air over the island, the simulated flow deceleration on the windward side is more significant with a wind speed minimum ($1\text{--}2 \text{ m s}^{-1}$) at the foothills as compared to ($3\text{--}4 \text{ m s}^{-1}$) at 1400 HST. The winds over the island interior are calm ($1\text{--}2 \text{ m s}^{-1}$). Weak katabatic winds were simulated on the eastern slopes of Mt. Wai‘ale‘ale. Over the western coast, downslope/offshore flow dominates at night.

5.3.2 Simulated Total Rainfall of CTRL

There is a simulated rainfall accumulation maximum at the top of Mt. Wai‘ale‘ale with a secondary maximum over the Makaleha Mountaintops, which are located on the northeastern side of Mt. Wai‘ale‘ale. There is a minimum in rainfall accumulation over the southwestern coast (Fig.

5.4d). These rainfall distributions are in agreement with observed rainfall which show that less than 10 mm of rainfall occurs over the southwestern coast and that maximum rainfall (466 mm) occurs at the Mt. Wai‘ale‘ale rain gauge (station 13) at 1570 m in elevation. The observed rainfall distributions reveal large spatial variations according to the terrain. On the northern coast, the observed rainfall accumulation at station 2 (128 mm) is much larger than at station 4 (30 mm), even though station 4 is on the mountain slopes (30 m). Over the eastern slopes of Mt. Wai‘ale‘ale, the observed rainfall accumulation at station 12 (466 mm) is twice that of station 13 (235 mm). However, the distance between these two stations is only ~ 7 km. For the windward stations (1, 5, and 7) and the western stations (6, 9, 10, and 11), the observed rainfall accumulations are relatively homogeneous, compared to the northern coast and the mountain regions.

The time series of daily observed and simulated rainfall during the trade wind days are shown in Fig. 5.5. Even under trade wind conditions, the daily rainfall still has a great deal of variation among stations, from over 60 mm to less than 10 mm (stations 2, 12, and 13, Fig. 5.5). The error statistics of accumulated rainfall show that the model successfully simulates a pattern of precipitation with extreme gradients of rainfall near the eastern slopes of Mt. Wai‘ale‘ale and the highest rainfall amount over the crest of Mt. Wai‘ale‘ale. However, the model has positive bias for the stations over the western slopes of Mt. Wai‘ale‘ale (stations 10 and 11).

5.3.3 Sensitivity to Terrain Heights, Steepness of Mountain, and Geolocations

With a reduced terrain height (RTH) comparable to the Ko‘olau Mountains (~ 800 m), Fr of the RTH run is greater (~ 0.7) than Fr of the CTRL. The simulated airflows over the windward slopes decelerate from 5 m s^{-1} upstream to 2.5 m s^{-1} due to orographic blocking, but airflow deflection over the island becomes insignificant. The orographic rainfall index ($\text{ORI} = \text{TPW} \times w_{sfc}$), where w_{sfc} represents vertical motion at the surface due to orographic lifting, has been

proposed as a predictor of orographic precipitation (<http://www.soest.hawaii.edu/met/Students/ter/HOP/index.html>). Comparing the ORI of CTRL and RTH, RTH exhibits smaller ORI over the windward slopes due to less orographic lifting (Fig. 5.8c). Trade wind rainfall over the top of Mt. Wai‘ale‘ale (6.9 mm day^{-1} , Fig. 5.7c) is about 43% of that found in the control run (15.8 mm day^{-1} , Fig. 5.7a), and rainfall gradients between the windward coast ($\sim 1 \text{ mm day}^{-1}$) and the mountaintops (6.9 mm day^{-1}) decrease. The position of the rainfall maximum, which is still simulated at the mountaintops, is relatively uninfluenced by Fr or terrain steepness for mountaintops below the trade wind inversion. These results indicate that the rainfall maximum is controlled by more than just Fr , and that the ORI may not serve as a precise predictor for the orographic rainfall amount.

In the RTH run for Kaua‘i, the top of Mt. Wai‘ale‘ale is close in the height to the top of the Ko‘olau Mountains ($\sim 800 \text{ m}$) on O‘ahu. Nevertheless, the simulated rainfall amount at the top of Mt. Wai‘ale‘ale (6.9 mm day^{-1} , Fig. 5.7c) is less than the simulated rainfall over the Ko‘olau Mountains (11.8 mm day^{-1} , Fig. 5.7b). Orographic lifting on the windward side of O‘ahu is also more significant than on the windward side of Kaua‘i due to steeper terrain. To investigate the effects of terrain steepness further, the model is run with the island of Kaua‘i shrunk in the E–W direction (the SZ run) under trade wind conditions while the elevation of the mountaintop is kept the same as in the CTRL run. With steeper terrain, orographic blocking is more significant with greater flow deflection over the windward slope of Mt. Wai‘ale‘ale. Wind speeds decrease (1 m s^{-1}) off the windward coast (Fig. 5.7d) as well as a result of orographic blocking. The ORI of the SZ run over the windward slope increases due to the doubled steepness (Fig. 5.8d). Rainfall is primarily simulated over Mt. Wai‘ale‘ale (17.4 mm day^{-1}) and the Makaleha Mountains (11.5 mm day^{-1}) in the SZ run with a significant rainfall gradient from the windward coast ($\sim 3 \text{ mm day}^{-1}$) to

the mountaintops ($>10 \text{ mm day}^{-1}$). Over the windward slope, the simulated rainfall amount above 500 m in the SZ run is significantly greater than in the CTRL run (Fig. 5.7d). Less rainfall is simulated over the leeward coast and western slopes in the SZ run as compared to the CTRL run. Despite the Fr being the same between the SZ and CTRL runs (~ 0.7), the simulated rainfall on the windward slopes and over the peaks of Mt. Wai‘ale‘ale is higher (17.4 mm day^{-1} vs. 15.8 mm day^{-1}) in the SZ than in the CTRL. The location of the rainfall maximum in the SZ run also shifts 1 km westward as compared to the CTRL run.

The results of the sensitivity test signify the importance of factoring in terrain steepness in the modeling of island scale rainfall gradients and the prediction of rainfall amount (Table 5.5). CTRL and SZ have the same height of mountaintop. With doubled steepness in SZ, daily rainfall maximum of SZ is only 10% greater than it of CTRL. Compared RTH and RP runs, both simulations have the same height of mountaintop ($\sim 790 \text{ m}$) with the same Fr . The steepness of RP is ~ 4 times greater than it of RTH, but the daily rainfall maximum of RP is only 2 times larger than it of RTH. These results indicate that steepness is not linear correlated to rainfall amount. The steepness is included in the estimation of orographic precipitation using ORI. However, the ORI maximum is not location at the rainfall maximum. Thus, the results from the sensitivity test in which the island size is shrunk imply the effect of steepness on rainfall amount. With a reduced size, orographic lifting is more significant (Fig. 5.8d), and the simulated rainfall is 10% greater than in the CTRL run due to a steeper terrain (Fig. 5.7d). The location of the rainfall maximum shifts westward 1 grid point (1 km) compared to the CTRL as well due to enhanced orographic lifting (Fig. 5.7d).

In addition to steepness, rainfall production is also related to the available moisture in the environment. The synoptic environment of Kaua‘i has greater moisture than O‘ahu during July–

August 2013 (Fig. 3.2b). Despite having less moisture in the environment, the ridge tops of the Ko‘olau Range receive more rainfall (11.8 mm day⁻¹, Fig. 5.7b) than the RTH run (6.9 mm day⁻¹, Fig. 5.7c) even though the mountain heights for both runs are almost identical. However, the steepness of the windward slope of O‘ahu is greater than the slopes in the RTH run. To assess the specific effects of environmental moisture on rainfall production, the simulated terrain of O‘ahu is transferred to the location of Kaua‘i (the RL run). The simulated rainfall for O‘ahu in the RL run is higher (14.0 mm day⁻¹) than at its original location (11.8 mm/day) but still less compared to the Kaua‘i control run (15.8 mm day⁻¹). Based on the ORI calculation, the location of the ORI maximum (Figs. 5.8b,e) is not over the ridge tops of the Ko‘olau Range, where one finds the simulated rainfall maximum (Figs. 5.7b,e).

The moisture budget of the atmosphere over a model grid point is calculated as (Seager and Henderson 2013):

$$P - E = -\frac{1}{g} \frac{\partial}{\partial t} \int_0^{p_s} q dp - \frac{1}{g} \int_0^{p_s} \nabla \cdot (\mathbf{u}q) dp - \frac{1}{g} q_s \mathbf{u}_s \cdot \nabla p_s \quad (6.1)$$

where P is precipitation, E is evaporation, \mathbf{u} is the horizontal wind vector, q is the water vapor mixing ratio, P_s is the surface pressure, and g is the gravitational acceleration. In equation 6.1, the first term on the right-hand side is the moisture storage term, the second term is the vertically integrated moisture flux convergence, and the third term is the boundary term, which represents orographic lifting at the slope surface. The spatial patterns of the terms on the right-hand side of equation 6.1 are shown in Figs. 5.9–5.11. The analysis of the moisture budget shows that under trade wind conditions the storage term is negligible compared to the other two terms. The vertically integrated moisture flux convergence and the vertical moisture transport due to orographic lifting tend to cancel each other out over the windward slopes, suggesting that

horizontal moisture flux convergence may play an important role in the moisture budget for orographic rainfall under trade wind conditions (Figs. 5.10 and 5.11). The results indicate that orographic lifting is an important factor for rainfall production on the mountaintops below the trade wind inversion. However, orographic lifting alone may not be adequate to account for the trade wind rainfall.

5.4 Summary

In the moisture budget equation, orographically induced moisture flux convergence and orographic lifting at the slope surface are the two most dominant terms in regions with sloping terrain. The storage term is insignificant when computing monthly averages. Under undisturbed summer trade-wind weather, the moisture flux convergence over mountainous islands is related to orographic and local effects including: flow deceleration on the windward side due to orographic blocking, interactions between the incoming flow and offshore flow due to nocturnal and/or evaporative cooling, and convergence between the prevailing winds and opposing sea breezes in the leeside. Furthermore, moisture flux convergence is enhanced by latent heat release. The vertical motion above the slope surface could be attributed to mechanical lifting, convergence due to orographic blocking, or convergence between the thermally induced flows and prevailing flow, and enhanced by latent heat release as shown by previous observational studies. In addition, the orographic lifting could be affected by the diurnal heating cycle with daytime upslope/nighttime downslope flows. Based on the results of the sensitivity tests, previous theoretical arguments concerning orographic precipitation based on Fr or ORI are shown to be inadequate to account for the orographic precipitation amount under undisturbed trade-wind conditions. In these theoretical arguments the orographically induced moisture convergence and convective feedbacks are largely ignored.

Chapter 5 Tables

Table 5.1 The temporal resolution and geolocation of the nine weather stations during the 38 trade wind days in July–August 2013. The italicized stations represent the stations with observation time ending at 34–35 min.

STNID	NETWORK	Temporal Resolution	Lat	Lon	elevation(m)
HFO07	NWS	hourly (end at 02 min)	21.88	-159.43	12.192
HFO09	NWS	hourly (end at 02 min)	21.90	-159.60	6.096
MKAH1	RAWS	hourly (end at 11 min)	22.13	-159.72	548.64
PHLI	NWS	hourly (end at 53 min)	21.98	-159.34	45.1104
PHBK	NWS	hourly (end at 56 min)	22.04	-159.79	3.9624
<i>MNRH1</i>	RAWS	hourly (end at 34 min)	22.03	-159.76	26.2128
<i>PLRH1</i>	RAWS	hourly (end at 35 min)	22.09	-159.68	997.9152
<i>POPH1</i>	RAWS	hourly (end at 34 min)	22.04	-159.70	630.3264
<i>WHGH1</i>	RAWS	hourly (end at 35 min)	21.97	-159.66	159.7152

Table 5.2 Error statistics for the weather stations on the trade wind days.

STNID	U (m s ⁻¹)			V (m s ⁻¹)		
	BIAS	MAE	RMSE	BIAS	MAE	RMSE
HFO07	-0.7	1.2	1.4	-0.2	0.7	0.9
HFO09	1.5	2.2	2.7	0.4	1.1	1.4
MKAH1	-0.4	1.0	1.2	-0.7	1.2	1.5
MNRH1	-0.6	1.1	1.4	-0.3	1.3	1.7
PHBK	-0.5	1.2	1.5	-0.4	1.6	2.2
PHLI	0.7	1.4	1.8	0.7	1.1	1.4
PLRH1	-0.5	1.3	1.6	-0.7	1.1	1.2
POPH1	-0.6	1.3	1.6	-0.6	1.3	1.5
WHGH1	-0.6	1.9	2.8	-0.4	1.1	1.5
STNID	T (°C)			Td (°C)		
	BIAS	MAE	RMSE	BIAS	MAE	RMSE
HFO07	NaN	NaN	NaN	NaN	NaN	NaN
HFO09	-0.7	1.2	1.5	NaN	NaN	NaN
MKAH1	-1.1	1.5	1.9	-1.6	2.1	2.7
MNRH1	-2.0	2.1	2.5	-0.8	1.4	1.8
PHBK	0.5	1.0	1.2	-0.6	1.3	1.7
PHLI	-0.7	1.2	1.5	0.0	0.7	0.9
PLRH1	-1.7	2.1	2.4	-2.3	2.6	3.4
POPH1	-1.4	2.1	2.5	-1.6	2.2	2.9
WHGH1	-1.4	1.6	1.9	-0.9	1.5	2.0

Table 5.3 The geolocation and elevations of the 13 rain gauge stations during the 38 trade wind days in July–August 2013.

station name	station No.	network	Elevation (ft.)	Lat	Lon
Anahola NO.2	1	Hydronet	240	22.133333	-159.316667
Hanalei	2	Hydronet	5	22.195556	-159.493611
Hanapepe	3	Hydronet	370	21.936389	-159.588611
Ph Wainiha	4	Hydronet	101	22.2	-159.5667
Kapahi	5	Hydronet	530	22.102222	-159.386111
Kokee	6	Hydronet	4200	22.148611	-159.644722
Wailua UH EXP STN	7	Hydronet	550	22.065833	-159.396111
Kilohana	8	USGS	4000	22.15416667	-159.5947222
Waiakoali	9	USGS	3420	22.1245	-159.625
Mohihi Crsg	10	USGS	3420	22.11708333	-159.6011111
Waialae	11	USGS	4000	22.087	-159.5663889
Mt. Wai‘ale‘ale	12	USGS	5150	22.07088889	-159.4980556
N. Wailua Ditch	13	USGS	1110	22.0625	-159.4677778

Table 5.4 Error statistics for the 13 rain gauge stations during the trade wind days.

Station name	Station No.	Elevation (ft.)	Bias (mm)	MAE (mm)	RMSE (mm)
Anahola NO.2	1	240	0.0	3.2	6.8
Hanalei	2	5	-1.1	4.5	9.3
Hanapepe	3	370	0.5	0.7	1.6
Ph Wainiha	4	101	2.7	3.9	8.1
Kapahi	5	530	0.9	3.5	5.3
Kokee	6	4200	0.4	1.0	1.8
Wailua UH EXP STN	7	550	0.8	3.0	4.5
Kilohana	8	4000	-0.8	3.9	6.2
Waiakoali	9	3420	0.7	1.7	3.3
Mohihi Crsg	10	3420	1.5	2.2	3.9
Waialae	11	4000	3.7	4.4	9.6
Mt. Wai‘ale‘ale	12	5150	0.0	9.7	13.7
N. Wailua Ditch	13	1110	-2.6	5.5	11.3

Table 5.5 *Fr*, steepness over the eastern slope, and daily rainfall maximum (mm) sensitivity tests.

Run	Rainfall maximum (mm/day)	Mountaintop (m)	Steepness ($\frac{\partial h}{\partial x}$) (m/km)
CTRL Kaua‘i (CTRL)	15.8	1,424.7 (<i>Fr</i> ~0.7)	-75
CTRL O‘ahu (CTRL_Oahu)	11.8	791.6 (<i>Fr</i> >1)	~150
Reduced Kaua‘i Mt. top to Ko‘olau Mt. top (RTH)	6.9	769.3 (<i>Fr</i> >1)	~40
Double steepness of CTRL Kaua‘i (SZ)	17.4	1,424.7 (<i>Fr</i> ~0.7)	~150
Move O‘ahu to Kaua‘i (RP)	14.0	791.6 (<i>Fr</i> >1)	~150

Chapter 5 Figures

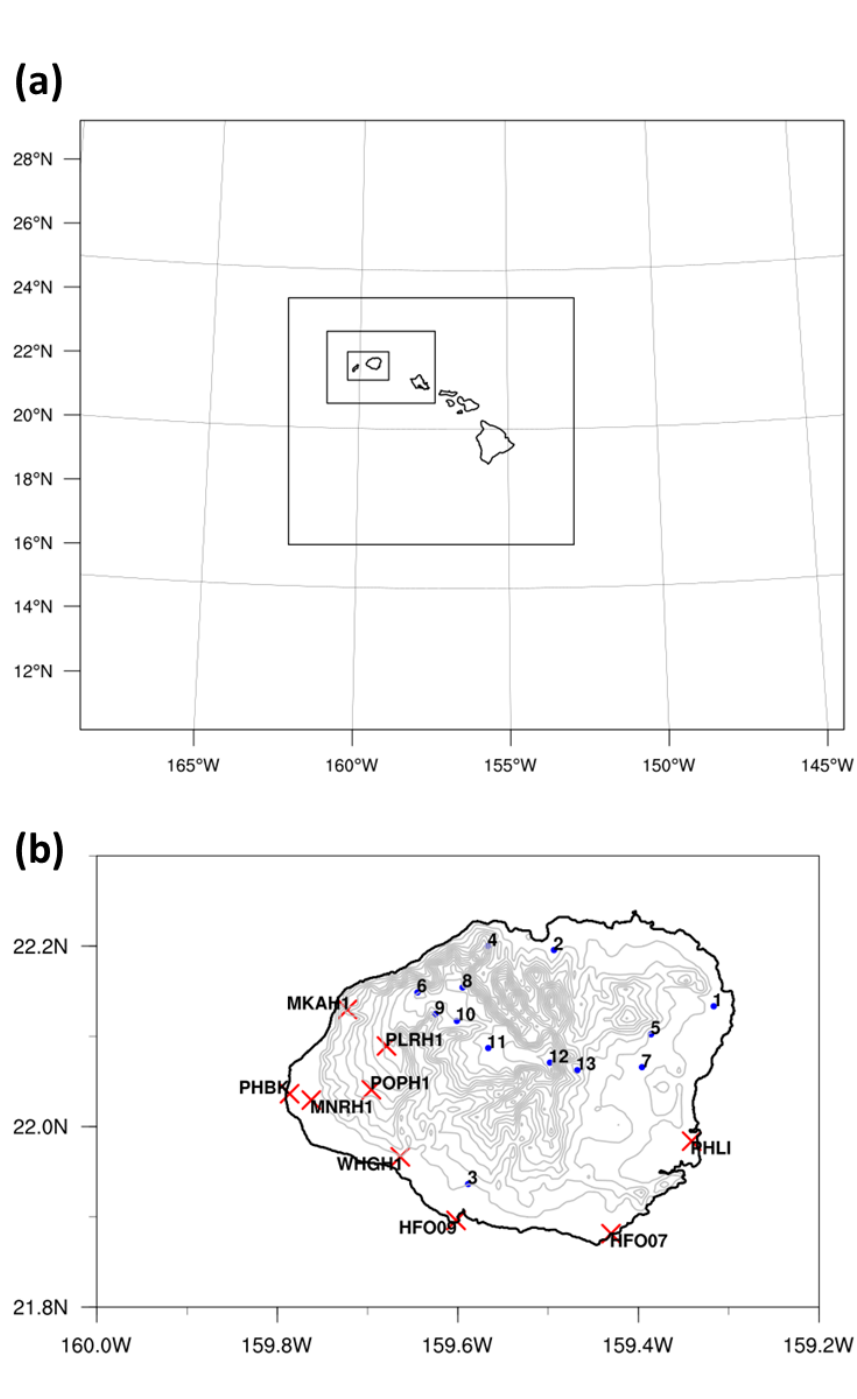


Fig. 5.1 (a) A map of the Hawaiian Islands. The 4 nested domains employed in the simulations with grid sizes of 27 km, 9 km, 3 km, and 1 km, respectively. (b) The island of Kaua'i.

Elevation contours are in 100-m intervals. A red x represents a surface weather station.
A blue dot represents a rain gauge.

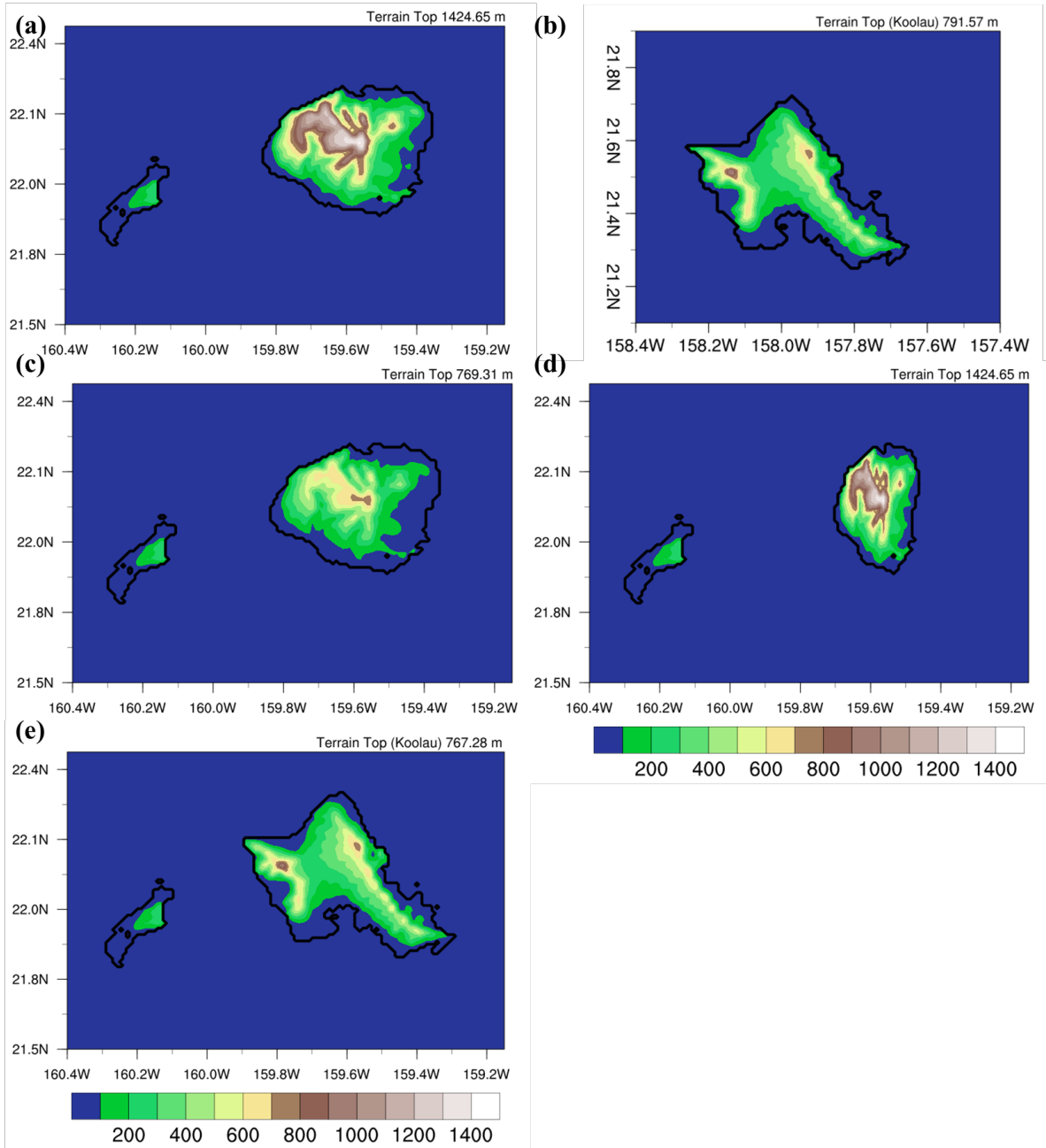


Fig. 5.2 The model terrain height (m) for (a) CTRL; (b) CTRL_Oahu; (c) RTH; (d) SZ and (e) RP.

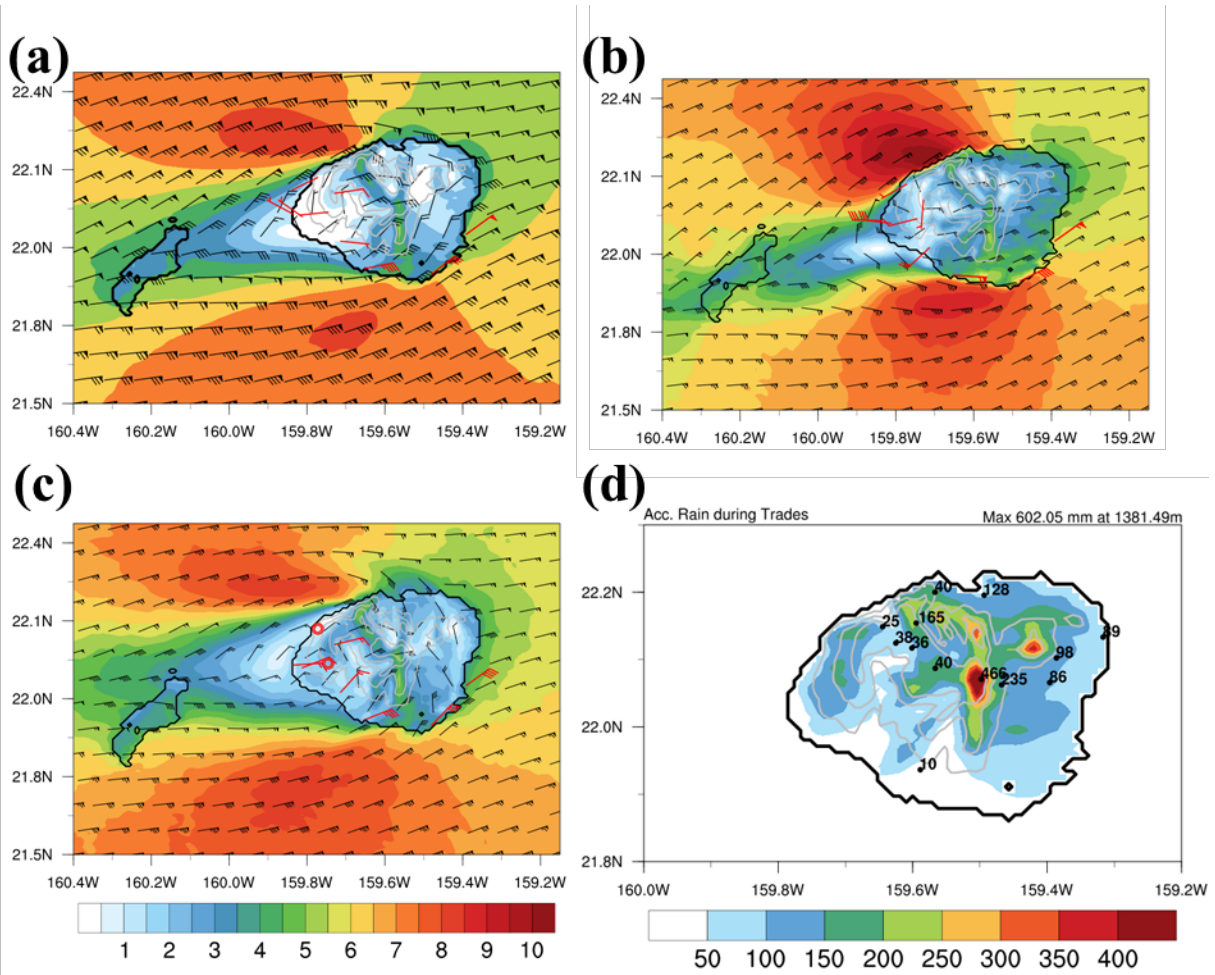
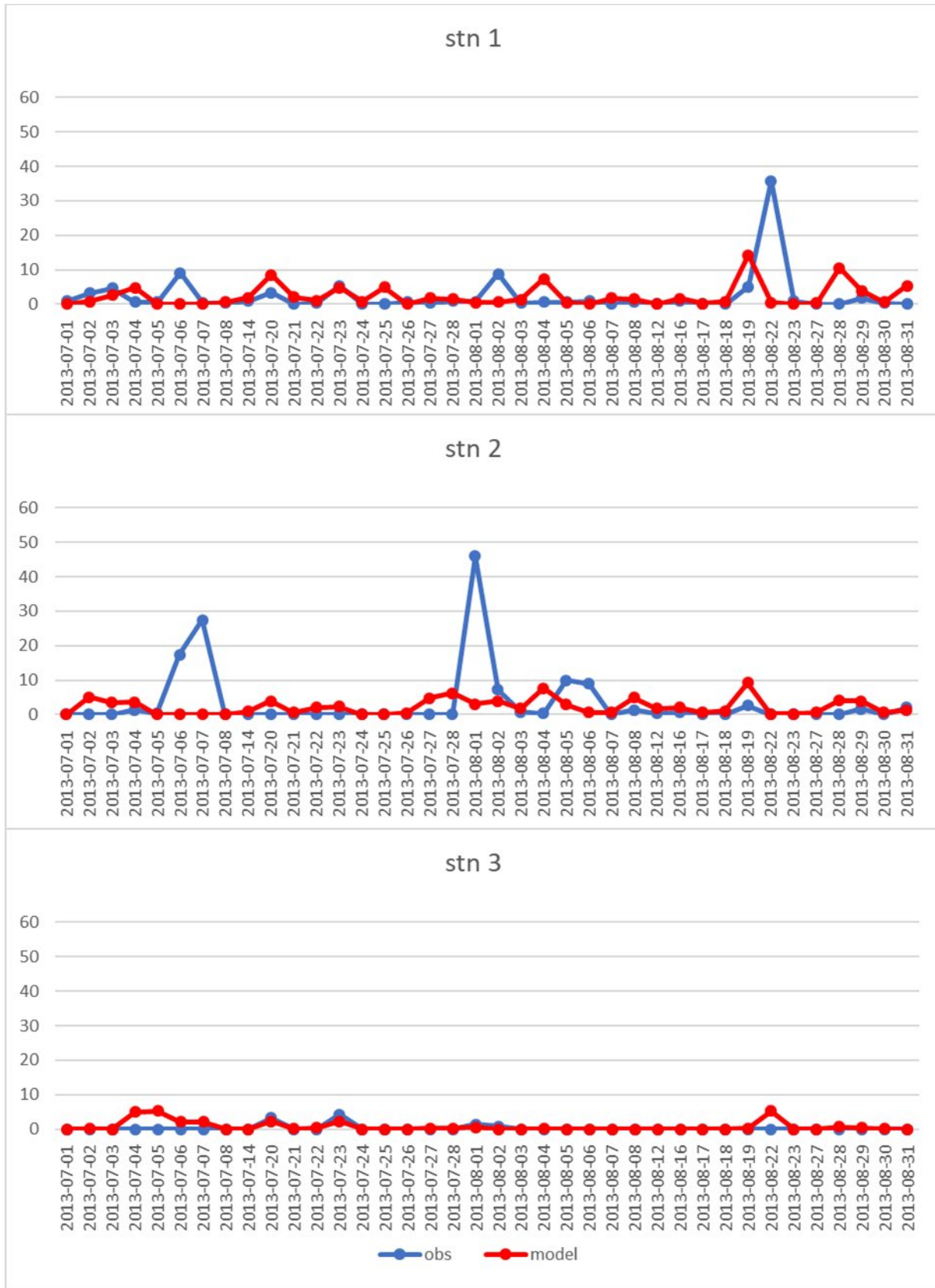
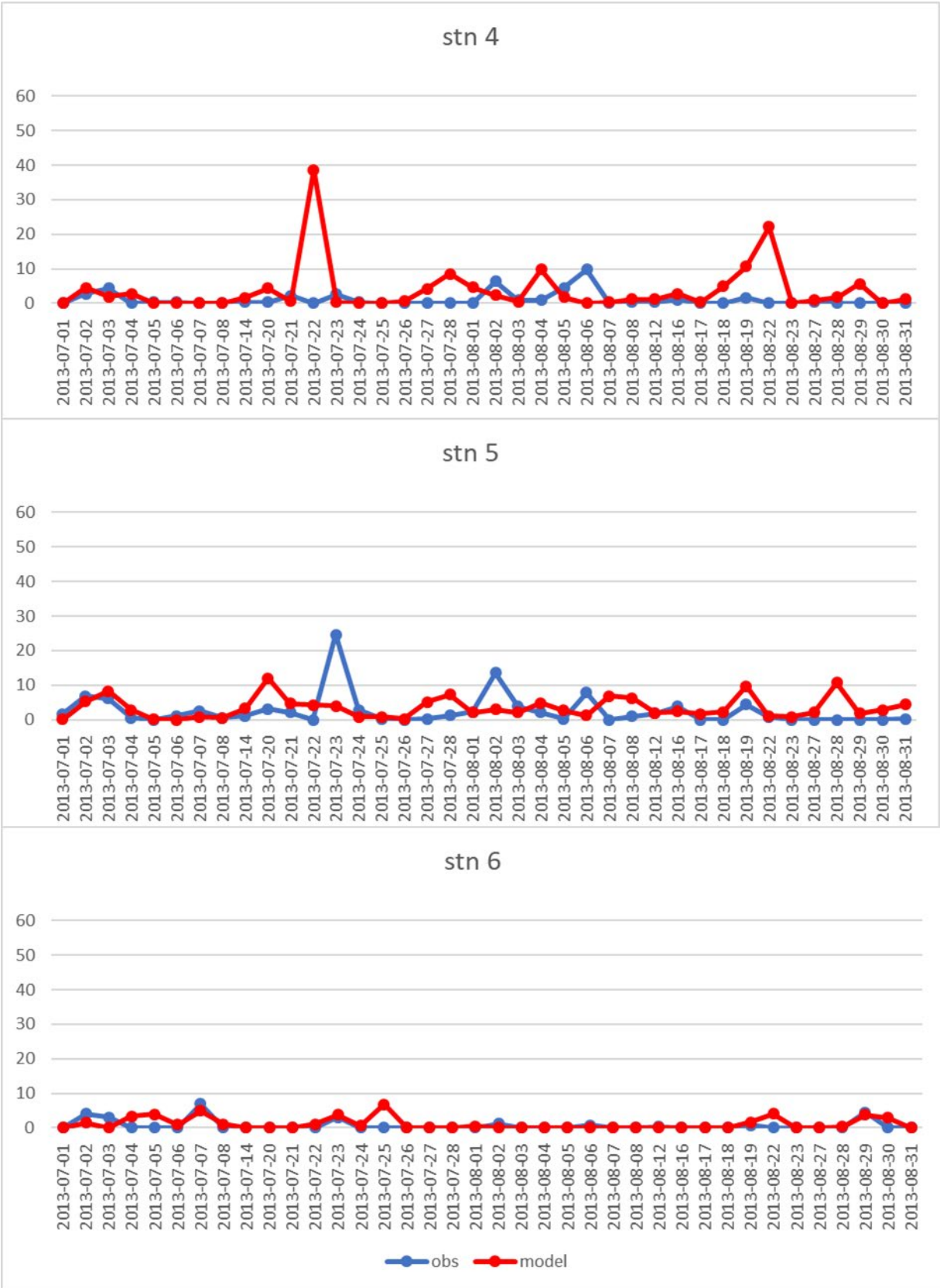
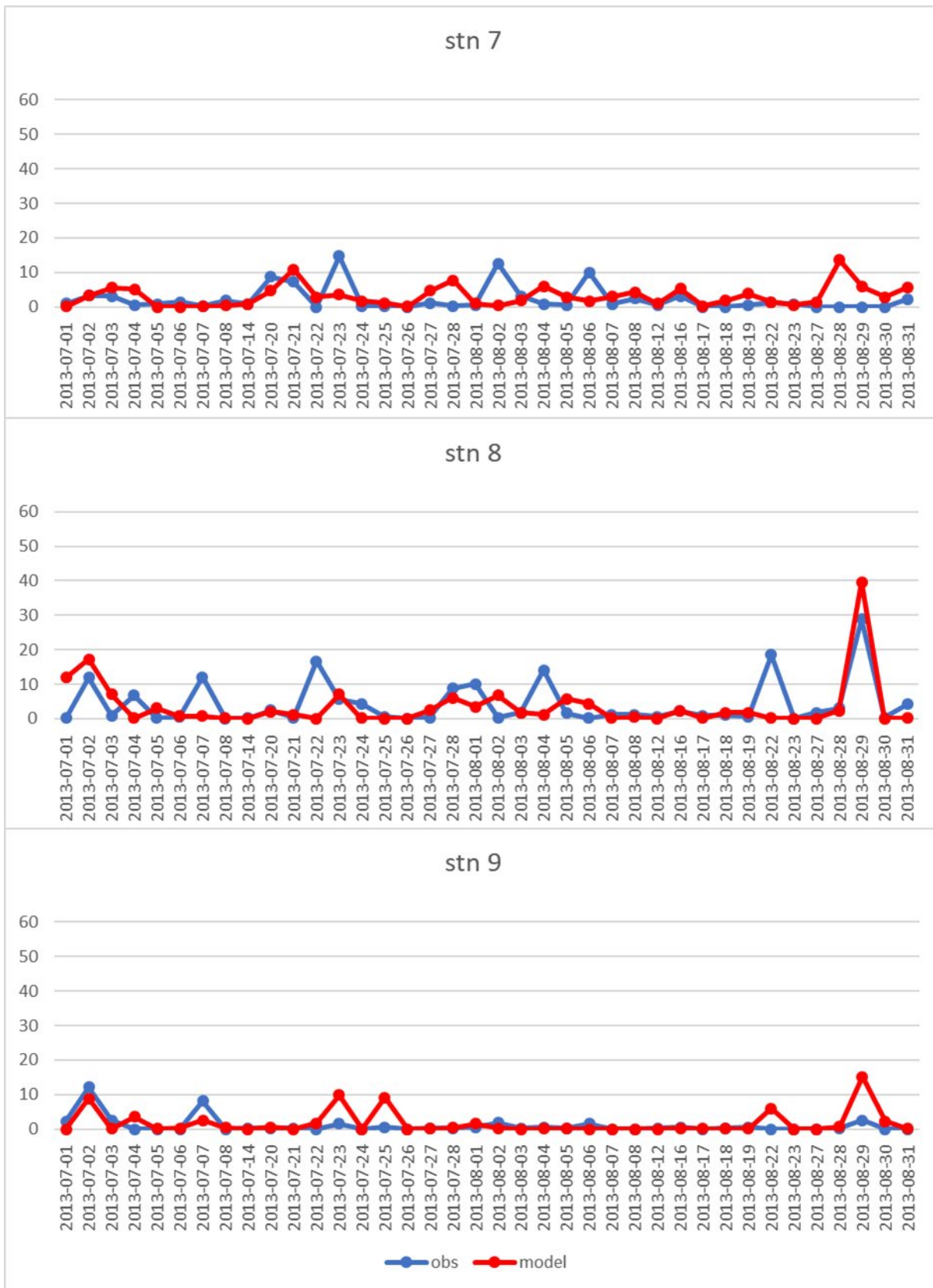
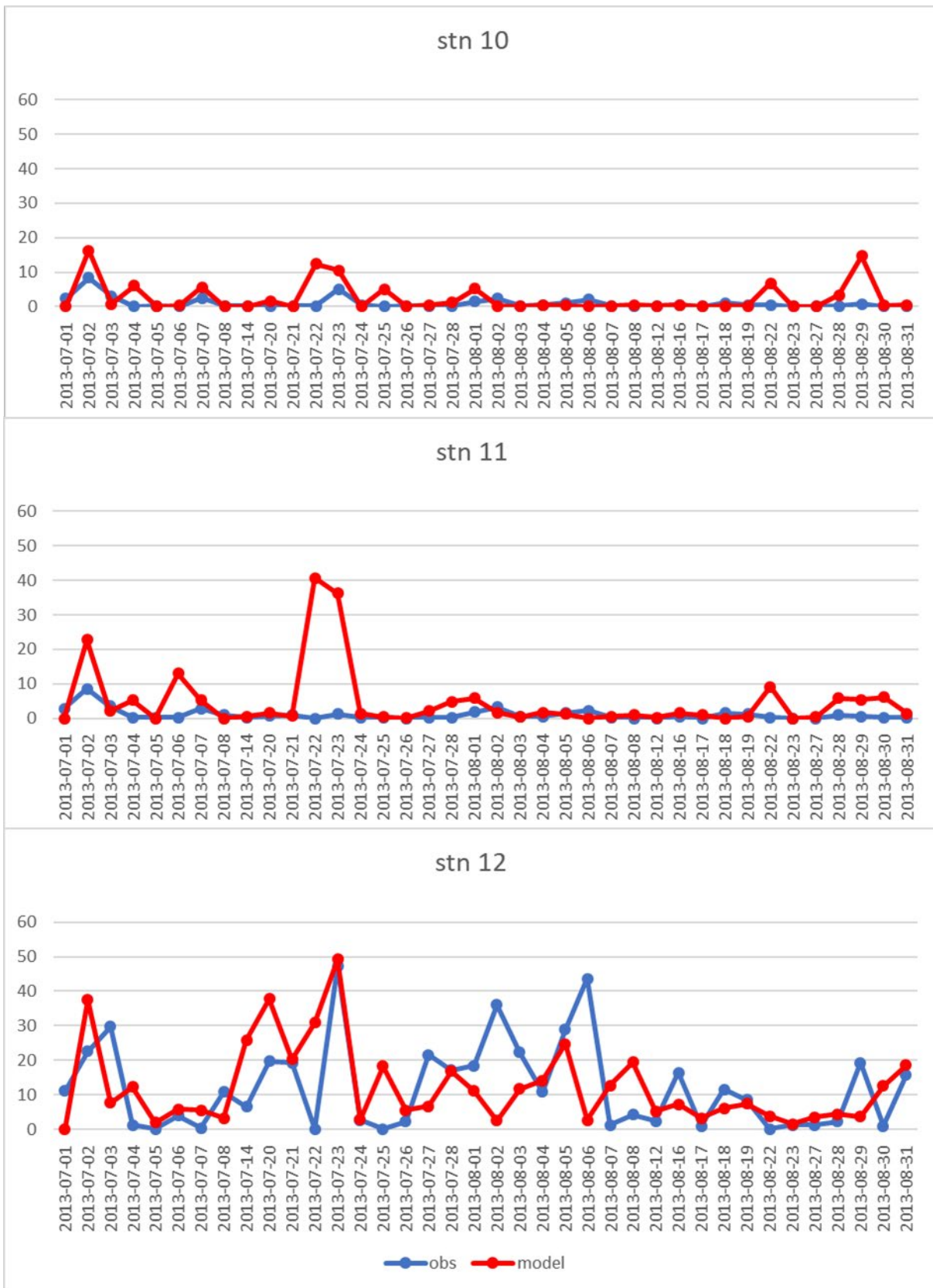


Fig. 5.3 The simulated mean surface wind (m s^{-1} , black wind barb), observed surface wind (m s^{-1} , red wind barb) and model terrain height (grey contour with interval of 100 m) (a) during the trade wind conditions at (b) 1400 HST and (c) 0500 HST. (d) The accumulated rainfall (mm, color shading) during the 38 trade wind days in July–August 2013.









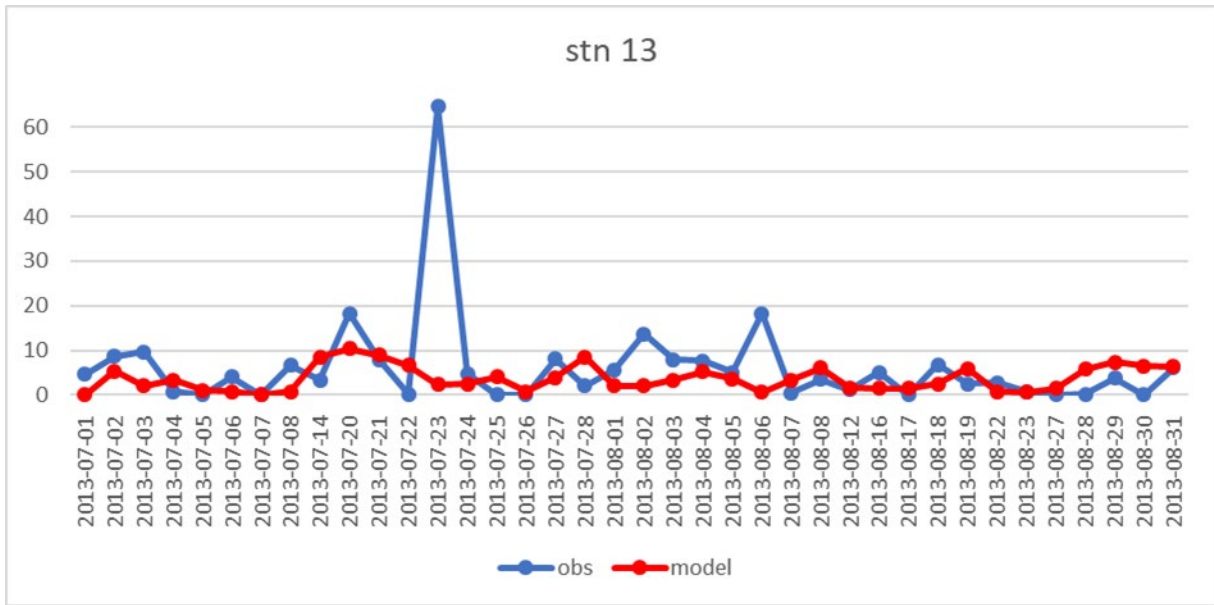


Fig. 5.4 The time series of daily rainfall accumulation (mm) at the 13 rain gauges during the trade wind days.

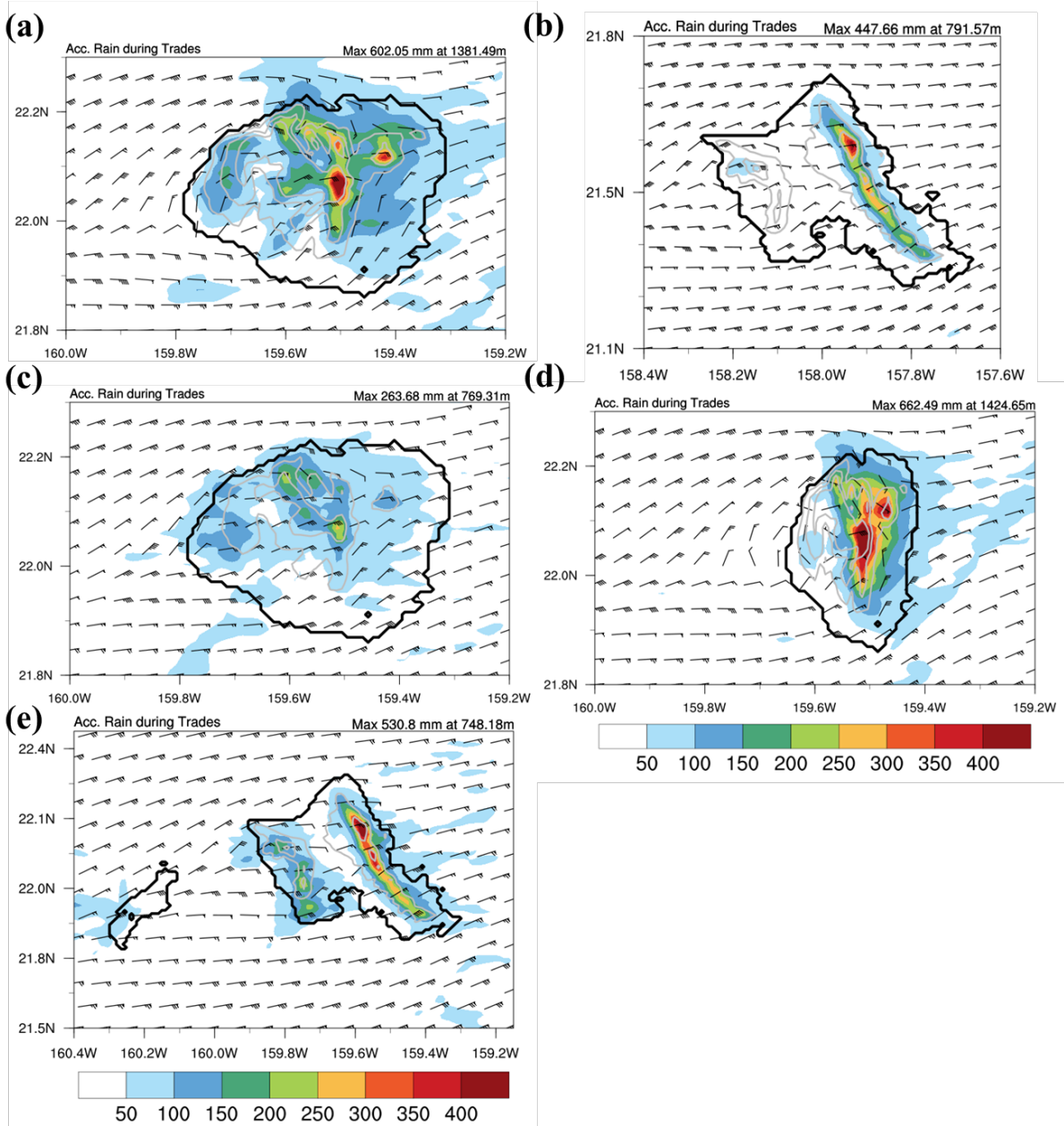


Fig. 5.5 The simulated accumulated rainfall (mm) during the 38 trade wind days for (a) CTRL, (b) CTRL_Oahu, (c) RTH, (c) SZ, and (d) RP.

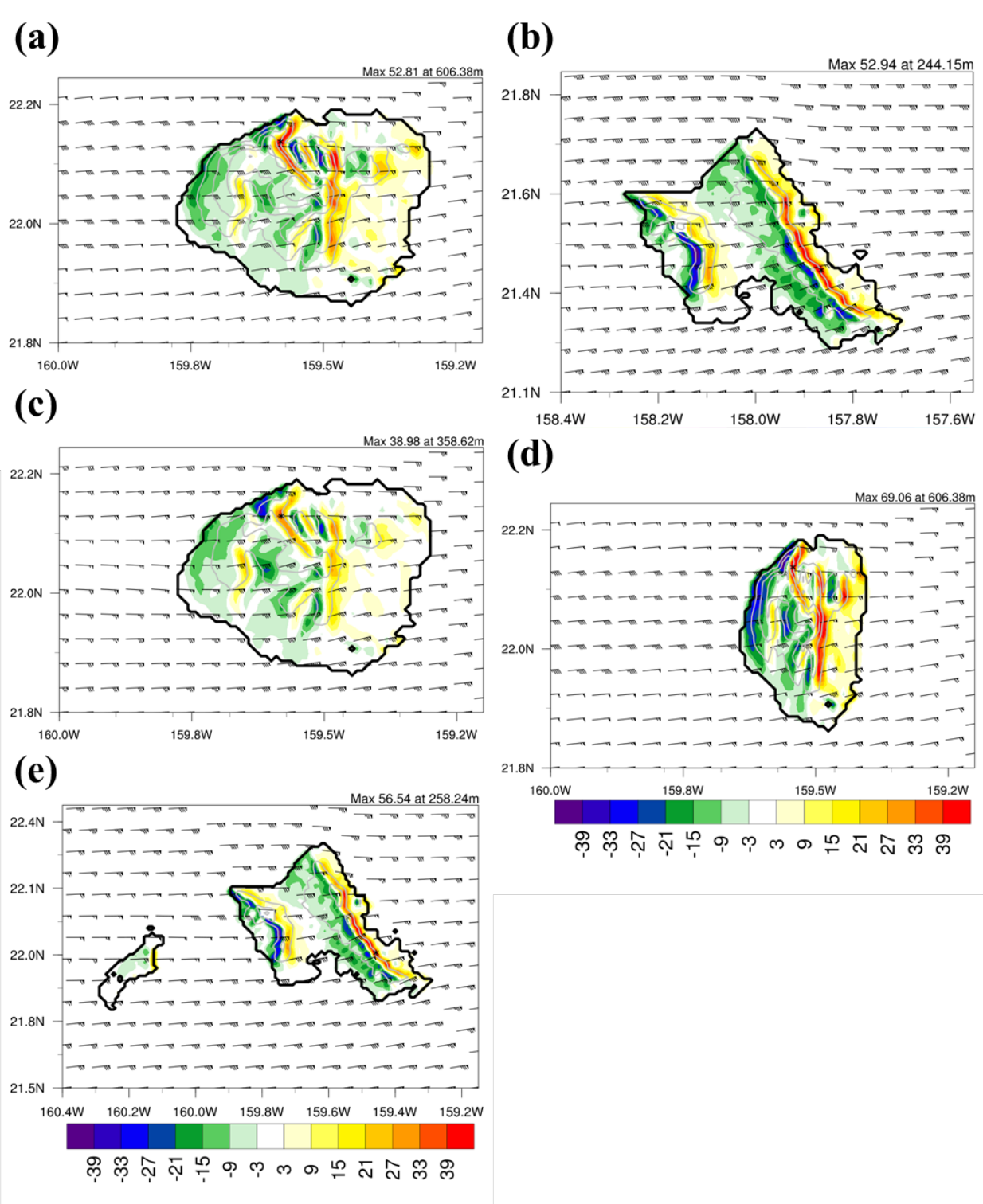


Fig. 5.6 The simulated ORI (kg m⁻¹ s⁻¹) during the trade wind days for (a) CTRL, (b) CTRL_Oahu, (c) RTH, (c) SZ, and (d) RP. The black asterisks indicate the ORI maximum.

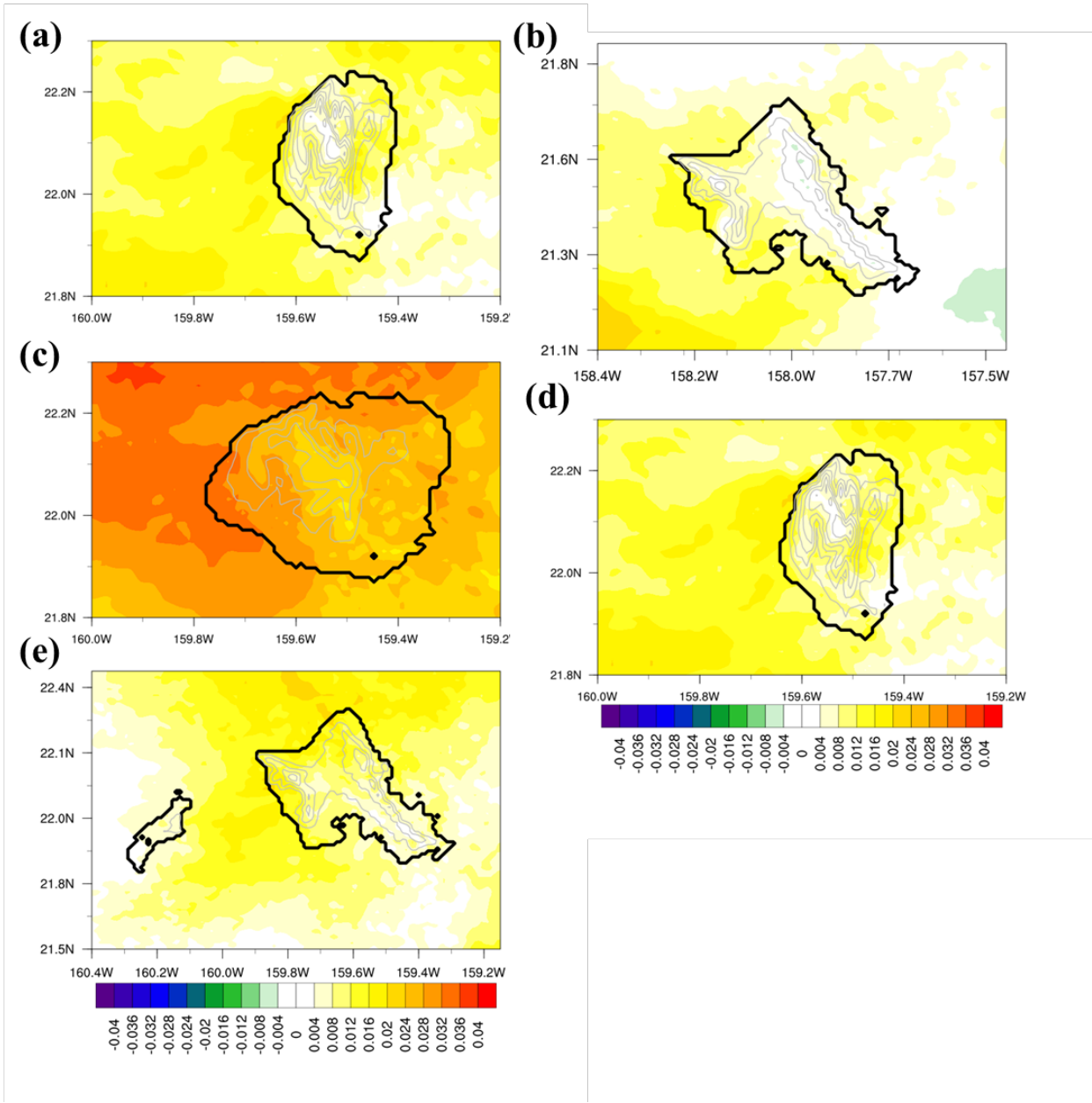


Fig. 5.7 The simulated storage term (mm day^{-1} , color shading) during the trade wind days for (a) CTRL, (b) CTRL_Oahu, (c) RTH, (c) SZ, and (d) RP.

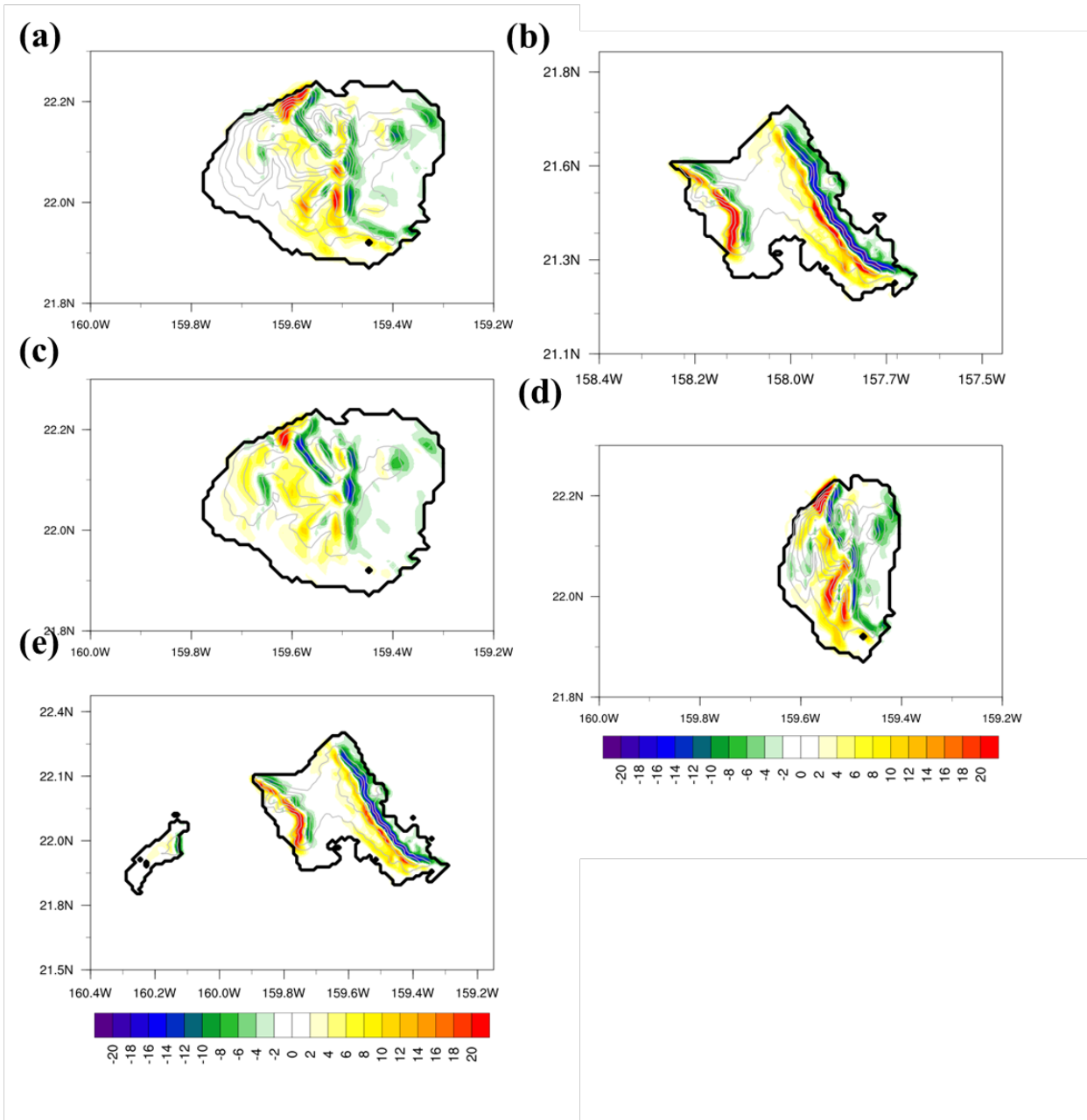


Fig. 5.8 The vertically integrated moisture flux convergence (mm day^{-1} , color shading) during the trade wind days for (a) CTRL, (b) CTRL_Oahu, (c) RTH, (c) SZ, and (d) RP.

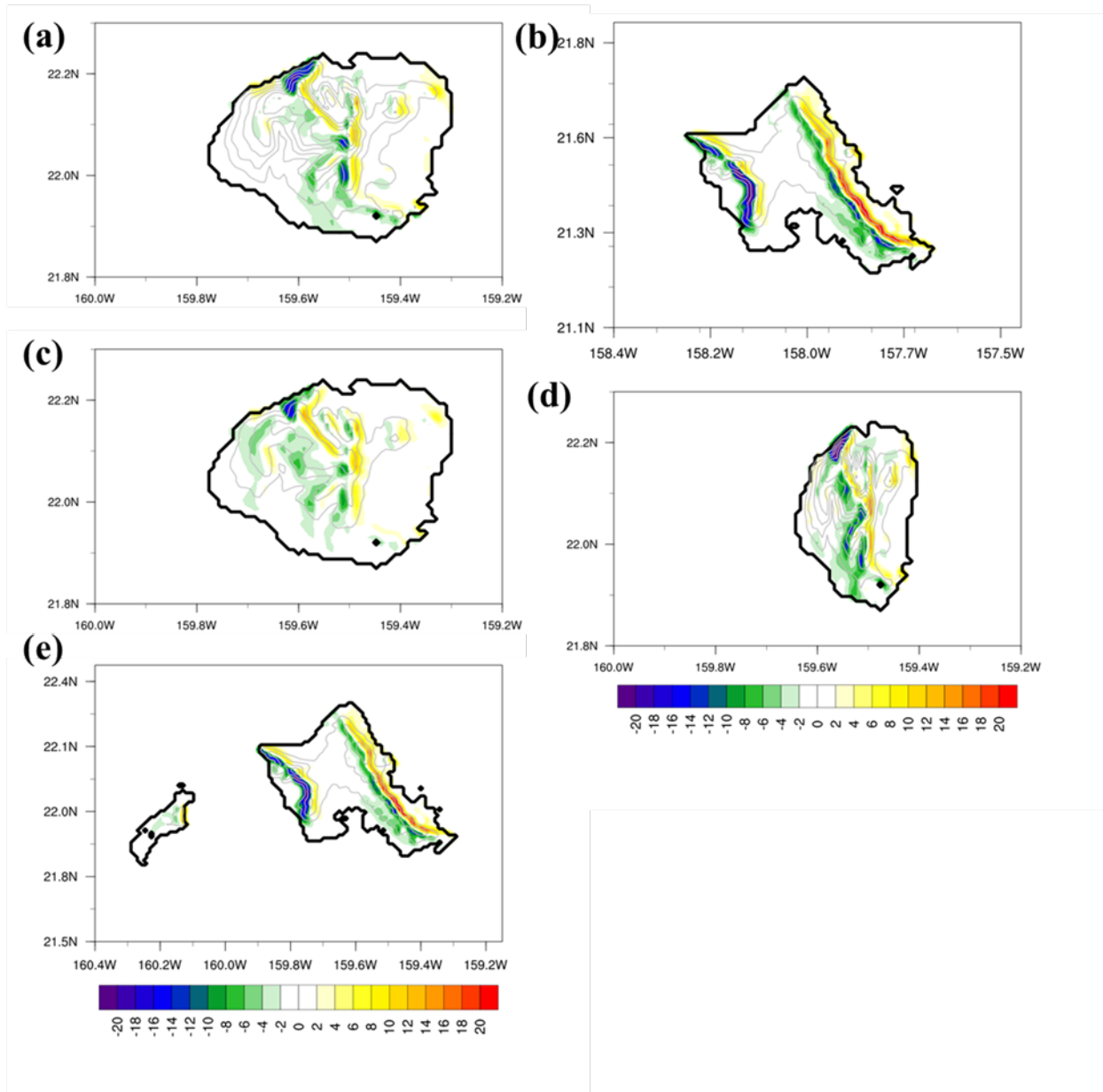


Fig. 5.9 The vertical moisture transport due to orographic lifting (mm day^{-1} , color shading) during the trade wind days for (a) CTRL, (b) CTRL_Oahu, (c) RTH, (c) SZ, and (d) RP.

Chapter 6 The Influences of Different El Niño Flavors on Island-scale Rainfall and Weather for the Hawaiian Islands with Mountaintops below and above the Trade Wind Inversion

6.1 Introduction

Northeast/east trade winds prevail over the Hawaiian Island chain especially during the summer months. The prevailing trade winds contribute to the Hawaiian rainfall with a 90% trade wind frequency in summer compared to a 50% trade wind frequency in the winter (Lyons 1982). The rainfall in Hawai'i is strongly influenced by large-scale modes of climate variability, particularly the El Niño-Southern Oscillation (ENSO), the Pacific Decadal Oscillation (PDO), and the Pacific North American pattern (PNA) (Lyons 1982; Chu et al. 1993; Chu and Chen 2005; Jayawardena et al. 2012; Elison Timm et al. 2011). ENSO is of the most concern for rainfall variability in the tropical Pacific islands on seasonal time scales (Ropelewski and Halpert 1987). ENSO events are recognized through sea surface temperature (SST) anomalies in the equatorial Pacific region, most commonly in the Niño-3.4 region (5°S–5°N, 120°–170°W). The ENSO events are labeled as either a warm (El Niño) or cold (La Niña) phase. The ENSO seasonal cycle tends to peak in December when normal trade wind patterns are often interrupted by midlatitude fronts, Kona storms, and upper-level disturbances in Hawai'i (Ramage 1962; Schroeder 1993).

For the 20 El Niño events during 1905–1992, Chu (1995) suggested that the seasonal rainfall in Hawai'i is deficient in the El Niño winter and the following spring based on rain gauge data. Based on the analyses of synoptic circulation in this study, the thermally induced local Hadley circulation in the central north Pacific inhibits the southeastward propagation of strong

frontal systems into the island chain. The thermal contrast also enhances the upper-tropospheric jet stream with an eastward extension in the north Pacific. In this case, Hawai‘i is located under the right exit region of the jet, resulting in anomalous sinking motion over Hawai‘i. The anomalous sinking motion related to the jet location results in suppressed rainfall during the wintertime. However, the synoptic analyses of geopotential height at 850 and 200hPa, and the wind field at 200 hPa were only done in this study for 1983, 1987, and 1992 El Niño events. Features related to the Hadley circulation such as enhanced tropical convergence and subtropical subsidence over the central north Pacific are not discussed. It is well known that the main impact of El Niño in Hawai‘i is on water resources due to persistent below normal rainfall, resulting from weakened trade winds and anomalously strong subsidence over Hawai‘i (Chu, 1995; Diaz and Giambelluca 2012). However, the synoptic-scale analysis does not resolve island-scale circulations as the airflow and local meteorological conditions over Hawai‘i are strongly modulated by orographic effects and land/sea thermal contrast.

Recent studies have proposed that there exists a new type of El Niño in the tropical Pacific, whose center of positive SST anomalies is located near the dateline in the central equatorial Pacific (Larkin and Harrison 2005a, b; Ashok et al. 2007; Kao and Yu 2009; Kug et al. 2009). This type is referred to as a central-Pacific (CP) or warm pool (WP) El Niño. The typical El Niño with SST anomalies extending from the eastern to central equatorial Pacific is regarded as an eastern-Pacific (EP) or cold tongue (CT) El Niño. The wind stress and large-scale precipitation anomaly patterns associated with these two types of ENSO are quite different (Kao and Yu 2009). While the CT El Niño is associated with significant westerly wind anomalies covering a large part of the tropical Pacific, the westerly wind anomalies associated with the WP El Niño are centered in the central-to-western equatorial Pacific and have a smaller spatial scale compared to the CT events (Kao and

Yu, 2009; Kug et al. 2009). In terms of precipitation, positive anomalies associated with the CT El Niño typically extend from the eastern to central equatorial Pacific where the largest SST anomalies are located. For the WP El Niño, the precipitation anomalies are characterized by a dipole pattern, with positive anomalies located mainly in the western Pacific and negative anomalies in the eastern Pacific (Kao and Yu 2009). Murphy et al. (2014) showed that the main convergence zones for each type of El Niño are distinct and significantly different, accompanied by shifts in the rainfall patterns. The CT events have the largest SST anomalies and the largest changes in surface winds among all El Niño events, leading to an equatorward shift and merging of the intertropical convergence zone (ITCZ) and South Pacific convergence zone (SPCZ). The WP events have smaller SST anomalies and surface wind changes with less of an SPCZ shift as compared with other types of El Niño (Murphy et al. 2014).

However, less is known about the impacts of the two types of El Niño on spatial patterns of rainfall, moisture, and winds over the Hawaiian Islands on an island-scale. Better understanding of the impact of different types of El Niño events on different island communities over the Hawaiian Islands is important for water resources, agriculture, and terrestrial ecosystems, among other things. In this chapter, the differences in the impact of the two types of El Niño on the Hawaiian Islands will be studied using high-resolution model data for the first time, as the routine observational network in many areas over the Hawaiian Islands is too coarse to delineate these micro-scale climate changes. The island-scale flow response (including rainfall distributions) to the different ENSO types will be the main focus of this chapter.

6.2 Study Area and Methodology

6.2.1 Model Description and Initialization

To investigate the various impacts of the two El Niño types on regional airflow and climate over the Hawaiian Islands, WRF simulations during 1979 to 2016 with a 6-km horizontal grid covering the entire state of Hawai‘i (Fig. 7.1a) are conducted. The daily regional simulations with a 36-h time integration are initialized at 0000 UTC using the NCEP CFSR (1979–2011) and CFSv2 (2011–2016) with 0.5° grid-size data as initial and boundary conditions. Two two-way nested domains are employed with 38 vertical levels from the surface to the 100-hPa level with smaller increments (10 levels) at the lower levels and in the trade-wind inversion layer than above (Chen and Feng, 2001).

The physics options and land surface data for the regional simulations are the same as those described in Chapter 2, except for the microphysics scheme. For the regional simulations, the Ferrier microphysics scheme (Rogers et al. 2001), which is the operational microphysics scheme used in NCEP global models with simple hydrometer categories (including snow, rain, and cloud water) are used. To obtain appropriate initial soil moisture and soil temperature, the WRF/LSM is spun up for two months starting 1 January 1979. For each CT and WP event, the horizontal grid-sizes are 27, 9, and 3 km for the island of Hawai‘i (Fig. 7.1b) and 13.5, 4.5, and 1.5 km for the island of O‘ahu (Fig. 7.1c) with two-way nesting procedures. The vertical levels are the same as the regional 6-km simulations. The physics options are the same as those described in Chapter 2. The initial conditions of soil temperature and soil moisture for the LSM have followed the same procedures as in the regional simulations.

6.2.2 The Definitions of CT and WP El Niño Events

El Niño events have been traditionally quantified in terms of simple indices such as SST anomalies in the Niño3 region (5°N–5°S, 150°–90°W) and Niño4 region (5°N–5°S, 160°E–150°W) or a mixture of these two, the Niño3.4 region (5°N–5°S, 170°–120°W). Recently, Ren and Jin (2011) introduced two new Niño indices: N_{ct} and N_{wp} , which are defined as follows:

$$\begin{cases} N_{ct} = N_3 - \alpha N_4 \\ N_{wp} = N_4 - \alpha N_3, \end{cases} \quad \alpha = \begin{cases} 2/5, & N_3 N_4 > 0 \\ 0, & \text{otherwise.} \end{cases}$$

Here, N_3 and N_4 denote SST anomalies in the Niño3 region (Niño3 index) and Niño4 region (Niño4 index), respectively. Using anomalous Niño3 and Niño4 SST indices (1870/01 to 2017/05) obtained from the Climate Prediction Center (NOAA) (https://www.esrl.noaa.gov/psd/gcos_wgsp/Timeseries/), the time series of N_{ct} and N_{wp} are shown in Fig 7.2. Among 12 El Niño events during 1972 – 2017, the 1972/73, 1982/83, 1986/87, 1991/92, 1997/98 and 2015/16 El Niño are defined as eastern equatorial Pacific (CT) events, whereas the events of 1990/91, 1994/95, 2002/03, 2004/05, 2009/10, and 2014/15 are classified as central equatorial Pacific warming type (WP) events (Table 7.1). Note that most of the WP events occurred in and after 1990, indicating that this type of El Niño is not included in Chu's (1995) study covering only the period during 1905 – 1992 with 13 events before 1980.

Since CT and WP El Niño are characterized by a distinctive SST pattern, the associated atmospheric responses are also expected to be different. The synoptic response to the two types of El Niño on upper-level circulations, low-level trade wind flows, and moisture distribution are obtained from CFSR and CFSv2 data. To understand the synoptic-scale responses of the two types of El Niño events, a composite of CT and WP events are created. During the CFSR and CFSv2

data period (1979–2016), 5 CT events and 6 WP events are used to create composites of the winter and spring seasons. The same composite procedures for CT and WP events are also applied to regional and island-scale simulations. When calculating anomalies, the entire 1979–2016 period is used as the mean state climate.

6.3 Results

6.3.1 Key Features between CT and WP El Niño Events

To investigate the impacts of both CT and WP events on Hawai‘i, this chapter shows the atmospheric circulation patterns over the Hawaiian Islands. For the entire state, the composite of regional 6-km simulations during CT and WP events provides a synoptic flow pattern over the Hawaiian Islands. With large spatial variations of orography, which may not be well-described by regional simulations, the island-scale simulations show the impact of the two types of El Niño events on airflow patterns and rainfall distributions depending on the island height, especially for the ridge tops or mountains above or below the trade-wind inversion.

6.3.2 Synoptic Analysis

In this section, the synoptic airflow pattern during the CT and WP events are presented using the composite analysis of CFSR and CFSv2 data. Previous studies exhibit that one of the distinguishing synoptic circulation patterns is the North Pacific jet extending farther eastward following the onset of El Niño (Chu, 1995; Arkin, 1982). In consequence, the Hawaiian Islands have reduced rainfall and even drought during El Niño winters, resulting from the anomalous large-scale subsidence over the right exit region of the extended jet. Figure 7.3 exhibits the location of the North Pacific jet stream at 200 hPa for CT and WP events. The definition of the jet core is the area where wind speed exceeds 40 m s^{-1} . The composite of wind speed during CT

winters shows that the jet core extends farther eastward to 140°W (Fig. 7.3a). This feature is consistent with Chu's (1995) results. For the WP events, the jet core extends to about 150°W (Fig. 7.3b). For CT winters, the jet core shows more eastward extension than during WP winters.

Convergence anomalies at 200 hPa during the CT winters are located in the jet core and extend to the north of the Hawaiian Islands, instead of over the Hawaiian Island. The 200 hPa convergence during the CT winters is larger ($-5.0 \times 10^{-6} \text{ s}^{-1}$) than during the WP winters (Fig. 7.4a,c). For the WP winters, the anomalous convergence ($-3.0 \times 10^{-6} \text{ s}^{-1}$) is located on the north side of the jet core with no significant convergence over Hawai'i. The jet core shifts westward to the dateline during the springs of both types of El Niño events. Greater convergence occurs over the Hawaiian Islands during CT springs than WP springs.

Fig. 7.5 presents the convergence at 200 hPa as diagnosed from the ageostrophic wind equation based on jet dynamics. The ageostrophic wind can be expressed as:

$$\mathbf{V}_{\text{ag}} = \frac{\mathbf{K}}{f} \times \left(\frac{\partial}{\partial t} + \mathbf{V} \cdot \nabla_p + \omega \frac{\partial}{\partial p} \right) \mathbf{V},$$

where p is pressure; ω is the vertical p velocity; \mathbf{V} is the actual horizontal wind vector; and f is the Coriolis parameter. For a seasonal composite or long-term mean, the tendency term can be neglected. The vertical advection term is also rather small in comparison to the horizontal advection term at the 200-hPa level. Therefore, the ageostrophic wind can be approximated as:

$$\mathbf{V}_{\text{ag}} \cong \frac{\mathbf{K}}{f} \times (\mathbf{V} \cdot \nabla_p) \mathbf{V}$$

The Hawaiian region is located at the edge of the diagnosed convergence during winter (Figs. 7.5a, c, and e). The magnitude of the diagnosed convergence ($-5.0 \times 10^{-6} \text{ s}^{-1}$) is greater than the convergence of the actual wind ($-2.0 \times 10^{-6} \text{ s}^{-1}$). For the CT winters, the convergence anomalies of

ageostrophic wind at 200 hPa are negative over the jet core, not over the Hawaiian region. During the WP winters, no significant convergence anomalies occur over the jet core or its exit region. Although the upper-level jets of both CT and WP winters extend eastward (Figs. 7.5a,c) based on seasonal composites (Fig. 7.5e), the corresponding actual and diagnosed convergence over the right exit region are different (Fig. 7.4 a,c and 7.6a,c). As the jet stream shifts westward in spring, the diagnosed convergence zone is located to the north of the Hawaiian region (Figs. 7.5b, d, and f). The actual convergence anomalies during CT springs (Fig. 7.4b) are absent in the diagnosed convergence (Fig. 7.6b).

The vertical velocity at 500 hPa is shown in Fig. 7.7 in order to discuss the synoptic subsidence. Even though the upper-level jet extends more eastward during the CT winters, the most subsidence occurs ($\sim 0.06 \text{ Pa s}^{-1}$) near the right exit of the jet core is at 28°N , 175°W (Fig. 7.7a). In comparison, as the upper-level jet extends less eastward in the WP winters, the subsidence weakens without moving westward (Fig. 7.7c). The subsidence anomalies over the mid-latitudes are less significant ($< 0.03 \text{ Pa s}^{-1}$) during the WP winters than during the CT winters. The displacement between the right exit region of the upper-level jet and the mid-tropospheric subsidence implies that the location of the upper-level jet may not be a clear indicator of mid-tropospheric subsidence (Figs. 7.8a,c). In the following CT and WP springs, the upper-level jet retreats to about 170°E (Figs. 7.7b,d), and the mid-tropospheric subsidence is located over the Hawaiian Islands during CT spring while it is at 20°N , 170°E for WP spring. The anomalies of vertical motions at 500 hPa (Fig. 7.8) show that the ITCZ shifts toward the equator and the SPCZ moves far to the north during CT El Niño, consistent with the results of Murphy et al. (2014).

Vertical cross-sections along 160°W are obtained from the CT and WP seasonal composites. For the CT winters, a region of major subsidence ($> 0.05 \text{ Pa s}^{-1}$) occurs between 15°N and 25°N

extending from the surface to 200 hPa (Fig. 7.9a) while a merged ITCZ and SPCZ demonstrate ascending motion between 5 °N and 15 °S. For the WP winters, two branches of rising motion are located at 5°N and 10°S, respectively, associated with the ITCZ and SPCZ. In contrast, the major subsidence band is narrower in the WP winters than in the CT winters (Fig. 7.9c). During the CT springs, wide-spread ascending motion from the merged ITCZ and SPCZ splits into two branches, however the branch at 15°S is wider than the branch at 7°N (Fig. 7.9b). However, only the northern branch occurs during the WP springs (Fig. 7.9d). A region of subsidence remains near 22°N during the spring of both types, but the magnitude of subsidence weakens from winter. CT events have subsidence anomalies over ~20 °N while WP events demonstrate no significant difference from the long-term mean (Fig. 7.10). The subsidence feature is consistent with the anomalous convergence at 200 hPa (Figs. 7.4; 7.6), showing greater anomalous convergence during CT events than WP events.

The north-south vertical cross-sections along 160°W show easterlies at the equator from 1000 hPa to 200 hPa (Fig. 7.11a,b) and southerlies across the equator (Fig 7.12a,b), indicating the merged ITCZ and SPCZ during CT events. The merged convergence zone in the tropics enhances the Hadley circulation with anomalous subsidence in the mid-latitudes (Fig. 7.9). The circulations associated with WP events are similar to the long-term seasonal composite. Positive SST anomalies over the central Pacific during WP events yield anomalous rising motion over the tropics, however the magnitude of SST anomalies during WP events is smaller than CT events. The CT events produce the largest changes in large-scale circulations, leading to the largest shift in rainfall patterns under the equatorial convergence zone and in the regions of the strongest vertical motion anomalies. As a result, the Hawaiian Islands are expected to experience mid-

tropospheric subsidence during CT events not only from the change in the position of the jet but also from enhanced low-level convergence in the tropics.

Figs. 7.13 and 7.15 depict the wind and geopotential height at 1000 hPa. The winter composite shows the Aleutian Low with cyclonic circulation over the mid-latitudes and a subtropical high located along the eastern boundary of the North Pacific with a trade wind belt in subtropics (Figs. 7.13e; 7.15e). During the CT winter, a deeper Aleutian Low and attendant enhancement of the North Pacific westerlies north of Hawai'i is evident (Figs. 7.13a and 7.15a). The anomalous cyclonic circulations with a band of anomalous westerlies to the north of Hawai'i occur during both the CT and WP winters (Fig. 7.14). Anomalous westerlies along the equator indicate a weakened Walker circulation during both El Nino flavors. For the CP winters (Fig. 7.14a), the anomalous cyclonic circulations in the mid-latitudes, with negative geopotential height anomalies (Fig. 7.16a) and anomalous westerlies over the equator, are larger than for WP winters (Fig. 7.14c). Northwesterly wind anomalies are found over the Hawaiian Islands, indicating weakened trade wind speed during CT winters (Fig. 7.14a). For WP winters, westerly wind anomalies also imply weakened trade wind speed. However, for the Hawaiian Islands, the magnitude of the trades is only weakened during winter (Fig. 7.14c). As expected, negative geopotential height and positive temperature anomalies at 1000 hPa occur in the eastern equatorial Pacific during the CT winters (Figs. 7.14a; 7.18a), while these anomalies are located in the central Pacific during the WP winters (Fig. 7.18b). In spring, the Aleutian Low and its cyclonic circulations are absent while the subtropical high strengthens and extends westward off the west coast of the US. With an intensified subtropical high, the trade wind belt moves northward and the trade wind speed over the Hawaiian Islands is greater compared to winter (Fig. 7.13b,d,f and 7.15b,d,f). During the CT springs, northwesterly wind anomalies ($\sim 1.5 \text{ m s}^{-1}$) also occur over the Hawaiian region. The

wind anomalies during the WP springs are negligible ($< 0.5 \text{ m s}^{-1}$) (Figs. 7.14b,d), indicating that the trade wind speed is less influenced than during CT springs.

The magnitude of the temperature anomalies is larger during the CT winters than the WP winters. The surface temperatures over the Hawaiian Islands are also cooler in CT winters than in WP winters (Figs. 7.18a,c). Additional information regarding the relationship between Hawaiian rainfall and large-scale circulations can be obtained from the total precipitable water field (TPW, Fig. 7.19). The TPW anomalies show substantial differences between the CT and WP events (Fig. 7.20). In winter, conditions which are drier than climatology are observed over the Hawaiian Islands during CT events (Fig. 7.20a,b). In contrast, wintertime WP events have conditions which are near to climatology (Fig. 7.20c,d). Positive TPW anomalies occur mainly over the region of the ITCZ (Fig. 7.20a). With stronger descending motions and cooler temperatures during the CT winters than in WP winters, the TPW anomalies are drier ($\sim -4 \text{ mm}$) in CT winters than in WP winters ($\sim -1 \text{ mm}$) over Hawai'i. Airflow patterns at low-levels are also important to trade wind speed, trade wind frequency, and trade wind showers, throughout the seasonal changes. Similar low-level temperature patterns occur are exemplified by both CT and WP composites during the springs, but there is a clear difference in the strength and the location of the SST anomalies between the two types. In spring, the CT composite shows persistent dry conditions but with less magnitude ($\sim -2 \text{ mm}$) than the CT winters. Conversely, the WP spring exhibits positive anomalies ($\sim 2 \text{ mm}$) over Hawai'i (Fig. 7.20b,d).

The monthly precipitation from the Global Precipitation Climatology Project (GPCP), a global precipitation dataset under the World Climate Research Program (WCRP), provides long-term synoptic rainfall patterns to assess the impact of ENSO (Adler et al. 2003). Linear regressions of GPCP precipitation data during 1979/01 – 2017/02 with a 2.5° resolution onto N_{CT} and N_{WP} indices

show similar dry anomalies during CT events. However, when WP events occur, the rainfall over the Hawaiian Islands is slightly greater than the climatological average (Fig. 7.21).

6.3.3 El Niño Impacts on Rainfall over the Hawaiian Region

The distinct circulation patterns for both El Niño types suggest that the Hawaiian region should expect quite different impacts on rainfall for CT events than WP events. In this section, the orographic effects related to El Niño over the Hawaiian region are examined using long-term (1979–2017) regional WRF simulations. The simulated surface winds in the Hawaiian regional domain have been validated with ocean buoy data and QuikSCAT ocean surface winds (Hitzl et al. 2014). The 34-year downscaled surface winds are also used to hindcast the Hawaiian wave climatology. The surface winds used in this hindcast were validated with satellite data and buoy data during 2000 – 2009, and the wave hindcast was compared with buoy measurements and altimetry data during 1979–2013 (Li et al. 2016).

The 38-year (1979–2017) seasonal composite of simulated surface wind shows easterly trade winds of $3 \sim 5 \text{ m s}^{-1}$ with deceleration along the windward side and acceleration in channels and off the southern shore of Hawai‘i Island. Northeasterly trade winds occurred during the CP winters over the entire region with higher wind speed ($> 5 \text{ m s}^{-1}$) over the tips of the Hawaiian Islands and in the Alenuihāhā Channel, between Maui and Hawai‘i Island. Relatively calm regions ($< 2 \text{ m s}^{-1}$) are found over the windward and leeward side of the Hawaiian Islands (Fig. 7.22a). During WP winters, the prevailing northeasterly wind turns to easterly and wind speed decreases to 3 m s^{-1} upstream of O‘ahu and Kaua‘i (Fig. 7.22c). The calm region over the leeward side of Hawai‘i extends to 158°W , and the wind speed over the Alenuihāhā Channel decreases, resulting from weak incoming flows during the WP winters. The incoming wind speeds during the both CT and WP winters decrease from $\sim 5 \text{ m s}^{-1}$ at 18°N to $\sim 2 \text{ m s}^{-1}$ at 23°N . The composite anomalous surface

winds reveal anomalous northwesterlies during CT events as a deeper Aleutian Low with anomalous cyclonic circulations exists at mid-latitudes (Fig. 7.23a). The anomalous westerlies with large magnitude ($\sim 1.6 \text{ m s}^{-1}$) during the WP winters indicate that the trade wind speed of the WP winters is weakened (Fig. 7.23c). With anomalous northwesterlies (westerlies) during the CT (WP) winters, the areas north/south (west/east) of the island of Hawai‘i have a minimum in anomalous wind speed as result of orographic blocking (Fig. 7.23a,c).

The upstream wind speed of the CT springs is $\sim 5 \text{ m s}^{-1}$ (Fig. 7.22b), but greater during the WP springs ($\sim 6 \text{ m s}^{-1}$) (Fig. 7.22c and d). The trade wind speeds of both CT and WP are smaller than the long-term spring composite ($\sim 6.5 \text{ m s}^{-1}$). The wind speed over the Alenuihāhā Channel and the southern tip of Hawai‘i Island (South Point) was over 10 m s^{-1} during the WP springs and in the long-term mean. Anomalous northwesterlies continuously occurred during the CT springs (Fig. 7.23b). Meanwhile the wind anomalies of the WP springs are small ($< 0.4 \text{ m s}^{-1}$), suggesting that the impacts of WP events over the Hawaiian Islands tend to weaken after winter (Fig. 7.23d).

TPW plots show a generally zonal distribution, increasing from the tropics to the subtropics (Fig. 7.24). During wintertime, the meridional gradient of regional TWP is smaller ($3 \text{ mm}/500 \text{ km}$) than springtime ($4\text{--}5 \text{ mm}/500 \text{ km}$) in the regional domain (from 18°N to 23°N). The TPW during the CT winters (Fig. 7.24a) shows the minimum ($< 27 \text{ mm}$) among the seasonal composite and WP events. The TPW of the CT winters shows a maximum (25 mm) over the windward and leeward sides of Hawai‘i Island and windward Maui. During the CT events, the TPW is less (Fig 7.19; 7.24) in combination with negative temperature anomalies over the Hawaiian region (Figs. 7.18a,b). For the WP winters, the maximum TPW (28 mm) also occurs over the windward and leeward sides of Hawai‘i Island. Negative anomalous TPW covers the whole regional domain,

and is more significant in the CT winters (~ -3 mm). The TPW in the Hawaiian regional domain increases as the season moves from winter to spring.

For spring, the patterns of TPW are similar to those of winter, with increasing TPW from south to north and maximum TPW over the windward side and leeward wake of Hawai'i Island (Figs. 7.24b,d,f). During the CT springs, a local TPW minimum (< 27 mm) is located over the southern tip of Hawai'i Island (Fig. 7.24b). The CT spring still shows negative anomalies, however, they have less magnitude (~ 2 mm) (Fig. 7.25b). The WP spring mirrors the pattern of the long-term mean with less than 1 mm difference (Fig. 7.25d). Conditions with less moisture predominate during the CT events over the WP events, and these dry conditions are more significant in winter with negative anomalies of ~ 3 mm (Fig. 7.25).

Fig. 7.26 and Fig. 7.27 examine the anomalous water vapor mixing ratio from 900 hPa to 700 hPa. Negative anomalies during the CT and WP events are consistent with the dry conditions found in the synoptic analyses. The negative anomalies are largest at 700 hPa during the CT winters (Fig. 7.26e), resulting from synoptic subsidence. For the WP winters, significant dry anomalies (-0.4 mm) occur at 800 and 700 hPa (Figs. 7.26d,f). At the 900 hPa level, more moisture exists (~ 2 mm) over the wake zone of Maui and Hawai'i Island, indicating that the localized orographic effects are limited to low-levels due to subsidence (Fig. 7.26b).

During the seasonal transition, the dry conditions occurring during the CT spring weaken with TPW anomalies evolving from ~ -4 mm to ~ -2 mm due to weakened subsidence (Figs. 7.27 a,c,e). The WP spring has positive TPW anomalies over the wake zones at 900 hPa (Fig. 7.27b) as the synoptic subsidence weakens.

Higher TPW over the windward regions and leeward side of Hawai'i island are shown in Fig. 7.24 for both event types and seasonal composite, resulting from orographic effects. The windward maximum is a result of the incoming trade wind flow being blocked and lifted by orography while the leeward maximum is caused by low-level convergence between the counterrotating eddies along the wake axis. These leeward counterrotating vortices have been observed and simulated over Hawai'i Island and Maui, but only presented over Hawai'i Island in the regional simulations (Fig. 7.22). Orographic effects are significant below 900 hPa with less negative or positive anomalies over the wake zones and $> 0.15 \text{ g kg}^{-1}$ mixing ratio anomalies over the windward side of the island of Hawai'i during winter (Fig. 7.26a,b).

The simulated surface temperature also responds to the synoptic subsidence. For instance, the mountaintops over Hawai'i Island show significant warming during El Niño events (Fig. 7.28). For the other islands, both types of El Niño winter show negative surface temperature anomalies. The maximum of positive anomalies occurs ($> 0.85 \text{ K}$) over the mountaintops of Hawai'i Island during CT winters (Fig 7.28a). Negative surface temperature anomalies are shown over the other islands as well and typically occur around 900 hPa (Fig. 7.29a). Conversely, the temperature above 800 hPa is warmer than the mean in response to synoptic subsidence (Figs. 7.29c,e) with less moisture ($\sim -0.5 \text{ g kg}^{-1}$) (Fig. 7.26e). With negative temperature anomalies below and positive anomalies above 700hPa, the inversion during the CT winters is expected to be enhanced and the atmosphere generally more stable. During the WP winters, the surface temperature anomaly patterns are similar to the CT winters, but with less warming over the mountaintops of Hawai'i Island. The temperature from 900 hPa to 700 hPa also exhibits positive anomalies with a maximum anomaly at 700 hPa. However, the magnitude of warming is less than the CT winters due to weaker subsidence (Fig. 7.29).

During the spring, surface temperatures are warmer over the mountaintops and the leesides of the Hawaiian Islands than in the seasonal composite (Fig. 7.28b,d). The CT springs still show positive temperature anomalies over the mountaintops and leeward side of Hawai'i Island (Fig. 7.28b). As CT El Niño decays in spring and subsidence weakens, the temperature anomaly at 700 hPa (~ 0.2 K) becomes less than in winter (Fig. 7.30e). Below 700 hPa, negative temperature anomalies are consistent with synoptic temperature analyses (Fig. 7.19b). For the WP springs, the positive surface temperature anomalies over the mountaintops are at a minimum as a result of weakening synoptic subsidence (Fig. 7.28d). However, the temperature from 900 hPa to 700 hPa shows positive anomalies (Figs. 7.30b,c,f).

In this section, the simulated WRF rainfall is compared with the Rainfall Atlas of Hawai'i, which provides spatial patterns of rainfall for the major Hawaiian Islands. Maps are available for mean monthly rainfall with a resolution of ~ 250 m during 1920 – 2012 (Giambelluca et al. 2013). For Maui and Hawai'i Island, high seasonal accumulated rainfall is found over the windward mountain slopes, and much less rainfall occurs over the leeward coasts and atop the highest mountains. For the other islands, the rainfall maximum is found over the windward mountaintops. This pattern is mainly controlled by orographic lifting of persistent east-northeast winds which gives rise to distinct windward-leeward rainfall gradients, including thermal effects on the leeward coast which induce westerly onshore flows with orographic lifting on leeward slopes, and dry conditions at the summits above the trade wind inversion. In comparing the rainfall patterns of the Rainfall Atlas of Hawai'i, both types of El Niño events exhibit drier conditions, consistent with the stronger large-scale subsidence and weaker trades. The rainfall deficiency is the greatest (475 mm) over the windward region of Hawai'i Island and over the mountaintops of Kaua'i during the CT winters (Fig. 7.32a). With less moisture and

greater subsidence during the CT winters, dry conditions are widespread over the Hawaiian Islands even though the trade wind speed is less affected compared to the WP winters. For WP winters, significant westerly anomalies are associated with trade wind speed weakening, resulting in rainfall deficiency over the windward slopes of the islands with mountaintops above the trade wind inversion and over the mountaintops of islands wholly below the trade wind inversion (Fig. 7.32c). During the WP winters, increased rainfall over the windward slopes under decreasing trade wind conditions implies that the synoptic subsidence and moisture patterns are dominant factors to Hawaiian rainfall. For CT events, the drier than normal conditions continue from winter to spring (Fig. 7.32b) over Kaua'i and O'ahu. Note that rainfall over the eastern coast of Maui is greater than the seasonal composite during the CT winters (Fig. 32.a).

In general, seasonal accumulated rainfall increases from winter to spring (Figs. 7.31b,d,f). The greatest rainfall accumulation is located over the windward slopes of Hawai'i Island with ~ 500 mm more rainfall during the CT springs. The increasing rainfall also occurs over the mountaintops of Hawai'i Island where orographic rainfall is usually absent (Fig. 7.31b). The only positive rainfall anomaly during the CT winters over Maui become significantly negative (- 475 mm) in the CT springs. The WP springs show similar rainfall patterns to the WP winters, but with less rainfall deficiency (Fig. 7.32d).

The seasonal accumulated rainfall found in the Rainfall Atlas of Hawai'i shows systemically greater rainfall amount compared to the simulated seasonal rainfall accumulation (Fig. 7.33). In general, the simulated rainfall maximum is found over the windward slopes while rainfall minimums exist over the leeward regions. The leeward coast of Hawai'i Island exhibits wetter conditions due the island's thermal effects which alter the wake circulations. These features are consistent with the Rainfall Atlas of Hawai'i. Note that the simulated rainfall maximum during

the WP spring and spring composite moves over the mountaintops, implying the 6 km regional may be insufficient to resolve the steep terrain of Hawai‘i Island (Figs. 3.3d,f). During the CT winter, the rainfall patterns exhibit drier conditions over the mountains except along the northern coast of Hawai‘i Island, Maui, and windward O‘ahu (Fig. 7.33a). The mountaintops of Maui, Hawai‘i, and Kaua‘i experience the largest rainfall deficiency (475 mm). During WP winters, the dry conditions are also simulated over Kaua‘i, east Maui, and Hawai‘i Island (Fig. 7.34c). The widespread drier than normal conditions have less magnitude when compared to the CT winters. The rainfall of the WP winters shows a ~ 275 mm deficiency over windward Maui and Hawai‘i Island (Fig. 7.34c). For O‘ahu, the rainfall differences between WP winter and the seasonal composite are insignificant (~ -75 mm).

Drought conditions continue during the CT springs, and are more severe over Maui where there is a larger area of rainfall deficiency (Fig. 7.33b). The dry conditions over Maui are represented in the Rainfall Atlas of Hawai‘i during the CT springs. These dry conditions persist over the mountaintops of Hawai‘i Island (-474 mm) and its windward slopes (-325 mm). However, the Rainfall Atlas of Hawai‘i shows only minor drying from the CT winter to the CT spring (Figs. 7.32a,b). For the other islands, the increase in moisture from winter to spring is simulated in CT events (Figs. 7.32a,b; Fig. 7.34a,b). As the seasons transition, the enhanced subsidence and negative TPW anomalies become less significant, resulting in more moisture over the Hawaiian region from winter to spring in both types of El Niño. The Hawaiian regional simulations indicate similar anomalous rainfall patterns with relatively drier conditions in CT events than in WP events and more severe drought in winter than in spring coupled with rainfall deficiency over windward slopes and mountains (Fig. 7.36).

6.3.4 El Niño Impacts on Rainfall over the Islands with Mountaintops below and above the Trade Wind Inversion

Rainfall distributions over the Hawaiian Islands have large spatial variations related to terrain and local winds (Chen and Nash 1993; Chen and Feng 1995; Hartley and Chen 2010; Giambelluca et al. 1986, 2013). Regional simulations with a 6-km grid size are inadequate to reproduce these rainfall distributions on an island-scale. For islands with mountaintops below the trade-wind inversion (Hartley and Chen 2010; Winning et al. 2017), the rainfall maximum occurs over the mountaintops or ridge tops. For islands with tops above the trade-wind inversion, maximum rainfall occurs on the windward side below the inversion while areas of low rainfall are found in leeward areas and atop the highest mountains (Chen and Feng 1995). High-resolution simulations (<6-km) will provide detailed rainfall distributions under the influence of El Niño. The El Niño related changes in the rainfall patterns and island-scale circulations may impact the severity of wildfires, watersheds and water resources, agricultural production, land use, and terrestrial ecosystems. In this study, the island of Hawai‘i and the island of O‘ahu are selected to represent the islands with mountaintops above and below the trade-wind inversion, respectively, in order to resolve the important weather characteristics related to each during the two types of El Niño. Hawai‘i and O‘ahu were also chosen as the islands for the island-scale simulations (3-km grids and 1.5-km grids, respectively) because O‘ahu has a large population density and Hawai‘i’s agricultural production is a strong component of the State of Hawai‘i economy.

The simulated composite island-scale precipitation response to CT and WP events is compared with the Rainfall Atlas of Hawai‘i during 1979 to 2012. In the comparison of simulated rainfall and the Rainfall Atlas of Hawai‘i over Hawai‘i Island during the CT winters (Figs. 7.37a,b), both sources exhibit a pattern with a rainfall minimum over the mountaintops and northwestern

coasts. The daily rainfall maximum is simulated over the mountaintops of Kohala, however, the maximum in the Rainfall Atlas of Hawai‘i occurs over the windward slopes of Mauna Kea. For the WP winters (Figs. 7.37b,d), both simulations and observations reveal more widespread rainfall over Hawai‘i Island than the CT winters and a daily rainfall maximum over the windward slopes of Mauna Kea. More daily rainfall (~ 5 mm) is simulated over the mountaintops than is found in the Rainfall Atlas of Hawai‘i. During ENSO neutral winters, the rainfall pattern found in the simulations is similar to that of WP winters. Both simulations and the Rainfall Atlas of Hawai‘i show greater daily rainfall over the island during the neutral winters than during the CT and WP winters. The simulated rainfall shows systematic overestimations in the island-scale domain (Fig. 7.37). For O‘ahu Island, the simulated rainfall pattern is comparable to the Rainfall Atlas of Hawai‘i with a daily rainfall maximum over the mountaintops, and a minimum over the southwestern coasts. Similarly, the daily rainfall is overestimated in model simulations compared to the Rainfall Atlas of Hawai‘i (Fig. 7.38). During the springtime, both Hawai‘i Island and O‘ahu have greater daily rainfall widespread over land than during the wintertime model simulations or in the Rainfall Atlas of Hawai‘i (Figs. 7.39 and 7.40). For Hawai‘i Island, daily rainfall over the windward slope increases significantly with the daily rainfall maximum simulated over the windward slope of Mauna Kea, consistent with the Rainfall Atlas of Hawai‘i. For O‘ahu Island, the daily rainfall maximum is simulated over the mountaintop of the Ko‘olau Range. In contrast, the daily rainfall maximum of the Rainfall Atlas of Hawai‘i occurs over the southern portion of the Ko‘olau ridge. Generally, the simulated rainfall patterns are comparable to the Rainfall Atlas of Hawai‘i but with systemic overestimations in the simulations.

For the island of Hawai‘i, the prevailing wind during the CT winters is more northerly compared to the neutral winters (Fig. 7.41a). The TPW is lower over the island (~2 mm) during

the CT winters, especially over the windward coast and wake zone (~ 3 mm) (Fig. 7.42a). With north-northeasterly wind anomalies and negative TPW anomalies, the simulated rainfall composite for the island of Hawai‘i reveals drier conditions during the CT winters than during neutral winters (Fig. 7.43a). The maximum rainfall deficiency (>9 mm day⁻¹) is simulated over the windward slopes of Mauna Kea and Mauna Loa (between 1000 to 2000 m in elevation). The second rainfall deficiency maximums (7 mm day⁻¹) are simulated over the Kohala Mountains. The portion of the island least affected by rainfall deficiency during the CT winters is along the northeastern coast (~ 1 mm day⁻¹) (Fig. 7.43a). This is due to orographic lifting of the incoming NNE flow.

During the WP winters, the prevailing ENE trade wind speed is weaker (~ 1 m s⁻¹) (Fig. 7.41b) and the simulated rainfall is less compared to the neutral winters (Fig. 7.43b), with less TPW (-1 mm) (Fig. 7.42b). The maximum rainfall deficiency (~ 9 mm day⁻¹) is simulated over the windward slopes of Mauna Kea and Mauna Loa (between 1000 to 1500 m) (Fig. 7.43b). The second rainfall deficiency maximum (~ 3 mm day⁻¹) is over the Kohala Mountains (~ 1000 m) and Kona leeward slopes (~ 1500 m). The southwestern coast has the least difference in rainfall (< 1 mm day⁻¹) between the WP winters and the neutral winters.

For O‘ahu, the increased northerly wind component is more significant (> 1 m s⁻¹) than for the island of Hawai‘i during the CT winters (Fig. 7.41c). Negative TPW anomalies (~ 2.6 mm) are simulated (Fig. 7.42c). With less TPW, the simulated rainfall during the CT winters is also less than during the neutral winters (Fig. 7.43c). The maximum rainfall deficiency is simulated over the Ko‘olau Mountains (7 mm day⁻¹). The next most important rainfall deficiencies (~ 5 mm day⁻¹) are simulated over the Wai‘anae mountaintop and along the southern flank of the Wai‘anae Mountains (Fig. 7.43c).

During the WP winters, trade wind speed weakens due to northwesterly wind anomalies ($\sim 1 \text{ m s}^{-1}$) (Fig. 7.41d). TPW anomalies during WP winters are still negative, but with less magnitude ($\sim 1 \text{ mm}$) (Fig. 7.42d). The weakened trade wind speed and low TPW are associated with less simulated rainfall than during the neutral winters, especially over mountainous regions (Fig. 7.43d). The rainfall deficiencies are 6 mm day^{-1} over the of Ko‘olau mountaintop and 3 mm day^{-1} over the Wai‘anae Mountains. The rainfall deficiencies over the other regions are relatively small ($1\text{-}2 \text{ mm day}^{-1}$). The dryness which occurs during the WP winters is less significant than during the CT winters.

Simulated temperatures above and below the trade wind inversion are also modified by the ENSO cycle. For O‘ahu and the areas below the trade wind inversion on the island of Hawai‘i, nighttime cooling is more significant ($0.45 \text{ K}\text{-}0.75 \text{ K}$) (Fig. 7.44), due to less available water vapor, during the CT and WP winters than during neutral winters. Conversely, for mountaintops above the trade wind inversion, the simulated temperature tends to be warmer during the CT and WP winters due to stronger descending motion associated with the Hadley circulation. For the CT winters, the warming above the trade wind inversion is greater (0.85 K) than during WP winters (0.45 K) (Figs. 7.44a,b). The cooling over the area below the trade wind inversion is also more evident during the CT winters ($\sim 0.2 \text{ K}$) than during the WP winters ($\sim 0.1 \text{ K}$). Furthermore, enhanced nighttime cooling below the trade wind inversion strengthens katabatic flows. Hence, the nocturnal rainfall before sunrise off the Kona coast, caused by the convergence of katabatic flows with the westerly return flow offshore, is greater during El Niño years (Fig. 7.45).

During the CT springs, over the island of Hawai‘i, the trade wind speed is slightly weaker with a northwesterly wind anomaly (0.4 m s^{-1}) off the windward coast (Fig. 7.46a) and less TPW (-2.2 mm) (Fig. 7.47a) compared to neutral springs. The simulated rainfall is less over the

windward slope of Mauna Loa with a 7 mm day^{-1} rainfall deficiency maximum (Fig. 7.48a). The accentuated nighttime cooling due to lower TPW is still evident during the CT springs, with lower ($\sim 0.35 \text{ K}$) surface temperature over the regions below 2.5 km in elevation than during the neutral springs (Fig. 7.49a). For the regions above 2.5 km, warmer surface temperature due to increased subsidence ($\sim 0.55 \text{ K}$) is still present.

Over the island of Hawai'i, the wind anomalies are mainly northerly over the windward side (0.8 m s^{-1}) and westerly over the wake zone (0.6 m s^{-1}) (Fig. 7.46b). The TPW during the WP springs is less (-1.0 mm) compared to the neutral springs (Fig. 7.47b). The simulated rainfall is also less over the windward slope of Mauna Loa (-6 mm day^{-1}) but slightly greater off the southwestern coast ($<1 \text{ mm day}^{-1}$) (Fig. 7.48b). Nighttime cooling is less significant ($\sim 0.05 \text{ K}$) than during CT winters due to lesser TPW anomalies (Fig. 7.49b). Warming above the trade wind inversion during the WP springs is greater than during the CT springs.

For O'ahu, the wind direction anomalies between the CT springs and the neutral springs are northwesterly ($0.6\text{--}0.8 \text{ m s}^{-1}$) (Fig. 7.46c), indicating weakening trade winds during the CT springs. With less TPW ($\sim 1.5 \text{ mm}$, Fig. 7.47c) and weaker trades, the rainfall along the Ko'olau Mountains during the CT springs is less than during neutral years with maximum rainfall deficiency (8 mm day^{-1}) at the mountaintop (Fig. 7.48c). The pattern of rainfall deficiency along the Ko'olau Mountains also extends westward to central O'ahu. The rainfall deficiency along the Wai'anae mountaintop is relatively small ($<2 \text{ mm day}^{-1}$) compared to the Ko'olau mountaintop.

During the WP springs, the wind anomalies are easterly ($0.4\text{--}0.6 \text{ m s}^{-1}$, Fig. 7.46d) and the TPW is 0.6 mm less than during neutral springs (Fig. 7.47d). With slightly increased trade wind speed and slightly lower TPW, the maximum rainfall deficiency occurs over the Ko'olau mountaintop (6 mm day^{-1}). For an island with mountaintops below the trade wind inversion, the

thermal effects on wake circulations are expected to produce more rainfall over the leeside under weak trade wind conditions. Nevertheless, less rainfall is simulated over the southwestern coasts ($\sim 1 \text{ mm day}^{-1}$) during the CT springs than during the WP springs, resulting from less available TPW during the CT springs (Fig. 7.48c,d). In the afternoon, the simulated surface temperature during the WP springs is warmer over land than during neutral springs. The warmer surface temperatures over land suggest that the thermally driven circulation over the wake zone would be more significant than during neutral springs, resulting in more rainfall over the southwestern coast (Fig. 7.48d).

6.4 Summary

During the winter of El Niño events, SST anomalies reach their peak over the tropics enhancing the thermally-driven Hadley circulations creating a greater tropical convergence zone and increasing subsidence between 15°N to 30°N Pacific. During the CT winter, synoptic subsidence is greater over Hawai‘i than during the WP winters due to a merged ITCZ and SPCZ. Composites of TPW during the CT and WP winters both show less synoptic moisture than the climatological mean over the Hawaiian Islands. However, the TPW anomaly of the CT winters is -3 mm , much drier than during the WP winters ($\sim -1 \text{ mm}$). During the seasonal transition, the enhanced tropical convergence weakens with less significant impacts on the subsidence over the Hawaiian region than in winter. In spring, CT events are associated with persistent dry conditions with negative TPW anomalies ($\sim -2 \text{ mm}$) over Hawai‘i. Conversely, WP springs exhibit positive anomalies ($\sim 1 \text{ mm}$). The analysis of simulations with a 6-km grid size during 1979–2017 indicates that the TPW reveals relatively drier conditions during the CT events than during the WP events, and the dry conditions are more significant in winter. Under wintertime synoptic subsidence, the Hawaiian region has positive temperature anomalies at the 700 hPa level. The warming at 700 hPa

is more significant (~ 1.0 K) during the CT winters than during the WP winters. The results of a comparison between simulated rainfall and the Rainfall Atlas of Hawai‘i indicate that the regional model is capable of simulating the rainfall response to different El Niño types. The simulated rainfall patterns are consistent with observations.

Five CT, six WP, and six neutral events during winter and spring are simulated with an island-scale model over O‘ahu and Hawai‘i. The simulated rainfall patterns are comparable to the Rainfall Atlas of Hawai‘i, however, the high-resolution model overestimates the rainfall amount. For an island with mountaintops above the trade-wind inversion, during the CT winters, less rainfall is simulated over windward slopes than during WP winters due to weaker trade wind speed and less moisture. Drought conditions are expected during the CT winters over the mountaintops of Mauna Kea and Mauna Loa and in the leeward side of the Kohala Mountains due to a -65% change in daily rainfall. During the WP winters, the lack of moisture over the mountaintops of Mauna Kea and Mauna Loa is not as profound as during the CT winters.

During the CT springs, persistently weak trade wind speed and low TPW result in maximum rainfall deficiencies over the windward slopes and mountaintops below the trade wind inversion. However, the dry conditions over the windward slopes are less significant than during the CT winters. Similar to the CT winters, drought conditions are expected over the mountaintops of Mauna Kea and Mauna Loa and the leeward side of the Kohala Mountains with a negative change in the rainfall percentage. The only region with greater simulated rainfall during the CT springs is off the Kona coast, before sunrise, resulting from the convergence of katabatic flows with the westerly winds offshore. The rainfall distributions during the WP springs are quite similar to those during the CT springs, however, the dry conditions are less significant due to higher TPW in the environment. For islands with mountaintops below the trade-wind inversion, increased synoptic

subsidence and low TPW are crucial in creating drier or even drought conditions over the windward slopes, e.g. the Ko‘olau Mountains on O‘ahu during the CT winters. Rainfall amounts over the Ko‘olau mountaintop are therefore lower during the CT winters than the WP winters, despite stronger trade winds. The percent change of rainfall indicates that droughts are likely over the southwestern coast during the CT winters as well. During the WP winters, the dry conditions over O‘ahu are less significant than during the CT winters.

In spring, the rainfall over the Ko‘olau Mountains decreases substantially (6–8 mm day⁻¹) for both types of events. The droughts during the CT springs are more significant over mountainous regions as compared to the WP springs. More rainfall is simulated over the southwestern coasts in the afternoon hours during the WP springs than during the CT springs due to enhanced thermally driven circulations over the leeward coasts. During the WP springs, the surface daytime temperature over land is warmer as compared to the CT springs. During both types of El Niño events, the nighttime cooling accentuated by less atmospheric water vapor affects the simulated surface temperatures over the regions below the trade wind inversion. For island regions above the trade wind inversion, surface warming is accentuated by increased subsidence associated with the Hadley circulation. The diurnal variations of airflow circulation and rainfall in response to surface temperature changes will be analyzed in future work.

Chapter 6 Tables

Table 6.1 Classification of El Niño events from 1950–2017 based on Ren and Jin (2011) indices.

TYPE	YEARS
COLD TONGUE	1972/73, 1982/83, 1986/87, 1991/92, 1997/98, 2015/16
WARM POOL	1990/91, 1994/95, 2002/03, 2004/05, 2009/10, 2014/15

Chapter 6 Figures

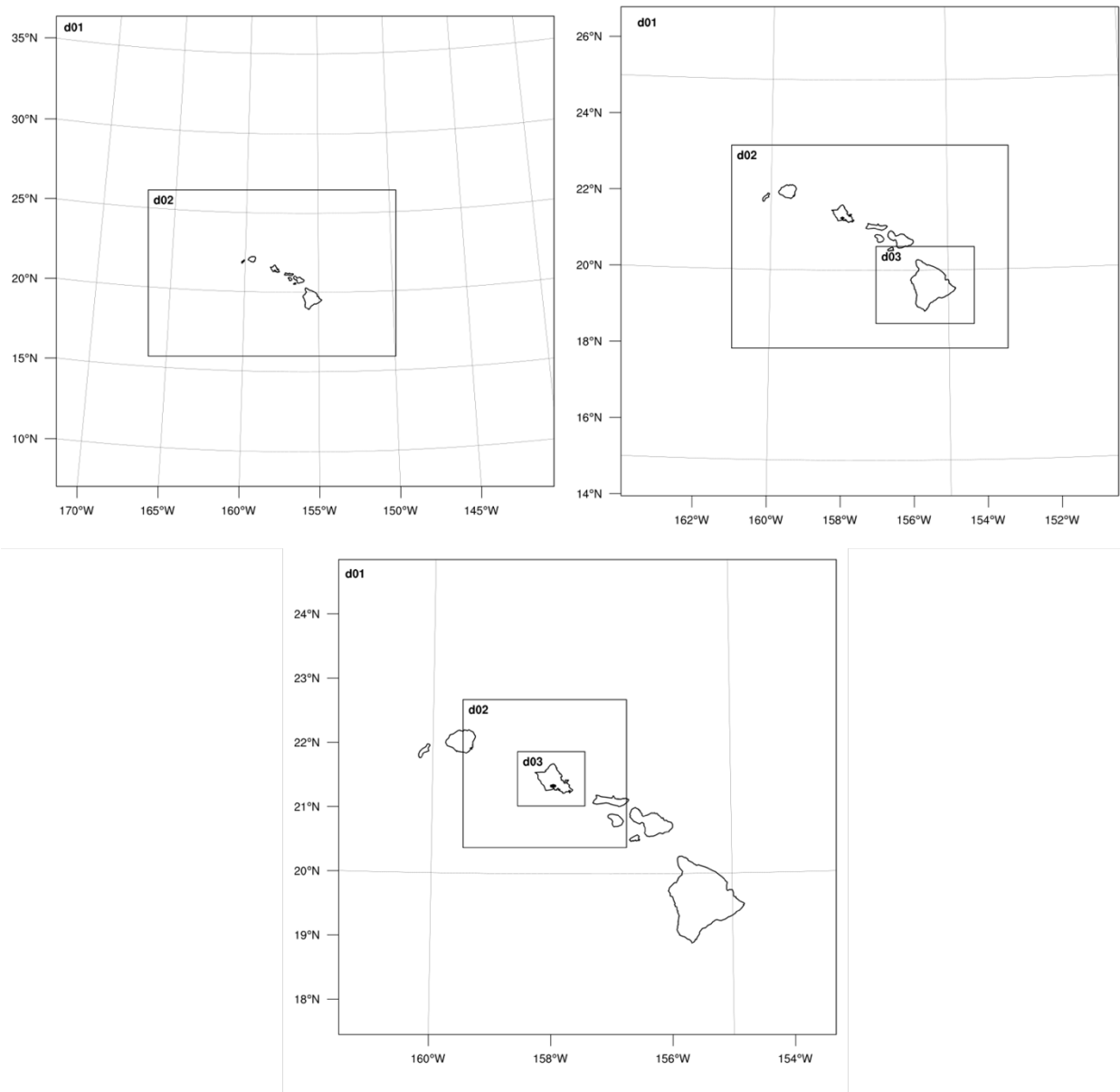


Fig. 6.1 (a) Domains of regional simulation (grid size: 18, 6 km), (b) domains of island-scale simulations for Hawai'i (grid size: 27, 9, 3 km), and (c) domains of island-scale simulations for O'ahu (grid size: 13.5, 4.5, 1.5 km).

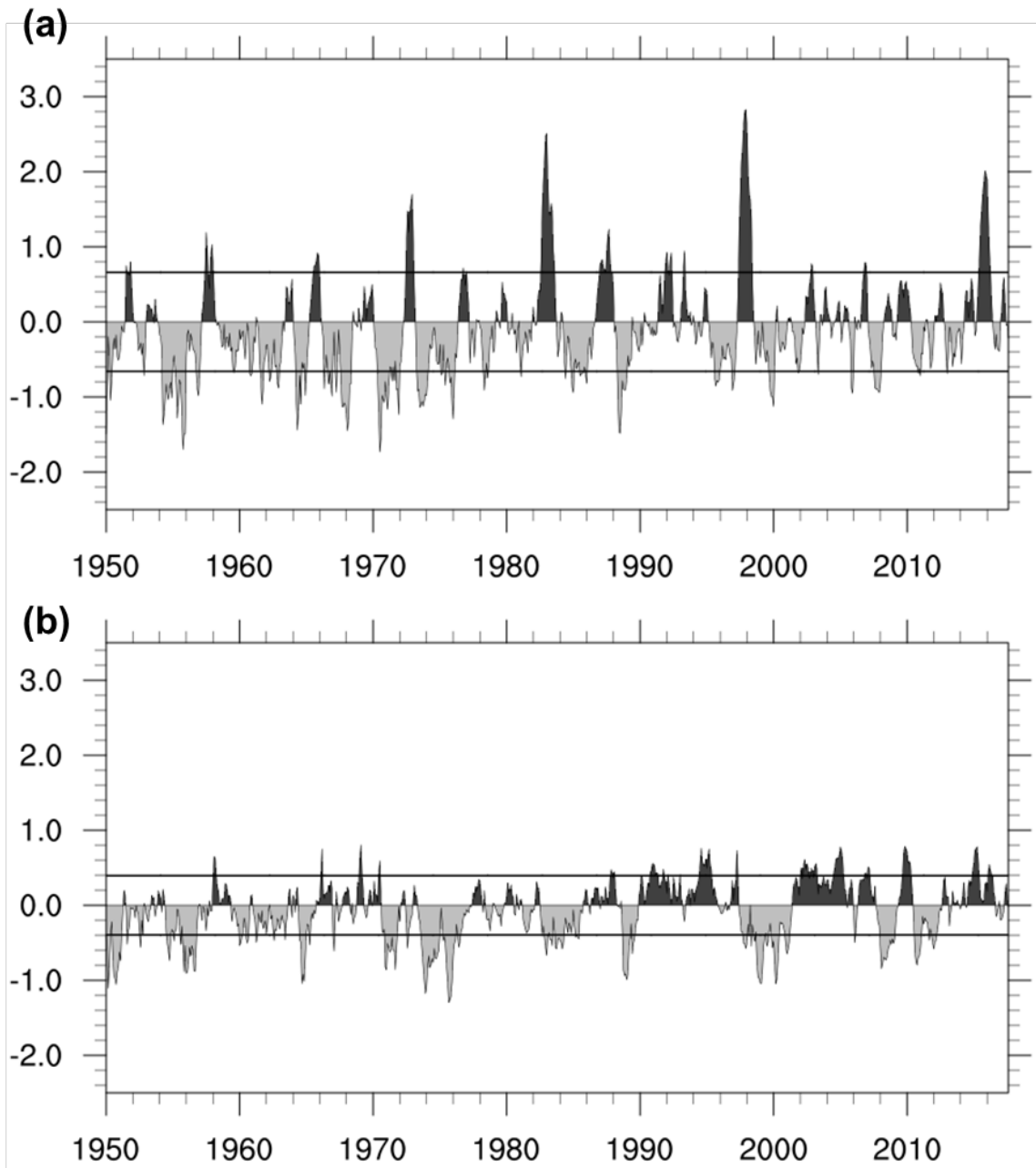


Fig. 6.2 Time series of (a) N_{ct} and (b) N_{wp} indices. Black lines indicate one standard deviation of N_{ct} and N_{wp} indices.

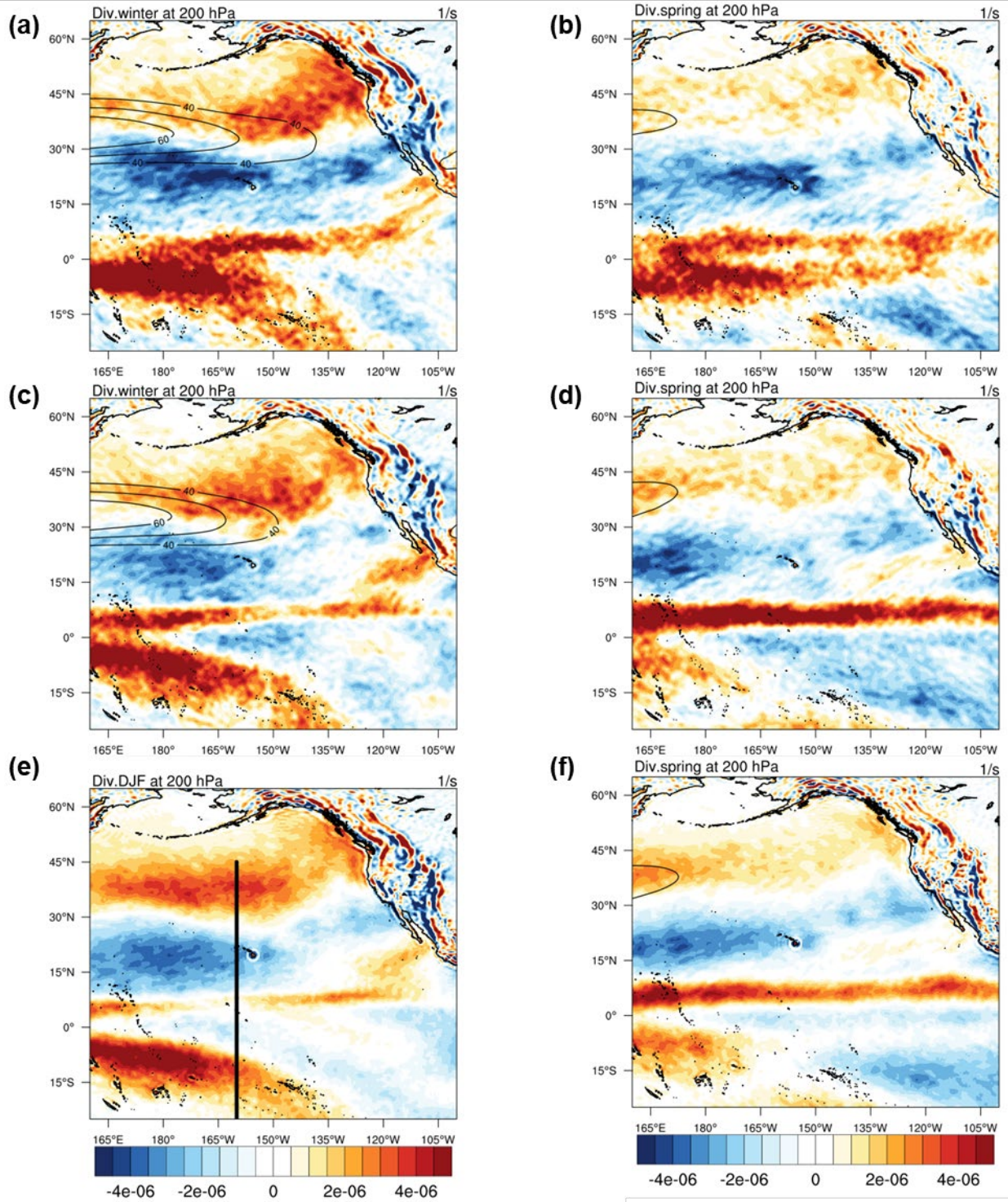


Fig. 6.3 The seasonal composite of divergence (s^{-1} , color shading) and wind speed ($m s^{-1}$, contour) at 200 hPa for (a) CT winters, (b) CT springs, (c) WP winters, (d) WP springs,

(e) all 38 winters, and (f) all 38 springs. The black thick line indicates the location of vertical cross-sections.

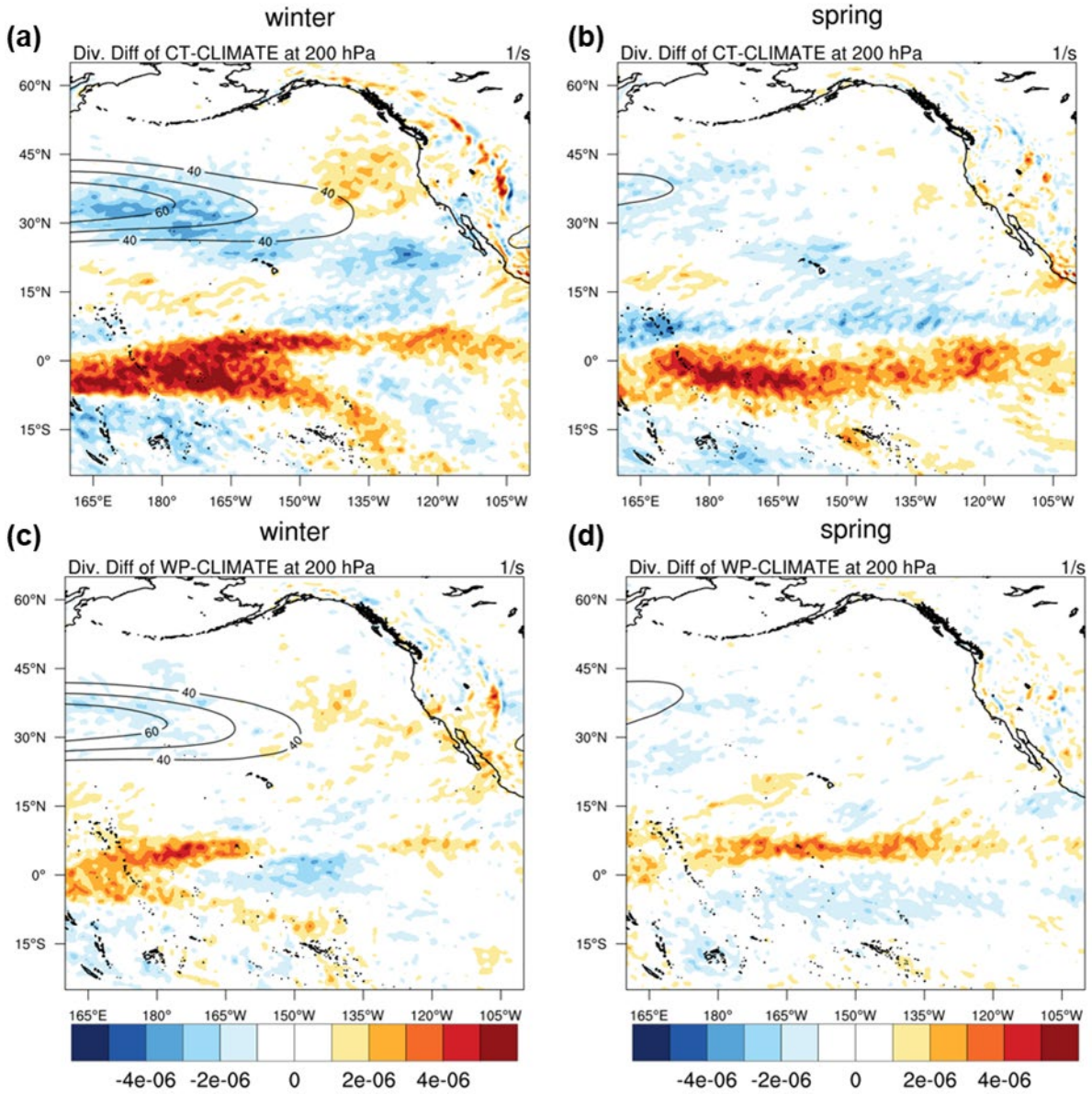


Fig. 6.4 The seasonal anomalies of divergence (color shading: s^{-1}) at 200 hPa for (a) CT winters, (b) CT springs, (c) WP winters, and (d) WP springs.

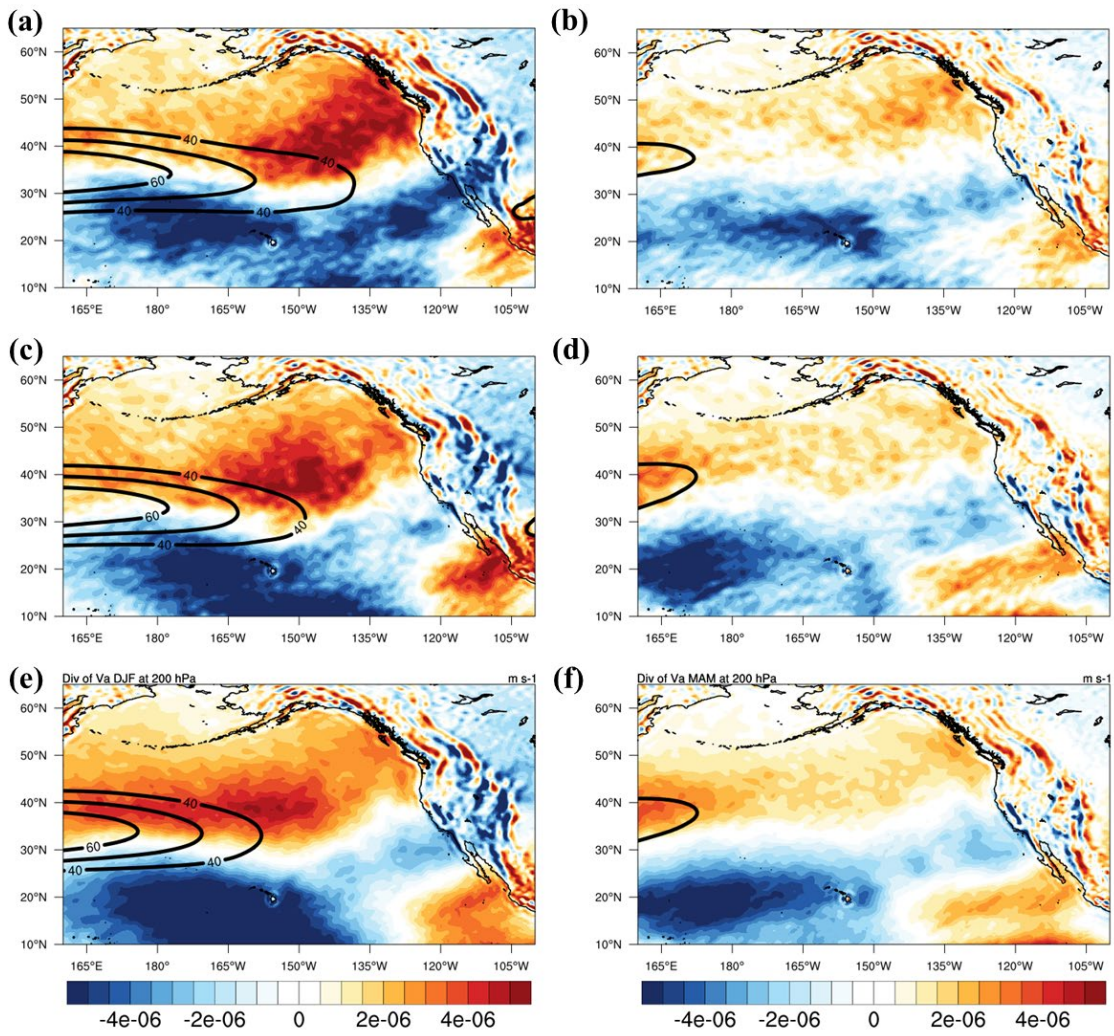


Fig. 6.5 Same as Fig. 6.3, but divergence is calculated using the ageostrophic wind at 200 hPa.

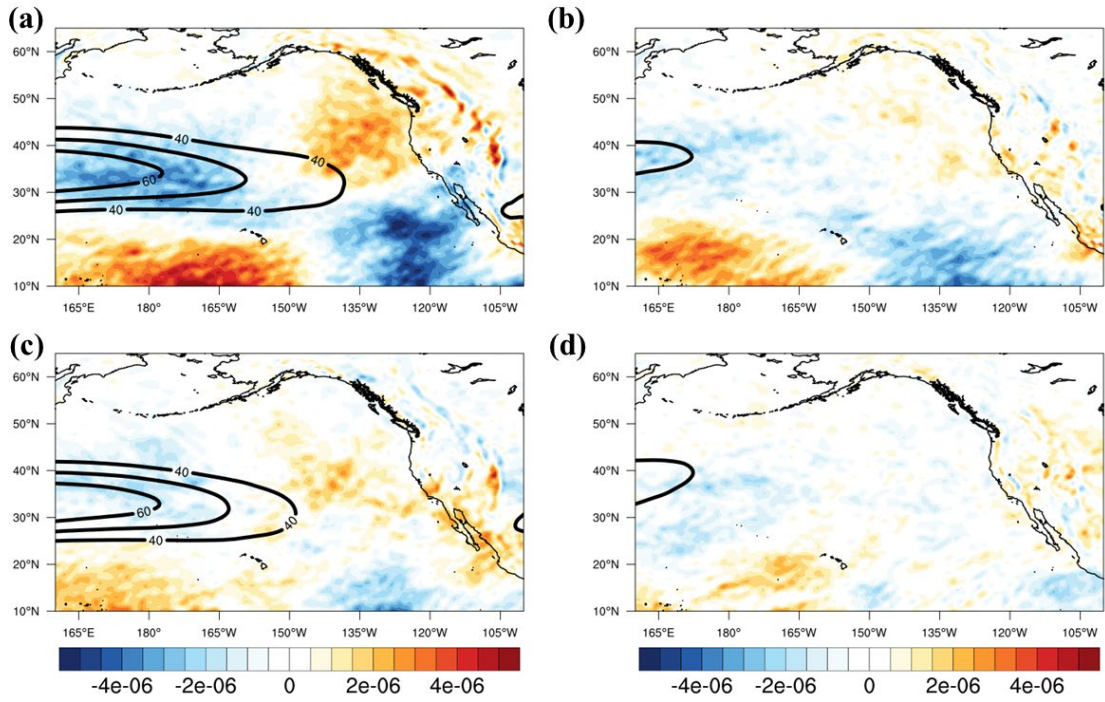


Fig. 6.6 Same as Fig. 6.4, but divergence is calculated using the ageostrophic wind at 200 hPa.

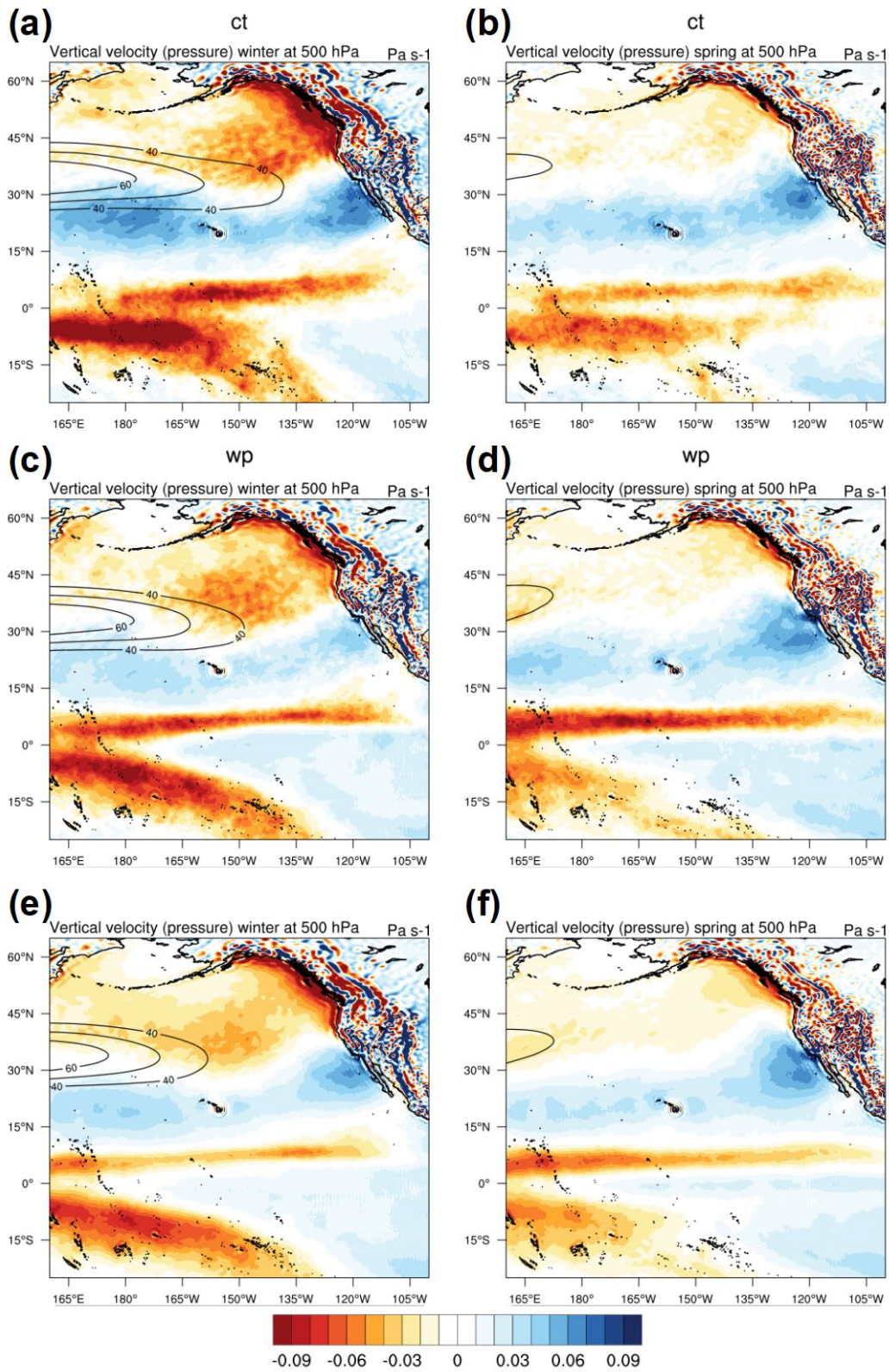


Fig. 6.7 The composite of vertical velocity (Pa s^{-1} , color shading) at 500 hPa and wind speed (m s^{-1} , contour) at 200 hPa for (a) CT winters, (b) CT springs, (c) WP winters, (d) WP

spring, (e) all 38 winters, and (f) all 38 springs.

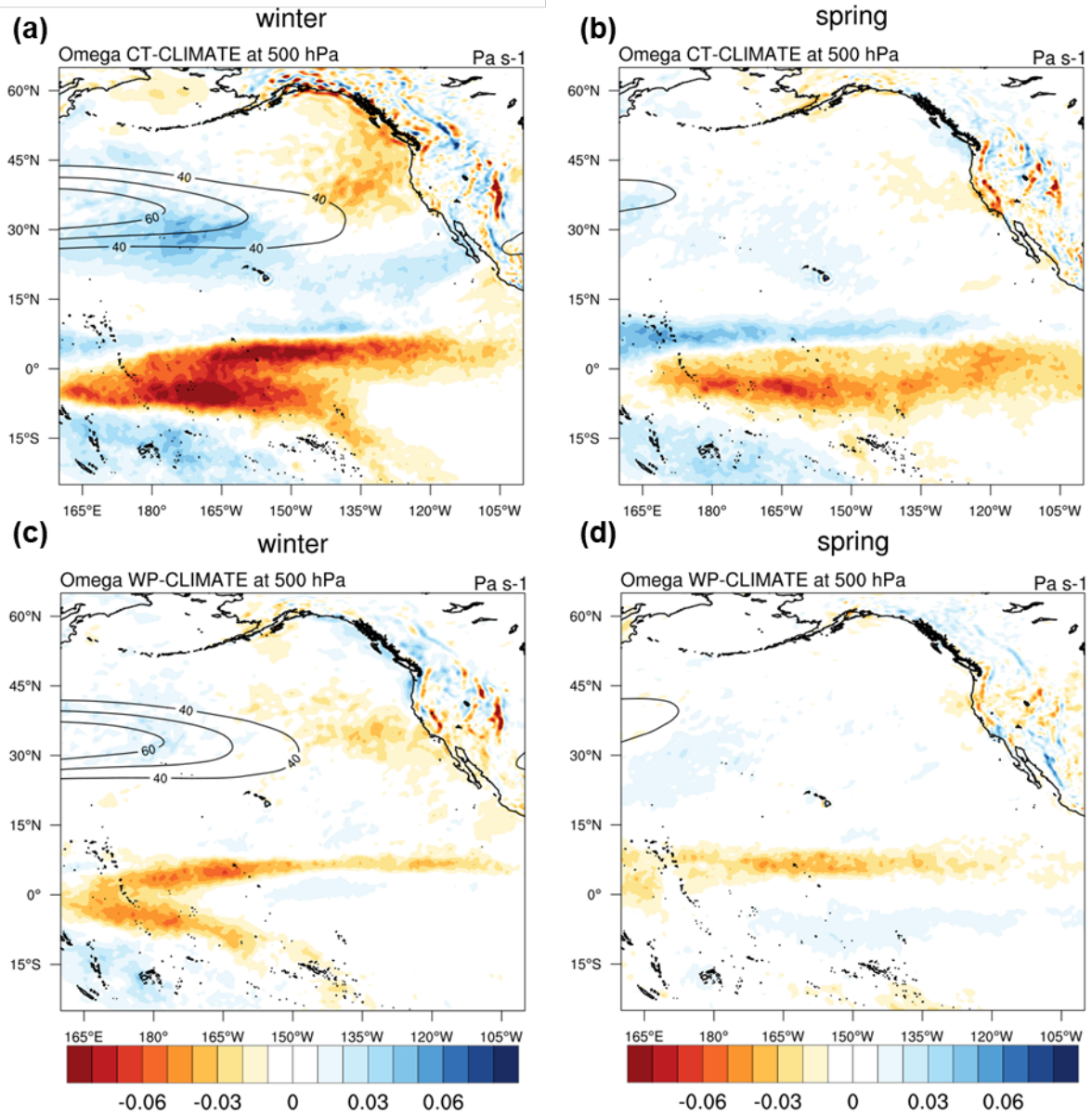


Fig. 6.8 The seasonal anomalies of vertical velocity (Pa s^{-1} , color shading) at 500 hPa for (a) CT winter, (b) CT spring, (c) WP winter, and (d) WP spring.

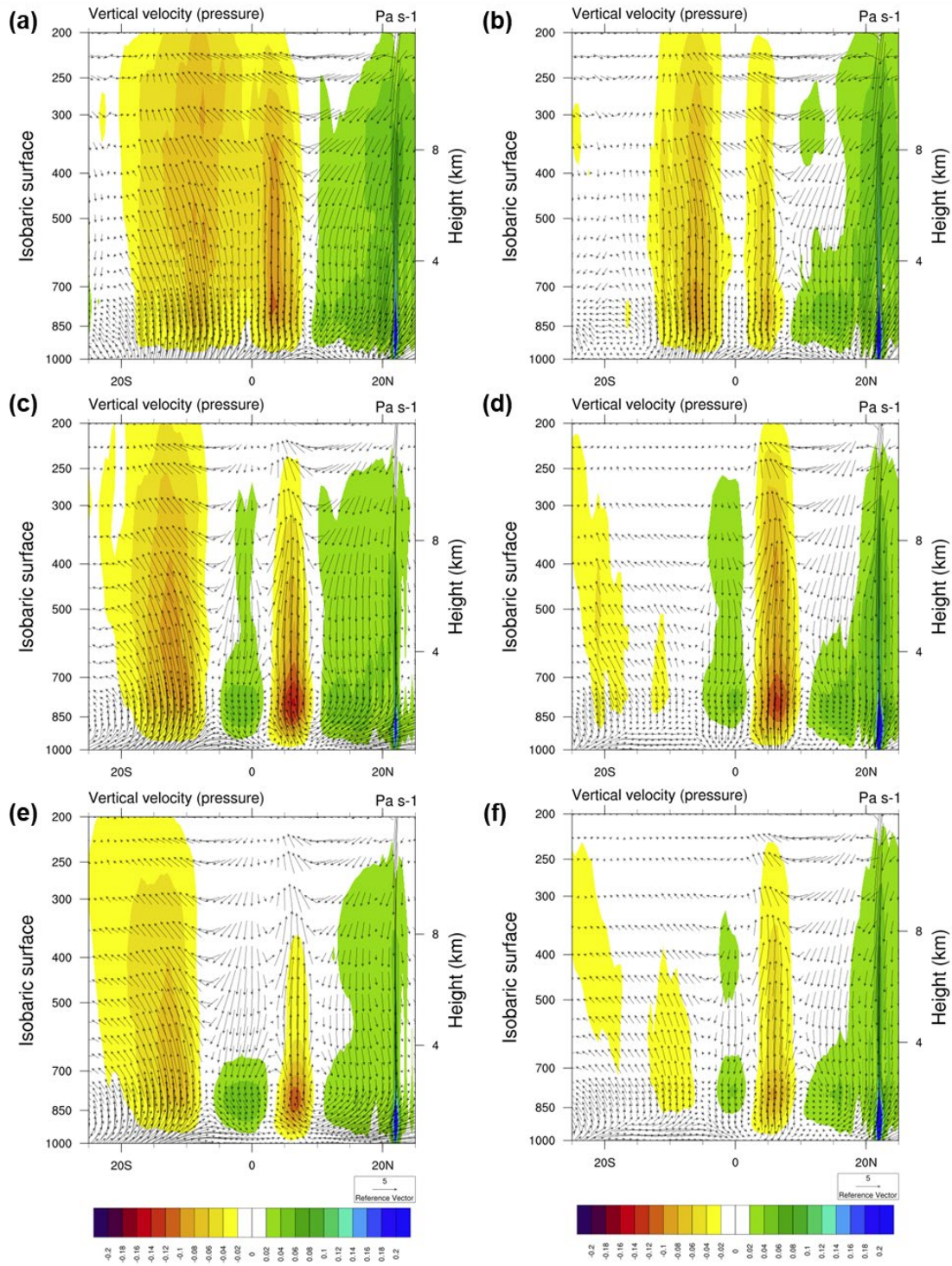


Fig. 6.9 The seasonal composite of a north-south vertical cross-section along 160 °W for (a) CT winters, (b) CT springs, (c) WP winters, (d) WP springs, (e) all 38 winters, and (f) all 38

springs. Color shading is pressure vertical motion (Pa s^{-1}); vectors are meridional wind ($V: \text{m s}^{-1}$) and negative vertical velocity ($-\omega: 0.01 \text{ Pa s}^{-1}$).

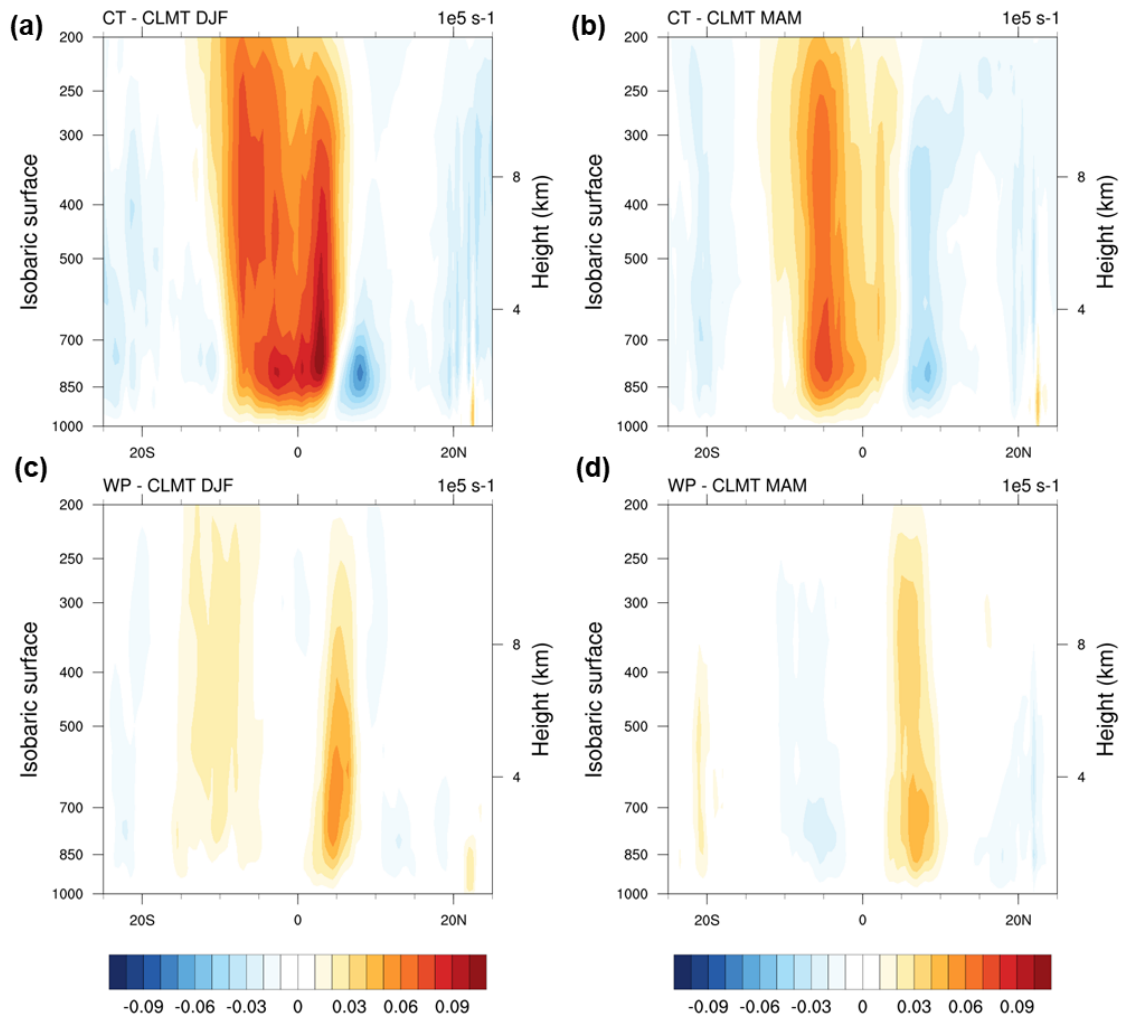


Fig. 6.10 The seasonal anomalies of a north-south vertical cross-section along 160 °W for (a) CT winters, (b) CT springs, (c) WP winters, (d) WP springs, (e) all 38 winters, and (f) all 38 springs. Color shading is pressure vertical motion (Pa s^{-1}).

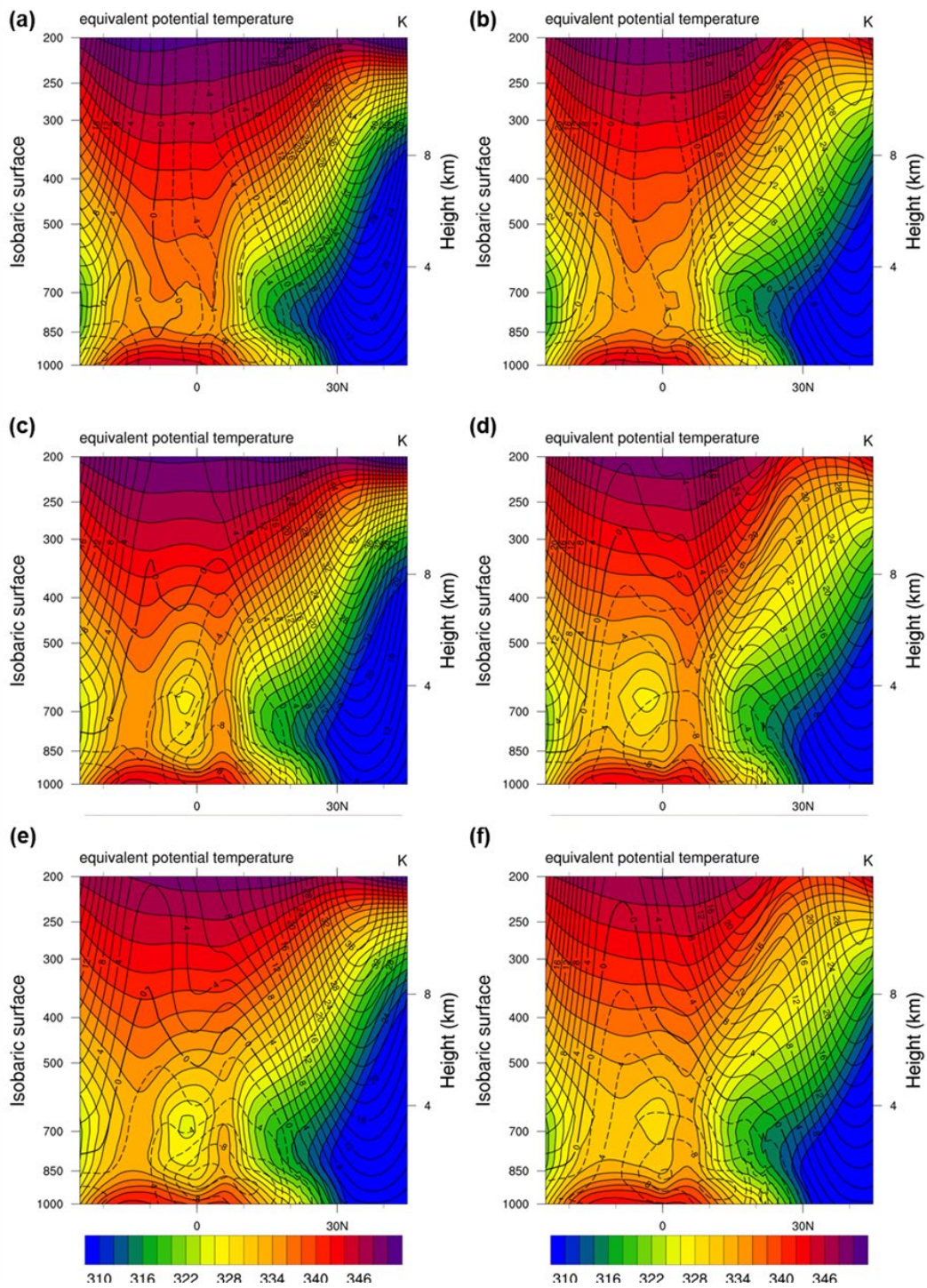


Fig. 6.11 The seasonal composite of a north-south vertical cross-section along 160 °W for (a) CT winters, (b) CT springs, (c) WP winters, (d) WP springs, (e) all 38 winters, and (f) all 38 springs. Color shading is equivalent potential temperature (K); Contours are zonal wind (U : m s^{-1}).

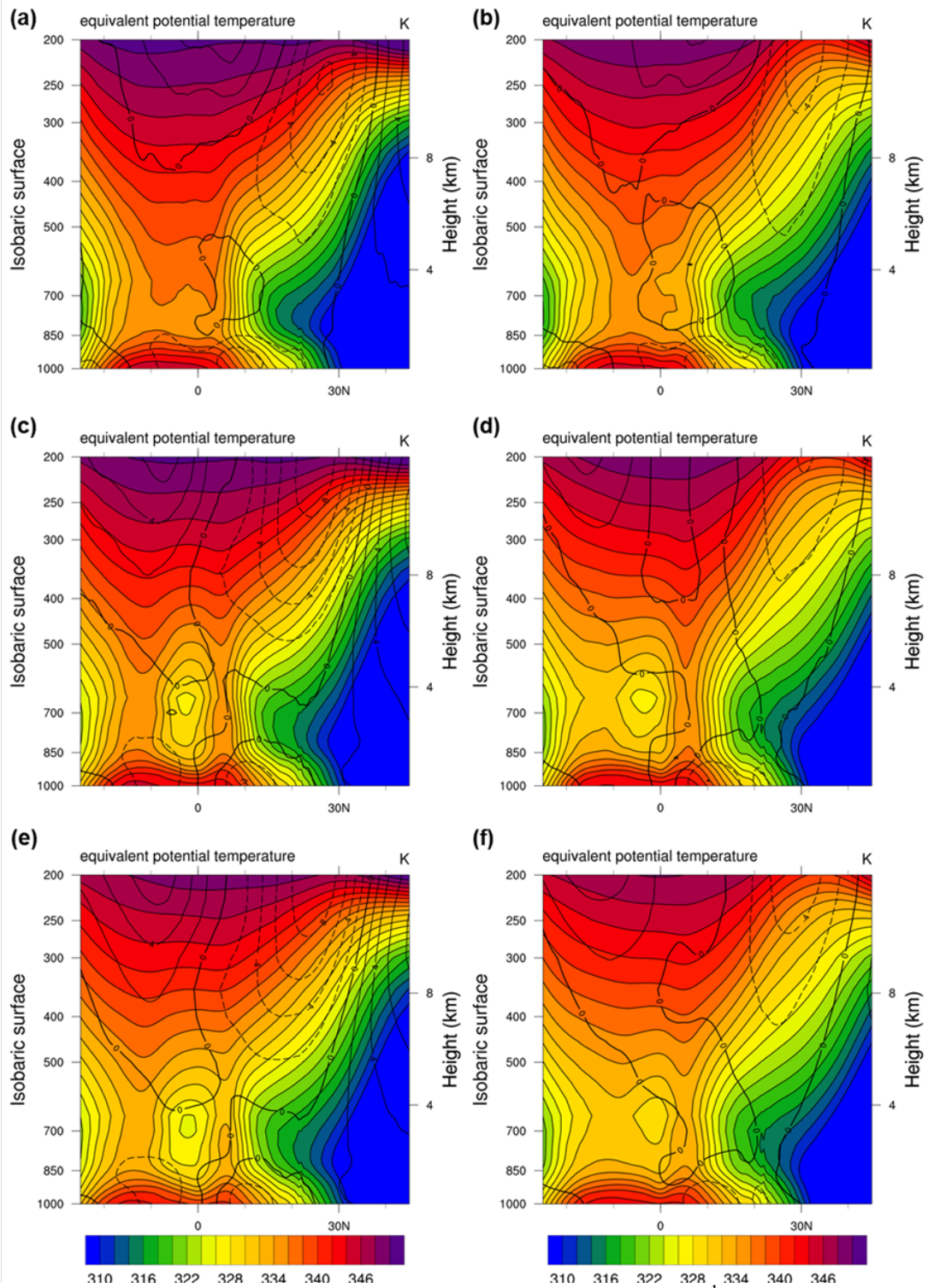


Fig. 6.12 Same as Fig. 6.11, but contours are meridional wind (V : m s^{-1}).

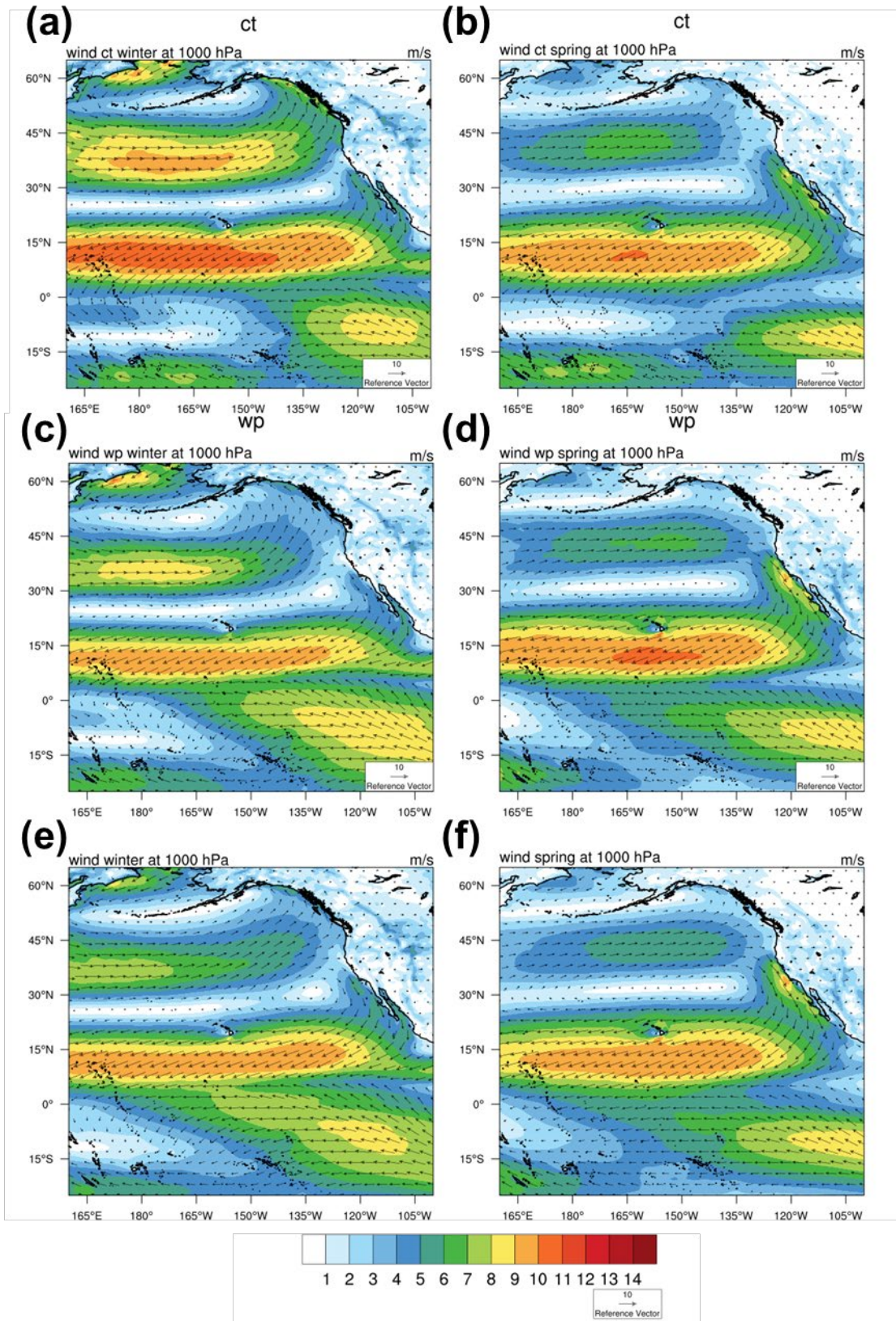


Fig. 6.13 The seasonal composite of wind (m s^{-1}) at 1000 hPa for (a) CT winters, (b) CT springs,

(c) WP winters, (d) WP springs, (e) all 38 winters, and (d) all 38 springs. The reference arrow represents 10 m s^{-1} .

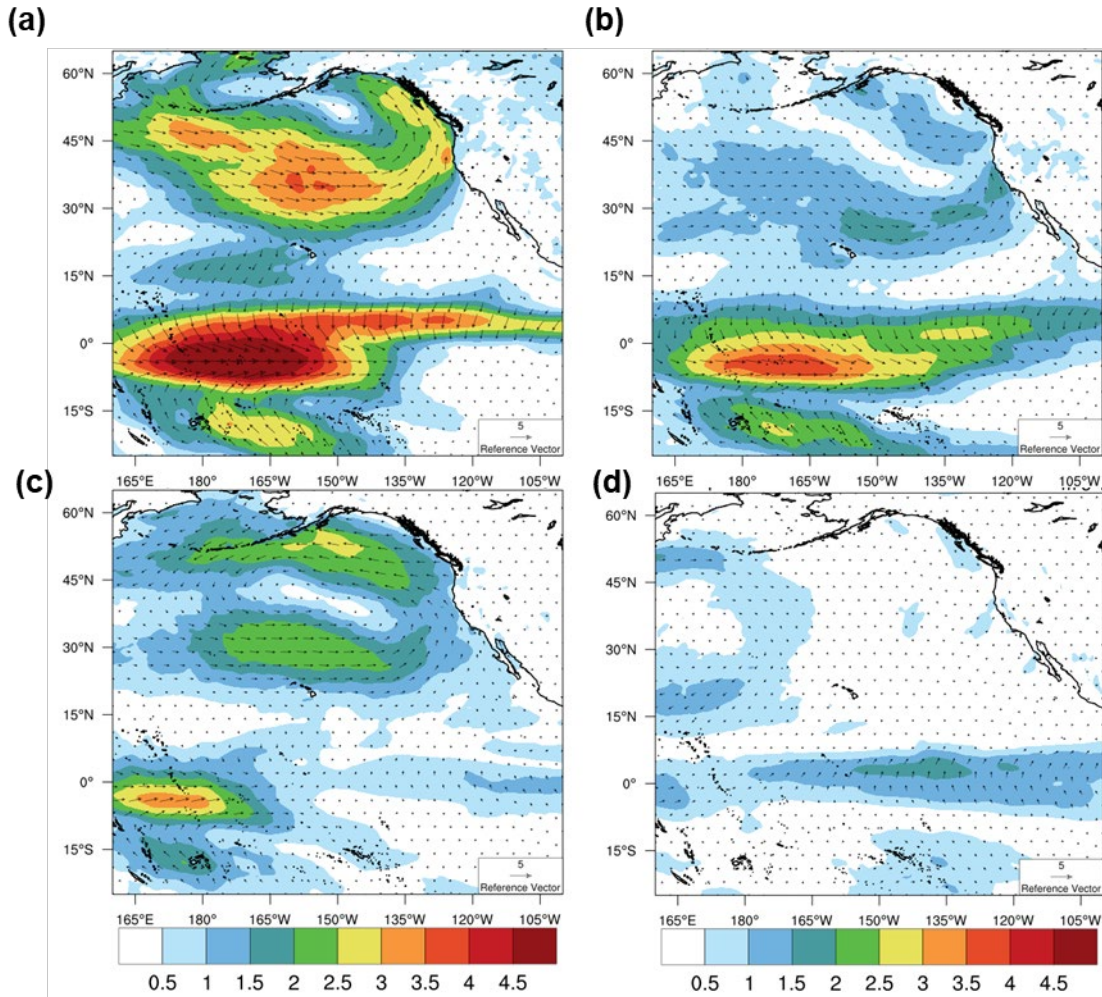


Fig. 6.14 The seasonal anomalies of wind (m s^{-1}) at 1000 hPa (a) CT winters, (b) CT springs, (c) WP winters, (d) WP springs, (e) all 38 winters, and (d) all 38 springs. The reference arrow represents 10 m s^{-1} .

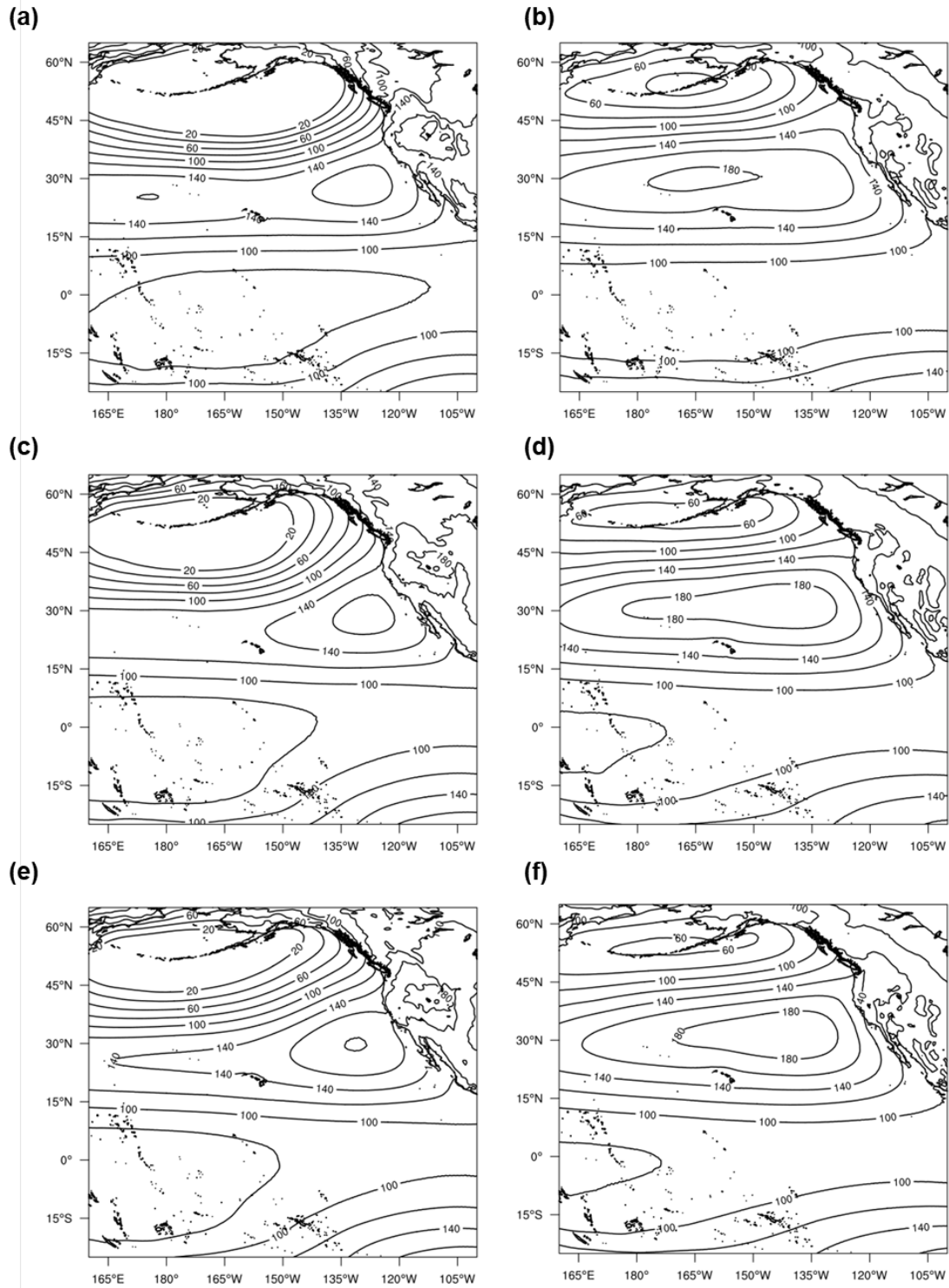


Fig. 6.15 Same as Fig. 6.13, but for geopotential height (m, contour) at 1000 hPa.

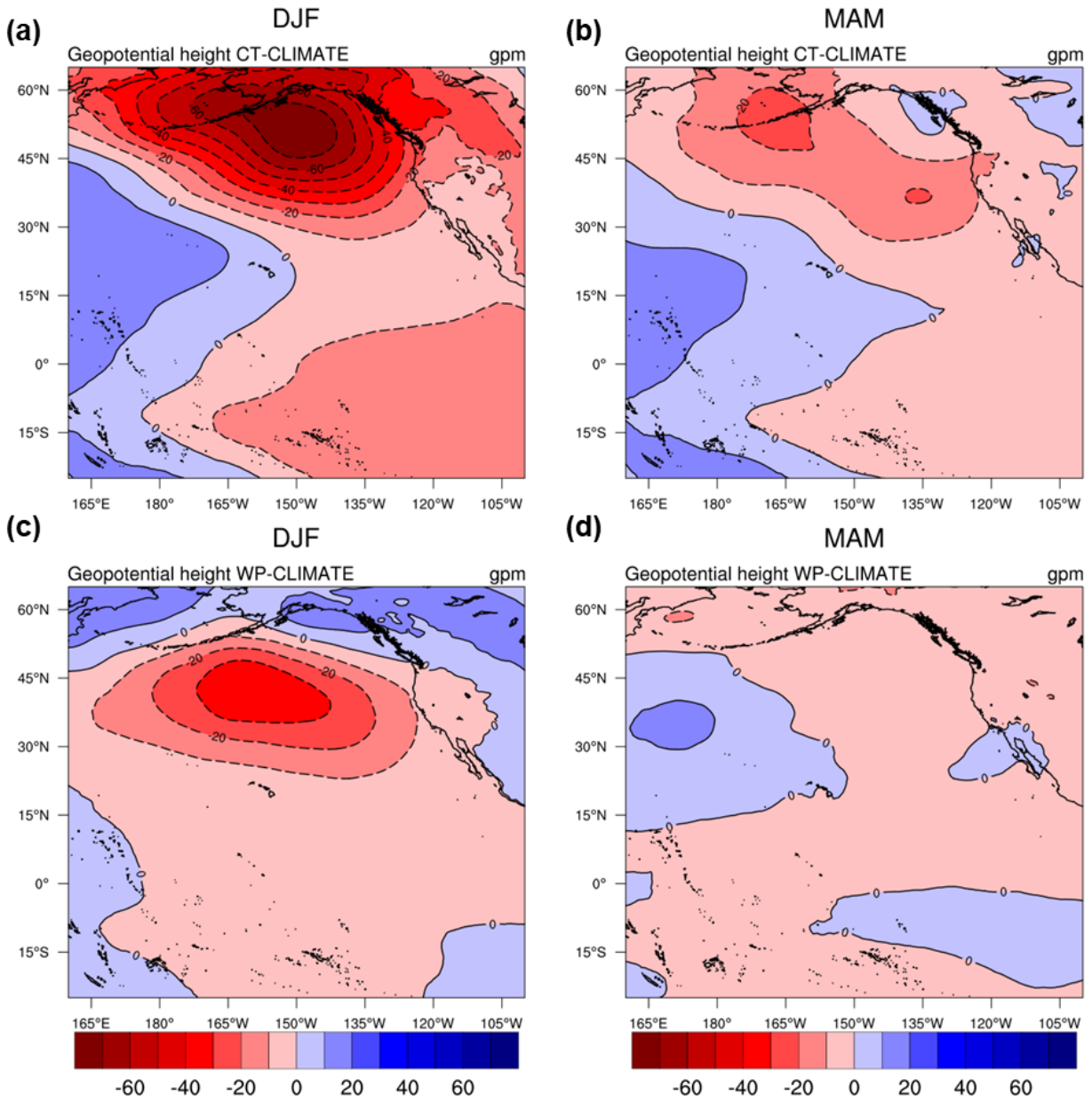


Fig. 6.16 Same as Fig. 6.14, but for geopotential height (m, contour) at 1000 hPa.

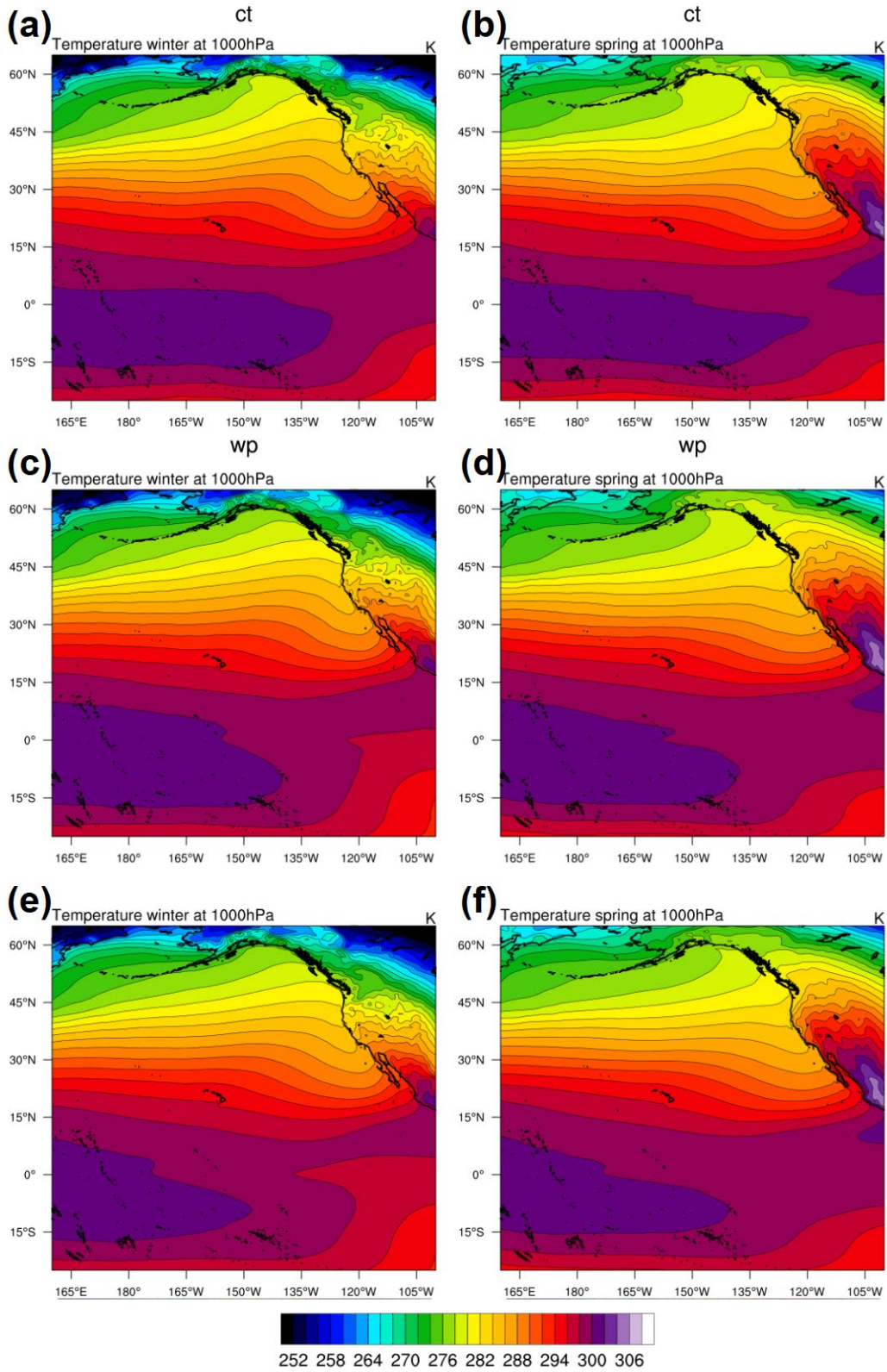


Fig. 6.17 Same as Fig. 6.13, but for temperature (K, color shading) at 1000 hPa.

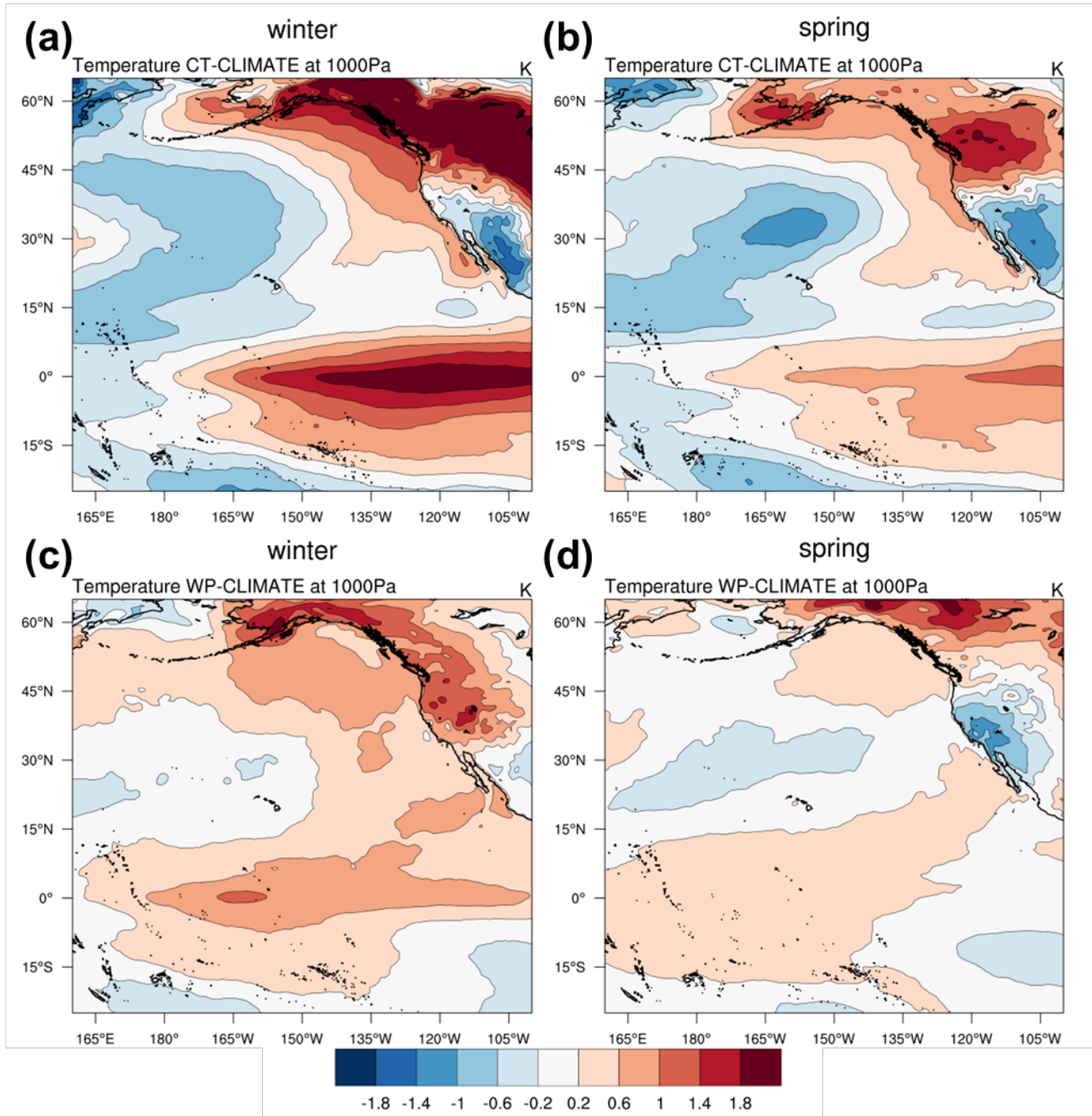


Fig. 6.18 Same as Fig. 6.14, but for temperature (K, color shading) at 1000 hPa.

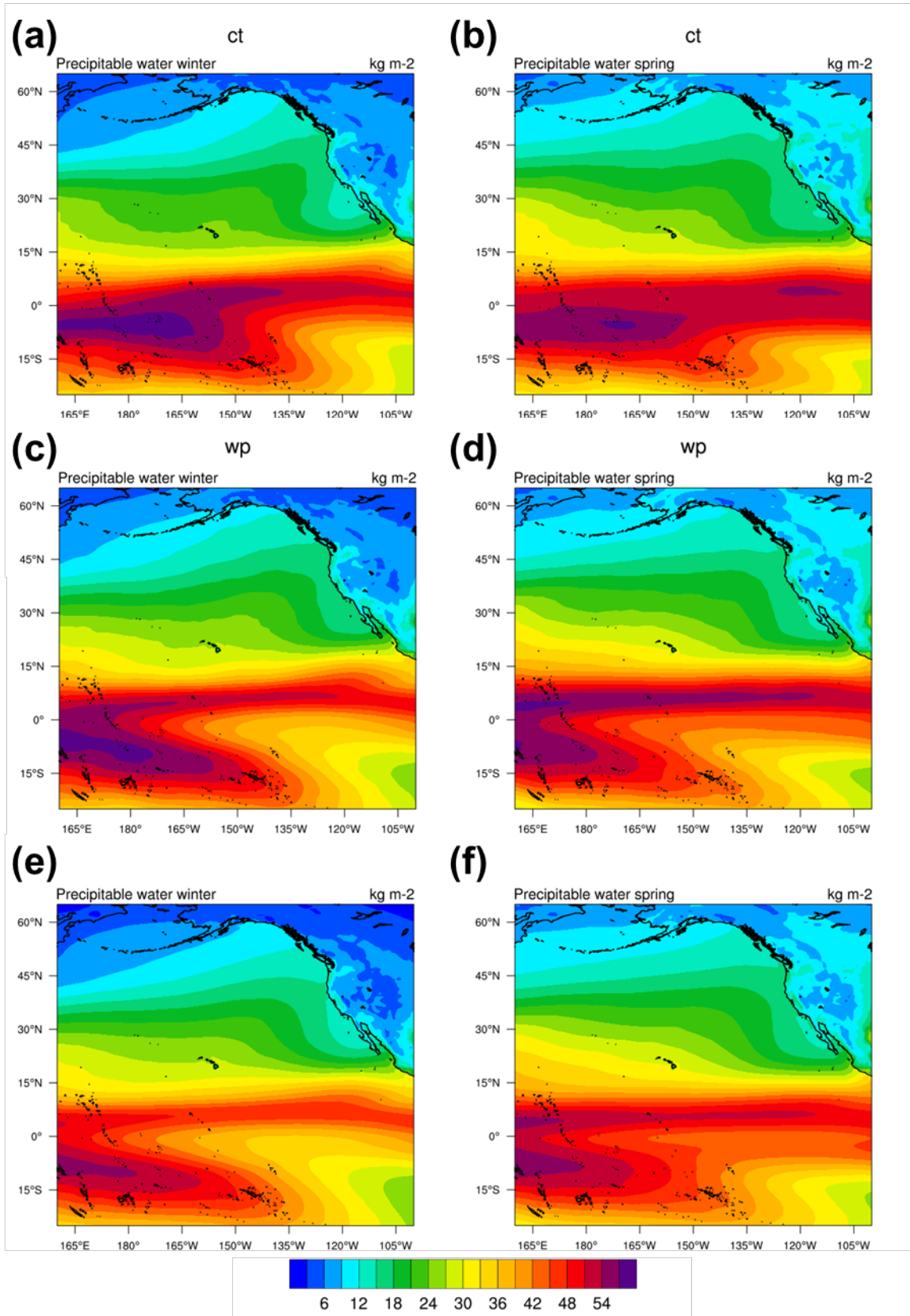


Fig. 6.19 Same as Fig. 6.13, but for total precipitable water (mm, color shading).

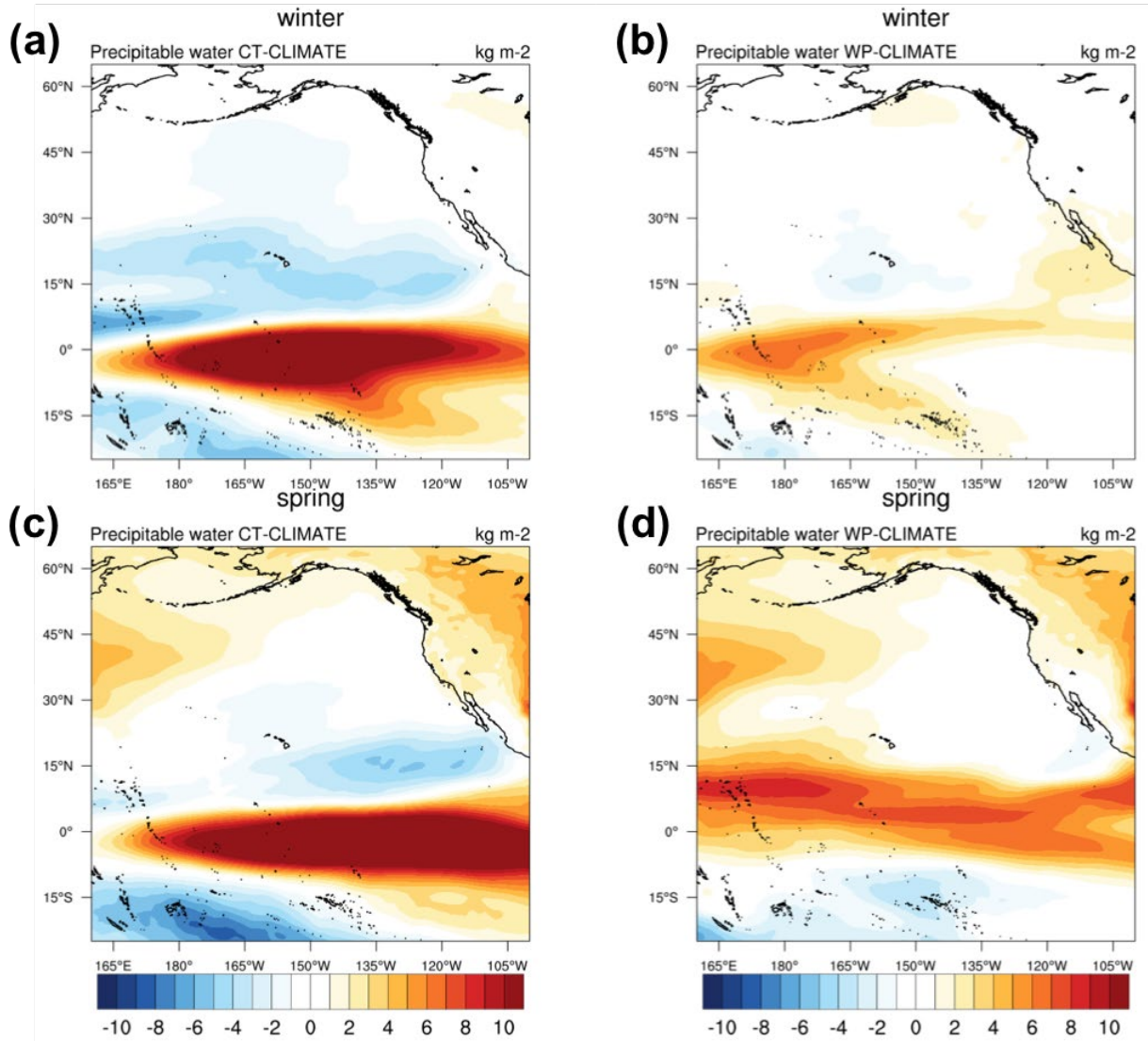


Fig. 6.20 Same as Fig. 6.14, but for total precipitable water (mm, color shading).

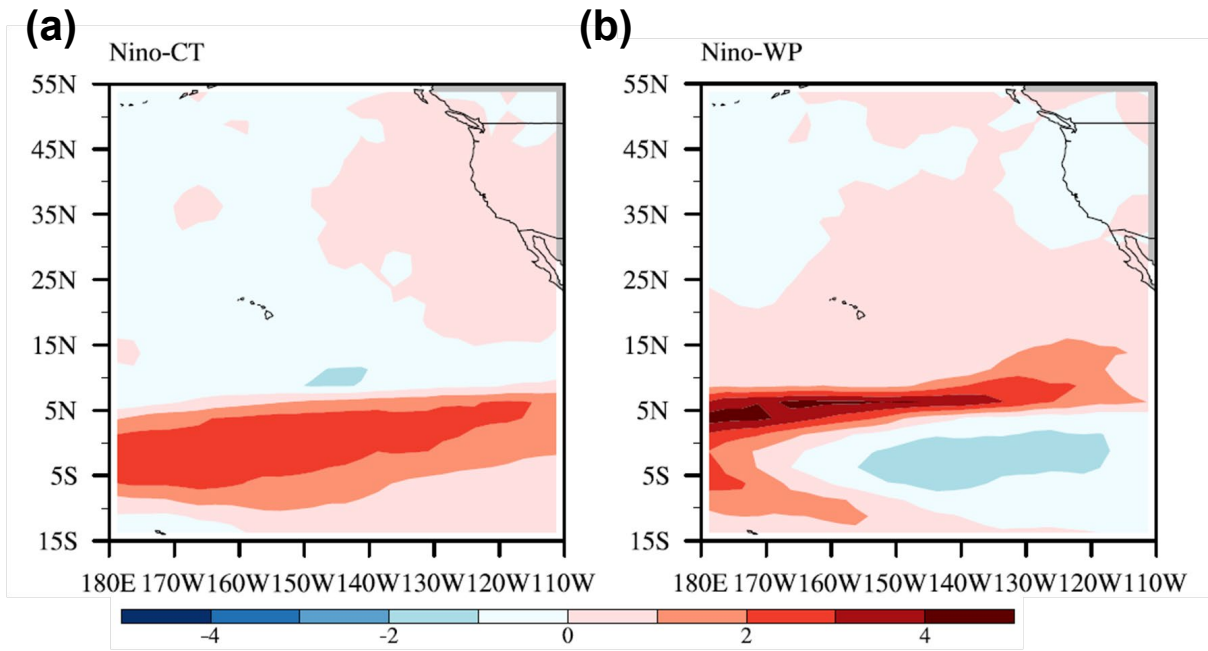


Fig. 6.21 The regressions of GPCP rainfall data onto (a) N_{ct} and (b) N_{wp} indices.

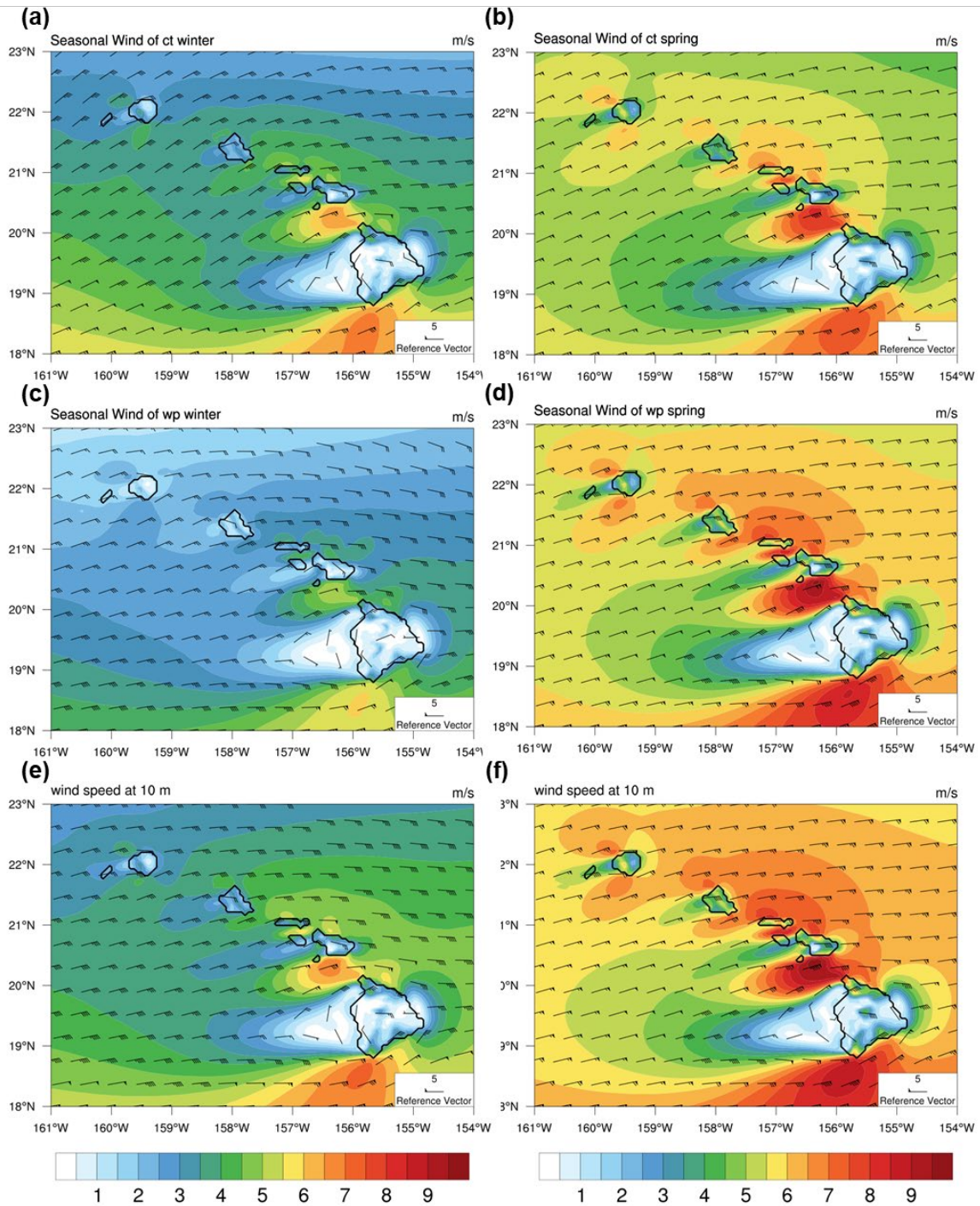


Fig. 6.22 The seasonal composite of simulated surface wind (m s^{-1} , color shading) for (a) CT winters, (b) CT springs, (c) WP winters, (d) WP springs, (e) all 38 winters, and (f) all 38 springs.

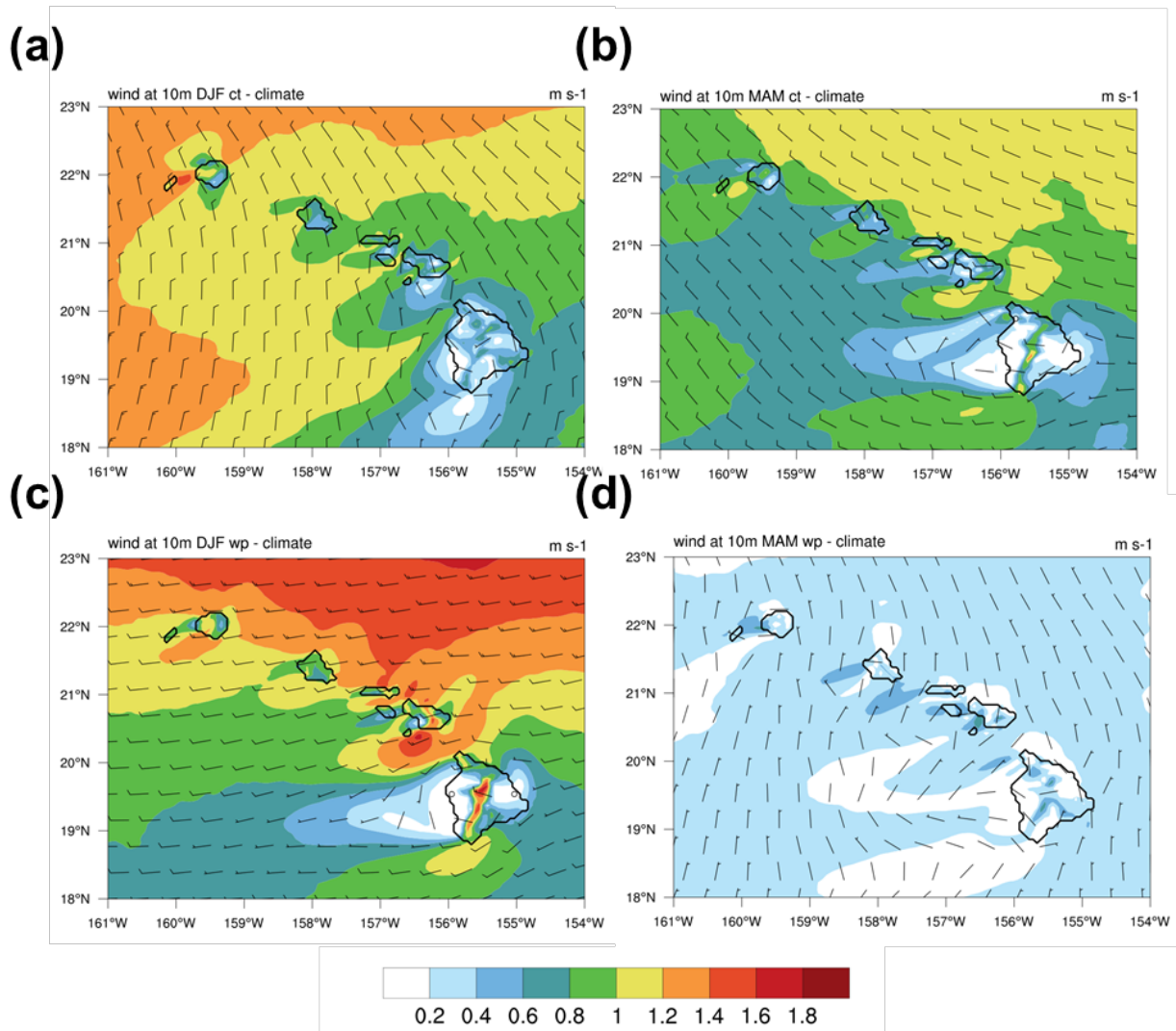


Fig. 6.23 The seasonal anomalies of simulated surface wind (m s^{-1} , color shading) for (a) CT winter, (b) CT spring, (c) WP winter, and (d) WP spring.

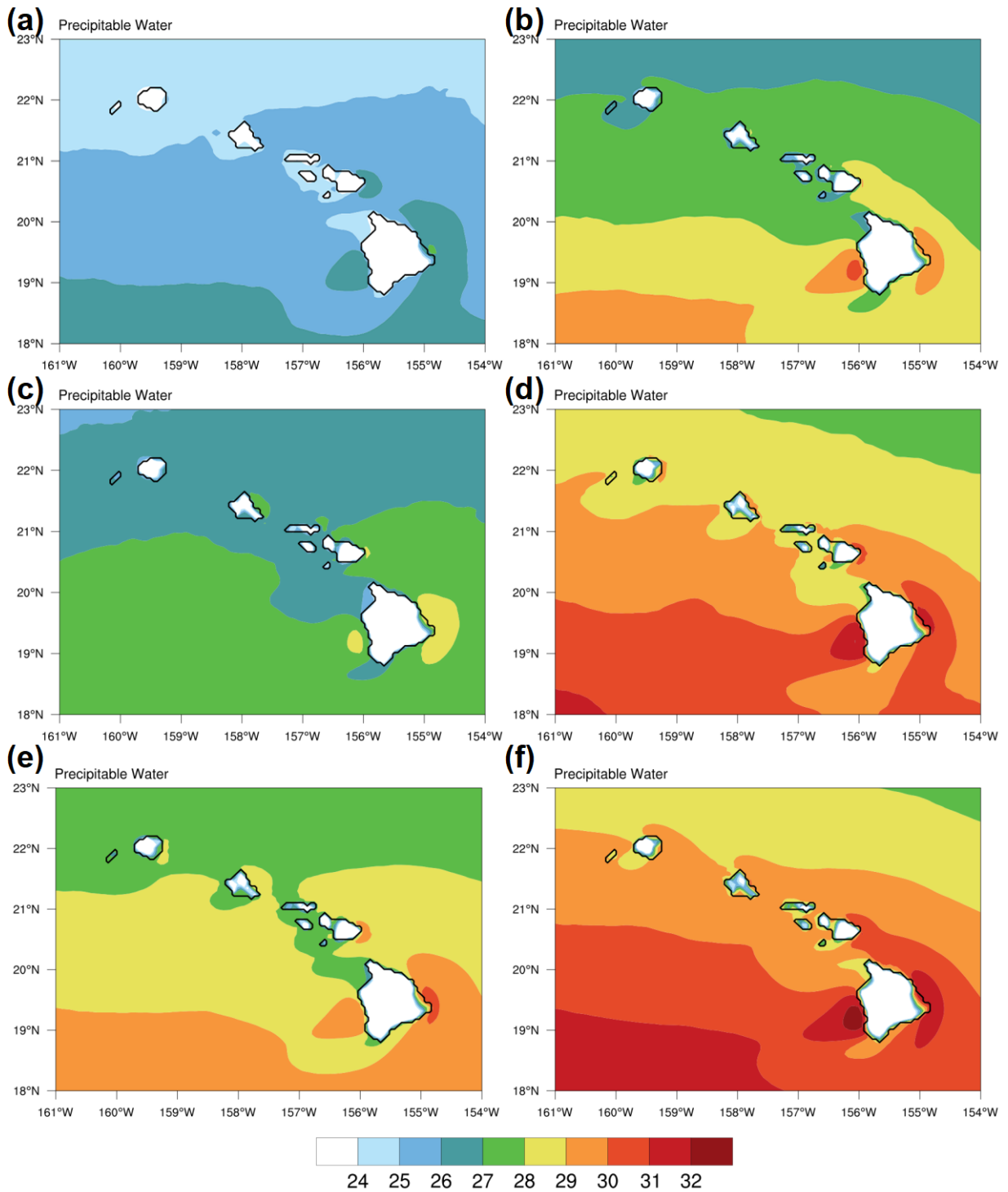


Fig. 6.24 Same as Fig. 6.22, but for simulated total precipitable water (mm, color shading).

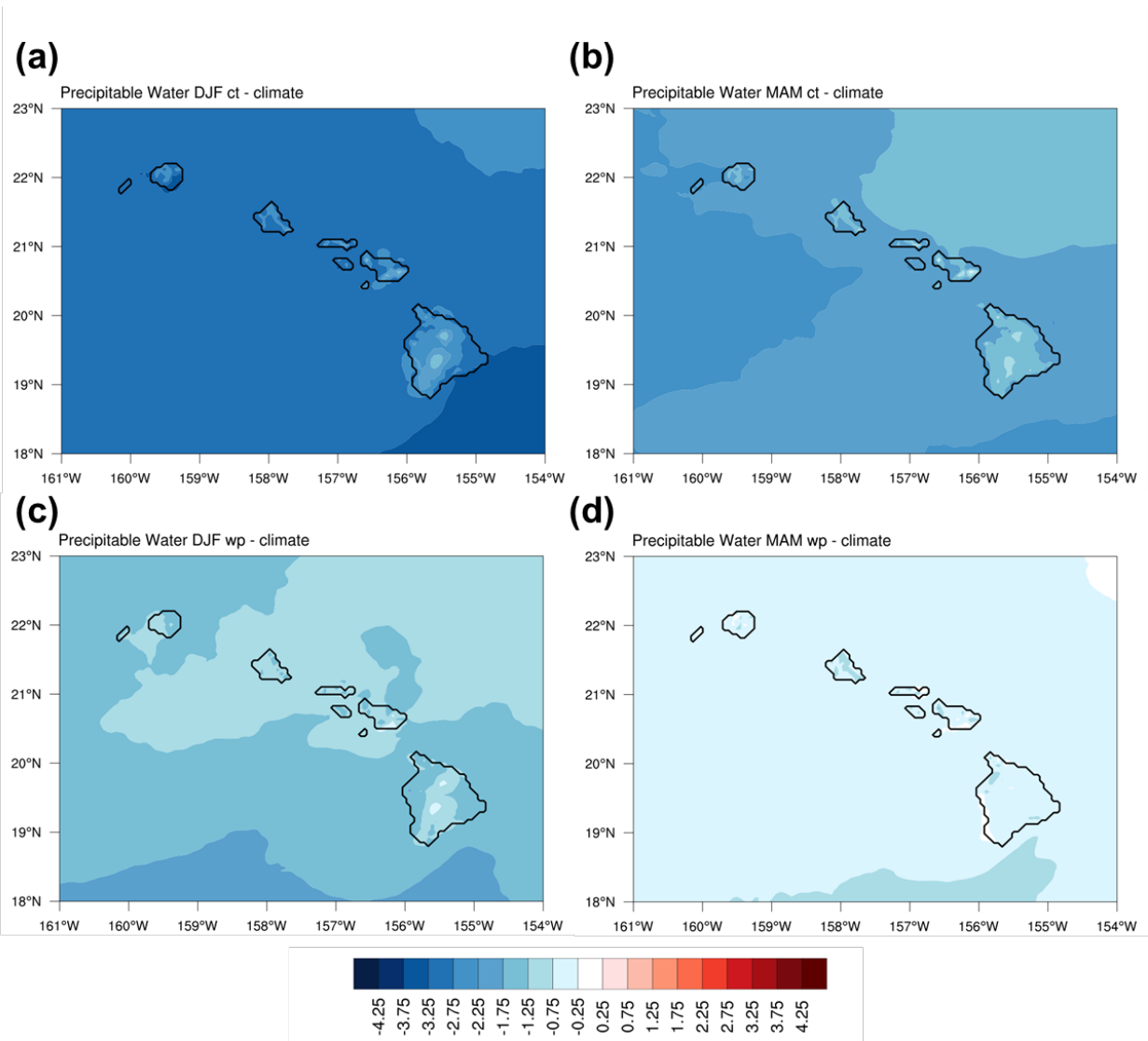


Fig. 6.25 Same as Fig. 6.23, but for simulated total precipitable water (mm, color shading).

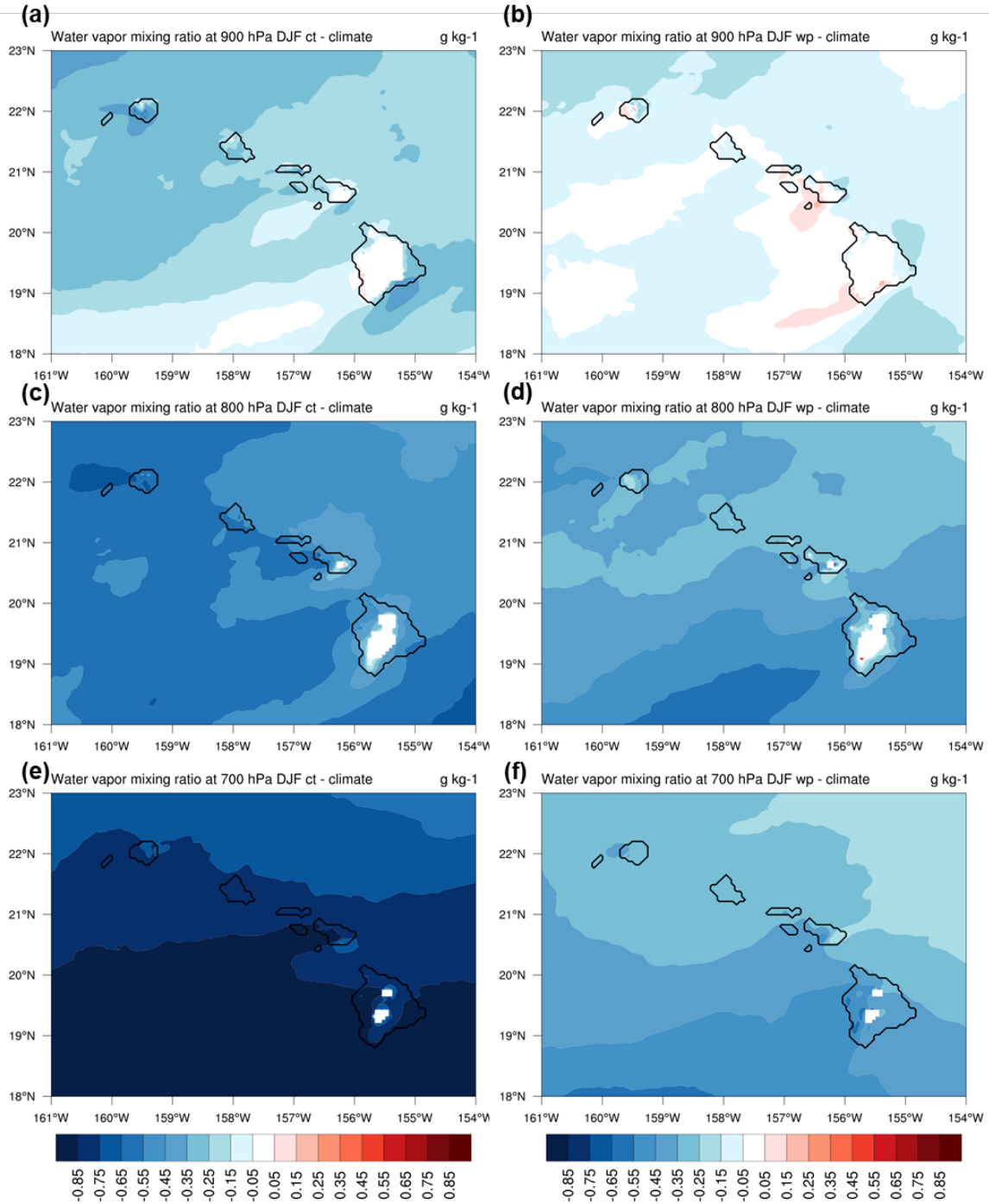


Fig. 6.26 The composite anomalies of simulated water vapor mixing ratio (g kg^{-1} , color shading) for the CT winters at (a) 900 hPa, (c) 800 hPa, and (e) 700 hPa. (b), (d), and (f) are same as (a), (c), and (e), but for WP winters.

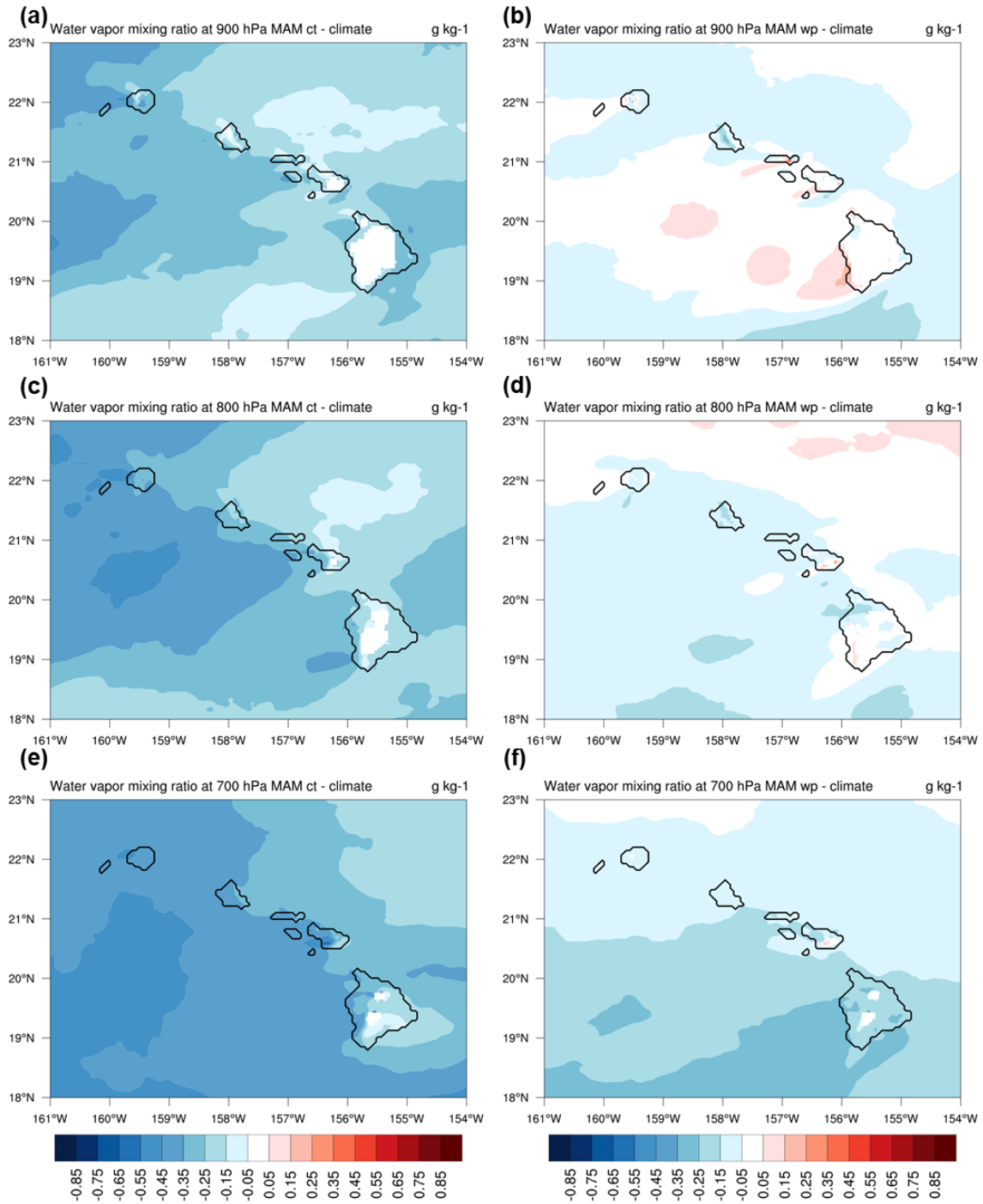


Fig. 6.27 Same as Fig. 6.26, but for spring.

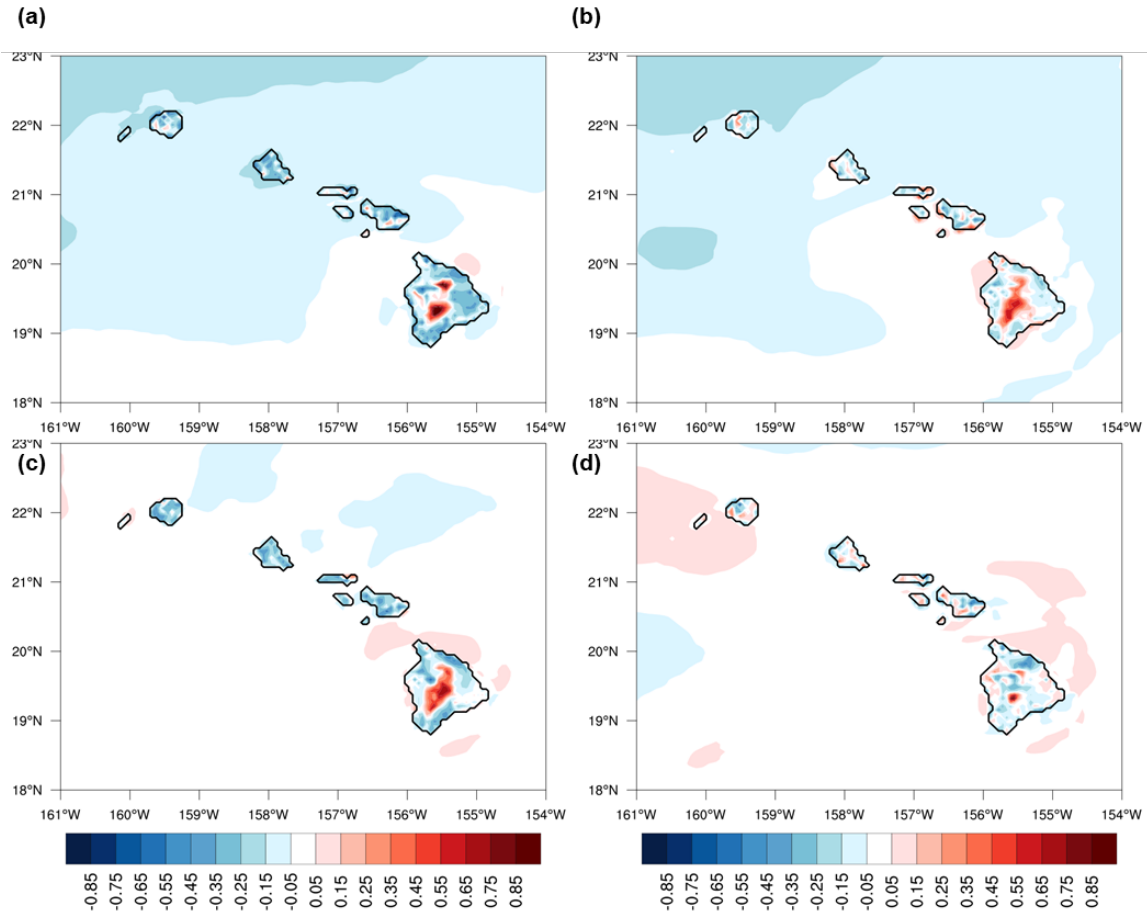


Fig. 6.28 Same as Fig. 6.23, but for simulated surface temperature (K, color shading).

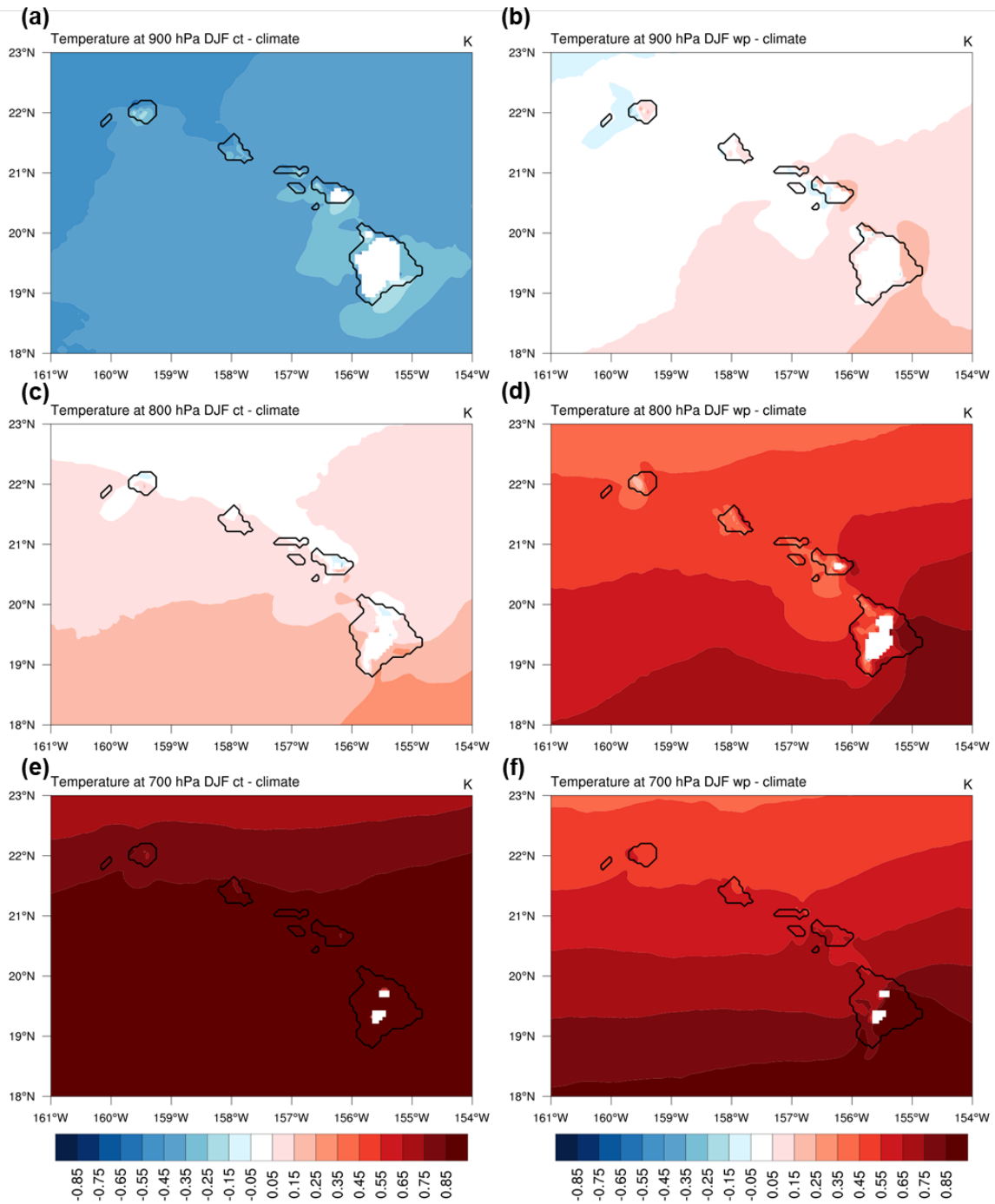


Fig. 6.29 Same as Fig. 6.26, but for simulated temperature (K, color shading).

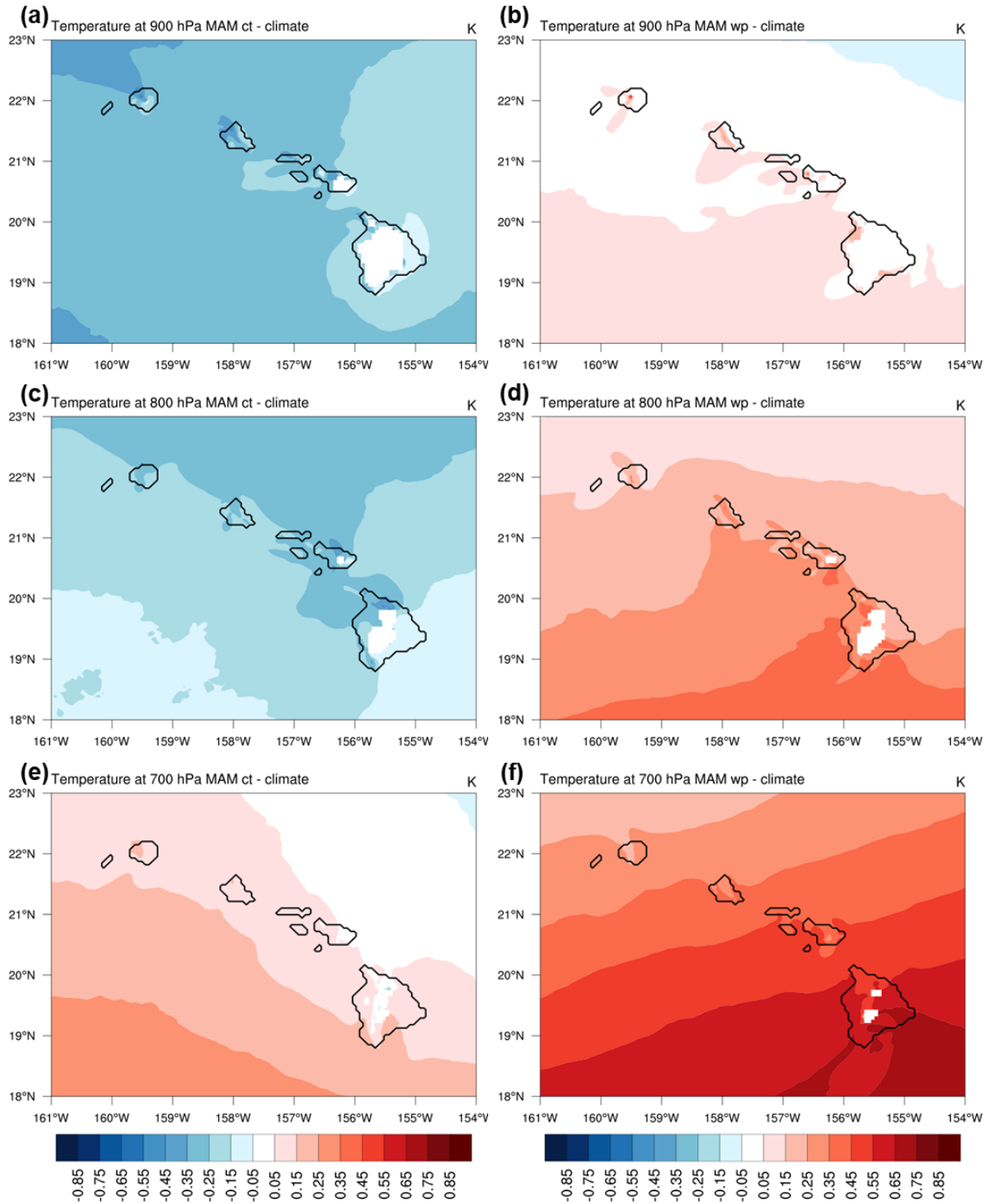


Fig. 6.30 Same as Fig. 6.27, but for simulated temperature (K, color shading).

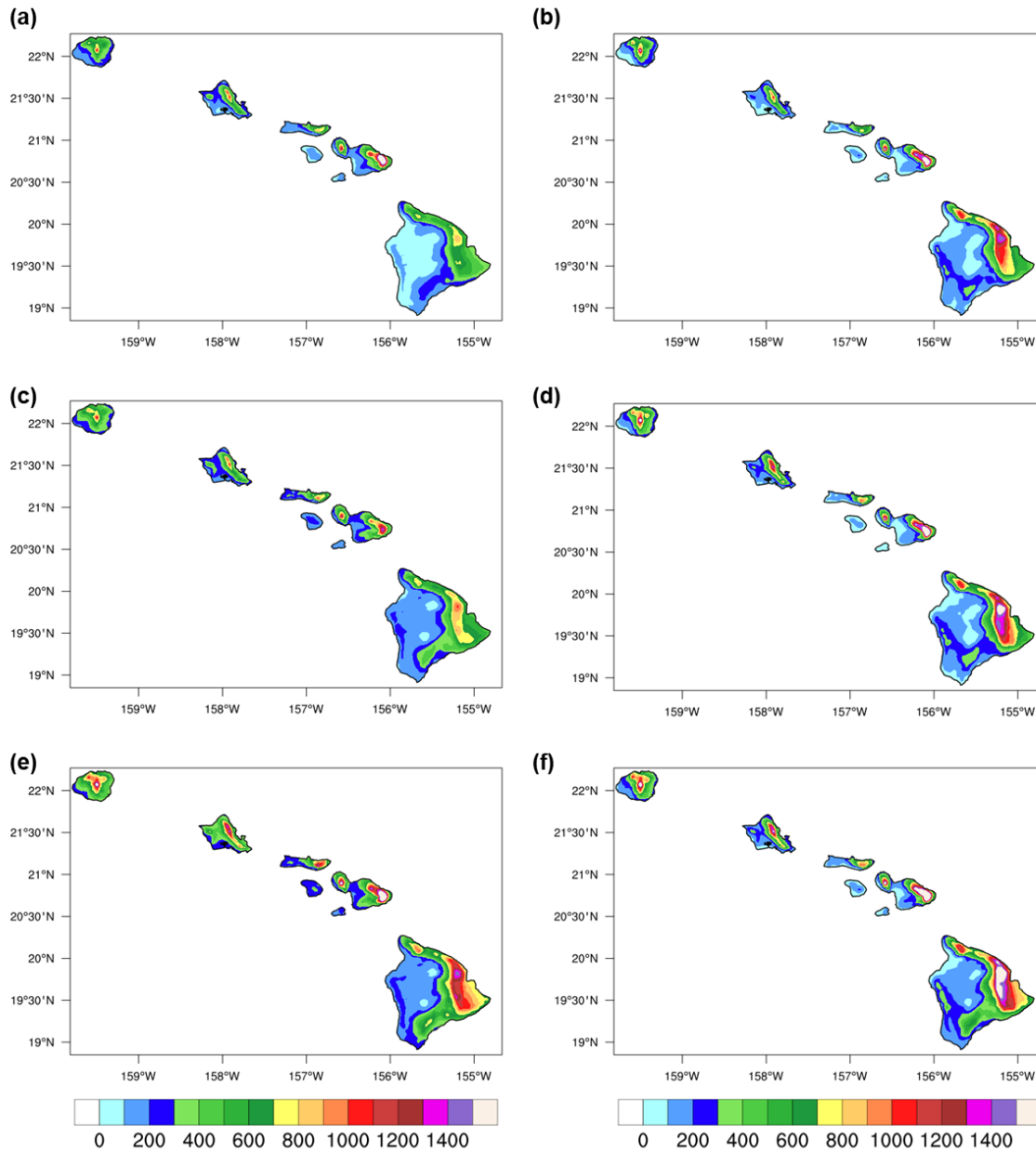


Fig. 6.31 The composite seasonal rainfall accumulation from the Rainfall Atlas of Hawai‘i (mm, color shading) for (a) 4 CT winters, (b) 4 CT springs, (c) 5 WP winters, (d) 5 WP springs, (e) all 33 winters, and (f) all 33 springs during 1979–2012.

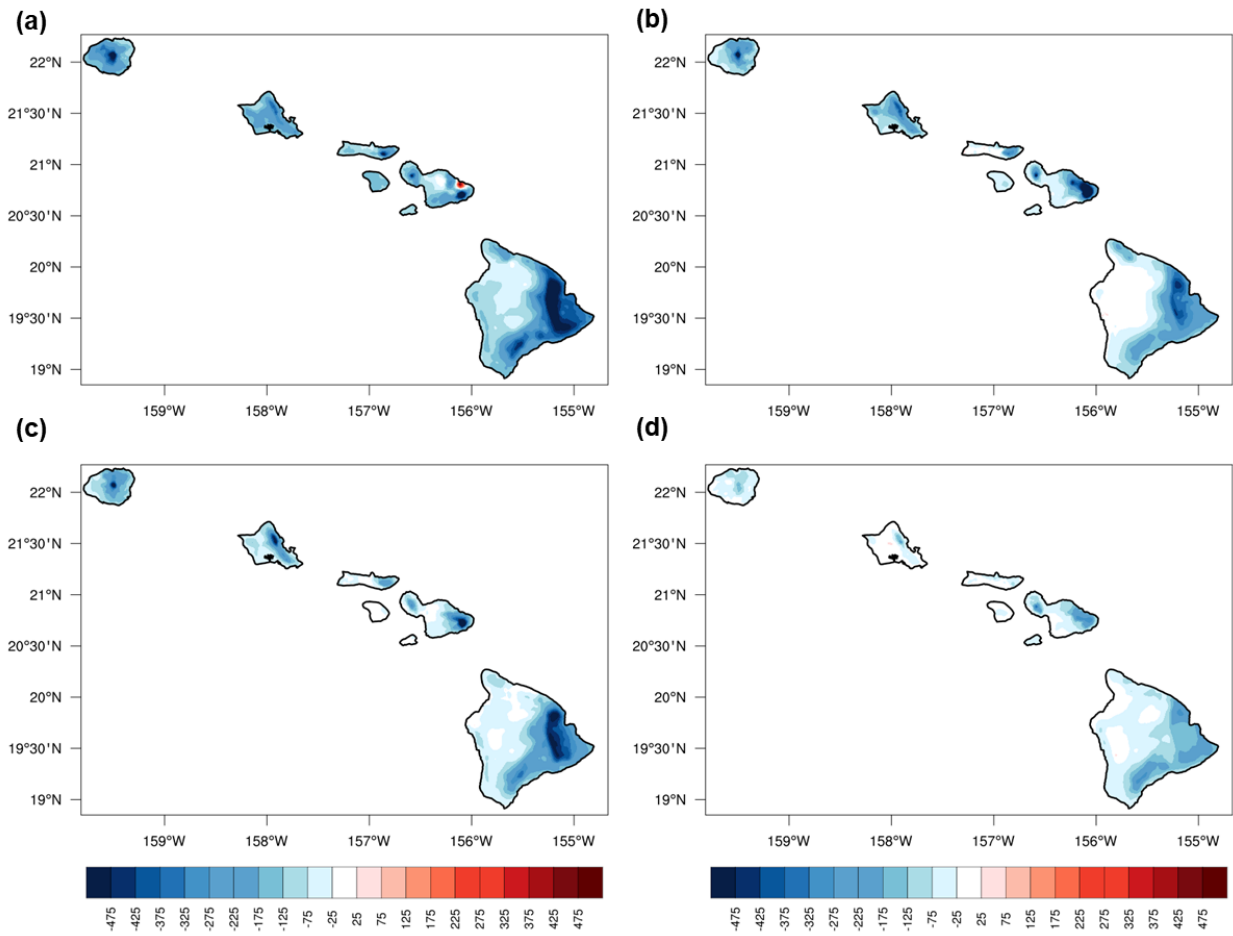


Fig. 6.32 The anomalies of seasonal rainfall accumulation from the Rainfall Atlas of Hawai'i (mm, color shading) for (a) 4 CT winters, (b) 4 CT springs, (c) 5 WP winters, and (d) 5 WP springs during 1979–2012.

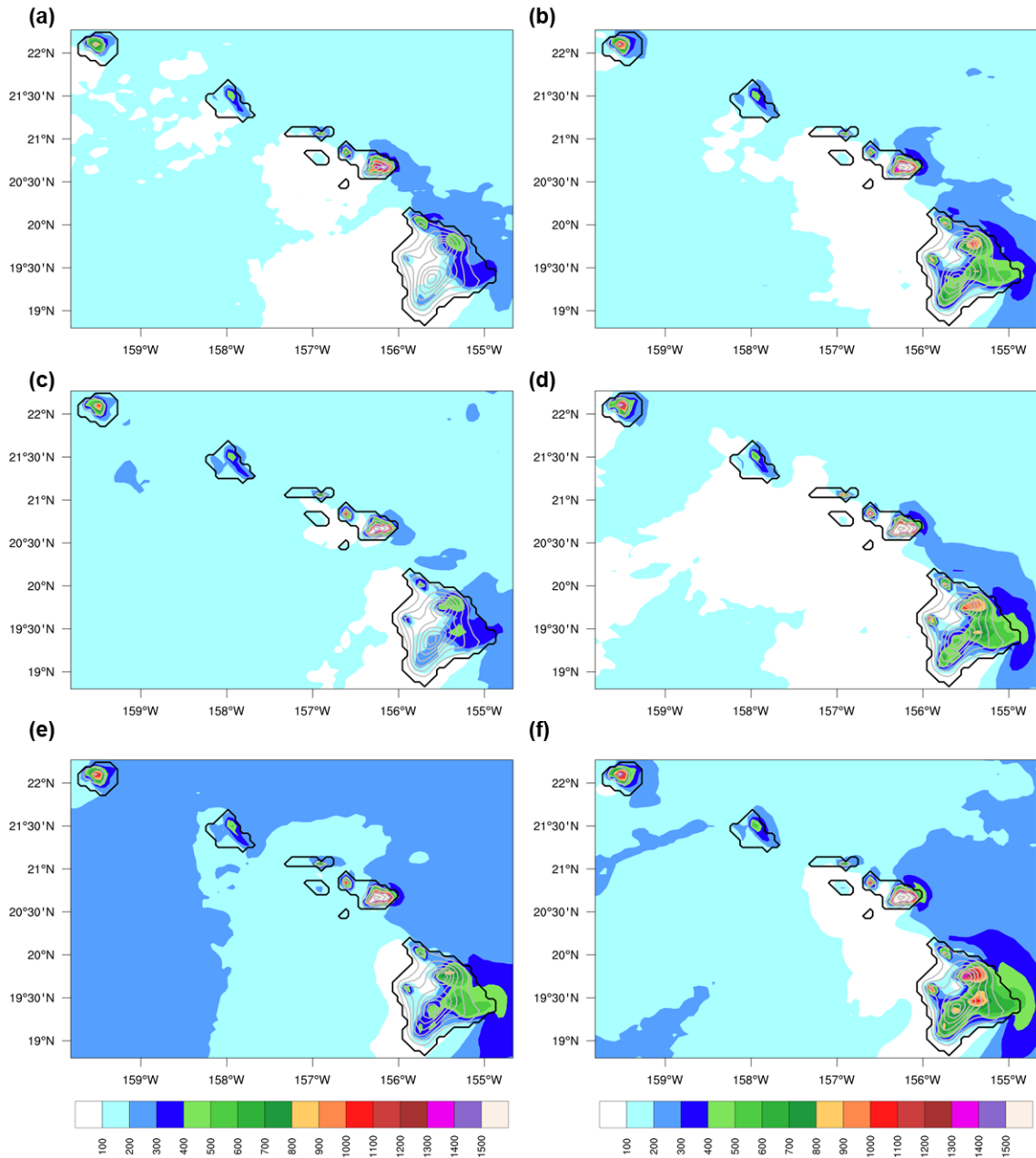


Fig. 6.33 Same as Fig. 6.31, but for simulated seasonal rainfall accumulation (mm, color shading).

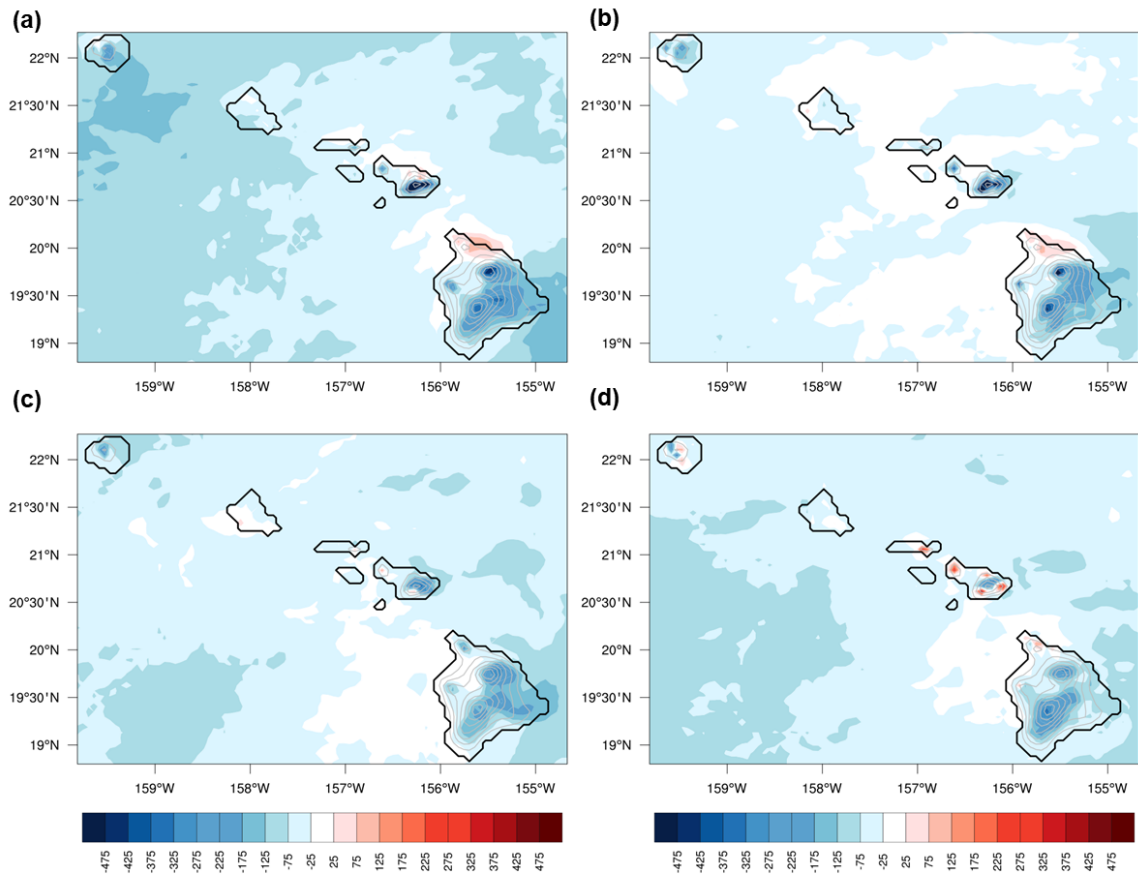


Fig. 6.34 Same as Fig. 6.32, but for seasonal simulated rainfall accumulation (mm, color shading).

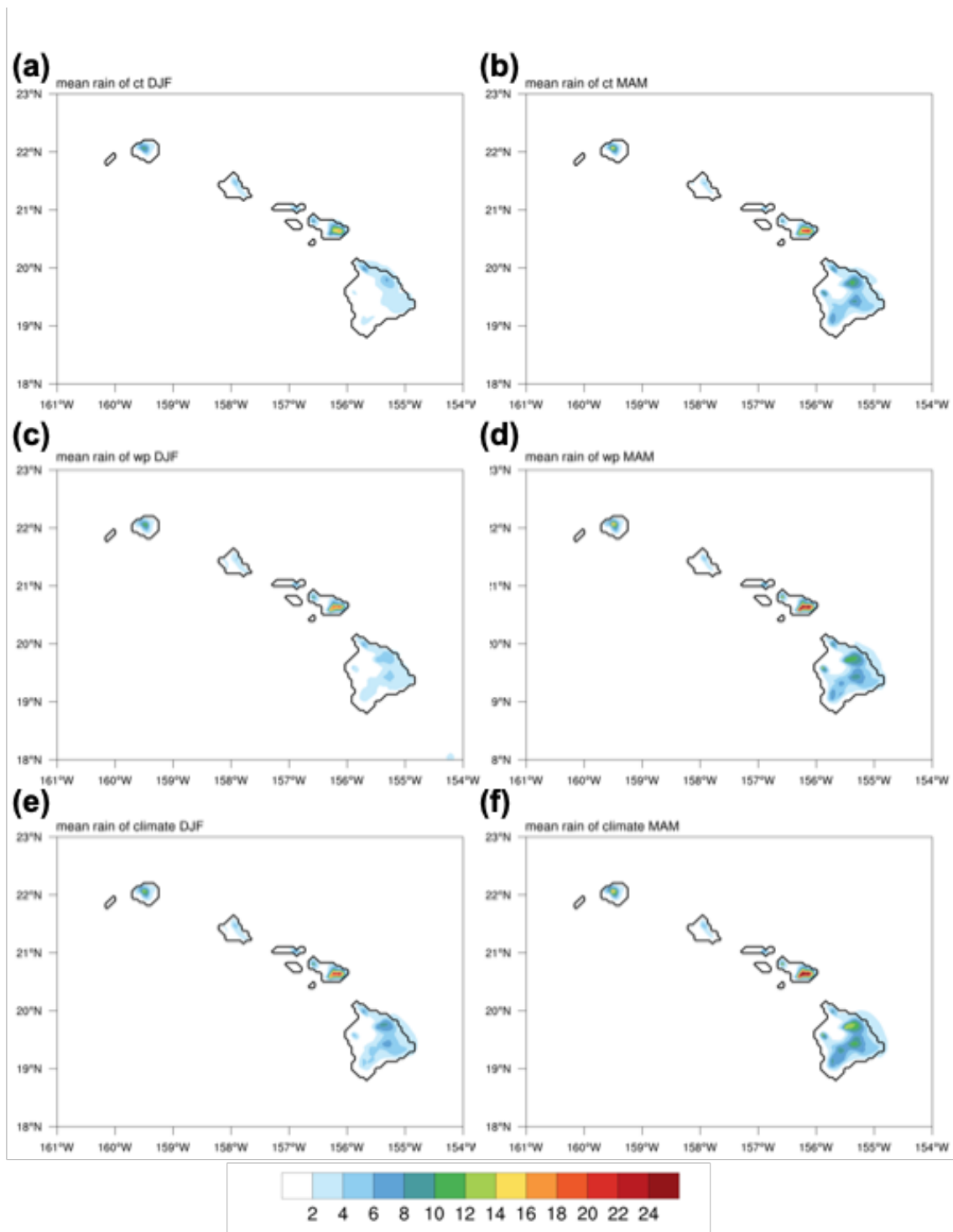


Fig. 6.35 The seasonal composite of simulated daily rainfall (mm, color shading) for (a) CT winters, (b) CT springs, (c) WP winters, (d) WP springs, (e) all 38 winters, and (d) all 38 springs.

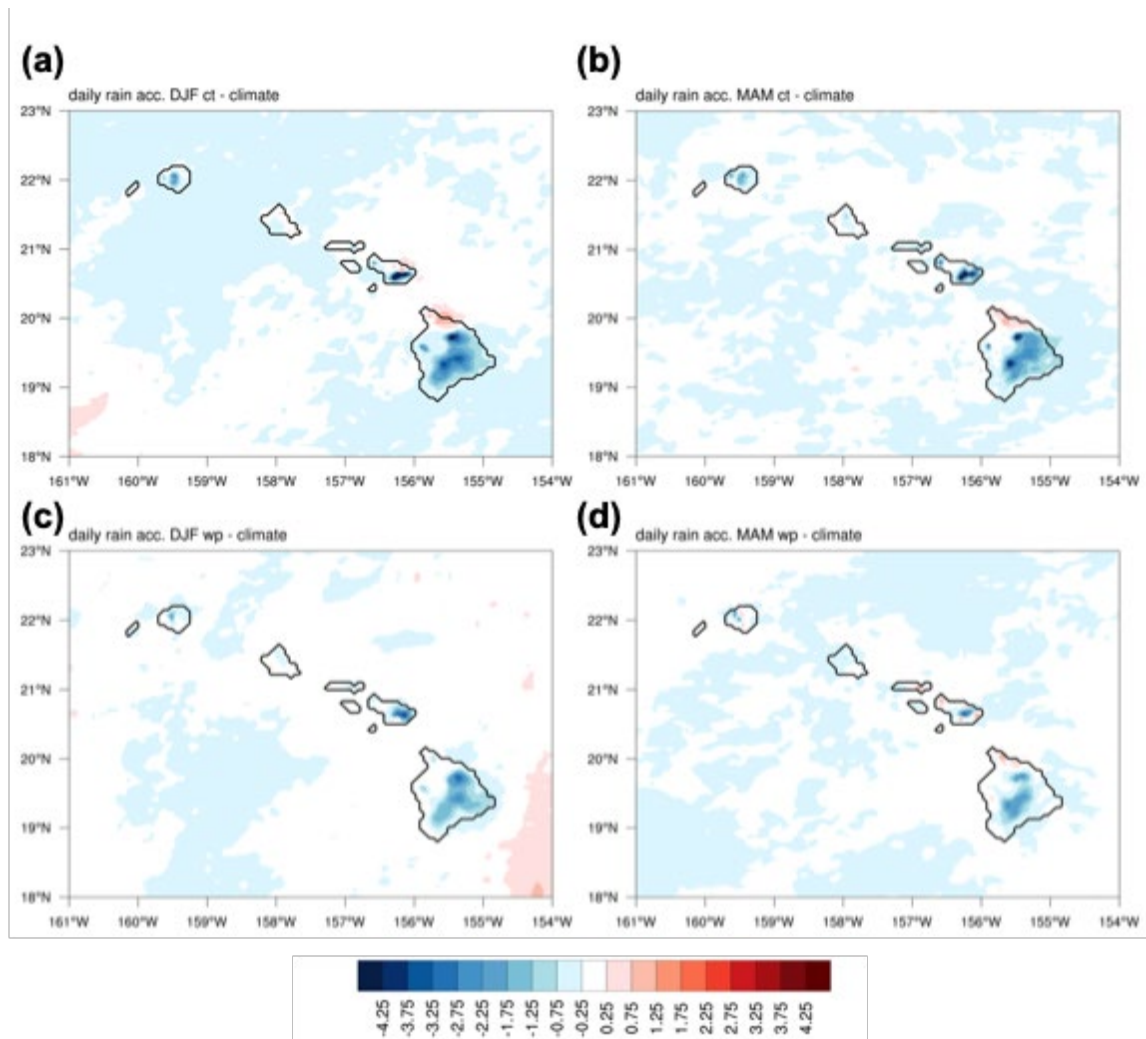


Fig. 6.36 The seasonal anomalies of simulated daily rainfall (mm, color shading) for (a) CT winters, (b) CT springs, (c) WP winters, and (d) WP springs.

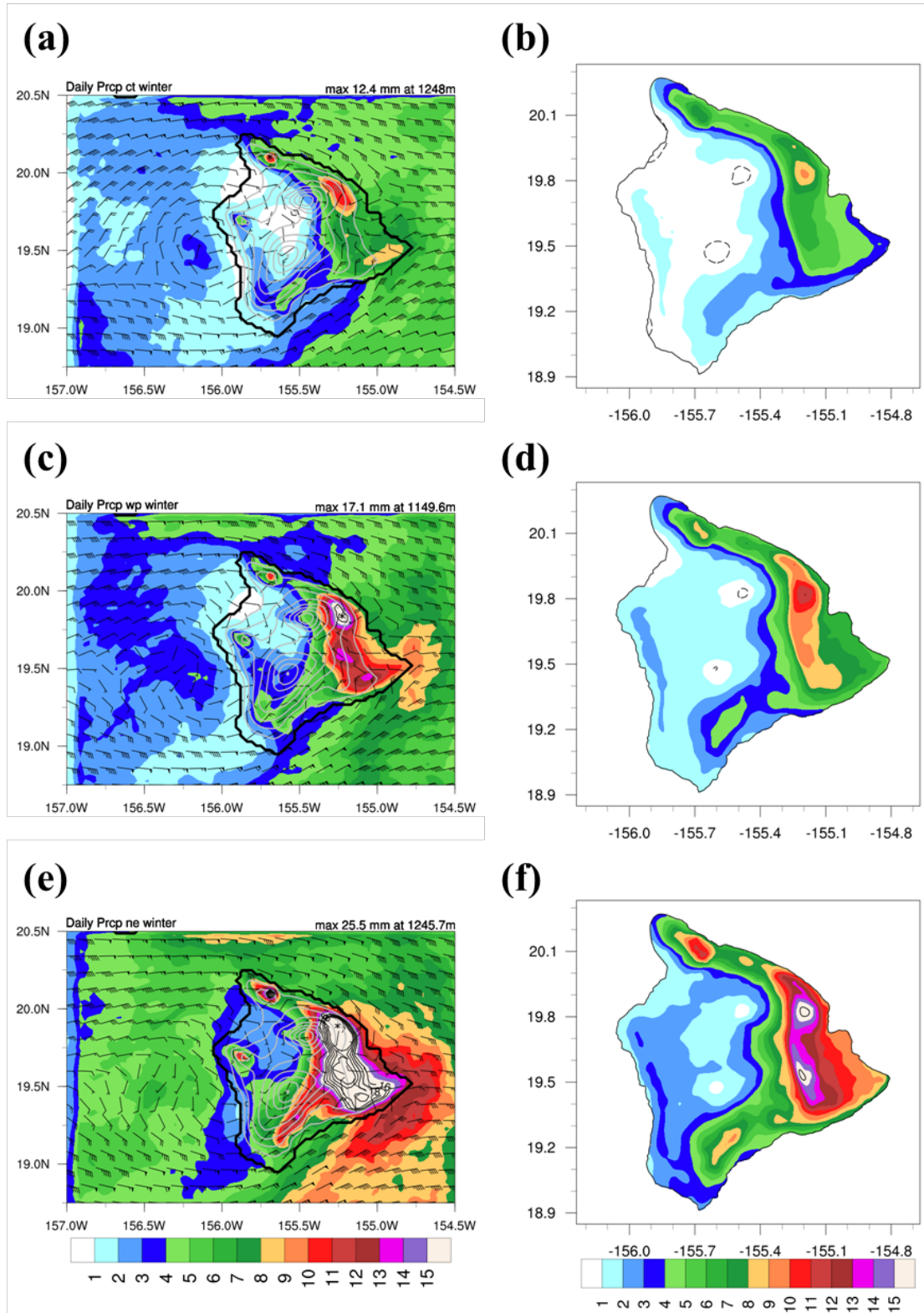


Fig. 6.37 The simulated daily rainfall (mm, color shading) over Hawai'i Island during (a) the CT winters, (c) the WP winters, and (e) the neutral winters. The seasonal rainfall from the

Rainfall Atlas of Hawai'i during (b) the CT winters, (d) the WP winters, and (f) the neutral winters. Black solid contours represent simulated daily rainfall over 17 mm (interval 1 mm). Black dashed line represents 0.5 mm simulated daily rainfall contour. Black asterisk represents the location of daily rainfall maximum.

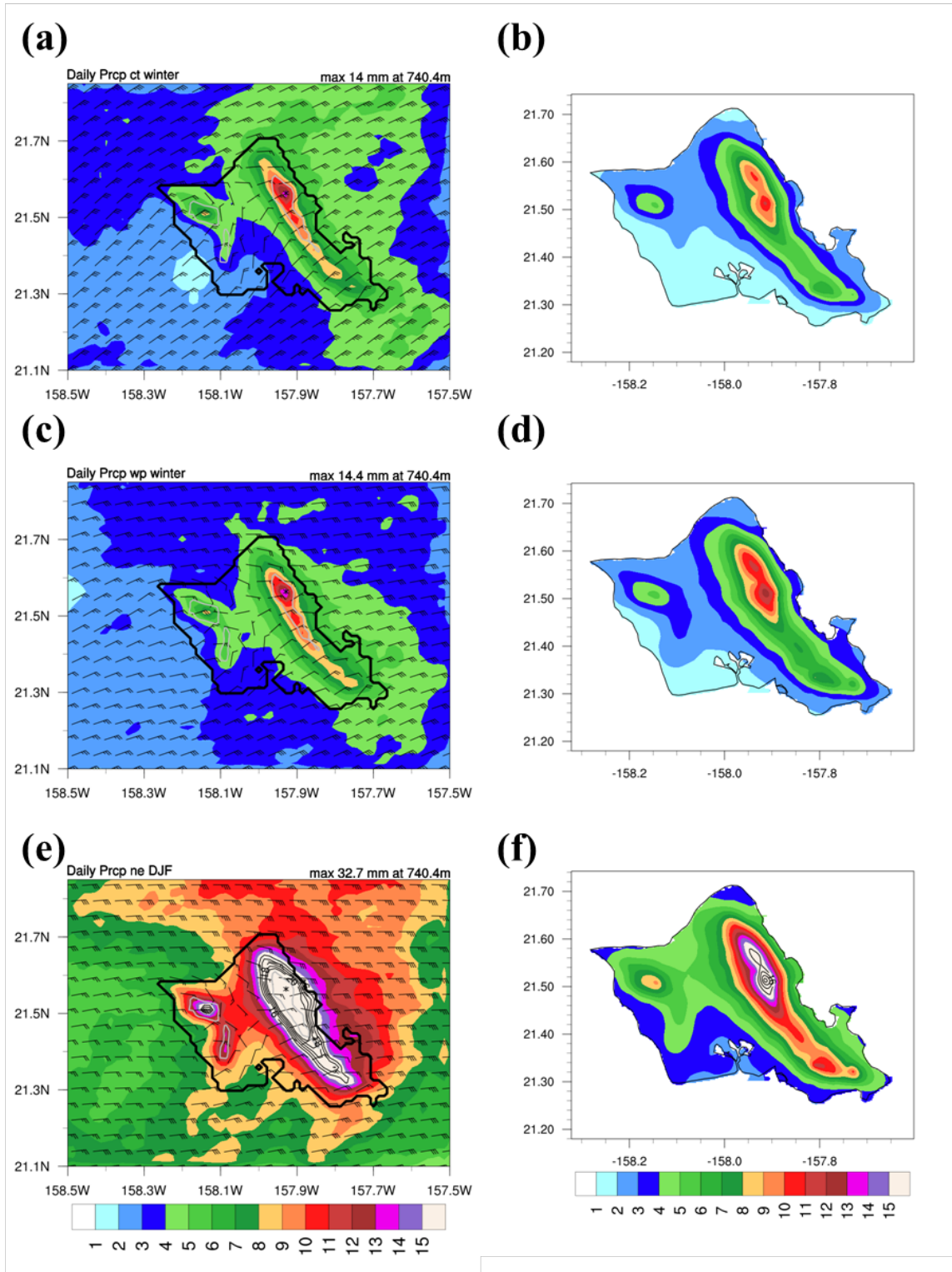


Fig. 6.38 The simulated daily rainfall over O'ahu Island during (a) the CT winters, (c) the WP winters, and (e) the neutral winters. The seasonal rainfall from the Rainfall Atlas of Hawai'i during (b) the CT winters, (d) the WP winters, and (f) the neutral winters. Black

solid contours represent simulated daily rainfall over 16 mm (interval 1 mm). Black dashed line represents 0.5 mm simulated daily rainfall contour. Black asterisk represents the location of daily rainfall maximum.

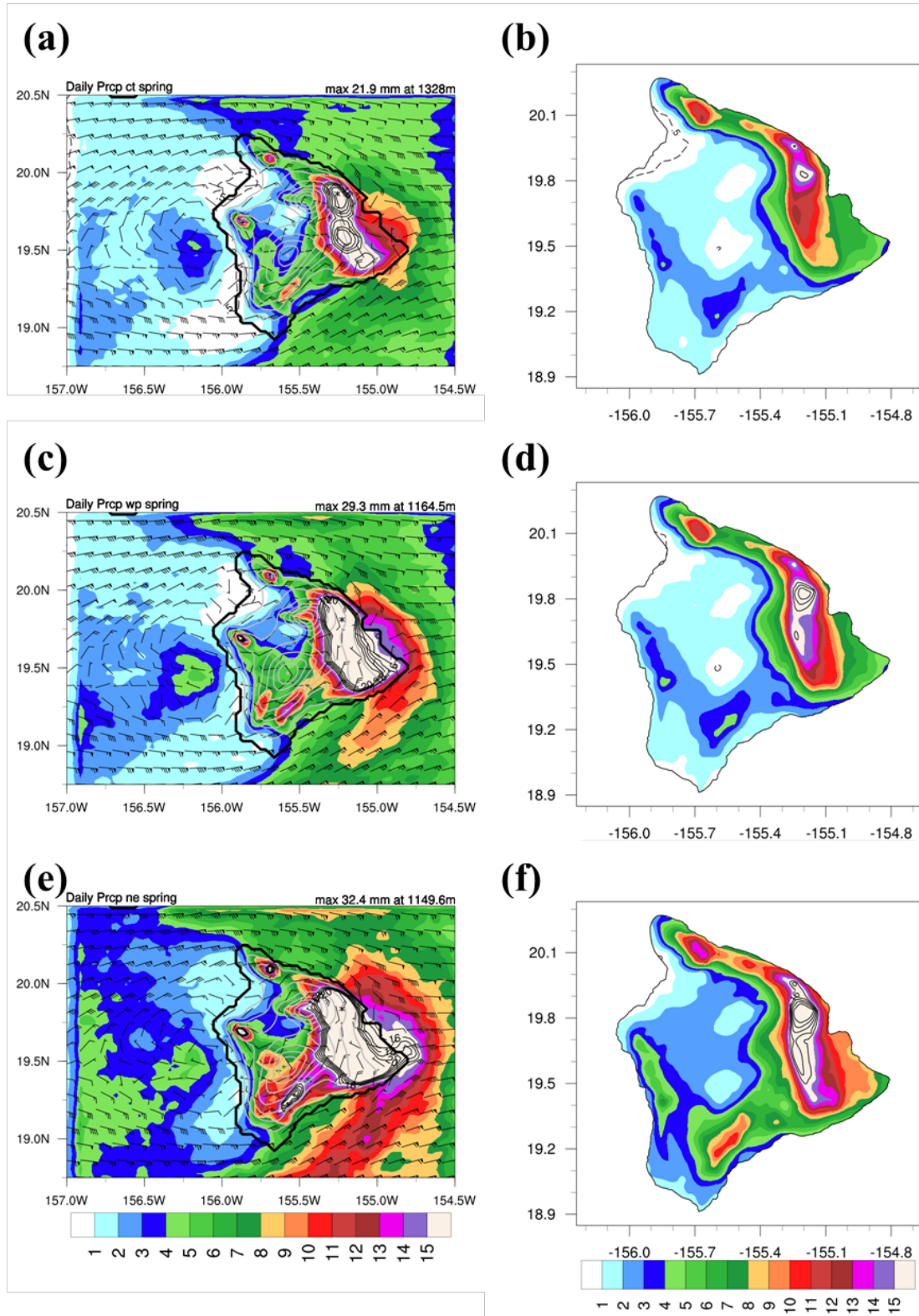


Fig. 6.39 Same as Fig. 6.37, but for springs.

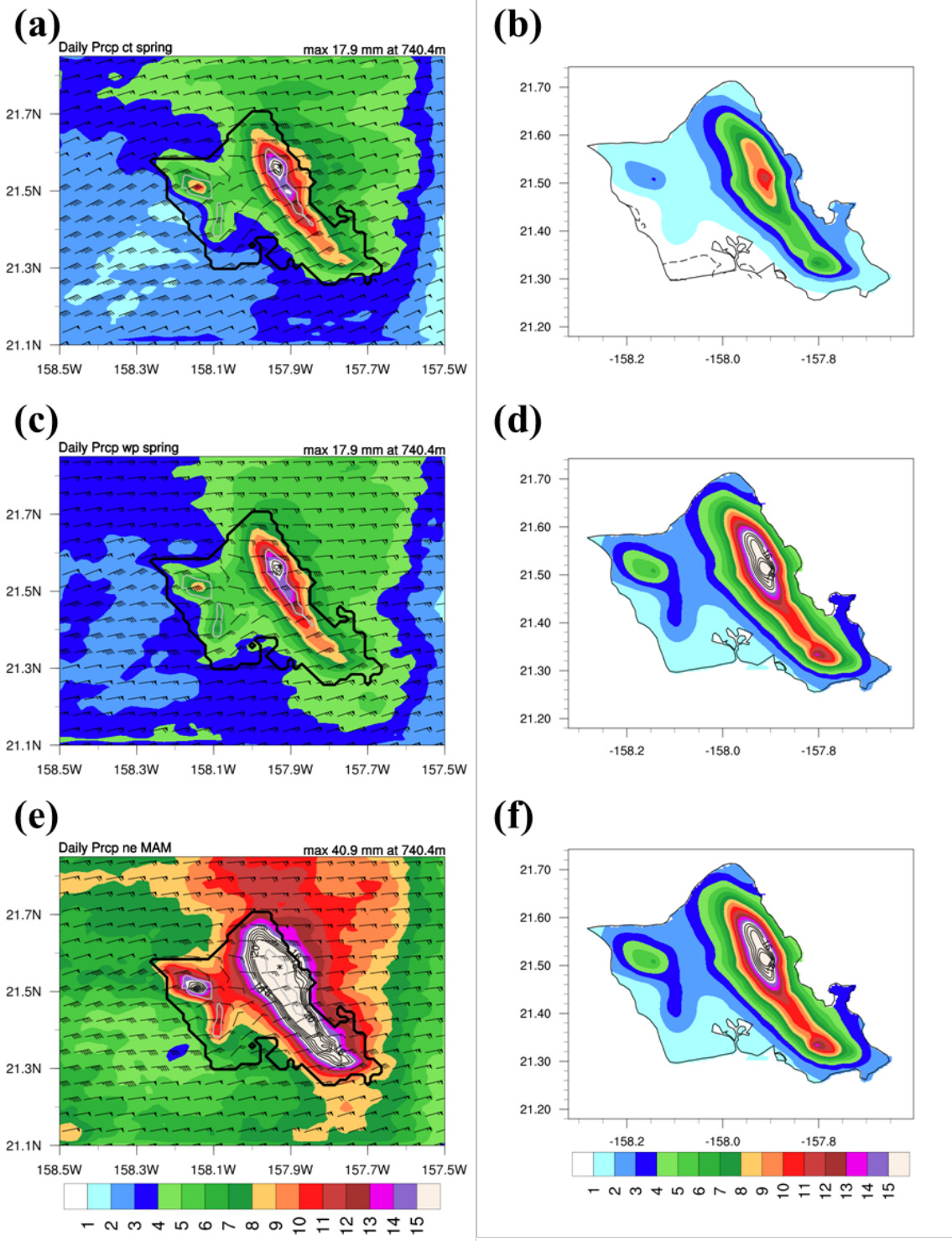


Fig. 6.40 Same as Fig. 7.38, but for springs.

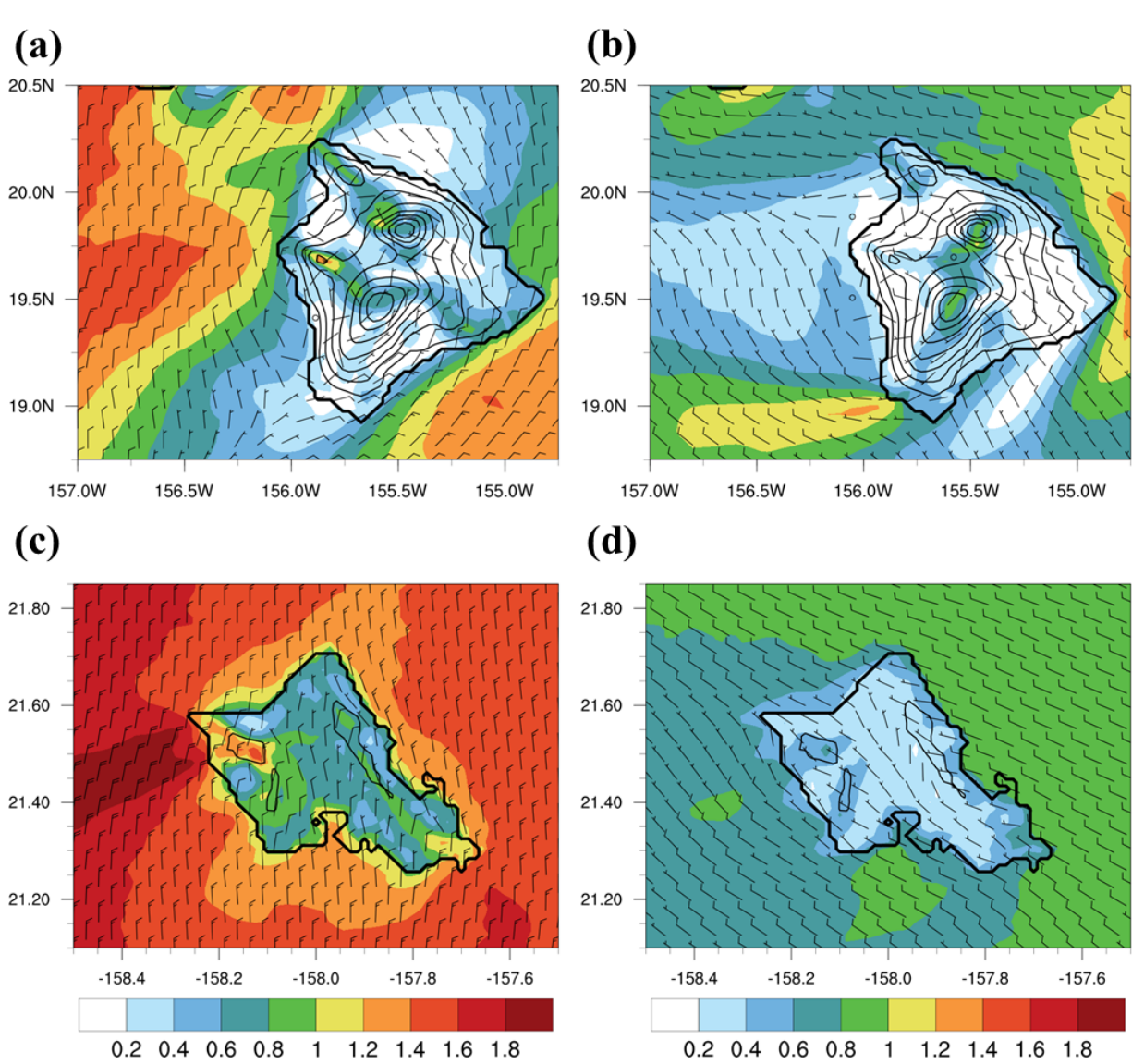


Fig. 6.41 The seasonal anomalies of simulated surface wind (m s^{-1} , color shading) over Hawai'i Island during (a) CT winters and (b) WP winters. (c) Same as (a), but over O'ahu Island. (d) Same as (c), but over O'ahu Island. Black contours represent model elevation in 500 m intervals.

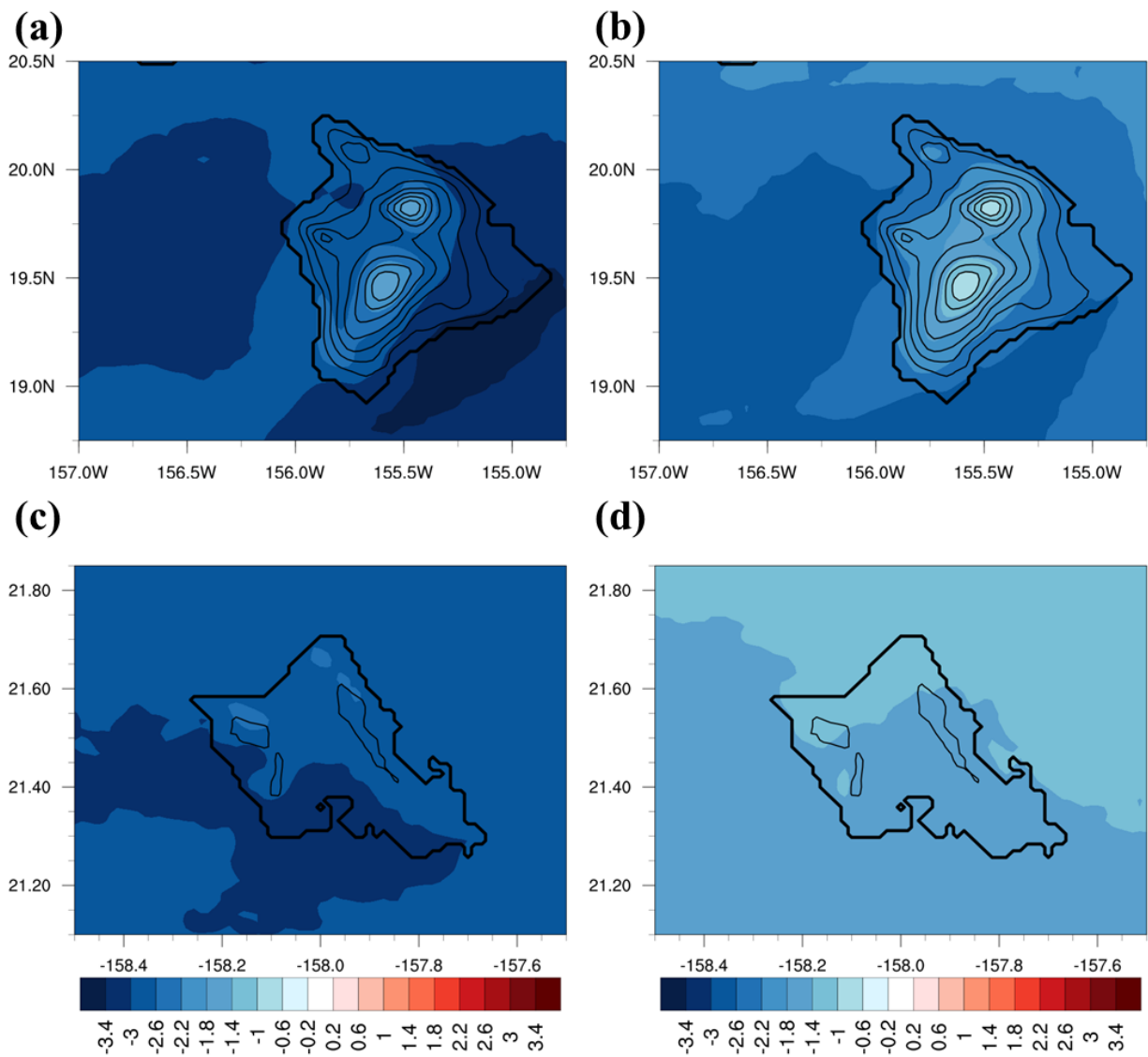


Fig. 6.42 The seasonal anomalies of simulated TPW (mm, color shading) over Hawai'i Island during (a) CT winters and (b) WP winters. (c) Same as (a), but over O'ahu Island. (d) Same as (c), but over O'ahu Island. Black contours represent model elevation in 500 m intervals.

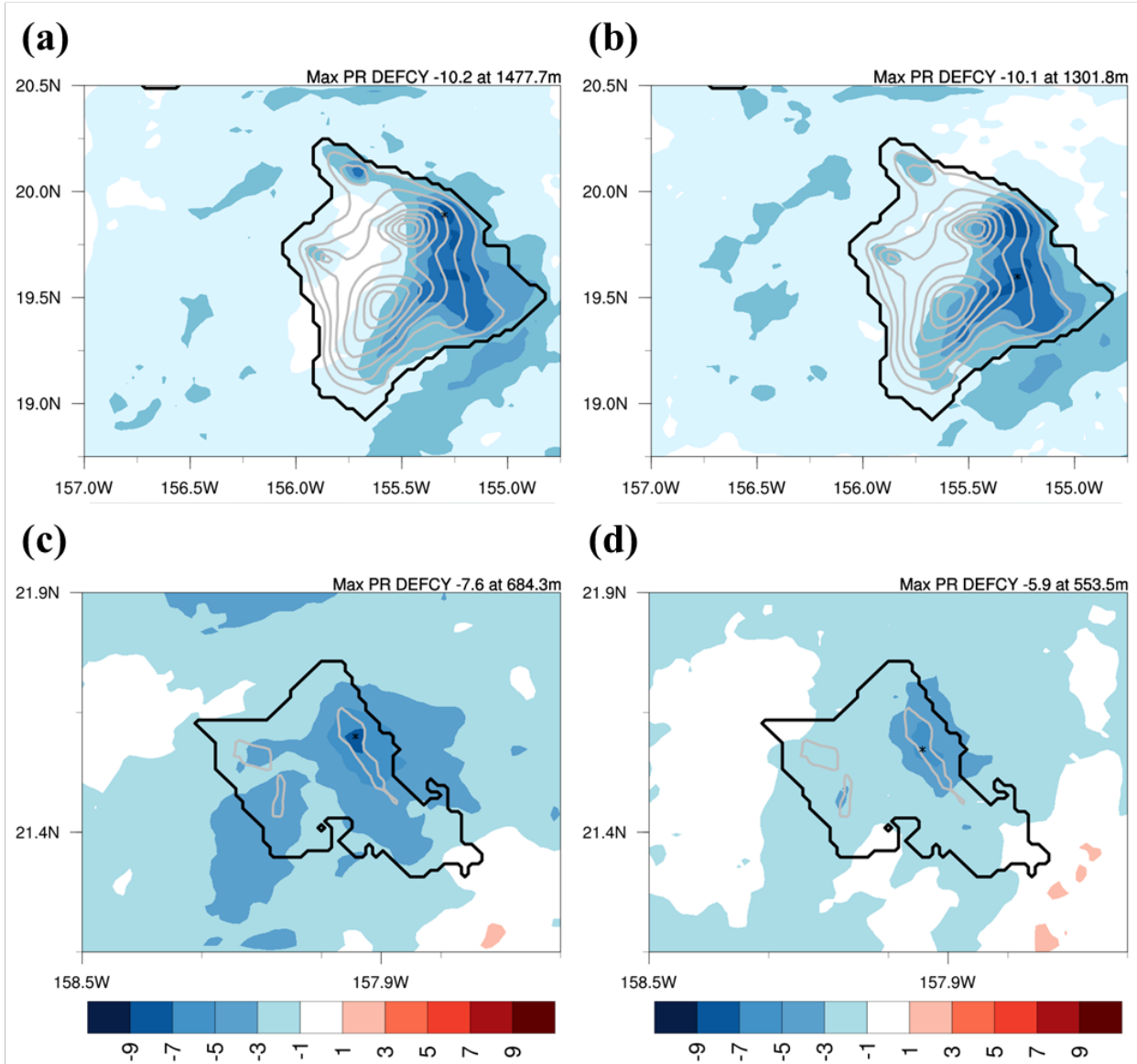


Fig. 6.43 The accumulated daily rainfall (mm, color shading) over Hawai'i Island during (a) CT winters, and (b) WP winters. (c) Same as (a), but over O'ahu Island. (d) Same as (b), but over O'ahu Island. Grey contours represent model elevation in 500 m intervals. Black asterisk represents the location of daily rainfall deficiency maximum.

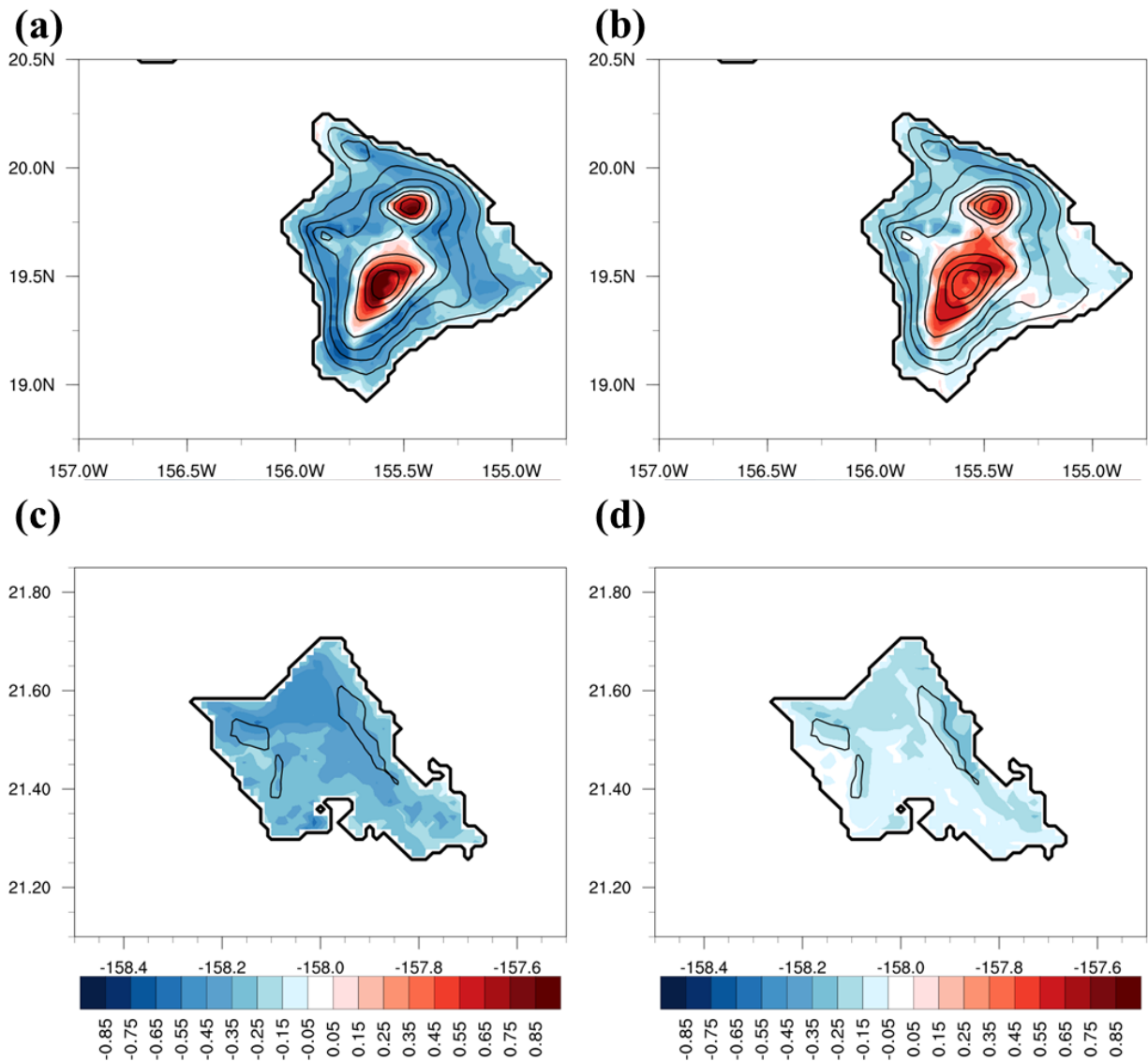


Fig. 6.44 The seasonal anomalies of simulated surface temperature (K, color shading) over Hawai'i Island during (a) CT winters and (b) WP winters. (c) Same as (a), but over O'ahu Island. (d) Same as (c), but over O'ahu Island. Black contours represent model elevation in 500 m intervals.

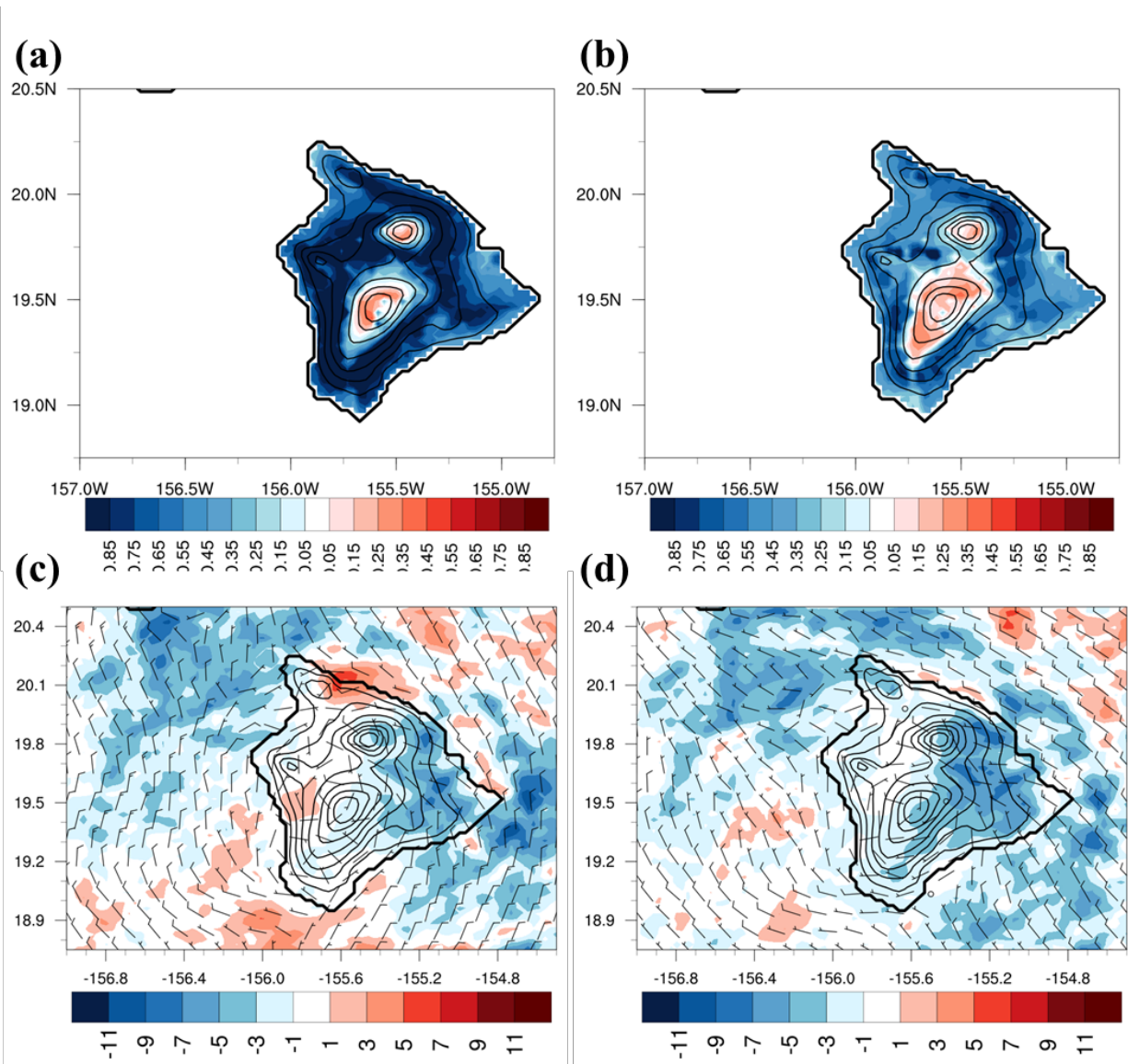


Fig. 6.45 AT 0500 HST, the seasonal anomalies of simulated surface temperature (K, color shading) over Hawai'i Island during (a) CT winters and (b) WP winters. At 0500 HST, the seasonal anomalies of simulated surface wind (m s^{-1} , wind barb) and rainfall anomalies (mm day^{-1} , color shading) over Hawai'i Island during (c) CT winters and (d) WP winters.

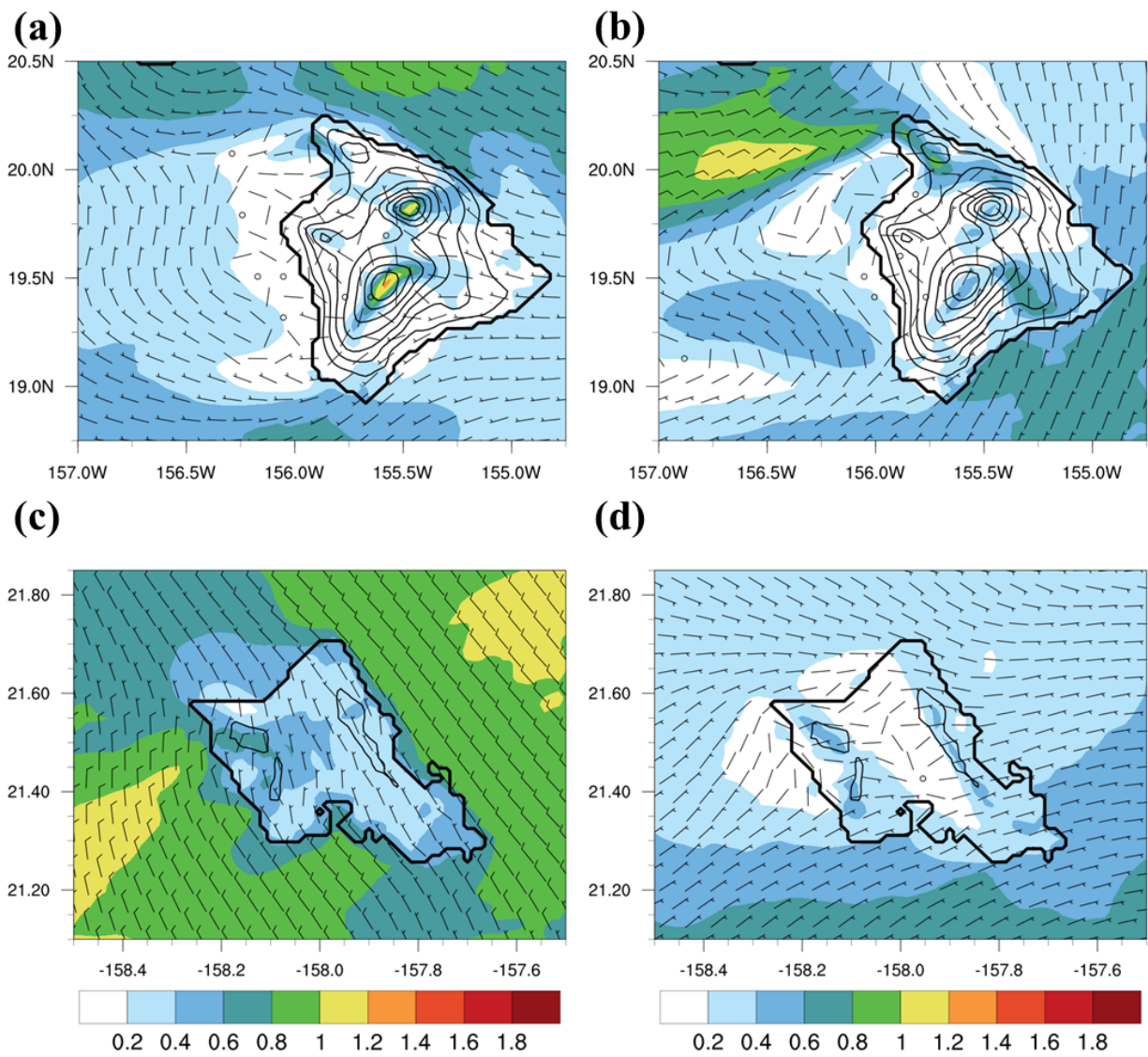


Fig. 6.46 Same as Fig. 6.41, but during springs.

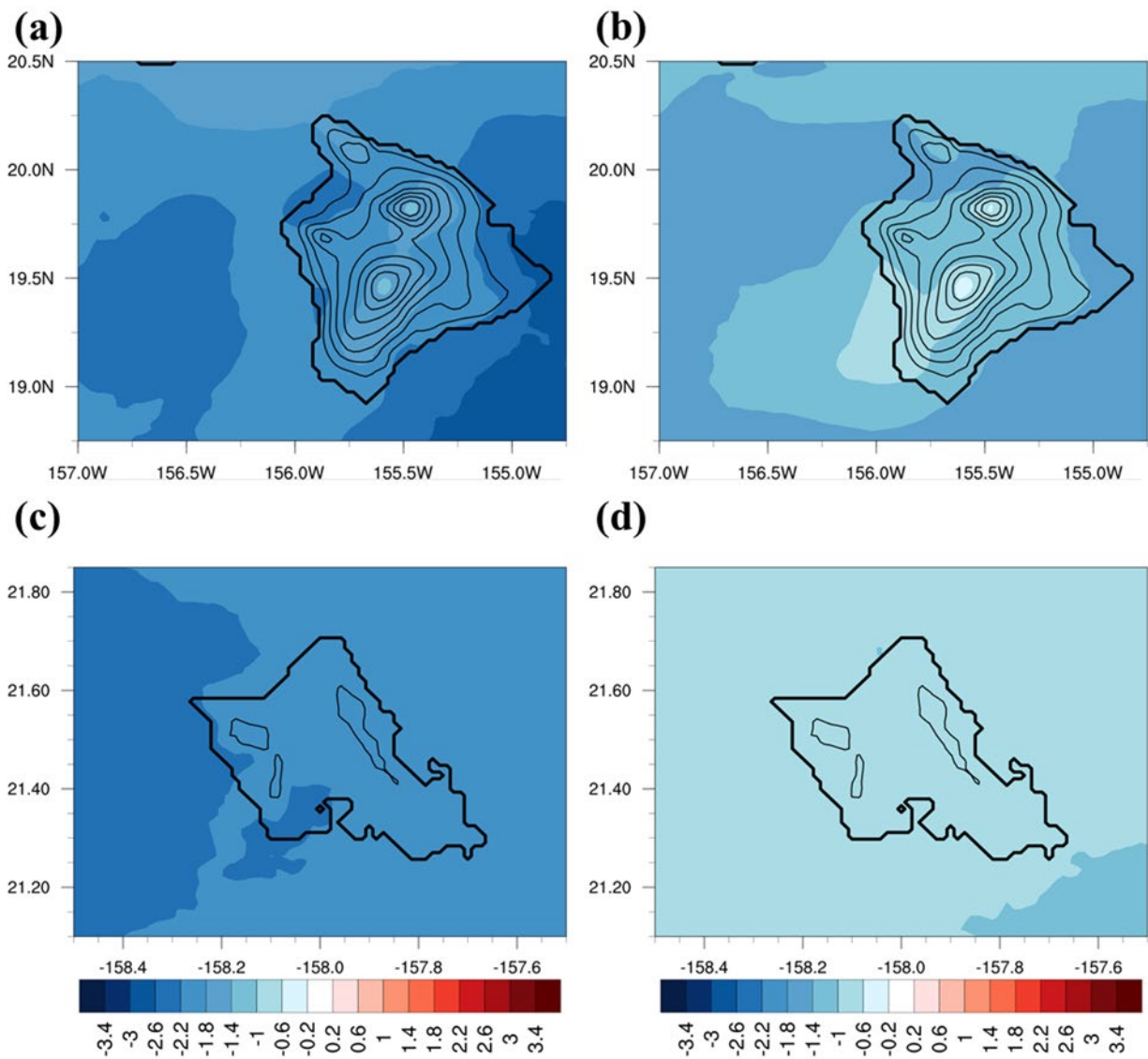


Fig. 6.47 Same as Fig. 7.42, but during springs.

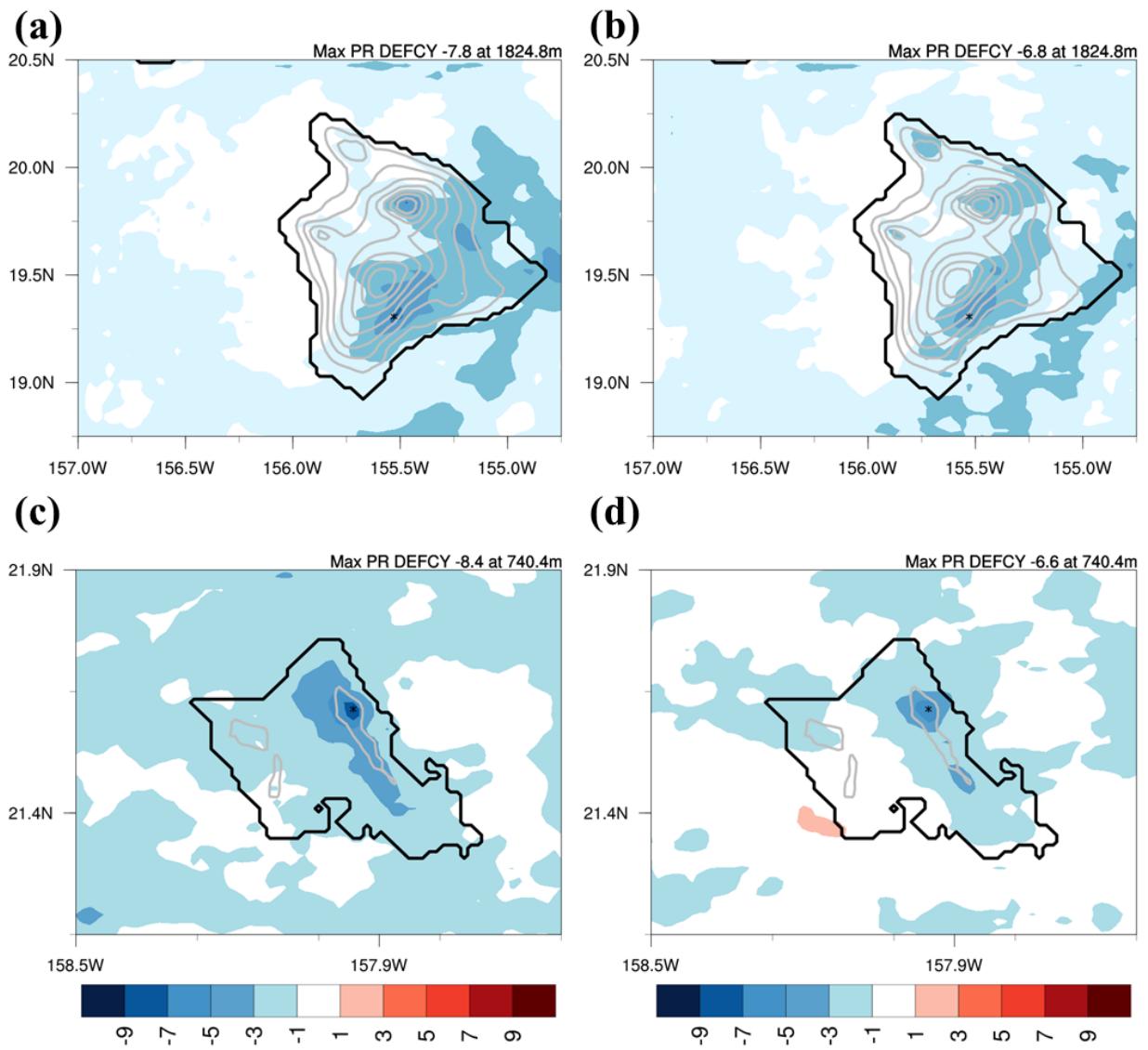


Fig. 6.48 Same as Fig.6.43, but during springs.

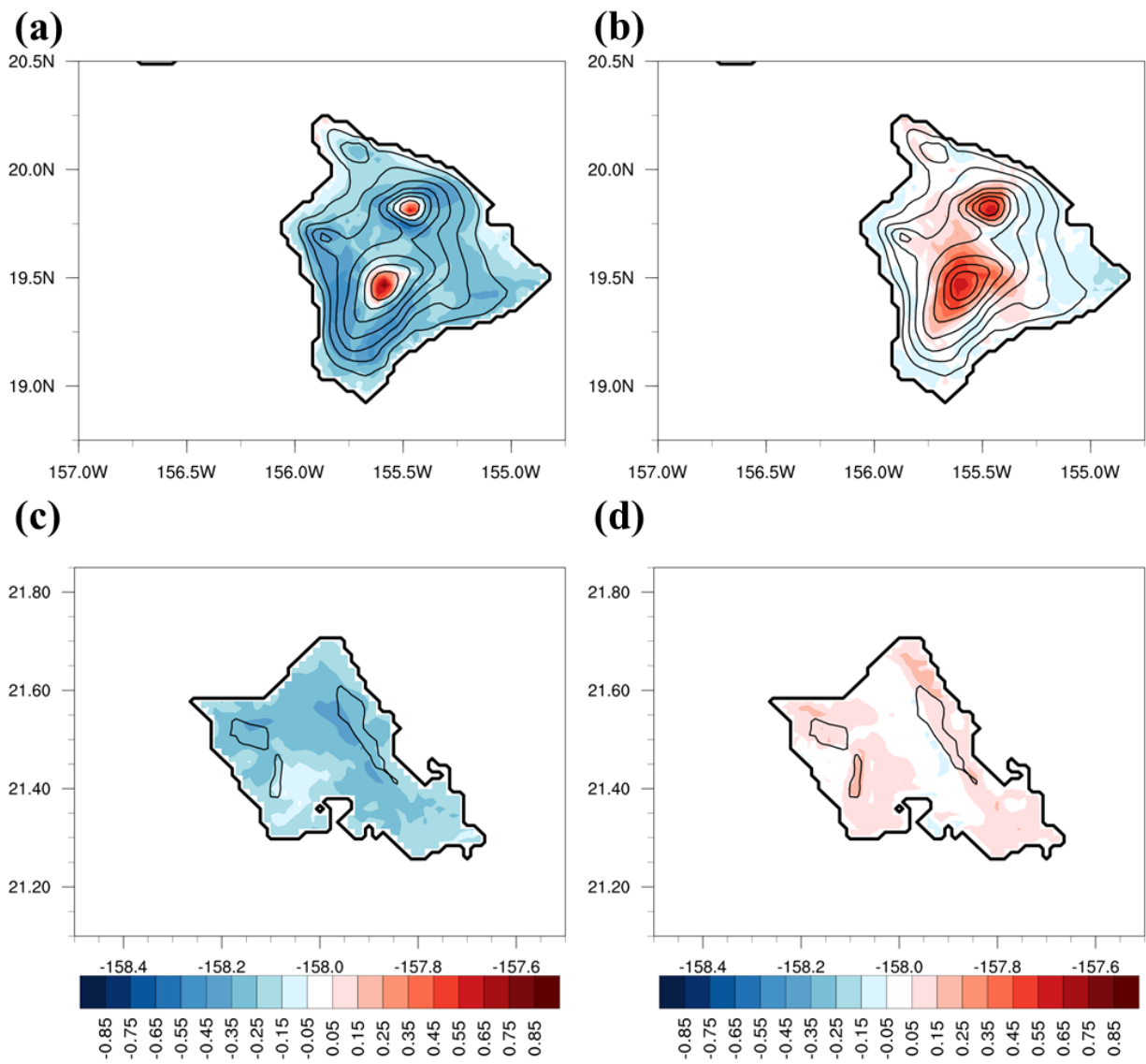


Fig. 6.49 Same as Fig. 6.44, but during springs.

Chapter 7 Discussion and Summary

Over isolated mountainous tropical and subtropical islands, rainfall enhancement is frequent due to terrain and local circulations. Rainfall modulated by terrain and locally-driven diurnal winds has been studied for various subtropical islands around the world. Many of these studies focus on orographic lifting, which "anchors" orographic clouds and rainfall over the ridge tops and windward slopes. According to observational studies, the Froude number and the orographic rainfall index may be used to better understand the rainfall enhancement over mountainous islands while simultaneously functioning as indicators for orographic rainfall. In contrast to orographic rainfall over windward slopes, which is positively correlated to the incoming wind speed, weather and rainfall under weak wind conditions over leeward wake zones and central island plains are less studied. These and other island effects are difficult to resolve using operational global models because of the relatively coarse model resolution.

Due to the presence of steep terrain, and sharp land–sea thermal gradients, rainfall distributions over Hawai'i have large spatial variations related to terrain and local winds (Giambelluca et al. 2013). Variations of microscale climate regimes ranging from humid tropical to hot and semi-arid, with diverse vegetation cover are common in the Hawaiian Islands. Considerable work in this area has been done in regards to the Island of Hawai'i, after the Hawaiian Rain Band Project (Chen et al. 1994; and others), and for the Island of Maui (Carlis et al. 2010). The goal of this research is to investigate the island effects on rainfall and cloud over various local communities for islands with mountain heights below the typical trade wind inversion height (e.g., O'ahu and Kaua'i). Furthermore, the island-scale rainfall during different El Niño flavors is localized in nature and related to terrain and local winds. Thus, fine-tuned island-scale models are used to diagnose and provide physical reasoning for the island-scale rainfall distributions for an island

with tops above the inversion (Hawai'i) and an island with tops below the trade-wind inversion (O'ahu). A well-validated high-resolution model is a valuable tool to study the island-scale flow response and island effects on rainfall, weather, and climate over different island communities under various large-scale settings, including different summer trade-wind conditions (Chapter 3), heavy rainfall events during seasonal transitions (Chapter 4), factors influencing summer trade wind rainfall (Chapter 5), and large-scale modes of climate variability, particularly those associated with difference El Niño types (Chapter 6).

1. Wake zone dynamics under trade wind conditions over O'ahu

Objective: Investigate the physical processes responsible for wake circulation and cloudiness under different trade-wind strengths for islands with mountaintops below the trade-wind inversion. The hypothesis that the afternoon westerly reversed flow off O'ahu's leeward coast is related to thermal forcing and/or warm advection from the island interior is investigated using observations and model simulations.

Yang et al. (2008) proposed a combination of mechanical lee side convergence of island-deflected airflows and warm advection to explain the circulation and cloud formation in the wake zone of Kaua'i in the afternoon hours. As the island interior heats up during the daytime hours, the trades advect warm air from the island to the wake zone, decreasing the air pressure. This enhances the low-level convergence off the leeward coast, resulting in more cloud trails in the wake zone. Nguyen et al. (2010) suggest that the afternoon lee-side wake circulations on the west side of Oahu are affected by not only warm air advection but latent heat release due to orographic precipitation.

To reexamine the aforementioned hypotheses, the circulations and cloud formations in the wake zone of O'ahu, an island with mountaintops below the trade-wind inversion, are analyzed

under trade wind conditions using observations and simulations. The summer of 2013, in which El Niño was in a neutral phase, is used to represent typical trade-wind conditions. In the absence of synoptic disturbances over the Central Pacific (e.g., tropical storms, upper-level lows/troughs, and shearlines associated with mid-latitude storms) typical trade wind conditions may be classified into strong ($>9.5 \text{ m s}^{-1}$) and weak trade ($<7.1 \text{ m s}^{-1}$) categories. In this dissertation, satellite data and model simulations are used to investigate the influence of trade wind strength on lee side wake circulations and cloudiness. The simulated surface wind, surface air temperature, and surface dew point during July–August 2013 are validated with surface observations.

For strong trades, with stronger winds moving down the Wai‘anae Mountains, the adiabatic warming and drying along the western leeside coast of O‘ahu is more significant. A mountain wave pattern is also simulated over the Wai‘anae Mountains. The daytime westerly onshore flow off the leeside coast is weaker or does not exist when trades are strong. Nevertheless, the wake zone extends farther downstream. Satellite observations show that high (>0.25) effective albedo occurs over the Ko‘olau Mountains at 1400 HST, resulting from orographic lifting under strong trades. The afternoon linear cloud trail over the wake zone is thin and weakly organized with an effective albedo maximum of ~ 0.1 .

For weak trades, westerly onshore flow develops over the western coast between 1100 HST – 1700 HST, with upslope flow over the western slopes of the Wai‘anae Mountains. The moist onshore flow is lifted by the Wai‘anae Mountains with an easterly return flow aloft. At 1400 HST, the effective albedo shows that orographic clouds are less extensive over the Ko‘olau Mountains as compared with strong trades. In contrast, the cloudiness over the Wai‘anae

Mountains is much greater, with high (>0.25) effective albedo, and extends westward into the wake zone.

Our model results, in agreement with satellite observations, show that in addition to orographic blocking, orographic lifting and thermally driven circulations due to solar heating are important for cloud formation over O‘ahu and its wake. Contradicting results from Yang et al. (2008), which showed that more offshore cloudiness under strong trades due to warm advection from heating island, the thin, narrow cloud trail extends further downstream from the central leeward coast under strong trades. During weak trades, the cloudiness over the Wai‘anae Mountains and wake zone and the afternoon westerly reversed flow are more significant. This is hypothesized to be the result of thermally induced afternoon sea-breeze circulations which are more pronounced under weak trades.

2. Short-lived afternoon heavy rainfall events over central O‘ahu during the warm season (May – October)

Objective: Investigate the initiation of convective storms over the Central O‘ahu Plain during the warm season under weak wind conditions using observations and high-resolution simulations

Over Central O‘ahu, between the Ko‘olau and Wai‘anae mountain ranges, winds are relatively weak with low rainfall frequency ($<5\%$) and amount ($<1 \text{ mm day}^{-1}$) in the afternoon hours during the warm season (May–October). Occasionally, short-lived afternoon heavy rainfall events form over central O‘ahu under weak wind ($<3 \text{ m s}^{-1}$) conditions. An event of this type (8 June 2003) is selected for a detailed case study. This event reveals that the favorable large-scale settings include a deep moist layer with relatively high TPW ($>40 \text{ mm}$),

a northeast–southwest moist tongue from low latitudes ahead of an upper-level trough, relatively high CAPE ($> 900 \text{ J kg}^{-1}$) values in the absence of a trade wind inversion, and weak ($< 3 \text{ m s}^{-1}$) low-level winds.

Our nested 1.5 km high-resolution model domain results show that afternoon land surface heating deepens the mixed layer to the lifting condensation level in the late morning. Land surface heating results in increased temperature and specific humidity in the mixed layer as it grows deeper after sunrise. The convective available potential energy also increases over central O‘ahu as the day progresses. Furthermore, with land/sea thermal contrast under weak surface winds, sea breezes develop along the coasts bringing in warm, moist marine air over the island interior. Finally, convergence of the onshore flows over central O‘ahu provides the localized lifting for the release of instability.

Model sensitivity tests are performed to address the role of orographic effects and land surface forcing in the development of short-lived afternoon heavy rainfall events over central O‘ahu. After removing the model topography but keeping the land surface (NO run), the destabilizing effects of daytime heating, horizontal advection of warm, moist maritime air inland by the onshore/sea-breeze flows, localized convergence over central O‘ahu, and the subsequent development of heavy showers over land are still simulated. In contrast to both the control run and the NO runs, when model surface fluxes are turned off (NF runs), convective cells are not simulated in the area even though large-scale conditions are favorable.

To confirm the results of the case study, high-resolution simulations are conducted for all 13 heavy rainfall cases over central O‘ahu under weak wind conditions identified during the 2000–2015 period. These events all formed during the seasonal transition period between the cool (warm) and warm (cool) season. Similar to the 8 June 2003 case, the large-scale settings

for these events are characterized by the presence of a moist tongue from the tropics with large TPW and CAPE values and weak ($< 3 \text{ m s}^{-1}$) south/southeasterly surface winds prior to the arrival of an upper-level trough. The 13 control simulations are validated with surface and radar observations. For all these cases, the heavy afternoon rainfall over central O'ahu is successfully simulated in agreement with radar observations.

Model simulations and sensitivity tests indicate that under weak south/southeasterly flow with a moisture tongue extending from the deep tropics, and favorable large-scale settings, the daytime heating is crucial for the growth of the mixed layer, increase of potential instability, development of daytime onshore/sea breezes, and generation of localized convergence over central O'ahu. As a result, deep convection develops over the relatively flat terrain of central O'ahu within the localized convergence zone leading to the occurrence of heavy rainfall events.

3. Factors affecting orographic precipitation over Kaua'i under summer trade-wind conditions

Objective: To study the orographic precipitation during the summer months over the island of Kaua'i and discuss the factors (e.g. mountain height, steepness of terrain, and geo-location) that affect orographic rainfall over Kaua'i using model sensitivity tests.

A previous observational study over the island of Hawai'i (Carbone et al. 1998) showed a strong positive linear relationship between the rainfall over the windward side and the Froude number (Fr). For example, the rainfall maximum increases to 10 times the oceanic average with elevated Fr (> 0.3). In contrast, for Fr below typical trade wind conditions (< 0.3) the maximum rainfall is only five times greater than over the open ocean. Carbone et al. (1998) suggest that the rainfall production on the windward side of the Island of Hawai'i is statistically

related to the strength of orographic blocking as defined by Fr and modeled by Smolarkiewicz et al. (1988).

In addition to upstream wind speed, stability, and mountain height, the steepness of the terrain will affect orographic precipitation (Alpert 1986; Lin et al. 2001). The orographic rainfall index (ORI) has been proposed as a predictor of orographic precipitation (Nieman et al. 2002, 2008, 2009). In the moisture budget equation $[\frac{\partial q}{\partial t} = -\nabla_h(\mathbf{V}_h q) - \frac{\partial}{\partial p}(\omega q) - (c - e)]$ used by Tu et al. (2012), the primary contribution to the total rainfall production in the subtropics comes from the vertical integral of vertical moisture flux, which mostly results from vertical moisture flux at the surface ($\omega_s q_s$). ORI, which includes moisture and low-level vertical motion, is an approach of vertically integral of vertical moisture flux. However, under undisturbed summer trade-wind weather, the moisture flux convergence over mountainous islands is related to orographic and local effects, which is not considered in ORI

The mountaintops of O‘ahu and Kaua‘i are 1220 m and 1,98 m, respectively, well below the typical height of the trade wind inversion (~ 1.9 km, Winning et al. 2017). Moreover, the mountaintop of Wai‘ale‘ale Mountains over Kaua‘i is well known as one of the wettest spots on earth. To study the orographic rainfall during the summer months over Kaua‘i, the period of July – August 2013 is selected to represent the typical trade wind conditions due to its comparability with the patterns of TPW and trade wind conditions in the long-term summer climatology. Simulated surface winds and rainfall over both islands are validated with observations from surface weather stations and rain gauges. Model sensitivity tests are used to investigate the island flow response and orographic rainfall differences due to differences in terrain height, steepness of terrain, and geographic location.

For the CTRL run, the ENE trade wind airflow decelerates along the windward coastal areas and is deflected to the NNE along the southern windward slopes of Wai‘ale‘ale Mountains as a result of island blocking. The simulated rainfall pattern of the CTRL run shows a local maximum over the northern part of Wai‘ale‘ale Mountains, the mountaintop of Wai‘ale‘ale Mountains, and the mountaintop of Makaleha Mountains (a mountain range on northeastern side of Kaua‘i). The simulated rainfall pattern is generally consistent with the distribution of observed rainfall.

In the reduced terrain height sensitivity test (RTH), the mountaintop of Wai‘ale‘ale Mountains is reduced to the height of the Ko‘olau Mountains (~800 m, 54% of the CTRL terrain height). With lower mountaintops and unaltered U and N , the Fr of the RTH runs (~1) is greater than CTRL (~0.7) for Kaua‘i. The simulated airflows over windward Wai‘ale‘ale Mountains decelerate from 5 m s⁻¹ upstream to 2.5 m s⁻¹ due to terrain blocking but airflow deflection over the island becomes insignificant. The trade wind rainfall over Wai‘ale‘ale Mountains (6.9 mm day⁻¹) is about 43% that of CTRL (15.8 mm day⁻¹), and rainfall gradients between the windward coast (~1 mm day⁻¹) and the mountaintops (6.9 mm day⁻¹) decrease. The position of the rainfall maximum, which is still simulated at the mountaintops, is relatively uninfluenced by Fr or terrain steepness. In contrast to Carbone et al. (1998), with larger Fr , the simulated rainfall maximum of RTH is only 43% of the rainfall maximum of CTRL. With lower terrain height and more gently sloped terrain in RTH, orographic lifting on the slopes is less significant than in CTRL.

In the RTH run for Kaua‘i, the mountaintop of Wai‘ale‘ale Mountains is close to the height of the Ko‘olau Mountains (~800 m) on O‘ahu. Nevertheless, the simulated rainfall amount over the mountaintop of Wai‘ale‘ale Mountains (6.9 mm day⁻¹) is lower than the simulated

rainfall over the Ko‘olau Mountains (11.8 mm day^{-1}). The orographic lifting on the windward side of O‘ahu is more significant than the windward side of Kaua‘i because of steeper terrain. To investigate the effects of steepness further, we shrink the island of Kaua‘i in the E-W direction (SZ run) under trade wind conditions, and although the Fr is the same as in the CTRL run the mountain terrain is steeper in the E-W direction. With a steeper terrain, orographic blocking is more significant with greater flow deflection over the windward slope of Wai‘ale‘ale Mountains. Rainfall is primarily simulated over Wai‘ale‘ale Mountains (17.4 mm day^{-1}) and Makaleha Mountains (11.5 mm day^{-1}) in the SZ run with a significant rainfall gradient from the windward coast ($\sim 3 \text{ mm day}^{-1}$) to the mountaintops ($>10 \text{ mm day}^{-1}$). With a steeper mountain slope, the effect of orographic lifting becomes more significant in the distribution of rainfall. Despite the Fr being the same between the SZ and CTRL runs (~ 0.7), the simulated rainfall on the windward slopes and over the peaks of Wai‘ale‘ale Mountains is higher (17.4 mm day^{-1} vs. 15.8 mm day^{-1}) in SZ than CTRL. The location of the rainfall maximum also shifts 1 km westward as compared to the CTRL run. The results of the sensitivity test attest to the importance of factoring in terrain steepness in the modeling of island scale rainfall gradients and the prediction of rainfall amount ($\sim 10\%$ increment). The steepness is included in the estimation of orographic precipitation using ORI.

In addition to steepness, rainfall production may also be related to the moisture amount in the environment. Our analysis shows that the synoptic environment of Kaua‘i also has more moisture than O‘ahu during July–August 2013. The rainfall over the Wai‘anae Mountains is much less than over the Ko‘olau Mountains due to the removal of moisture by orographic precipitation over the Ko‘olau Mountains (Nguyen et al. 2010). Relocating O‘ahu to the location of Kaua‘i (RL) results in higher rainfall (14.0 mm day^{-1}) than its original location

(11.8 mm day⁻¹) but still lower rainfall compared with the Kaua‘i control run (15.8 mm day⁻¹). It is shown from moisture budget calculations that the higher rainfall over Wai‘ale‘ale Mountains than the ridge tops of the Ko‘olau Range is attributed two factors: higher TPW in the environment of Kaua‘i and more significant orographic lifting due to stronger winds impinging on the windward slopes of higher mountaintops.

In the moisture budget equation, orographically induced moisture flux convergence and orographic lifting at the slope surface are the two most dominant terms in regions with sloping terrain. The storage term is insignificant for monthly time averaging. Under undisturbed summer trade-wind weather, the moisture flux convergence over mountainous islands is related to orographic and local effects, including: flow deceleration on the windward side due to orographic blocking, interactions between the incoming flow and offshore flow due to nocturnal and/or evaporative cooling, and convergence between the incoming winds and opposing sea breezes in the leeward side. Furthermore, moisture flux convergence is enhanced by latent heat release. The vertical lifting by winds on the slope surface could be attributed to mechanical lifting and modified by daytime upslope and nighttime downslope winds. Therefore, previous theoretical arguments concerning orographic precipitation based on *Fr* or ORI are inadequate to account for the orographic precipitation amount under undisturbed trade-wind conditions. The orographically induced moisture convergence and convective feedbacks are largely ignored.

4. Island-scale flow response to El Niño events (O‘ahu vs. Hawai‘i Island)

Objective: Determine the influence of different El Niño flavors on the regional-scale climate patterns and island-scale rainfall and weather for the island of O‘ahu, which has mountains

and ridges with tops below the trade wind inversion, and for the island of Hawai‘i, which has high mountains extending well above the trade wind inversion, using global analyses, simulated regional climate patterns, and downscaled island-scale climate.

4.1 Large-scale settings

The El Niño-Southern Oscillation (ENSO) is a prominent mode of climate variability at the inter-annual time scale. It is well known that during the negative phase of ENSO (El Niño), Hawai‘i experiences droughts in winter, which continue into the following spring (Chu and Chen 2005). Chu (1995) suggested that the droughts affecting Hawai‘i during El Niño are related to the eastward expansion of the upper-level jet and that the State of Hawai‘i is on the right-hand side of the jet exit region with enhanced upper-level subsidence. Recent studies have shown that there are two different flavors of El Niño [east Pacific type/Cold Tongue (CT) and central Pacific type/warm pool (WP)] that influence the global climate in various ways (Kao and Yu 2009; Murphy et al. 2014; and others). The El Niño cases studied by Chu (1995) and others were mainly CT type El Niños. In this section, the differences in large-scale circulations between the two types of El Niño events over the Pacific Ocean during the cold season (winter and spring) and the impacts of these differences on seasonal circulations over Hawai‘i will be reexamined using NCEP CFSR data with a 0.5 x 0.5-degree grid during the 1979 – 2017 period.

The CT and WP events are defined by the Niño-CT index and Niño-WP index (Ren and Jin 2011) using Niño3 and Niño4 SST indices from the NOAA Climate Prediction Center. Five CT (1982/1983; 1986/1987; 1991/1992; 1997/1998; 2015/2016) and six WP (1990/1991; 1994/1995; 2002/2003; 2004/2005; 2009/2010; 2014/2015) events are analyzed within a seasonal composite.

a) El Niño winters

During both types of El Niño events, the enhanced subsidence over the Hawaiian Island chain during winter is not only related to upper-level convergence on the right-hand side of the upper-level jet exit region as suggested by Chu (1995) but also the enhanced, thermally induced, sinking motion in the subtropics due to a stronger ITCZ in the central equatorial Pacific and an eastward shift of the Walker circulation.

During the CT winters, large-scale subsidence is more significant over Hawai‘i than during the WP winters due to increased upward vertical motion over the equatorial central Pacific related to an enhanced Hadley circulation and a merging of the ITCZ with SPCZ. During the CT winters, the upper-level jet extends farther eastward to 140°W. Anomalous convergence is found over the jet core (35°N, 170°E), extending southeastward to the Hawaiian Islands. The upper-level jet of the WP winters only reaches 135°W, and anomalous convergence is limited to the jet core. Over the Hawaiian Islands, mean TPW during both the CT and WP winters is lower than the climatological winter mean due to anomalous subsidence. The TPW anomaly during the CT winters is -3 mm, significantly lower than during the WP winters (~-1 mm).

During the CT winters, a deeper Aleutian Low (55°N, 150°W) with enhanced westerlies north of Hawai‘i is evident. Anomalous northwesterly wind associated with the Aleutian Low and a subtropical ridge extending eastward over the Hawaiian Islands result in weakened trade wind speeds (~4 m s⁻¹) as compared with the long-term winter mean (~5 m s⁻¹). For the WP winters, with westerly anomalies associated with a deeper Aleutian Low (45°N, 160°W), the trade wind speed over the Hawaiian region is also slower (~3 m s⁻¹) as compared to the winter climatology. The increasing of the temperature gradient between the Arctic and the tropics

produces an upper-level jet which extends eastward during El Niño winter, especially during the CT winters.

b) El Niño springs

In spring, the low-level tropical convergence over the equatorial central Pacific is weaker during both types of El Niño than in winter due to decreasing SST anomalies. The upper-level jets associated with the CT and WP springs both retreat east of 170°E, but the anomalous upper-level convergence over the Hawaiian Islands is found only during the CT springs. During the CT springs, the rising motions associated with the Walker circulation remain over the mid-Pacific with persistent dry conditions and negative TPW anomalies (~ -2 mm) over Hawai‘i as compared with the long-term spring composite. The stronger Aleutian Low during the CT winters is also evident during the CT springs, but is not quite as strong.

For the WP springs, the TPW field exhibits positive anomalies (~ 1 mm) over the Hawaiian region. The magnitude of the Aleutian Low is comparable to the long-term mean, and the anomalous westerly winds associated with the deeper Aleutian Low during the WP winters are absent. The trade wind conditions over the Hawaiian Islands are similar to the long-term spring mean.

A regression of the Global Precipitation Climatology Project (GPCP) precipitation data with 2.5° resolution onto Niño-CT and Niño-WP indices from 1979–2017 reveals a dry anomaly during the CT events. For WP events, however, the rainfall over the Hawaiian Islands is close to the climatological average.

4.2 Regional domain simulations with a 6-km grid over Hawai‘i

The impacts of both types of El Niño events on regional circulations and thermodynamic variables over Hawai‘i during the winter and spring seasons are addressed using simulations

with a 6-km domain. A recent study by Huang and Chen (2019) shows that in addition to large-scale subsidence, trade-wind speed and TPW are two important factors affecting seasonal variations in the island flow response and orographic rainfall distributions over the island of Hawai‘i.

a) El Niño winters

An analysis of the anomalies within the simulations with a 6-km grid size from 1979–2017 indicates that the trade wind speed decreases during both CT and WP events. When comparing the difference in the composite wind between CT and WP winters, the trade wind speed is higher ($\sim 1 \text{ m s}^{-1}$) during the CT winter than during the WP winter. During the CT winters, the mean TPW is 4 mm less than the long-term winter mean with northwesterly wind anomalies ($\sim 1 \text{ m s}^{-1}$) over the Hawaiian Islands. The CT winters are warmer and drier than the long-term winter mean at 700 hPa over Hawai‘i with anomalous subsidence. For the WP winters, the Hawaiian Islands are marked by -2 mm TPW anomalies and westerly wind anomalies ($\sim 1.5 \text{ m s}^{-1}$). During the WP winters, the warm and dry conditions at 700 hPa are less significant as compared to the CT winters due to weaker anomalous subsidence.

In the 6-km simulations, the negative rainfall anomalies of the CT winters are more significant than those of the WP winters due to significant synoptic subsidence and lower TPW values. The spatial patterns of the rainfall anomalies for CT and WP winters are discussed in the section pertaining to the island-scale domains.

b. El Niño springs

Analysis of the CT springs shows similar patterns as the CT winters with northwesterly wind anomalies and negative TPW anomalies. In comparing the CT springs with CT winters, the wind speed anomalies ($\sim 1 \text{ m s}^{-1}$) and TPW anomalies (-2 mm) are smaller during CT

springs. In contrast, the TPW anomalies during the WP springs are 1 mm lower with northerly wind anomalies ($\sim 0.5 \text{ m s}^{-1}$). The TPW during the CT events is less than during the WP events, and the drought conditions are less significant in El Niño spring than El Niño winter.

4.3 Island-scale El Niño climates for Hawai‘i and O‘ahu

Most of the previous studies concerning El Niño drought conditions over the Hawaiian Islands have focused on CT events without assessing the impacts of these events on local microclimates. The differences in island-scale local climates during the two types of El Niño events are presently addressed using high-resolution WRF model output for the first time. Since the island circulation is dependent on whether the mountain tops are above or below the trade wind inversion (Leopold 1949; Chen and Feng 2001; Nguyen et al. 2010), five CT, six WP and five El Niño neutral events during winter and spring are simulated with an island-scale model over O‘ahu (1.5-km grid) and Hawai‘i Island (3-km grid). The simulated rainfall patterns are comparable to the Rainfall Atlas of Hawai‘i (Giambelluca et al. 2013).

a) El Niño winters

For the island of Hawai‘i, the prevailing wind during the CT winters shows more northerly wind component as compared to the neutral winters. The TPW is lower over the island (~ 2 mm) during the CT winters, especially over the windward coast and wake zone (~ 3 mm). With prevailing NNE winds and lower TPW, the simulated rainfall composite for the island of Hawai‘i reveals drier conditions during the CT winters than during neutral winters. The maximum rainfall deficiency ($>9 \text{ mm day}^{-1}$) is simulated over the windward slopes of Mauna Kea and Mauna Loa (between 1000 to 2000 m in elevation). The second rainfall deficiency maximums (4 mm day^{-1}) occur over the Kona leeward coast and the Kohala Mountains. The

portion of the island least affected by rainfall deficiency during the CT winters is along the northeastern coast ($\sim 1 \text{ mm day}^{-1}$). This is due to orographic lifting of the incoming NNE flow.

During the WP winters, the prevailing ENE trade wind speed is weaker ($\sim 1 \text{ m s}^{-1}$) and the simulated rainfall is less compared to the neutral winters, with less TPW (-1 mm). The maximum rainfall deficiency ($\sim 9 \text{ mm day}^{-1}$) is simulated over the windward slopes of Mauna Kea and Mauna Loa (between 1000 to 1500 m). The second rainfall deficiency maximum ($\sim 7 \text{ mm day}^{-1}$) is over the Kohala Mountains ($\sim 1000 \text{ m}$). The southwestern coast has the least difference in rainfall ($< 1 \text{ mm day}^{-1}$) between the WP winters and the neutral winters.

For O‘ahu, the increased northerly wind component is more significant ($> 1 \text{ m s}^{-1}$) than for the island of Hawai‘i during the CT winters. With less TPW, the simulated rainfall during the CT winters is also less than during the neutral winters. The maximum rainfall deficiency is simulated over the Ko‘olau Mountains (7 mm day^{-1}). The next most important rainfall deficiencies ($4\text{--}5 \text{ mm day}^{-1}$) are simulated over the Wai‘anae mountaintop and along the southern flank of the Wai‘anae Mountains.

During the WP winters, weakened trade wind speed and low TPW are associated with less simulated rainfall than during the neutral winters, especially over mountainous regions. The rainfall deficiencies are 6 mm day^{-1} over the of Ko‘olau mountaintop and $2\text{--}3 \text{ mm day}^{-1}$ over the Wai‘anae Mountains. The rainfall deficiencies over the other regions are relatively small ($1\text{--}2 \text{ mm day}^{-1}$). The dryness which occurs during the WP winters is less significant than during the CT winters.

Simulated temperatures above and below the trade wind inversion are also modified by the ENSO cycle. For O‘ahu and the areas below the trade wind inversion on the island of Hawai‘i, nighttime cooling is more significant ($0.45 \text{ K}\text{--}0.75 \text{ K}$), due to less available water vapor,

during the CT and WP winters than during neutral winters. Conversely, for mountaintops above the trade wind inversion, the simulated temperature tends to be warmer during the CT and WP winters due to stronger descending motion by the Hadley circulation. For the CT winters, the warming above the trade wind inversion is greater (~ 0.85 K) than during WP winters (~ 0.45 K). The cooling over the area below the trade wind inversion is also more evident during the CT winters (~ 0.2 K) than during the WP winters (~ 0.1 K). Furthermore, enhanced nighttime cooling below the trade wind inversion strengthens katabatic flows. Hence, the nocturnal rainfall before sunrise off the Kona coast, caused by the convergence of katabatic flows with the westerly return flow offshore, is greater during El Niño years.

b) El Niño springs

During the CT springs, over the island of Hawai'i, the trade wind speed is slightly weaker with a northwesterly wind anomaly (0.4 m s^{-1}) off the windward coast and less TPW (-2.2 mm) compared to neutral springs. The simulated rainfall is less over the windward slope of Mauna Loa with a 7 mm day^{-1} rainfall deficiency maximum. The accentuated nighttime cooling due to lower TPW is still evident during the CT springs, with lower (~ 0.35 K) surface temperature over the regions below 2.5 km in elevation than during the neutral springs. For the regions above 2.5 km, warmer surface temperature due to increased subsidence (~ 0.55 K) is still present.

Over the island of Hawai'i, the wind anomalies are mainly northerly over the windward side (0.8 m s^{-1}) and westerly over the wake zone (0.6 m s^{-1}). The TPW during the WP springs is less (-1.0 mm) compared to the neutral springs. The simulated rainfall is also less over the windward slope of Mauna Loa (-6 mm day^{-1}) but slightly greater off the southwestern coast ($<1 \text{ mm day}^{-1}$). Nighttime cooling is less significant (~ 0.05 K) than during CT winters due to

lesser TPW anomalies. Warming above the trade wind inversion during the WP springs is greater than during the CT springs.

For O‘ahu, the wind direction anomalies between the CT springs and the neutral springs are northwesterly ($0.6\text{--}0.8\text{ m s}^{-1}$), indicating weakening trade winds during the CT springs. With less TPW ($\sim 1.5\text{ mm}$) and weaker trades, the rainfall along the Ko‘olau Mountains during the CT springs is less than during neutral years with maximum rainfall deficiency (8 mm day^{-1}) at the mountaintop. The pattern of rainfall deficiency along the Ko‘olau Mountains also extends westward to central Oahu. The rainfall deficiency along the Wai‘anae mountaintop is relatively small ($<2\text{ mm day}^{-1}$) compared to the Ko‘olau mountaintop.

During the WP springs, the wind anomalies are easterly ($0.4\text{--}0.6\text{ m s}^{-1}$) and the TPW is 0.6 mm less than during neutral springs. With slightly increased trade wind speed and slightly lower TPW, the maximum rainfall deficiency occurs over the Ko‘olau mountaintop (6 mm day^{-1}). For an island with mountaintops below the trade wind inversion, the thermal effects on wake circulations are expected to produce more rainfall over the leeside under weak trade wind conditions. Nevertheless, less rainfall is simulated over the southwestern coasts ($\sim 1\text{ mm day}^{-1}$) during the CT springs than during the WP springs, resulting from less TPW during the CT springs. In the afternoon, the simulated surface temperature during the WP springs is warmer over land than during neutral springs. The warmer surface temperatures over land suggests that the thermally driven circulation over the wake zone would be more significant than during neutral springs, resulting in more rainfall over the southwestern coast.

In summary, during El Niño events, enhanced subsidence by the Hadley circulation and low TPW throughout the region lead to drought conditions over the Hawaiian Islands, especially in winter. For an island with mountaintops above the trade-wind inversion, during

the CT winters, less rainfall is simulated over windward slopes than during WP winters due to weaker trade wind speed and less moisture. Drought conditions are expected during the CT winters over the mountaintops of Mauna Kea and Mauna Loa and in the leeward side of the Kohala Mountains due to a -65% change in seasonal rainfall. During the WP winters, the lack of moisture over the mountaintops of Mauna Kea and Mauna Loa is not as profound as during the CT winters.

During the CT springs, persistently weak trade wind speed and low TPW result in maximum rainfall deficiencies over the windward slopes and mountaintops below the trade wind inversion. However, the dry conditions over the windward slopes are less significant than during the CT winters. Similar to the CT winters, drought conditions are expected over the mountaintops of Mauna Kea and Mauna Loa and the leeward side of the Kohala Mountains with a negative change in the rainfall percentage. The only region with greater simulated rainfall during the CT springs is off the Kona coast, before sunrise, resulting from the convergence of katabatic flows with the westerly winds offshore. The rainfall distributions during the WP springs are quite similar to those during the CT springs, however, the dry conditions are less significant due to higher TPW in the environment.

For islands with mountaintops below the trade-wind inversion, increased synoptic subsidence and low TPW are crucial in creating drier or even drought conditions over the windward slopes, e.g. the Ko'olau Mountains on O'ahu during the CT winters. Rainfall amounts over the Ko'olau mountaintop are therefore lower during the CT winters than the WP winters, despite stronger trade winds. The percent change of rainfall indicates that droughts are likely over the southwestern coast during the CT winters as well. During the WP winters, the dry conditions over O'ahu are less significant than during the CT winters.

In spring, the rainfall over the Ko‘olau Mountains decreases substantially (6-8 mm day⁻¹) for both types of events. The droughts during the CT springs are more significant over mountainous regions as compared to the WP springs. More rainfall is simulated over the southwestern coasts in the afternoon hours during the WP springs than during the CT springs due to enhanced thermally driven circulations over the leeward coasts. During the WP springs, the surface daytime temperature over land is warmer as compared to the CT springs. During both types of El Niño events, the nighttime cooling accentuated by less atmospheric water vapor affects the simulated surface temperatures over the regions below the trade wind inversion. For island regions above the trade wind inversion, surface warming is accentuated by increased subsidence associated with the Hadley circulation. The diurnal variations of airflow circulation and rainfall in response to surface temperature changes will be analyzed in future work.

Reference

- Austin, G. R., R. M. Rauber, H. T. Ochs III, and L. J. Miller, 1996: Trade wind clouds and Hawaiian rainbands. *Mon. Wea. Rev.*, **124**, 2126-2151.
- Banta, R. M., 1990: The role of mountain flows in making clouds. Chapter 9 in Atmospheric Processes over Complex Terrain. *Meteor. Monogr.*, No. **45**, Amer. Meteor. Soc., 229-284.
- Blumenstock, D. I., and S. Price, 1967, Climate of Hawai'i. In: *Climates of the States*, No. 60-51, Climatography of the United States, U.S. Department of Commerce.
- Burk, S.D. T. Haack, L. T. Rogers, and L. J. Wagner, 2003: Island wake dynamics and wake influence on the evaporation duct and radar propagation. *J. Appl. Meteor.*, **42**, 349–367.
- Burroughs, L. D., and R. N. Larson, 1979: Wave clouds in the vicinity of Oahu Island, Hawaii. *Mon. Wea. Rev.*, **107**, 608-611.
- Carbone, R. E., W. A. Cooper, and W. C. Lee, 1995: On the forcing of flow reversal along the windward slopes of Hawaii. *Mon. Wea. Rev.*, **123**, 3466-3480.
- Carlis, D., L., Y.-L. Chen, and V. Morris, 2010: Numerical simulations of island-scale airflow and the Maui vortex during summer trade-wind conditions. *Mon. Wea. Rev.*, **138**, 2706-2736.
- Chen, F., and J. Dudhia, 2001a: Coupling an advanced land surface–hydrology model with the Penn State/NCAR MM5 modeling system. Part I: model implementation and sensitivity. *Mon. Wea. Rev.*, **129**, 569-585.

- , and ——, 2001b: Coupling an advanced land surface–hydrology model with the Penn State–NCAR MM5 modeling System. Part II: preliminary model validation. *Mon. Wea. Rev.*, **129**, 587–604.
- Chen, Y.-L., and J. Feng, 1995: The influence of inversion height on precipitation and airflow over the Island of Hawaii. *Mon. Wea. Rev.*, **123**, 1660-1676.
- , and ——, 2001: Numerical simulations of airflow and cloud distributions over the windward side of the island of Hawaii. Part I: the effects of trade wind inversion. *Mon. Wea. Rev.*, **129**, 1117-1134.
- , and A. J. Nash, 1994: Diurnal variation of surface airflow and rainfall frequencies on the island of Hawaii. *Mon. Wea. Rev.*, **122**, 34-56.
- , and J. J. Wang, 1994: Diurnal variation of surface thermodynamic fields on the island of Hawaii. *Mon. Wea. Rev.*, **122**, 25-38.
- Chu, P.-S., 1995: Hawaii rainfall anomalies and El Nino. *J. of Climate*, **8**, 1698-1703.
- Chu, P.-S., and H. Chen, 2005: Interannual and interdecadal rainfall variations in the Hawaiian Islands. *J. Climate*, **18**, 4796-4813.
- Dudhia, J., 1989: Numerical study of convection observed during the Winter Monsoon Experiment using a meso-scale two-dimensional model. *J. Atmos. Sci.*, **46**, 3077– 3107.
- Esteban, M. A., and Y.-L. Chen 2008: The impact of trade wind strength on precipitation over the windward side of the Island of Hawaii. *Mon. Wea. Rev.*, **136**, 913-928.

- Feng, J., and Y.-L. Chen, 1998: The evolution of katabatic flow on the island of Hawaii during 10 August 1990. *Mon. Wea. Rev.*, **126**, 2185-2199.
- , and ———, 2001: Numerical simulations of airflow and cloud distributions over the windward side of Hawaii. Part II: Nocturnal flow regime. *Mon. Wea. Rev.*, **129**, 1135-1147.
- Foote, D. E., E. L. Hill, S. Nukaman, and F. Stephens, 1972: Soil survey of the islands of Kauai, Oahu, Maui, Molokai, and Lanai, State of Hawaii. USDA Soil Conservation Service and the University of Hawaii Agriculture Experiment Station. 232pp.
- Frye, J. L. and Y.-L. Chen, 2001: Evolution of downslope flow under strong opposing trade winds and frequent trade-wind rainshowers over the island of Hawaii. *Mon. Wea. Rev.*, **129**, 956-977.
- Garza J. A., P.-S. Chu, C.W. Norton, T. A. Schroeder, 2012: Changes of the prevailing trade winds over the islands of Hawaii and the North Pacific. *J. Geophys. Res.*, **117**, D11109, doi:10.1029/2011JD016888.
- Garrett, A. J., 1980: Orographic clouds over the eastern slopes of Mauna Loa Volcano, Hawaii, related to insolation and wind. *Mon. Wea. Rev.*, **108**, 931-941.
- Giambelluca, T.W., Q. Chen, A.G. Frazier, J.P. Price, Y.-L. Chen, P.-S. Chu, J.K. Eischeid, and D.M. Delparte, 2013: Online Rainfall Atlas of Hawai'i. *Bull. Amer. Meteor. Soc.* **94**, 313-316.
- , M. A. Nullet, and T. A. Schroeder, 1986: Rainfall atlas of Hawaii. Report R76, Dept. of Land and Natural Resources, State of Hawaii, Honolulu, HI, 267 pp.

- Hartley, T., and Y.-L. Chen, 2010: Characteristics of summer trade-wind rainfall over Oahu. *Wea. Forecast.*, **25**, 1797-1815.
- Hitzl, D.E., Y.-L. Chen and H.V. Nguyen, 2014: Numerical simulations and observations of airflow through the 'Alenuihaha Channel, Hawaii. *Mon. Wea. Rev.*, **142**, 4696-4718.
- Hong, S.-Y., Y. Noh, and J. Dudhia, 2006: A new vertical diffusion package with an explicit treatment of entrainment processes. *Mon. Wea. Rev.*, **134**, 2318–2341, doi:10.1175/MWR3199.1.
- Huang, Y.-F., and Y.-L. Chen, 2019: Numerical simulations of seasonal variations of rainfall over the Island of Hawai'i. *J. Appl. Meteor. and Climate*
- , and J.-O. J. Lim, 2006: The WRF single-moment 6-class microphysics scheme (WSM6). *J. Korean Meteor. Soc.*, **42**, 129–151.
- Hudson, J. G., 1993: Cloud condensation nuclei. *J. Appl. Meteor.*, **32**, 596–607.
- Janjic', Z. I., 1994: The step-mountain eta coordinate model: Further developments of the convection, viscous sublayer, and turbulence closure schemes. *Mon. Wea. Rev.*, **122**, 927–945, doi:10.1175/1520-0493(1994)122,0927:TSMECM.2.0.CO;2.
- , 2000: Comments on “Development and evaluation of a convection scheme for use in climate models.” *J. Atmos. Sci.*, **57**, 3686, doi:10.1175/1520-0469(2000)057,3686:CODAEO.2.0.CO;2.

- Jayawardena, S., Y.-L. Chen, A.J. Nash and K. Kodama, 2012: A comparison of three prolonged periods of heavy rainfall over the Hawaiian Islands. *J. Appl. Meteor. and Climate*, **51**, 722-744.
- Jiménez, P. A., J. Dudhia, J. F. González-Rouco, J. Navarro, J. P. Montávez, and E. García-Bustamante, 2012: A revised scheme for the WRF surface layer formulation. *Mon. Wea. Rev.*, **140**, 898–918, doi:10.1175/MWR-D-11-00056.1.
- Kao, H.-Y., and J.-Y. Yu, 2009: Contrasting eastern-Pacific and central-Pacific types of ENSO. *J. Climate*, **22**, 615–632.
- Kodama, K. R, and G. M. Barnes, 1997: Heavy rain events over the south-facing slopes of Hawaii: Attendant conditions. *Wea. Forecast.*, **10**, 347-367.
- Kug, J.-S., F.-F. Jin, and S.-I. An, 2009: Two types of El Niño events: Cold tongue El Niño and warm pool El Niño. *J. Climate*, **22**, 1499–1515.
- Lane, T. P., R. D. Sharman, R. G. Frehlich, and J. M. Brown, 2006: Numerical simulation of the wake of Kauai. *J. Appl. Meteor. Climatol.*, **45**, 1313–1331.
- Lavoie, R.L., 1967. Air motions over the windward coast of the island of Hawaii. *Tellus*, **19**, 354-358.
- , 1974: A numerical model of trade wind weather on Oahu. *Mon. Wea. Rev.*, **102**, 630 –637.
- Leopold, L. B., 1949: The interaction of trade wind and sea breeze, Hawaii. *J. Meteor.*, **8**, 533-541.

- Li, J., and Y.-L. Chen, 1999: A case study of nocturnal rainshowers over the windward coastal region of the island of Hawaii. *Mon. Wea. Rev.*, **127**, 2674-2692.
- Li, L. and Y.-L. Chen, 2017: Numerical Simulations of Two Trapped Mountain Lee Waves Downstream of Oahu. *J. Appl. Meteor. and Climate*, **56**, 1305-1324.
- Li, N., Cheung, K. F., Stopa, J. E., Hsiao, F., Chen, Y.-L., Vega, L., and Cross, P.: Thirty-four years of Hawaii wave hindcast from downscaling of climate forecast system reanalysis, *Ocean Model.*, **100**, 78–95, 2016.
- Loos, T. M., 2004: Diurnal Variation of Island Scale Weather over Oahu and Kauai during Summer Months. M.S. thesis, University of Hawaii, 254pp. [Available from Department of Meteorology, University of Hawaii, 2525 Correa Rd. Honolulu, HI, 96822]
- Lyons S. W., 1982: Empirical Orthogonal Function Analysis of Hawaiian Rainfall. *J. Appl. Meteor.*, **21**, 1713–1729.
- Mlawer, E. J., S. J. Taubman, P. D. Brown, M. J. Iacono, and S. A. Clough, 1997: Radiative transfer for inhomogeneous atmospheres: RRTM, a validated correlated-k model for the longwave. *J. Geophys. Res.*, **102** (D14), 16 663–16 682.
- Murphy, M. J., & Businger, S. (2011). Orographic Influences on an Oahu Flood. *Monthly Weather Review*, *139*(7), 2198–2217. <http://doi.org/10.1175/2010MWR3357.1>
- NCEI, 2017: Storm Events Database. NOAA, accessed 7 June 2017. [Available online at <http://www.ncdc.noaa.gov/stormevents.>]

- Nguyen, H. V., Y.-L. Chen, and F. M. Fujioka, 2010: Numerical simulations of island effects on airflow and weather during the summer over the island of Oahu. *Mon. Wea. Rev.*, **138**, 2253-2280.
- Nickerson, E. C., and M. A. Dias, 1981: On the existence of atmospheric vortices downwind of Hawaii during HAMEC project. *J. Appl. Meteor.*, **20**, 868-873.
- Nullet, D. and M. Mcgranaghan, 1988: Rainfall Enhancement over the Hawaiian Islands. *J. Climate*, **1**, 837-839.
- NWS, 2007: *Storm Data* preparation. National Weather Service Instruction 10-1605, 97 pp. [Available online at <http://www.nws.noaa.gov/directives/sym/pd01016005curr.pdf>.]
- Ramage, C. S., and T. A. Schroeder, 1999: Trade wind rainfall atop Mount Waialeale, Kauai. *Mon. Wea. Rev.*, **127**, 2217-2226.
- Rasmussen, R. M., P. K. Smolarkiewicz, and J. Warner, 1989: On the dynamics of Hawaiian cloud bands: comparison of model results with observations and island climatology. *J. Atmos. Sci.*, **46**, 1589-1608.
- Rasmussen, E. M., and T. H., Carpenter, 1982: Variations in tropical sea surface temperature and surface wind fields associated with the Southern Oscillation/ El Niño. *Mon. Wea. Rev.*, **110**, 354-384.
- Reisner, J. M., and P. K. Smolarkiewicz, 1994: Thermally forced low Froude number flow past three-dimensional obstacles. *J. Atmos. Sci.*, **51**, 117-133.

- Ren, H.-L., and F.-F. Jin, 2011: Niño indices for two types of ENSO. *Geophys. Res. Lett.*, **38**, L04704.
- Ropelewski, C. F., and M. S. Halpert, 1987: Global and regional scale precipitation patterns associated with the El Niño/Southern Oscillation. *Mon. Wea. Rev.*, **115**, 1606-1626.
- , and ———, 1989: Precipitation patterns associated with the high index phase of the Southern Oscillation. *J. of Climate*, **2**, 268-284.
- Sato, H. H., W. Ikeda, R. Paeth, R. Smythe, and M. J. Takehiro, 1973: Soil survey of the islands of Hawaii, State of Hawaii. USDA Soil Conservation Service and the University of Hawaii Agriculture Experiment Station, 196pp.
- Saha, S., and Coauthors, 2010: The NCEP Climate Forecast System reanalyses. *Bull. Amer. Meteor. Soc.*, **91**, 1015–1057.
- Saha, S., and Coauthors, 2014: The NCEP Climate Forecast System version 2. *J. Climate*, **27**, 2185–2208, <https://doi.org/10.1175/JCLI-D-12-00823.1>.
- Schär, C., and D. R. Durran, 1977: Vortex formation and vortex shedding in continuously stratified flows past isolated topography. *Atmos. Sci.*, **54**, 534-554.
- , and R. B. Smith, 1993: Shallow-water flow past isolated topography. Part I; Vorticity production and wake formation. *J. Atmos. Sci.*, **50**, 1373-1400.
- Schroeder, T., 1981: Characteristics of local winds in northwest Hawaii. *J. Appl. Meteor.*, **20**, 874-881.

- , 1993: Climate controls. *Prevailing Trade Winds*, M. Sanderson, Ed., University of Hawaii Press, 12-36.
- , B. Kilonsky, and B. Meisner, 1977: Diurnal variation in rainfall and cloudiness. *Water Resources Research Center Technical Report No. 112*.
- Scorer, R. S., 1949: Theory of waves in the lee of mountains. *Quart. J. Roy. Meteor. Soc.*, **75**, 41–56, doi:10.1002/qj.49707532308.
- , 1952: Mountain-gap winds—A study of the surface wind at Gibraltar. *Quart. J. Roy. Meteor. Soc.*, **78**, 53–59.
- Skamarock, W. C., and J. B. Klemp, 2008: A time-split non-hydrostatic atmospheric model for weather and forecasting applications. *J. Comput. Phys.*, **227**, 3465–3485, doi:10.1016/j.jcp.2007.01.037.
- Smith, R. B., 1982: Synoptic observations and theory of orographically disturbed wind and pressure. *J. Atmos. Sci.*, **39**, 348-364.
- , 1989: Mountain-induced stagnation points in hydrostatic flow. *Tellus*, **41A**, 270-274.
- , and V. Grubišić, 1993: Aerial observations of Hawaii's wake. *J. Atmos. Sci.*, **50**, 3728-3750.
- , P. Schafer, D. J. Kirshbaum, and E. Regina, 2009: Orographic precipitation in the tropics: Experiments in Dominica. *J. Atmos. Sci.*, **66**, 1698–1716, doi:10.1175/2008JAS2920.1.
- , and Coauthors, 2012: Orographic precipitation in the tropics: The Dominica Experiment. *Bull. Amer. Meteor. Soc.*, **93**, 1567–1579, doi:10.1175/BAMS-D-11-00194.1.

- Smolarkiewicz, P. K, and R. Rotunno 1990: Low Froude number flow past three-dimensional obstacles. Part II: upwind flow reversal zone. *J. Atmos. Sci.*, **47**, 1498-1511.
- , R. M. Rasmussen, and T. L. Clark, 1988: On the dynamics of Hawaiian cloud bands: Island Forcing. *J. Atmos. Sci.*, **45**, 1872-1905.
- Takahashi, T., 1977: Rainfall at Hilo, Hawaii. *J. Meteor. Soc. Japan*, **55**, 121-129.
- , 1988: Long-lasting trade-wind showers in a three-dimensional model. *J. Atmos. Sci.*, **45**, 3333-3353.
- Tu, C.-C., and Y.-L. Chen, 2011: Favorable conditions for the development of a heavy rainfall event over Oahu during the 2006 wet period. *Wea. Forecast*, **26**, 280-300.
- Ueyoshi, K., J. O. Roads, F. Fujioka, and D. E. Stevens, 1996: Numerical Simulation of the Maui Vortex in the trade-winds. *J. Meteor. Soc. Japan*, **74**, 723-744.
- USGS, 1986: Land use and land cover digital data from 1:250,000- and 1:100,000-scale maps' data user guide 4, U.S. Geological Survey, Reston, VA, 36 pp.
- Wang, J.-J., and Y.-L. Chen, 1995: Characteristics of near-surface winds and thermal profiles on the windward slopes of Hawaii. *Mon. Wea. Rev.*, **123**, 3481-3501.
- , and ———, 1998: A case study of trade-wind rainbands and their interaction with the island-induced airflow, *Mon. Wea. Rev.*, **126** 409-423.
- , ———, K. Kodama, S. Businger, Y.-L. Chen, and J. Partain, 1998: Application of the NCEP Regional Spectral Model to improve mesoscale weather forecasts in Hawaii., *Wea. Forecasting*, **13**, 560-575.

- Winning, T., Y.-L. Chen, F. Xie, 2017: Estimation of the Marine Boundary Layer Height Over the Central North Pacific Using GPS Radio Occultation. *Atmos. Res.* **183**, 362-370 (doi:10.1016/j.atmosres.2016.08.005)
- Worthley, L. E., 1967: Synoptic climatology of Hawai'i. Weather Phenomena in Hawai'i, Part I. Hawai'i Institute of Geophysics Rep.67-9, 1-40. [Available from Dept. of Meteorology, University of Hawai'i at Manoa, Honolulu, HI 96822.]
- Yang, Y., and Y.-L. Chen, 2003: Circulations and rainfall on the lee side of the island of Hawaii during HaRP. *Mon. Wea. Rev.*, **131**, 2525-2542.
- , and ———, 2008: Effects of terrain heights and sizes on island-scale circulations and rainfall for the island of Hawaii during HaRP. *Mon. Wea. Rev.*, **136**, 120-146.
- , ———, and F. M. Fujioka, 2005: Numerical simulations of the island-induced circulations over the island of Hawaii during HaRP. *Mon. Wea. Rev.*, **133**, 3693-3713.
- , ———, and ———, 2008a: Effects of trade-wind strength and direction on the leeside circulations and rainfall of the island of Hawaii. *Mon. Wea. Rev.*, **136**, 4799-4818.
- , S.-P. Xie, and J. Hafner, 2008b: The thermal wake of Kauai Island: Satellite observations and numerical simulations. *J. Climate*, **21**, 4568-4586.
- Yeh, S.-W., J.-S. Kug, B. Dewitte, M. H. Kwon, and B. P. Kirtman, 2009: El Niño in a changing climate. *Nature*, **461**, 511-514.
- Zhang, Y., Y.-L. Chen, T. A. Schroeder, and K. Kodama, 2005a: Numerical simulations of sea breeze circulations over northwest Hawaii. *Wea. Forecast.*, **20**, 827-846.

——, ——, and K. Kodama, 2005b: Validation of the coupled NCEP Mesoscale Spectral Model and an advanced Land Surface Model over the Hawaiian Islands. Part II: A high wind event. *Wea. Forecast.*, **20**, 873-895.

——, ——, S.-Y. Hong, H.-M. H. Juang, and K. Kodama, 2005c: Validation of the coupled NCEP Mesoscale Spectral Model and an advanced Land Surface Model over the Hawaiian Islands. Part I: Summer trade wind conditions and a heavy rainfall event. *Wea. Forecast.*, **20**, 847-872.